Conception et Modélisation des Dispositifs de Biocaptage à Base de Nanotubes de Carbone

C. Roman

INSTITUT NATIONAL POLYTECHNIQUE DE GRENOBLE

N° attribué par la bibliothèque
|__/__/__/__/__/__/__/__/__/__|

T H E S E

pour obtenir le grade de

DOCTEUR DE l'INPG

Spécialité : Microélectronique

préparée au laboratoire **TIMA** dans le cadre de
l'Ecole Doctorale d'« Electronique, Electrotechnique, Automatique, Télécommunications, Signal »

présentée et soutenue publiquement

par

Cosmin Ioan ROMAN

Le 06 juillet 2006

Titre :

MODELISATION DE DISPOSITIFS A BASE DE NANOTUBES DE CARBONE POUR LA DETECTION DE BIOMOLECULES

Directeur de Thèse : Bernard Courtois

JURY

M. Pierre GENTIL,	Président
Mme. Hélène BOUCHIAT,	Rapporteur
M. Adrian IONESCU,	Rapporteur
M. Stephan ROCHE,	Examinateur
M. Bernard COURTOIS,	Directeur

Acknowledgements

As I am writing these acknowledgements I realize that a thesis, or for that matter all human creation, is not the result of some individualistic effort, but rather the enfoldment of a network of human interactions. Several contributions stem from this activity, various in form and importance. There are people without whom this thesis would simply have not existed. There are others that helped me improve or advance my work and knowledge. And finally there are still others that helped me maintain the mood necessary to surmount the ups and downs of the long thesis process.

I would start by thanking Mr. Bernard Courtois for receiving me at TIMA, for accepting to supervise my thesis and for offering me the freedom to pursue the research topic of my choice. I also appreciate TIMA's funding that allowed me present my work at several conferences, sometimes far away from France. I feel the need to thank in this context the French Ministry for Education, Research and Technology (MENRT) for offering me a research grant, and France in general for hosting me.

I am most grateful to Mr. Pierre Gentil for his support in quality of Doctoral School director. His advice and benevolence has helped me overcome the stressing period precluding the defense. I would also like to thank him for accepting to chair the committee of my thesis.

I would like to acknowledge the defense committee Ms. Hélène Bouchiat, Mr. Adrian Ionescu and Mr. Stephan Roche for accepting to review my thesis. I have to stress the fact that their work is entirely voluntary. They are all recognized scientists in their field, and obviously time is an extremely precious resource for them. They have accepted however to sacrifice their time and undertake the job of reviewing my work, without any apparent benefit. Their remarks have helped me improve both my

dissertation and defense speech. I am also grateful for their advice in helping me find the best continuation for my career. To Mr. Stephan Roche I would also like to thank for his uncountable technical advices during the thesis; he has been a second supervisor to me.

Florin Ciontu is one of those men that have convinced me (indirectly) that destiny and predetermination exist, and that certain people appear in life precisely to help one make a sharp angle turn in life. His point of view has been of invaluable impact both during the thesis and in life in general. Without him, this thesis, as it is, would have not existed.

I would like to acknowledge the (non)scientific support and numerous discussions I had during my thesis with Misters Skandar Basrour, Salvador Mir, Libor Rufer and Emmanuel Simeu. To Nacer Zergainoh and Kholdoun Torki I have to thank for helping me orient my career, for their friendliness and cheerful nature.

I wish to thank Isabelle Amielh for her exceptional kindness and help in administrative matters. She has corrected the French of my detailed summary in her own spare-time for which I am deeply indebted.

I am finally approaching in my listing those people that influenced on other planes my work. It is hardly expressible in words the gratefulness I feel for the person that has shared with me all these years both the joys and hardships of life. Let's hope that in the future, I will have to offer my fiancée, Iuliana, only joys to share. Another pylon of my life is my mother who I would like to thank for her unconditional love and for her unyielding determination. I am grateful to my future mother- and father-in-law for guiding me towards TIMA and their help in life and at the Polytechnic Institute in Bucharest.

For indirectly shaping my past, present and future I would like to express my gratitude to Barbu Constantinescu, whose way of living will always inspire me in trying to become a better human being.

I wish to express my deepest gratitude to God for giving me the opportunity to evolve.

Sommaire détaillé

Les dernières années ont vu l'émergence des applications des nanotechnologies, alors que dans un avenir proche il est raisonnable de prévoir que les nanotechnologies vont pénétrer des domaines d'application principaux comme l'énergie, les matériaux, les dispositifs électroniques etc. Le développement explosif des nanotechnologies a été animé par les progrès considérables accomplis dans la fabrication contrôlée et la manipulation des nanostructures.

Découverts il y a quinze ans par Sumio Iijima [**1**] les nanotubes de carbone (NTC) sont devenus rapidement les fanions de la nanotechnologie avec les nanoparticules, les nanofils, les fullerenes et les couches moléculaires. Les nanotubes existent en plusieurs variétés et peuvent être classifiés par leur hélicité (appelée chiralité plus tard), nombre de feuillets, la présence des pentagones-heptagones dans leur structure, etc. La forme la plus simple est le nanotube de carbone monofeuillet (SWNT), qui peut être visualisé comme une feuille de graphite, ressemblant à un nid d'abeilles, roulée dans un cylindre.

Si les nanotubes de carbone occupent le rôle qu'ils ont aujourd'hui, cela est exclusivement dû à leurs exceptionnelles propriétés structurales, mécaniques, électroniques et optiques. Du point de vue électronique, seul le changement de la direction de roulement du graphite, a pour résultat des tubes métalliques ou semi-conducteurs. Les tubes métalliques sont des conducteurs balistiques sur des longueurs de l'ordre du micromètre, capables de ce fait de supporter très efficacement des courants sans perte de puissance par effet Joule. Ceci signifie également que les nanotubes peuvent soutenir des densités de courant énormes. Les tubes semi-conducteurs ont un bandgap dépendant de leur diamètre, et possèdent des mobilités de porteurs surpassant de loin ceux du matériel archétypal de l'électronique, le silicium.

En se rapportant aux propriétés mécaniques, les nanotubes de carbone sont souvent appelés "les fibres ultimes"; ils sont aussi durs que le diamant. Néanmoins les nanotubes restent flexibles grâce à leur facteur d'aspect (rapport longueur-diamètre) élevé. Ils peuvent aussi supporter des déformations de quelques pourcents tout en restant élastiques. La liste de leurs avantages ne doit pas s'arrêter ici, puisque les nanotubes de carbone possèdent des propriétés optiques, thermiques, électromécaniques et magnétiques également intéressantes.

Bien que de mieux en mieux contrôlée, la synthèse des nanotubes de carbone implique des mécanismes qui ne sont pas parfaitement compris à l'heure actuelle. Cette chaîne manquante est directement responsable de l'incapacité de synthétiser des nanotubes avec des propriétés contrôlés, et est probablement la raison principale pour laquelle les NTC ne sont pas employés sur une plus grande échelle. Toutefois des progrès géants sont faits chaque jour dans la synthèse [**3**, **4**, **5**], la functionalization [**6**, **7**, **8**], la solubilisation [**9**, **10**] et le triage [**11**, **12**] des nanotubes. Etant donné cette tendance, il est raisonnable d'extrapoler que dans les années à venir il sera possible d'avoir des nanotubes avec des propriétés bien contrôlées, aux coûts inférieurs, engendrant une pléthore d'applications.

Hormis ceci, un aspect essentiel laisse envisager la conception des dispositifs à base de nanotubes est l'accord toujours meilleur entre les prévisions théoriques et les données expérimentales. Comme note latérale, c'est par des calculs théoriques simples que la nature métallique-semiconducteur des nanotubes, leurs modules de Young et les transitions optiques ont été prédits dès tout début. Tandis qu'une partie importante des efforts de recherches sur les NTC se concentre sur l'amélioration des techniques de fabrication et de manipulation, une autre partie augmente sans interruption la compréhension physique des nanotubes, et d'autres essayent de développer des applications.

Une courte analyse de l'activité de brevetage sur des applications à base de nanotubes de carbone indique que les zones principales sont occupées par l'émission de champ, le stockage d'énergie, les composites, la nanoélectronique, les capteurs et les actionneurs, etc. Dans chacune de ces applications possibles les nanotubes sont loin de réaliser leur potentiel. D'ailleurs d'autres applications sont rajoutées à cette liste chaque jour. Nous pouvons alors sans risque dire que le secteur de recherches

d'applications à base de nanotubes est toujours dans sa petite enfance offrant beaucoup d'occasions de développement.

Dans cette thèse nous nous sommes focalisés sur l'application possible des nanotubes de carbone dans la détection biochimique ayant une vraie importance pour les biotechnologies, la médecine et même pour la défense et la sécurité. Notre but principal est d'avancer les modèles théoriques des nanotubes et de les employer en tant qu'outils prédictifs, non pas dans le but de calculer des propriétés fondamentales, mais plutôt pour concevoir des potentiels dispositifs d'intérêt pratique. De ce fait, le modèle général de cette thèse consiste à proposer des dispositifs de captage et à les modeler et les simuler comme preuve de concept, parfois doublée par des assertions de faisabilité basées sur des modèles semblables expérimentalement prouvés.

Valider théoriquement des dispositifs potentiels est évidemment le choix le moins coûteux dans un contexte où la manipulation des nanotubes est encore limitée, lente et par conséquence coûteuse. Ceci ne signifie pas nécessairement qu'on doive accepter la validité des calculs sans y réfléchir, au moins dans les approximations grossières parfois utilisées. Dans cette situation une idée serait d'établir des modèles théoriques suffisamment rapides et précis au moins à un premier ordre. Si le dispositif proposé s'avérait opérationnel en théorie il pourrait alors être pratiquement réalisé et caractérisé, rapportant des données qui pourraient être employées pour améliorer les modèles théoriques. Un avantage additionnel de la simulation est l'intuition gagnée dans les mécanismes intimes d'opération d'un dispositif.

Parfois les modèles utilisés dans cette thèse peuvent sembler plutôt simples au lecteur, et en effet ils le sont. Cependant on doit se rappeler que le grand nombre d'atomes qu'un dispositif de captage typique peut avoir est un goulot d'étranglement important. Le problème récurrent dans cette thèse est une certaine dépendance carrée ou cubique dans le nombre d'atomes qui peut rendre la simulation intraitable. Bien que le but des nanotechnologies soit de miniaturiser des dispositifs et de diminuer ainsi le nombre d'atomes, il existe souvent des simulations qui impliquent 10^5 atomes ou même plus. Le stockage d'une matrice ayant $10^5 \times 10^5 = 10^{10}$ éléments est coûteux mais ce n'est rien comparé au temps de calcul nécessaire pour inverser ou diagonaliser une telle matrice qui exigerait $(10^5)^3$ opérations. Ceci explique les différentes approches numériques que nous avons été forcés d'adopter pour résoudre les différents problèmes.

Nous proposons deux architectures différentes de capteur dans cette thèse. Le premier capteur implique un principe électromécanique et peut être utilisé pour mesurer des forces faibles de quelques piconewtons ou des masses de quelques zeptograms. Le deuxième capteur est basé sur les changements de conductance qu'un nanotube de carbone éprouverait une fois exposé aux acides aminés aromatiques. Les deux dispositifs ont des applications intéressantes dans la détection biochimique.

Le contenu de cette thèse est divisé en cinq chapitres. Le **Chapitre I** présente une brève introduction à la structure et aux propriétés des nanotubes de carbone. Des éléments cristallographiques de base comme les vecteurs de translation, la première zone de Brillouin etc. sont établis à partir de ceux du graphite. La structure électronique du graphene basé sur le modèle classique de liaisons fortes sera employée pour arriver à la structure de bande des nanotubes en imposant des conditions aux limites périodiques. Nous avons insisté ici à présenter seulement ces propriétés qui sont relevantes pour cette thèse, à savoir les propriétés de transport de charge et les propriétés mécaniques. Les sections correspondantes contiennent à part des prévisions théoriques, des mesures expérimentales qui généralement sont en bon accord avec la théorie.

Dans le **Chapitre II** nous détaillons la théorie de transport quantique dans les nanostructures pour le cas général des dispositifs multi-terminaux. Les deux capteurs à base de nanotubes mentionnés ci-dessus ont une sortie intégralement électrique (un courant typiquement) et ce chapitre servira ainsi de base théorique pour tous les calculs de transport rencontrés en **Chapitre III** et **Chapitre V**. Nous avons choisi d'arriver au formalisme de transport de Landauer-Büttiker à partir de la base rigoureuse des fonctions de Green de non-équilibre à plusieurs corps. Ainsi le chemin général que ce chapitre suit est une série d'hypothèses appliquées au cas général afin de simplifier la théorie vers des modèles qui sont à la fois numériquement traitables et qui approximent suffisamment bien les propriétés de transport dans les nanotubes de carbone. Car nous emploierons souvent des bases vectorielles non-orthogonales dans nos calculs, nous verrons à la fin de ce chapitre les changements nécessaires pour adapter la théorie de transport à cette situation.

La première contribution de cette thèse se trouve dans le **Chapitre III** qui contient un ensemble des calculs théoriques que nous avons effectués afin de valider le principe

d'opération d'un capteur électromécanique à base de nanotubes de carbone. Le dispositif proposé est une croix de nanotubes dans laquelle un tube joue le rôle de poutre, se pliant sous les forces externes, et l'autre le rôle de support mécanique et de potentiomètre transformant la flexion de la poutre en une différence de courant électrique. La mesure des forces, aussi basses que quelques piconewtons, est démontrée avec ce dispositif par des calculs de mécanique moléculaire. Nous montrons également dans ce chapitre qu'à température ambiante, la caractéristique flexion-courant est monotone. Par conséquent le dispositif proposé peut être employé comme capteur. Dans une autre configuration, basée sur le changement de fréquence de résonance libre de la poutre, nous prouvons que le même dispositif peut détecter théoriquement des corps moléculaires pesant quelques kilodaltons, la masse d'une petite protéine comme le streptavidin l'est. Ainsi ce dispositif est très utile dans la spectroscopie de masse et la détection biochimique.

Dans le **Chapitre IV** nous développons l'appareil de flots matriciels continus qui est un élément clé pour les calculs de transport du **Chapitre V**. Bien que cette théorie ait été développée par Moody Chu, notre contribution a été de l'appliquer et de l'étendre pour étudier des problèmes de transport quantique. Ce chapitre est plutôt mathématique par essence et essaye d'introduire des notions d'analyse fonctionnelle comme l'espace de Hilbert de matrices et les dérivés de Fréchet, et d'établir également un parallèle avec l'espace de Hilbert de l'équation de Schrödinger qui est plus familier aux physiciens. Une fois que ces concepts sont mis en place la théorie des flots matriciels est illustrée par deux exemples. Tandis que le premier est utilisé seulement pour familiariser le lecteur avec les ingrédients de base de cette théorie, le second a des applications pratiques importantes et sera employée dans le **Chapitre V**. Ce deuxième exemple est une méthode qui permet de "façonner" une paire généralisée de matrices comme les matrices Hamiltoniennes et de recouvrement, tout en préservant leur spectre. En ce qui concerne la théorie de Chu nous l'avons étendue pour augmenter la flexibilité de "façonnage" en modifiant la fonction objectif.

Même si les **Chapitres II** et **IV** pourraient être fusionnés dans un seul chapitre théorique, pour la clarté nous avons choisi d'inclure avant chaque type de capteur la théorie nécessaire pour comprendre le chapitre correspondant. Ainsi toute la théorie à la base du **Chapitre III** se trouve dans **II** et pour le **Chapitre V** se trouve dans **II** et

IV, découpant de ce fait la thèse en deux parties indépendantes groupées autour des deux capteurs.

La validation du deuxième capteur fait l'objet du **Chapitre V** et est la deuxième contribution principale de cette thèse. Dans ce chapitre nous avons essayé de répondre à la question de savoir si les capteurs de conductance à base de nanotubes de carbone pourraient détecter les quatre acides aminés aromatiques: Histidine, Phénylalanine, Tryptophane et Tyrosine. Car les dispositifs réalistes de nanotube de carbone ont un grand nombre d'atomes, il est extrêmement difficile de réaliser des calculs auto-cohérents dans la pratique, et nous avons ainsi choisi une approche alternative. Les quatre acides aminés sont étudiés sur une couche simple de graphene. Puis, un procédé basé sur les flots matriciels décrits en **Chapitre IV** est employé pour obtenir les matrices efficaces de Hamiltonien et de recouvrement qui préservent une bonne fidélité spectrale autour du niveau de Fermi, une condition nécessaire pour des calculs de transport. Avec ce modèle minimal nous pourrons calculer efficacement la conductance des capteurs à base de nanotubes de carbone considérablement grands.

Chapitre I - Nanotubes de carbone: Structure et propriétés

Ce chapitre offre une vue d'ensemble de la structure et des propriétés des nanotubes de carbone. La terminologie et la physique de base sont développées pour servir au reste de cette thèse qui se concentre sur des dispositifs à base de nanotubes de carbone. Ici nous avons choisi seulement ceux parties de la théorie de nanotubes qui sont fondamentaux pour la compréhension des chapitres suivants. Pour une vue d'ensemble de la théorie de nanotubes de carbone nous renvoyons le lecteur aux **Références 13**, **14**, **15**. Un autre but de ce chapitre est d'offrir un certain ensemble de données expérimentales qui viendront en support, et seront référencées dans les chapitres suivants.

Les éléments de base de la cristallographie des nanotubes sont le sujet de la **Section 1**, qui commence avec le graphite et la graphene qui facilitent la visualisation de la structure des nanotubes, et l'obtention d'une approximation de premier ordre de leurs propriétés électroniques et mécaniques. La cellule unité d'un nanotube peut être regardée comme une super-cellule de graphene qui s'avérera extrêmement utile pour le calcul de la structure de bande et des densités des états de nanotubes monofeuillets. Pour ces nanotubes toutes les propriétés structurales comme le diamètre, les

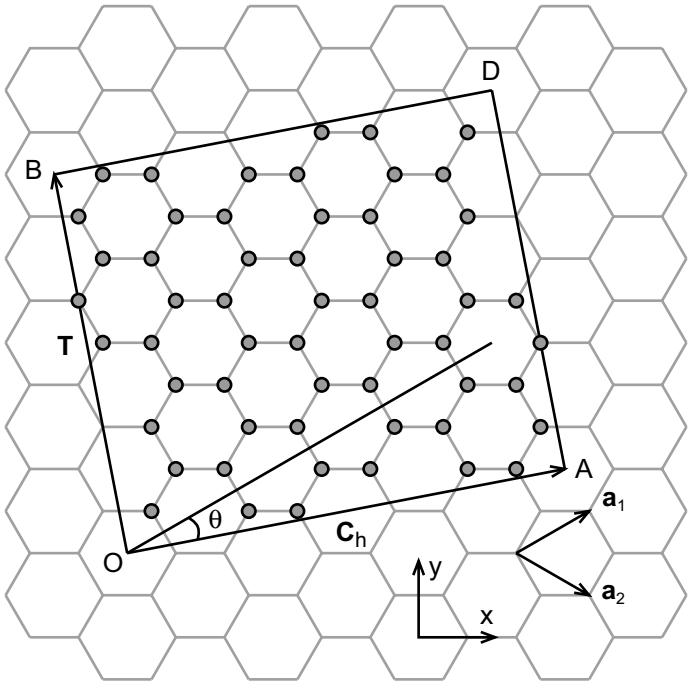

Figure 1. La cellule unité d'un nanotube (4, 2) délimitée par le rectangle OADB. Le tube est obtenu en pliant AD sur OB. Les cercles gris représentent les atomes inéquivalents du tube.

dimensions de la cellule unité et le nombre d'atomes, sont dépendantes d'un seul vecteur, le vecteur chiral, défini par deux nombres entiers.

Dans la **Section 2**, les propriétés électroniques des nanotubes monofeuillet sont dérivées de ceux du graphene dans une approximation de liaisons-fortes. La plupart des dérivations détaillées dans la **Section 2** suivent de près la **Référence 13**. La technique de "zone-folding" est appliquée dévoilant la quantification du vecteur transversal d'onde dans les nanotubes de carbone et la célébrée nature métallique ou semi-conductrice des nanotubes selon leur vecteur chiral.

Les régimes principaux de la théorie mésoscopique de transport sont brièvement rappelés dans la **Section 3,** afin d'identifier les échelles relevantes de temps et longueur pour les nanotubes de carbone. Nous passons en revue des résultats expérimentaux des régimes de transport dans les NTC. Un certain nombre d'excellentes revues sont disponibles à ce sujet [**16**, **17**, **18**, **19**]. Pour les nanotubes métalliques on a constaté que le libre-parcours moyen typique peut atteindre quelques micromètres, alors que les bandgaps des tubes semi-conducteurs sont conformes aux

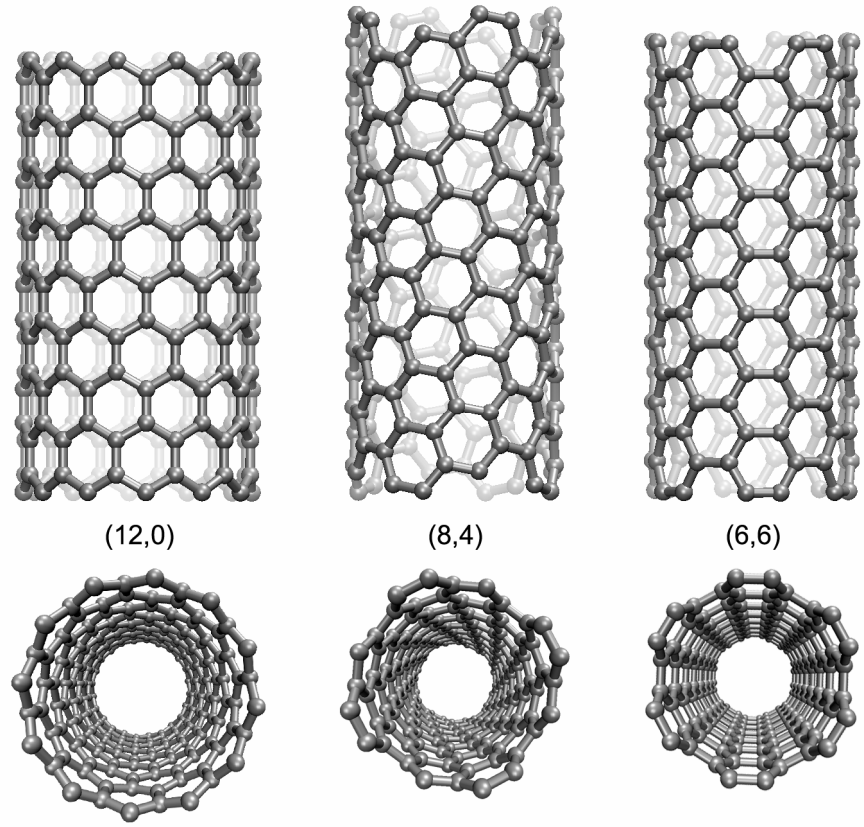

Figure 2. Quelques structures des nanotubes de carbone en vue latérale (haut) et axiale (bas). De gauche à droite (12, 0) est un zigzag (8, 4) un chiral et (6, 6) un nanotube armchair.

prévisions théoriques. Des problèmes liés aux barrières de Schottky, ou plus généralement aux contacts nanotubes-métaux, sont étudiés à la fin de cette section, ainsi que l'influence enduite par dopage ou défauts sur des propriétés de transport des nanotubes.

Dans la **Section 4** nous tournons notre attention vers les propriétés mécaniques des nanotubes pour lesquelles il y a un certain nombre d'excellentes revues [**16**, **20**, **21**]. D'abord une succincte étude des méthodes computationnelles disponibles pour la simulation de nanotube est offerte. Pour les nanotubes, la théorie a initialement prévu des modules de Young énormes, mais une recherche plus minutieuse a établi qu'à la base de ces résultats il y avait la définition inappropriée de l'épaisseur de la paroi. Enfin, les résultats théoriques et expérimentaux des propriétés mécaniques des NTC comme le module de Young, la rigidité de flexion et torsion, etc. sont énumérés à la fin de ce chapitre.

La structure d'un nanotube de carbone peut être regardée comme le résultat de l'enroulement d'une feuille de graphene dans un cylindre. Par rapport à la **Figure 1** ceci signifie de joindre les segments AD et OB. Lors de l'inspection, "l'enroulement" de la feuille de graphene peut être réalisé le long de différentes directions ayant pour résultat une grande variété de structures tubulaires. Quelques exemples de nanotubes sont donnés dans la **Figure 2**. Dans la **Section 2** nous prouvons que la direction d'enroulement a un rapport avec les propriétés électroniques du nanotube résultant.

La structure d'un nanotube de carbone est uniquement déterminée par un seul vecteur appelé vecteur chiral et marqué $\mathbf{C}_h$ sur la **Figure 1**, qui par le procédé d'enroulement décrit ci-dessus, devient la circonférence du tube. Le vecteur chiral peut être exprimé en fonction des vecteurs de translation de graphene avec l'aide de deux nombres entiers (n,m). Les tubes qui ont $n=m$ sont connus comme "armchair", ceux qui ont $m=0$ comme "zigzag", et tous les autres tubes sont appelés génériquement nanotubes "chiraux". D'autre part l'axe du tube est parallèle à un deuxième vecteur appelé vecteur de translation et marqué $\mathbf{T}$.

La structure de bandes des nanotubes de carbone monofeuillet peut être obtenue dans une première approximation à partir des relations de dispersion du graphene, en imposant des conditions de bord périodiques le long du vecteur chiral $\mathbf{C}_h$. Dans l'espace réciproque, le vecteur d'onde lié à $\mathbf{C}_h$ se quantifie, alors que ceux associés au vecteur de translation $\mathbf{T}$ restent continus pour les tubes de longueur infinie. Ces considérations sont équivalentes à l'échantillonnage des relations de dispersion du graphene le long du $\mathbf{K}_2$, aux p translations consécutives le long du $\mathbf{K}_1$ à partir de Γ, produisant la structure de bandes des nanotubes:

$$\varepsilon_p(\mathbf{k}) = \varepsilon_{1(2)}\left(k\frac{\mathbf{K}_2}{\|\mathbf{K}_2\|} + p\mathbf{K}_1\right) \qquad (1)$$

Les structures de bande d'un nanotube métallique (10, 10) et d'un semi-conducteur (14, 0) sont présentées dans la **Figure 3** avec leur densité d'états correspondante.

Pour les NTCs métalliques un développement de la surface de Fermi autour de n'importe lequel des six points spéciaux K, rapporte une vitesse de Fermi $v_F \simeq 10^6 \text{m/s}$, indépendante de la chiralité. Ainsi, dans l'absence de la diffusion électronique, la conductance intrinsèque d'un tube métallique devrait être $2G_0$ (où

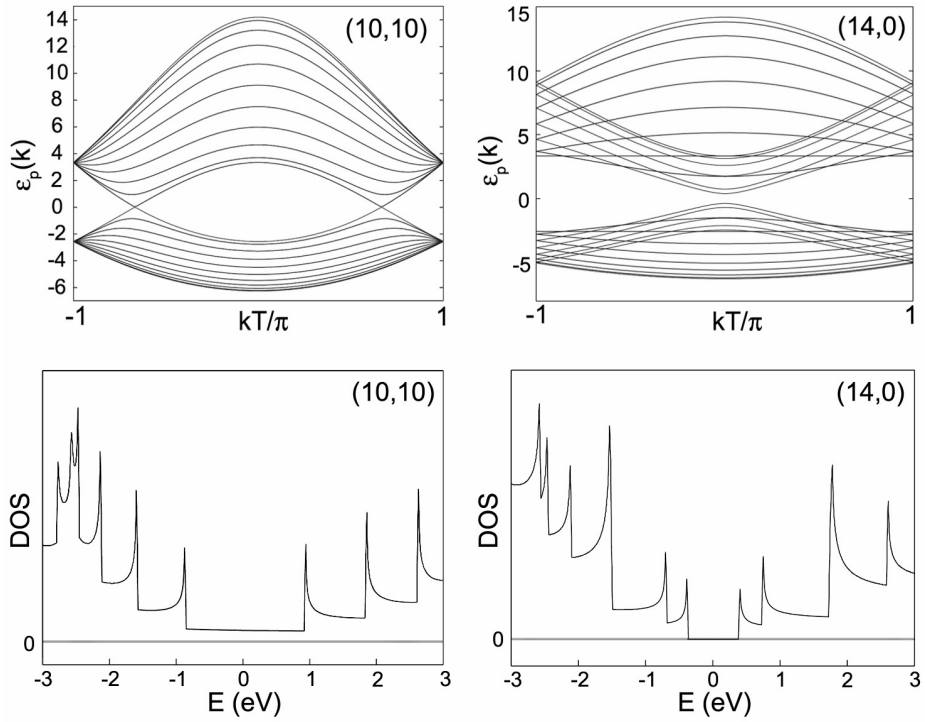

Figure 3. (haut) Structures de bandes pour un nanotube métallique (10, 10) et un tube semi-conducteur (14, 0), et (bas) leur densité des états correspondante.

$G_0 = 2e^2/h$ est le quantum de conductance) car il y a deux canaux ouverts au niveau de Fermi, chacun ayant une conductibilité G_0. D'autre part les NTCs semi-conducteurs ont un bandgap $E_g \simeq (0.9\,\text{eV})/d_t$, où d_t est le diamètre du tube en nanomètres.

L'hybridation sp^2 du carbone produit le lien covalent le plus dur en nature. Une feuille de graphene a un module de Young près de 1TPa, qui a été prévu et plus tard démontré d'être le même pour les nanotubes. La **Section 4** couvre les propriétés mécaniques de base des nanotubes de carbone monofeuillet à partir des prévisions théoriques et finalisant par des mesures expérimentales. On ne considère pas les propriétés de vibrations. Dans cette thèse nous nous sommes intéressés principalement aux propriétés élastiques "macroscopiques" comme la flexion et plus généralement la déformation des nanotubes, qui peuvent être caractérisés avec l'aide des quantités classiques de la théorie d'élasticité comme le module de Young, la rigidité, le stress et ainsi de suite.

À la base de la rigidité du graphite sont les liaisons fortes σ, faiblement aidées par les liaisons π. Comme le stress axial est principalement transformé dans une déformation des liaisons σ et de leurs angles, une résistance considérable à la déformation axiale doit être prévue. Au contraire, les stress normaux sur la surface du tube ne déforment pas les hexagones considérablement, ayant pour résultat une souplesse relativement élevée dans cette direction. En fait, les feuillets d'un NTC peuvent même collapser ensemble si le stress est suffisamment grand. Sous un stress axial, les nanotubes de carbone supportent des déformations de 5-10%. Celles-ci, cumulées avec leur rigidité et élasticité, ont mené divers auteurs à les appeler les fibres ultimes.

Chapitre II - Théorie du transport dans les nanostructures

Le but de ce chapitre est de présenter le formalisme à la base des calculs modernes de transport dans les nanostructures, le formalisme des fonctions de Green de non-équilibre (NEGF). La théorie de transport résultante est construite sur les fondements rigoureux des statistiques quantiques de non-équilibre. NEGF donne accès aux densités et aux courants de particules sous des champs forts et interactions fortes, étant de ce fait plus général que la théorie de la réponse linéaire de Kubo. Par plusieurs hypothèses de simplification, NEGF ramène au formalisme de Landauer-Büttiker largement appliqué, qui devrait être utilisé seulement dans le régime cohérent de transport. Bien que ce soit ce dernier formalisme que nous employons dans cette thèse, nous avons décidé qu'au lieu de donner une dérivation phénoménologique de la valeur moyenne du courant de particules, il serait préférable de commencer par sdes statistiques quantique de non-équilibre et de simplifier la théorie jusqu'au modèle utilisé.

Dans la **Section 1**, la théorie générale de transport NEGF dans les nanostructures sera détaillée. Nous commencerons par pointer les formules de statistiques quantiques d'équilibre pour calculer les valeurs moyennes des opérateurs dans le grand ensemble canonique. Pour des opérateurs à un corps, il est cependant plus efficace d'évaluer les fonctions de Green, qui contiennent suffisamment d'information pour calculer les moyennes d'opérateurs à un-corps. Puis l'image de non-équilibre est présentée, ce qui mènera à l'extension des fonctions de Green à leurs versions ordonnées sur contour. Pour des raisons pratiques ces fonctions de Green sont projetées sur l'axe réel à l'aide des règles de continuation de Langreth, qui introduisent les fonctions de Green moins

(plus) et retardées (avançées). D'ici à la fin de la première section nous suivrons de près les dérivations de Jauho en établissant les équations de transport non élastiques [**67**, **68**]. La valeur moyenne du courant est obtenue à partir de la définition de l'opérateur courant dans le contexte général à plusieurs corps, à l'exception des contacts métalliques qui admettent une description de champ moyen. À la fin de cette section l'application de l'hypothèse selon laquelle les contacts restent en équilibre même après "le couplage" des champs externes et interactions, aura comme résultat la formule de Meir-Wingreen [**69**].

La **Section 2** traitera de la situation du transport élastique, qui, comme indiquée plus tôt, est la théorie de choix pour les calculs de cette thèse. La formule de Fisher-Lee [**70**], une extension de la formule à un canal de Landauer, est dérivée de la valeur moyenne du courant de Meir-Wingreen, précédemment obtenue, en ajoutant l'hypothèse que dans la région centrale les électrons n'interagissent pas. Cette supposition transforme le problème de transport en un problème de champ moyen à un corps, pour lequel des méthodes efficaces de calcul peuvent être conçus (voir le **Chapitre III** et le **Chapitre V**.) La formule de transmission de Fisher-Lee est transformée en formule de Todorov [**71**] démontrant que le formalisme de Landauer-Büttiker est une théorie de diffusion élastique. Nous finirons cette section et le chapitre en considérant les ensembles de base non-orthogonaux, qui sont d'intérêt principal puisque la plupart des modèles hamiltoniens, soit des liaisons fortes soit *ab initio*, emploient de telles bases pour des raisons d'efficacité. Nous prouverons que la théorie de transport reste inchangée si les différentes matrices décrivant le formalisme satisfait certaines règles de représentation.

Des phénomènes de transport au delà de la théorie de la réponse linéaire ne peuvent pas être modelés seulement par des fonctions de Green *d'équilibre*. Heureusement il existe une extension du formalisme d'équilibre au régime de réponse non linéaire, qui est basée sur la fonction de Green non-équilibre, également connue sous le nom de formalisme de Keldysh-Kadanoff-Baym [**74**, **75**].

$$G(\mathbf{1},\mathbf{1}') \equiv -i\left\langle T_C[\hat{\psi}(\mathbf{1})\hat{\psi}^{\dagger}(\mathbf{1}')]\right\rangle \qquad (2)$$

Ce formalisme suppose que pour $t < t_0$ le système est en équilibre thermodynamique décrit par un hamiltonien $\hat{H}_0$. Commençant par t_0, des couplages entre des sous-

ensembles décrits par une interaction dépendante du temps $\hat{V}(t)$ sont introduites. Ce dernier terme d'interaction peut contenir, en plus des couplages de sous-ensembles, un champ externe dépendant du temps. Ainsi pour $t > t_0$ le système n'est plus en équilibre et ne peut pas correctement être décrit par la fonction de Green de Matsubara. Cependant, car l'état du système a été connu avant t_0, cet état peut être employé en tant que condition initiale et être formellement intégré en utilisant l'opérateur d'évolution temporelle. Dans des suppositions générales, cette intégration est équivalente à une intégration ordonnée sur contour.

Bien qu'un outil formel puissant, la fonction de Green ordonnée sur contour est remplacée dans la pratique par les quatre fonctions de Green en temps réel

$$G^{<}(\mathbf{1},\mathbf{1}') \equiv i\left\langle \hat{\psi}^{\dagger}(\mathbf{1}')\hat{\psi}(\mathbf{1})\right\rangle \qquad \textbf{(3.a)}$$

$$G^{>}(\mathbf{1},\mathbf{1}') \equiv -i\left\langle \hat{\psi}(\mathbf{1})\hat{\psi}^{\dagger}(\mathbf{1}')\right\rangle \qquad \textbf{(3.b)}$$

$$G^{r}(\mathbf{1},\mathbf{1}') \equiv -i\theta(t-t')\left\langle \left\{\hat{\psi}(\mathbf{1}),\hat{\psi}^{\dagger}(\mathbf{1}')\right\}\right\rangle \qquad \textbf{(3.c)}$$

$$G^{a}(\mathbf{1},\mathbf{1}') \equiv i\theta(t'-t)\left\langle \left\{\hat{\psi}(\mathbf{1}),\hat{\psi}^{\dagger}(\mathbf{1}')\right\}\right\rangle \qquad \textbf{(3.d)}$$

appelées les fonctions de Green moins, plus, retardées et avancées respectivement. Les définitions (**3.c-d**) contiennent l'anti-commutateur $\left\{\hat{A},\hat{B}\right\} \equiv \hat{A}\hat{B} + \hat{B}\hat{A}$. La fonction de Green (avançée) retardée peut être interprétée comme l'amplitude de probabilité quantique pour annihiler un électron (trou) de spin σ' à $(\mathbf{r}',t')$ sachant qu'un électron (trou) de spin σ a été créé plus tôt à $(\mathbf{r},t)$. Réciproquement la fonction de Green moins (plus) est la densité résolue en énergie des électrons (trous). Il n'est pas difficile de prouver que $G^{<}(\mathbf{1},\mathbf{1}')$ contient toute l'information nécessaire pour calculer n'importe quelle moyenne d'opérateur à un corps,

$$\left\langle \hat{A}(\mathbf{1})\right\rangle = -i\lim_{\mathbf{1}'\to\mathbf{1}} \hat{A}(\mathbf{1})G^{<}(\mathbf{1},\mathbf{1}') \qquad \textbf{(4)}$$

y compris la densité de particules et l'opérateur de courant. Ainsi, à l'aide de la machinerie des fonctions de Green de non-équilibre (NEGF), à partir de la définition de la moyenne du courant de particules,

$$I_{\alpha}(t) = -2e\cdot\partial_t\left\langle \hat{N}_{\alpha}\right\rangle \equiv -2e\cdot\partial_t\sum_{\nu}\hat{c}^{\dagger}_{\alpha;\nu}\hat{c}_{\alpha;\nu} = -\frac{2ie}{\hbar}\left\langle \left[\hat{H},\hat{N}_{\alpha}\right]\right\rangle \qquad \textbf{(5)}$$

une formule compacte est obtenue

$$\begin{aligned} I_\alpha &= \frac{2e}{h}\int_{-\infty}^{+\infty} dE \sum_{\mu,\mu'} \left(\Sigma^<_{\mu',\mu}(E)G^>_{\mu,\mu'}(E) - \Sigma^>_{\mu',\mu}(E)G^<_{\mu,\mu'}(E)\right) = \\ &= \frac{2e}{h}\int_{-\infty}^{+\infty} dE\, \mathrm{Tr}\left[\mathbf{\Sigma}^<_\alpha(E)\mathbf{G}^>(E) - \mathbf{\Sigma}^>_\alpha(E)\mathbf{G}^<(E)\right] \end{aligned} \qquad (6)$$

Cette formule simple indique qu'afin d'obtenir le courant à travers une région on doit simplement calculer la trace des taux résolus en énergie de dispersion-dans moins de dispersion-de.

Si le terminal α reste en équilibre thermique avec le potentiel chimique, même après que le couplage hamiltonien ait été allumé, alors les fonctions de Green moins (plus) en (6) peuvent être remplacées par leur version d'équilibre pour obtenir la bien connue formule de Meir-Wingreen [69].

$$I_\alpha = \frac{2e}{h}\int_{-\infty}^{+\infty} dE\, \mathrm{Tr}\left[\mathbf{\Gamma}_\alpha(E) i\mathbf{G}^<(E) + f(E-\mu_\alpha)\mathbf{\Gamma}_\alpha(E)\mathbf{A}(E)\right] \qquad (7)$$

L'approximation des électrons indépendants dans la région centrale implique que les seules self-énergies à inclure sont celles des contacts, qui résultent dans

$$I_\alpha = \sum_{\alpha'\neq\alpha} \frac{2e}{h}\int_{-\infty}^{+\infty} dE \mathcal{T}_{\alpha,\alpha'}(E)\left[f(E-\mu_\alpha) - f(E-\mu_{\alpha'})\right] = \sum_{\alpha'\neq\alpha} I_{\alpha,\alpha'} \qquad (8.a)$$

$$\mathcal{T}_{\alpha,\alpha'}(E) = \mathrm{Tr}\left[\mathbf{\Gamma}_\alpha(E)\mathbf{G}^r(E)\mathbf{\Gamma}_{\alpha'}(E)\mathbf{G}^a(E)\right] \qquad (8.b)$$

connue comme la formule de Fisher-Lee. Cette formule sera employée dans toute cette thèse particulièrement dans le **Chapitre III** et le **Chapitre V** pour le calcul des courants de particules ou la transmission des dispositifs à base de nanotubes de carbone. Comme montré dans le chapitre précédent, des mesures expérimentales indiquent un couplage faible électron-phonon dans les nanotubes de carbone, à la température ambiante pour des longueurs de <1μm. Ainsi pour des nanotubes de carbone une région "centrale" non-inter-agissante est une approximation appropriée.

Une autre formule du courant de particules basée sur la théorie de dispersion a été développée dans la **Référence 71**, à laquelle nous renvoyons le lecteur pour les suppositions générales et la dérivation de cette formule. Ici nous prouvons

l'équivalence exacte de la formule de Todorov à la formule de la Fisher-Lee (**8**). Cette équivalence est intéressante pour deux raisons. D'abord elle prouve encore que la formule de Fisher-Lee est valide pour le tunneling élastique seulement. Ensuite, la formule de Todorov simplifie les manipulations algébriques que nous employons pour montrer que dans une approximation de champ-moyen la valeur moyenne du courant de particules est uniquement déterminée par les propriétés spectrales (c.-à-d. des valeurs propres et des vecteurs propres) du hamiltonien autour du niveau de Fermi. L'équivalence des deux formules est capturée dans la relation

$$\begin{aligned}\mathcal{T}_{\alpha,\alpha'}(E) &= \mathrm{Tr}_C\left[\mathbf{\Gamma}_\alpha(E)\mathbf{G}_C^r(E)\mathbf{\Gamma}_{\alpha'}(E)\mathbf{G}_C^a(E)\right] = \\ &= \mathrm{Tr}_\alpha\left[\mathbf{A}_\alpha(E)\mathbf{t}_{\alpha\alpha'}(E)\mathbf{A}_{\alpha'}(E)\mathbf{t}_{\alpha\alpha'}(E)^\dagger\right] = \\ &= 4\pi^2\,\mathrm{Tr}_\alpha\left[\boldsymbol{\rho}_\alpha(E)\mathbf{t}_{\alpha\alpha'}(E)\boldsymbol{\rho}_{\alpha'}(E)\mathbf{t}_{\alpha\alpha'}(E)^\dagger\right]\end{aligned} \qquad (9)$$

Pour des raisons pratiques, le formalisme de transport, soit dans la dérivation de Fisher-Lee soit dans celle de Todorov, doit être étendue à des bases non-orthogonales. La plupart des calculs modernes de transport sont faits avec des extensions des codes de chimie quantiques [**76**, **79**, **80**], où les combinaisons linéaires des orbitales atomiques ou les ondes planes sont le choix typique. Les ondes planes ne satisfont pas la supposition de localisation de l'espace réel, que nous avons employée en dérivant les formules de transport de ce chapitre. Ainsi nous nous concentrons sur les orbitales atomiques. À part leurs avantages évidentes les orbitales atomiques souffrent d'un inconvénient, à savoir leur manque d'orthogonalité. Nous montrons comment la non-orthogonalité peut être simplement prise en considération, avec pratiquement aucune modification, par une simple convention de représentation.

L'essence de la non-orthogonalité est le fait que l'équation de Schrödinger $\hat{H}\left|\psi_n\right\rangle = \varepsilon_n\left|\psi_n\right\rangle$ peut assumer diverses formes matriciels, parmi lesquelles la forme de valeur propre généralisée $\mathbf{H}_{\downarrow\downarrow}\boldsymbol{\psi}_{\downarrow;n} = \varepsilon_n\mathbf{I}_{\downarrow\downarrow}\boldsymbol{\psi}_{\downarrow;n} \Leftrightarrow \mathbf{H}\boldsymbol{\psi}_n = \varepsilon_n\mathbf{S}\boldsymbol{\psi}_n$. Une autre équation d'intérêt est l'équation définissant la fonction de Green à un corps $\hat{G}(E)\left[E\hat{I} - \hat{H}\right] \equiv \hat{I}$. Cette équation peut aussi assumer différentes formes, mais nous employons principalement une forme particulière

$$\mathbf{G}(E)_{\uparrow\uparrow}\left[E\mathbf{I}_{\downarrow\downarrow} - \mathbf{H}_{\downarrow\downarrow}\right] = \mathbf{I}_{\uparrow\downarrow} = \mathbf{I} \Rightarrow \mathbf{G}(E)_{\uparrow\uparrow} = \left[E\mathbf{I}_{\downarrow\downarrow} - \mathbf{H}_{\downarrow\downarrow}\right]^{-1} \qquad (10)$$

La même est valide pour tous les produits d'opérateur. Par exemple la trace d'un opérateur dans une base non-orthogonale s'écrit

$$\begin{aligned}\mathrm{Tr}_n[\hat{A}] &= \sum_n a_n = \sum_n \langle a_n|\hat{A}|a_n\rangle = \sum_{n,\nu,\mu} \langle a_n|\nu\rangle A_\mu^\nu \langle\tilde{\mu}|a_n\rangle = \\ &= \sum_{n,\nu,\mu} \langle\tilde{\mu}|a_n\rangle\langle a_n|\nu\rangle A_\mu^\nu = \sum_{\nu,\mu} \langle\tilde{\mu}|\nu\rangle A_\mu^\nu = \sum_{\nu,\mu} \delta_\nu^\mu A_\mu^\nu = \sum_\nu A_\nu^\nu = \\ &= \mathrm{Tr}_\nu[\mathbf{A}_{\downarrow\downarrow}] = \mathrm{Tr}[\mathbf{I}_{\uparrow\uparrow}\mathbf{A}_{\downarrow\downarrow}] = \mathrm{Tr}[\mathbf{A}_{\downarrow\uparrow}] = \mathrm{Tr}[\mathbf{I}_{\downarrow\downarrow}\mathbf{A}_{\uparrow\uparrow}]\end{aligned} \qquad (11)$$

En appliquant ces observations nous pouvons choisir une représentation utile pour la trace de l'**Equation** (**8.b**)

$$\mathcal{T}_{\alpha,\alpha'}(E) = \mathrm{Tr}\left[\mathbf{\Gamma}_{\alpha;\downarrow\downarrow}(E)\mathbf{G}^r_{C;\uparrow\uparrow}(E)\mathbf{\Gamma}_{\alpha';\downarrow\downarrow}(E)\mathbf{G}^a_{C;\uparrow\uparrow}(E)\right] \qquad (12)$$

dans laquelle, l'intérieur de la trace, assume une représentation conformée à (**11**) et à la fonction de Green (**10**). Ceci donne l'idée qu'un formalisme cohérent (dans le sens des représentations d'opérateurs) peut être obtenu si on considère des hamiltoniens, des self-énergies et des fonctions d'élargissement de niveau ($\hat{H},\hat{\Sigma},\hat{\Gamma}$) être de type $\downarrow\downarrow$, et des fonctions de Green, des densités des états et des fonctions spectrales ($\hat{G},\hat{\rho},\hat{A}$) de type $\uparrow\uparrow$, ainsi

$$\left(\hat{H},\hat{\Sigma},\hat{\Gamma}\right) \rightarrow \left(\mathbf{H}_{\downarrow\downarrow},\mathbf{\Sigma}_{\downarrow\downarrow},\mathbf{\Gamma}_{\downarrow\downarrow}\right) \qquad (13.a)$$

$$\left(\hat{G},\hat{\rho},\hat{A}\right) \rightarrow \left(\mathbf{G}_{\uparrow\uparrow},\boldsymbol{\rho}_{\uparrow\uparrow},\mathbf{A}_{\uparrow\uparrow}\right) \qquad (13.b)$$

Ce sont les conventions que nous employons dans toute cette thèse pour tous les calculs de transport.

Chapitre III - Capteur électromécanique à base de NTC pour la mesure des masses et forces

Un *potentiel* capteur électromécanique à base des nanotubes de carbone est théoriquement étudié dans ce chapitre. Un tel dispositif n'a pas été expérimentalement démontré. Cependant, un des buts de ce chapitre est de démontrer qu'un tel dispositif fonctionnerait en conditions normales, et pourrait aussi être fabriqué avec des techniques actuelles de micro- et de nano-fabrication. À l'aide de la modélisation et de la simulation nous prouvons par la suite que le dispositif mentionné ci-dessus peut mesurer des forces faibles de l'ordre de dizaines de piconewtons (pN), ou avec des

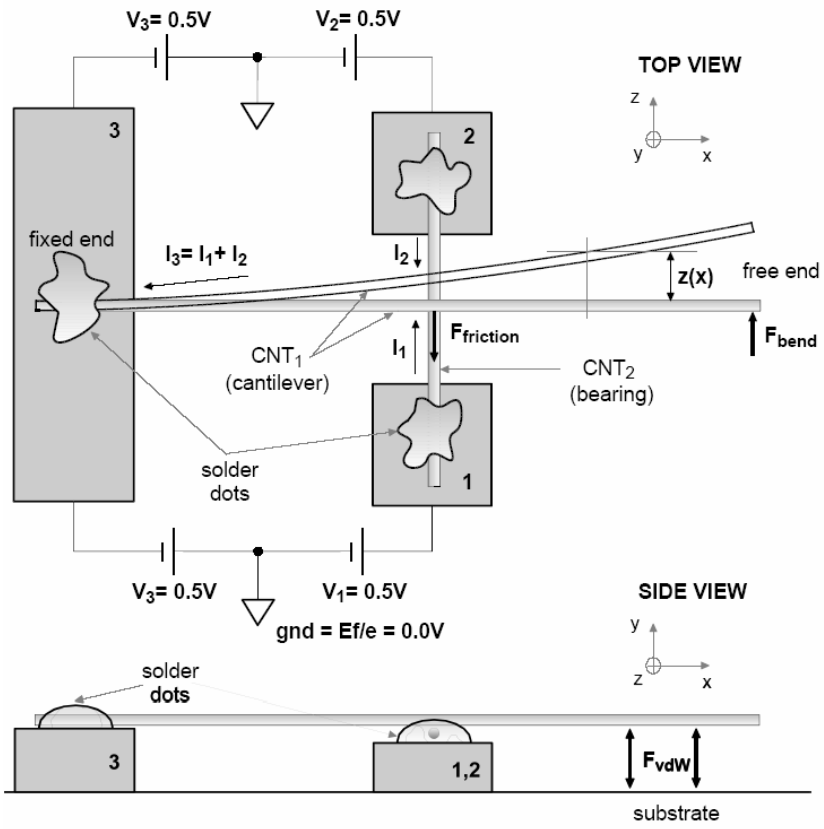

Figure 4. La représentation schématique du principe d'opération d'un capteur de flexion à base de nanotubes de carbone, y compris la polarisation électronique.

modifications mineures il peut détecter des corps petits pesant des kilodaltons (kDa) (zeptograms (zg)). Le même dispositif peut être utilisé de ce fait dans deux configurations distinctes, une pour mesurer des forces, l'autre pour peser des petits corps. Dans les deux configurations la sortie est un signal électrique, un courant différentiel.

Nous commençons ce chapitre avec une section décrivant le principe d'opération du dispositif central, nommé capteur de flexion, qui est commun au force-mètre et à la nanobalance. Puis les différences des deux configurations sont mises en évidence. Quelques considérations pratiques sont énumérées à la fin de la **Section 1** afin de prouver qu'un tel dispositif peut être réalisé expérimentalement. La **Section 2** consiste en l'évaluation du comportement mécanique et de la sensibilité du dispositif sous des forces de l'ordre du pN. À cette fin un champ de force classique est paramétrisé par des calculs *ab initio*. Par la suite la mécanique moléculaire est employée pour étudier

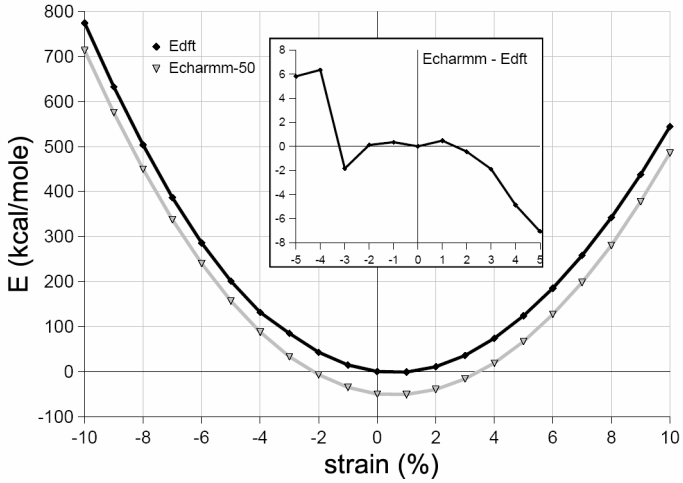

Figure 5. Caractéristiques de énergie-deformation comme obtenues avec SIESTA (DFT) et NAMD (CHARMM), respectivement. L'encart détaille l'erreur autour de l'origine (les courbes ont été décalées pour une meilleure visualisation).

la réponse du capteur à l'impulsion unité, rapportant des informations sur le frottement et la stabilité mécanique.

La **Section 3** se concentre sur la transduction de la flexion de la poutre dans un signal électrique dans le régime de transport cohérent. Une méthode efficace basée sur le partitionnement d'espace réel est développée afin de calculer la conductance multi-terminaux de Landauer-Büttiker. Plusieurs questions liées à l'importance des effets thermiques dans le fonctionnement du capteur sont traitées. Avec un procédé simple, nous incluons des effets de température non-nulle par la dynamique moléculaire, dans des calculs de conductance quantique. Ce procédé a comme conséquence une caractéristique flexion-courant thermiquement lissé. Cette caractéristique montre un comportement monotone et constitue la preuve-de-concept de notre dispositif.

Le mode d'opération de la nanobalance est caractérisé dans la **Section 4** où nous établissons qu'une seule molécule de streptavidin peut être détectée; une sensibilité sans précédent pour un dispositif électromécanique. Les simulations paramétriques trouvées à la fin de cette section montrent une grande robustesse du capteur par rapport aux paramètres difficilement-contrôlables d'opération et de dispositif comme la position de la molécule le long de la poutre et le rayon de cette dernière.

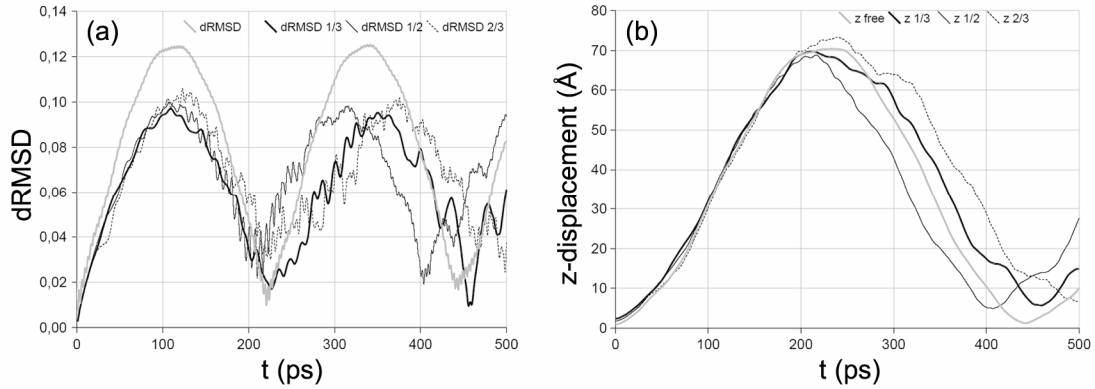

Figure 6. Différentes courbes concernant le comportement mécanique du capteur de flexion (a) RMSD différentiel de tous les atomes de la poutre, (b) Flexion de la poutre le long d'axe de z (d'un atome trouvé sur la pointe).

Bien que le capteur de mesure de force et la nanobalance diffèrent par la manière d'actionnement, elles sont toutes les deux basées sur un dispositif central qui transforme la déformation mécanique d'une poutre dans un signal électrique (illustré dans la **Figure 4**). Ce dispositif implique deux nanotubes de carbone perpendiculaires, c.-à-d. une croix des nanotubes. Trois des quatre extrémités des nanotubes sont fixées aux contacts métalliques et le restant est libre pour se déplacer. C'est à cette dernière extrémité qu'une force de déformation sera appliquée. Du point de vue mécanique un tube est une poutre et l'autre est un appui linéaire. L'appui est placé sous la poutre afin de retenir son mouvement vertical, qui est nécessaire parce que les longs nanotubes tendent à se plier et se coller au substrat, attirés par des forces de van der Waals.

À part la stabilité mécanique, les trois contacts métalliques servent de contacts électriques au dispositif. Dans cette thèse nous adoptons une polarisation simple de CC avec les deux bornes d'appui mises à +V (où V est un certain potentiel) et la borne de la poutre à -V. En équilibre, quand aucune force externe n'est appliquée sur la poutre, les courants traversant les deux branches d'appui, devraient être approximativement égaux. Cependant si une force externe est appliquée, la flexion élastique de la poutre, modifie la longueur et par conséquent le rapport des courants des deux branches. C'est ce courant différentiel que nous "mesurons" afin d'obtenir la flexion de la poutre. Brièvement, le capteur est un potentiomètre moléculaire dont la mise en action pourrait être effectuée par exemple par la motilité cellulaire ou par n'importe quelle autre excitation externe.

La mesure des forces avec le capteur précédemment décrit n'exige aucune addition. La flexion de la poutre est transformée en un courant différentiel qui est capturé par l'électronique d'interface. Le module et le signe de la force externe peuvent être obtenus en multipliant la constante élastique du système, par la flexion précédemment déterminée. La deuxième application que nous avons trouvée pour notre capteur est la pesée des petits corps ou la détection moléculaire. La transduction d'un événement de liage moléculaire dans un signal électrique est basée sur la différence d'oscillation de fréquence entre le mode fondamental d'une poutre libre contre la poutre avec un corps attaché. En mesurant ce décalage de fréquence on pourrait obtenir des informations précises sur la masse de corps joint qui pourrait être une macromolécule, un virus ou n'importe quelle autre petite particule. La détection de décalage de fréquence est cependant suffisante pour donne une signature d'un événement de liage.

La deuxième section de ce chapitre est consacrée à la modélisation et simulation du capteur de flexion. La **Figure 5** montre les courbes d'énergie-déformation qui ont été utilisées pour fitter les paramètres du champ de force CHARMM utilisés dans toutes les simulations de dynamique moléculaire (MD) de ce chapitre. Une fois que le champ de force CHARMM a été correctement paramétré nous avons effectué plusieurs simulations de MD pour mieux comprendre le comportement dynamique du capteur de flexion. Dans la première simulation MD, la poutre, mesurant 36nm a été poussée avec une force constante de 10pN également distribuée entre ses dix atomes terminaux, l'autre extrémité du tube étant fixé.

Trois positions différentes du nanotube (5,5) d'appui, mesurant 20nm, ont été choisies pour étudier l'influence du frottement; à $1/3$, $1/2$ et $2/3$ du bord de la poutre. Par opposition au cas de poutre libre, l'appui rajoute du frottement. Le travail mécanique qui est effectué pour déplacer la poutre contre le frottement, se transforme en chaleur comme il peut être observé dans le RMSD différentiel (**Figure 6**.)

La troisième section se concentre sur le comportement électrique du capteur lorsque l'on essaie de montrer que la flexion de la poutre se transforme en courant différentiel comme expliqué dans la **Figure 4**. Nous supposons qu'à la température zéro, le tunnelage de la jonction est cohérent, ce qui n'est pas une supposition triviale. Nous supposons également que la fluctuation thermique de la jonction se produit assez lentement que l'électron reste cohérent dans tout son chemin, de la poutre jusqu'à

Algorithme 1. Méthode rapide d'élimination pour calculer les fonctions de Green de la jonction

1. LET $\mathbf{K}_4 = E\mathbf{S}_4 - \mathbf{H}_4$
2. $\mathbf{G}_4 = \mathbf{K}_4^{-1}$; $\mathbf{\Sigma}_4 = \mathbf{K}_{4J}\mathbf{G}_4\mathbf{K}_{4J}^{\dagger}$
3. LET $\mathbf{K}_{p\infty} = E\mathbf{S}_{p\infty} - \mathbf{H}_{p\infty}$ FOR $p = \overline{1,3}$
4. $\mathbf{g}_{p\infty} = \left[\mathbf{K}_{p\infty;00} - \mathbf{K}_{p\infty;01}\mathbf{g}_{p\infty}\mathbf{K}_{p\infty;01}^{\dagger}\right]^{-1}$; $\mathbf{\Sigma}_{p\infty} = \mathbf{K}_{p\infty p}^{\dagger}\mathbf{g}_{p\infty}\mathbf{K}_{p\infty p}$
5. LET $\mathbf{K}_p = E\mathbf{S}_p - \mathbf{H}_p$ FOR $p = \overline{1,3}$
6. $\mathbf{G}_p = \left(\mathbf{K}_p - \mathbf{\Sigma}_{p\infty}\right)^{-1}$; $\mathbf{\Sigma}_p = \mathbf{K}_{pJ}^{\dagger}\mathbf{G}_p\mathbf{K}_{pJ}$
7. LET $\mathbf{K}_J = E\mathbf{S}_J - \mathbf{H}_J$
8. $\mathbf{G}_J = \left(\mathbf{K}_J - \mathbf{\Sigma}_1 - \mathbf{\Sigma}_2 - \mathbf{\Sigma}_3 - \mathbf{\Sigma}_4\right)^{-1}$

l'appui. L'effet tunnel assisté par des phonons est également ignoré dans ce traitement. Cependant nous tenons compte de la température finie en prenant la moyenne sur l'ensemble de positions nucléaires pour le calcul des courants de branche. Prendre en compte la température finie dans nos calculs a été nécessaire parce que, en pratique, notre capteur fonctionne à la température ambiante. De plus à la température zéro dans le régime balistique le mécanisme de captage est non-monotone et il n'a donc pas d'utilisation pratique.

La méthode que nous avons utilisée dans nos calculs de transport ressemble à celle décrite dans la **Reference 104**. Cependant nous avons modifié cette technique pour inclure des contacts multiples en présence de l'effet tunnel à travers une jonction non-covalente. Nous avons employé un hamiltonien de liaisons-fortes [**105**] seulement pour les orbitales π, auxquels nous avons rajouté le facteur cosinus de Slater-Koster pour expliquer le couplage inter-tube anisotrope. Une enveloppe exponentielle a été également considérée pour limiter le domaine d'interaction entre les atomes non-covalents des deux tubes distincts.

Après le remplissage de la matrice hamiltonienne, une méthode d'élimination rapide, basée sur les self-énergies a été utilisée pour inverser une matrice de système autrement importante. Bref, selon cette méthode des self-énergies ont été propagées des contacts vers la jonction. Pratiquement seules les fonctions de Green de la jonction ont été obtenues par inversion car son hamiltonien est dense par rapport aux autres domaines où l'interaction inter-tube pourrait être négligée.

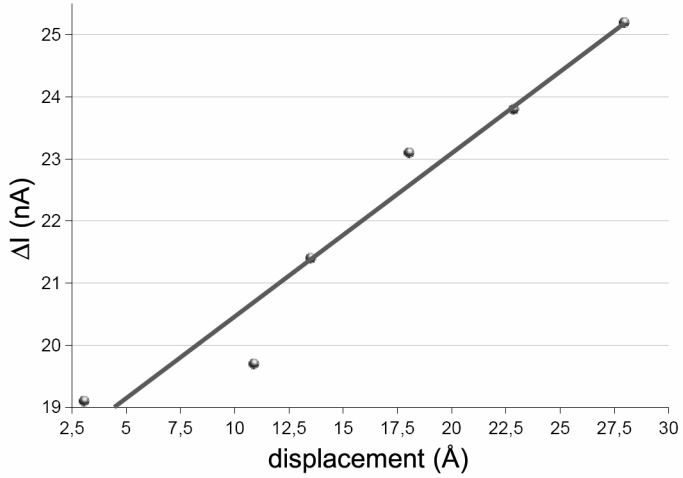

Figure 7. Caractéristique globale courant-flexion du capteur plus une ligne de régression linéaire.

Dans l'**Algorithme 1**, nous avons condensé toutes les étapes qui permettent le calcul des fonctions de Green de la jonction. Une fois que ces fonctions sont calculées, à une énergie donnée, les transmissions entre les quatre extrémités différentes de la jonction sont obtenues avec

$$\mathcal{T}_{\alpha,\alpha'}(E) = \mathrm{Tr}\left[\mathbf{\Gamma}_{\alpha}(E)\mathbf{G}_{J}^{r}(E)\mathbf{\Gamma}_{\alpha'}(E)\mathbf{G}_{J}^{r}(E)^{\dagger}\right]$$

Après le calcul des courants, nous avons convolué les valeurs trouvées pour les différentes positions d'échantillonnage avec une fonction gaussienne qui donne la courbe de la **Figure 7**. Cette figure parvient à montrer un accroissement global monotone du courant différentiel entre les deux branches d'appui, validant le principe d'opération du capteur de flexion.

Dans la dernière section nous avons utilisé de nouveau la mécanique moléculaire comme dans la **Section 2** afin d'évaluer la réponse en fréquence du système, avec et sans un corps moléculaire joint (streptavidin). L'appui a été placé au $2/3$ de la longueur de la poutre, plus près de l'extrémité libre. Ces simulations montrent que le capteur mécanique est suffisamment sensible pour détecter une seule molécule de streptavidin, qui pèse seulement quelques kDa. La réponse du capteur à cette molécule a été une baisse de fréquence de quatre fois. Après la validation réussie du capteur mécanique par la mécanique moléculaire, nous avons poursuivi par une phase de caractérisation du comportement du capteur en fonction des paramètres non

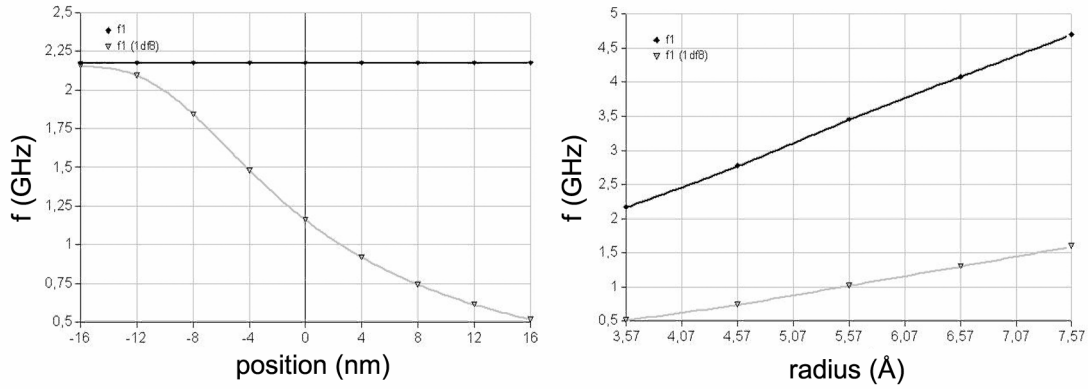

Figure 8. La dépendance du mode fondamental de la position de molécule le long de la poutre (gauche) et du rayon de la poutre (droit).

contrôlables de dispositif. Parmi ces paramètres, les plus importants sont la position du streptavidin le long de la poutre et le rayon de cette dernière, puisque sa longueur est plus ou moins contrôlable, et sa chiralité n'influence pas, à un premier ordre, son module de flexion. Brièvement nous avons fait une analyse de sensibilité.

Les résultats de ces analyses sont tracés dans la **Figure 8**. La figure gauche prouve que si le streptavidin se colle au milieu de la poutre à la place de sa pointe, le décalage de fréquence reste toujours d'au moins deux fois. Naturellement le capteur cesse de détecter la molécule quand celle-ci se colle près de l'extrémité fixée de la poutre. Le deuxième graphique indique qu'en assumant une grande déviation du rayon du nanotube (de 3.5 à 7.5Å), le décalage de fréquence continue à être important bien que le décalage de fréquence relative défini comme $\Delta f / f_0$ diminue moyennement de 77% à 66%. Nous avons ainsi trouvé un domaine extrêmement étendu des conditions d'opération et un décalage de fréquence impressionnant même pour une protéine si petite comme le streptavidin. Ainsi le capteur proposé est relativement peu sensible aux fluctuations de fabrication le rendant extrêmement approprié à l'intégration à grande échelle.

Chapitre IV - Flots matriciels et renormalisation

La puissante machinerie mathématique des flots matriciels continus est présentée dans ce chapitre. Cette méthodologie a été proposée comme solution à une classe de problèmes de valeurs propres inverses et compte sur des transformations infinitésimales de congruence agissant sur une paire de matrices dont le spectre

devrait être conservé [**111**]. À l'aide d'une fonction objectif spécialement conçue, la paire de matrices transformée peut être attirée vers la structure affine déterminée. Ainsi la théorie des flots matriciels permet de trouver une paire de matrices ayant un ensemble donné de valeurs propres et étant la plus proche possible d'une structure affine. Cette théorie sera employée dans le **Chapitre V** dans le contexte d'une méthode de réduction d'ordre d'un modèle hamiltonien que nous avons proposée dans le but de simplifier les calculs de transport quantiques dans les nanostructures.

Nous commençons ce chapitre avec une courte vue d'ensemble de l'analyse fonctionnelle qui présente des matrices en tant que "vecteurs" ordinaires dans un espace Hilbert, construit sur un sous-groupe de l'ensemble de matrices inversibles plus le produit intérieur des matrices de Frobenius. Des fonctions des matrices et les fonctionnelles linéaires sont présentées après, suivies de la définition de la dérivée de Fréchet. Le théorème de représentation de Riesz-Fréchet, qui occupe un rôle central dans le formalisme de ce chapitre, est énoncé. Ce théorème fournit un moyen de calculer le gradient d'une fonctionnelle de la dérivée de Fréchet.

La **Section 1** est consacrée à la théorie des flots matriciels. Un simple flot est d'abord détaillé afin de présenter au lecteur les diverses entités que cette théorie utilise, telles que les surfaces iso-spectrales et affines, la fonction objectif comme distance entre ces deux surfaces, des projecteurs affines, des gradients fonctionnels et le flot lui-même comme équation différentielle ordinaire (ODE). Ce flot est généralisé par la suite aux paires des matrices, qui sont plus près de notre contexte impliquant de valeurs propres généralisées. Pour une flexibilité maximale nous généralisons également la fonction objectif, du simple produit intérieur de Frobenius à une version pondérée de ce produit. Une formule très compacte résulte pour le gradient de la fonctionnelle qui sera instantiée en **Chapitre V**. Nous finissons le chapitre courant en mentionnant quelques perspectives et des développements ultérieurs pour la théorie des flots matriciels.

Dans notre travail nous nous sommes seulement concentrés sur des matrices réelles inversibles $n \times n$, appartenant à un certain sous-groupe du groupe linéaire général, un groupe de Lie d'ordre n^2. Il est cependant trivial d'appliquer les résultats obtenus ici à $GL_n(\mathbb{K})$ défini par rapport à un corps générique $\mathbb{K}$ tels que le corps des nombres complexes $\mathbb{C}$.

Un espace Hilbert nécessite, à part un espace vectoriel (ou linéaire), un produit intérieur. Pour les matrices un choix naturel est le produit intérieur de Frobenius défini comme

$$\langle \mathbf{A}, \mathbf{B} \rangle = \sum_{i,j} \mathbf{A}_{ij} \mathbf{B}_{ij} = \mathrm{Tr}\left[\mathbf{A}^{\mathrm{T}} \mathbf{B}\right] \qquad \textbf{(14)}$$

À l'aide du produit intérieur de Frobenius n'importe quelle matrice dans l'espace peut être exprimée comme une combinaison linéaire avec de coefficients réels dans une base de l'espace des matrices

$$\mathbf{A} = \sum_k \left\langle \mathbf{E}^k, \mathbf{A} \right\rangle \mathbf{E}^k \equiv \sum_k A_k \mathbf{E}^k \qquad \textbf{(15)}$$

Dans beaucoup d'autres situations il est plus commode de définir l'espace Hilbert des matrices sur un sous-espace comme par exemple l'ensemble des toutes les matrices réelles symétriques marquées $s_n(\mathbb{R})$ ou d'un autre groupe de Lie tels que $O_n(\mathbb{R})$, le groupe des matrices orthogonales réelles.

Une fonction de matrice en général $f : \mathcal{U}_n(\mathbb{R}) \to \mathcal{V}_m(\mathbb{R})$ lie les deux espaces Hilbert des matrices $\mathcal{U}_n(\mathbb{R}), \mathcal{V}_m(\mathbb{R}) \subset GL_n(\mathbb{R})$, chacun équipés du produit intérieur de Frobenius définis dans l'**Equation** (**14**). Dans ce cadre, l'analyse fonctionnelle établit qu'une dérivée généralisée connue sous le nom de dérivée de Fréchet $\left[\mathcal{D}f(\mathbf{A})\right](\boldsymbol{\delta})$ peut être définie par la relation suivante:

$$f(\mathbf{A} + \boldsymbol{\delta}) = f(\mathbf{A}) + \left[\mathcal{D}f(\mathbf{A})\right](\boldsymbol{\delta}) + \mathcal{O}(\boldsymbol{\delta}) \qquad \textbf{(16)}$$

Intuitivement la dérivée de Fréchet $\left[\mathcal{D}f(\mathbf{A})\right](\boldsymbol{\delta})$, qui se lit "dérivé de f en $\mathbf{A}$ actionnant sur $\boldsymbol{\delta}$", est le changement de premier ordre de la valeur de la fonction à un certain point $\mathbf{A}$ dans l'espace Hilbert, en appliquant une perturbation infinitésimale $\boldsymbol{\delta}$ à $\mathbf{A}$. Ainsi cette dérivée est "vectorielle", le long de la "direction" $\boldsymbol{\delta}$ dans l'espace Hilbert des matrices.

Un autre cas spécial, d'intérêt particulier, est quand le co-domaine de la fonction f, est $\mathbb{R}$ lui-même, c.-à-d. f est une fonctionnelle. L'analyse fonctionnelle a un résultat important au sujet des fonctionnelles linéaires agissant sur les espaces Hilbert, connu sous le nom du théorème de représentation de Riesz-Fréchet.

$$\left[\mathcal{D}F(\mathbf{A})\right](\boldsymbol{\delta}) = \langle \mathbf{B}, \boldsymbol{\delta} \rangle \equiv \langle \nabla F(\mathbf{A}), \boldsymbol{\delta} \rangle \qquad (17)$$

Cette équation est extrêmement utile dans le contexte des flots matriciels car elle fournit un moyen de calculer le gradient d'une fonctionnelle de la dérivée de Fréchet.

Le terme de flot matriciel représente une équation ordinaire continue (ODE) définie dans l'espace abstrait de Hilbert des matrices par rapport à un paramètre virtuel de "temps". Les différents constituants de l'ODE sont conçus afin d'amener le système "évolutif" dans un état désirable qui est typiquement la solution optimale d'une certaine fonction objectif.

D'une façon générale les techniques de flots matriciels peuvent être utilisées quand l'on veut trouver une matrice avec une certaine structure linéaire ou affine, qui simultanément a un certain spectre. La méthode est extrêmement flexible, et devrait plutôt être aperçue comme un environnement puisqu'elle permet de dériver de nouveaux flots après une certaine recette.

Premièrement deux surfaces sont définies, une incluant toutes les matrices d'une certaine structure affine, et l'autre incluant toutes les matrices qui ont un spectre donné. Ensuite une fonction de distance est définie entre ces deux surfaces qui devient la fonction objectif à minimiser. Pour l'optimisation de cette fonction le théorème de Riesz-Fréchet (**17**) offre le moyen de calculer le gradient, qui est ensuite utilisée pour définir un flot "de descente maximale" en fonction du paramètre de temps virtuel mentionné ci-dessus.

$$\mathrm{d}_t \mathbf{Q} = -\nabla F(\mathbf{Q}) \qquad (18)$$

Enfin un solveur ODE intégrera ce flot, et le minimum de la fonction objectif sera obtenu après que suffisamment de temps virtuel soit passé.

Typiquement dans les calculs de chimie quantique une base non-orthogonale est employée. Dans ce cas on est obligé de tenir compte également du tenseur de la métrique ou, comme connue par les physiciens, la matrice de recouvrement. Dans l'espace "fondamental" de Hilbert, l'équation de Schrödinger n'écrit plus $\mathbf{H}\boldsymbol{\psi}_n = \varepsilon_n \boldsymbol{\psi}_n$ mais plutôt $\mathbf{H}\boldsymbol{\psi}_n = \varepsilon_n \mathbf{S}\boldsymbol{\psi}_n$. Il sera ainsi nécessaire de modifier la théorie définie, dans la sous-section précédente, aux paires des matrices.

De nouveau il y a deux contraintes importantes, une liée au spectre et l'autre à la structure, chacune définit une surface particulière. La première surface est définie comme

$$\mathcal{M}(\mathbf{A},\mathbf{B}) = \left\{(\mathbf{T}^{\mathrm{T}}\mathbf{A}\mathbf{T},\mathbf{T}^{\mathrm{T}}\mathbf{B}\mathbf{T}) \in s_n(\mathbb{R}) \times s_n(\mathbb{R}) \middle| \mathbf{T} \in GL_n(\mathbb{R})\right\} \qquad (19)$$

La matrice $\mathbf{T}$ est une transformation de congruence, qui appliquée à la paire $(\mathbf{A},\mathbf{B})$ ne change pas ses valeurs propres. La deuxième surface, qui est liée aux contraintes structurales, est le produit de deux sous-espaces affines par un opérateur de projection

$$\mathcal{P}_{1(2)}(\mathbf{X}) = \mathbf{P}^0_{1(2)} + \sum_{j,k} \left\langle \mathbf{P}^j_{1(2)}, \mathbf{X} - \mathbf{P}^0_{1(2)} \right\rangle g^{-1}_{1(2);jk} \mathbf{P}^k_{1(2)} \qquad (20)$$

Minimiser la distance entre ces deux surfaces produira une paire de matrice

$$(\mathbf{X},\mathbf{Y}) = (\mathbf{T}^{\mathrm{T}}\mathbf{A}\mathbf{T},\mathbf{T}^{\mathrm{T}}\mathbf{B}\mathbf{T}) \qquad (21)$$

qui est iso-spectrale à $(\mathbf{A},\mathbf{B})$, et qui s'approche autant que possible, dans le sens des moindres carrés, de la structure imposée par l'opérateur de projection $\mathcal{P}$.

La fonction objectif que nous utilisons ici est la distance entre les surfaces iso-spectrales et affines

$$\begin{aligned} F(\mathbf{T}) &= \frac{1}{2}\left(\left\|\mathbf{U} \circ \left(\mathbf{T}^{\mathrm{T}}\mathbf{A}\mathbf{T} - \mathcal{P}_1(\mathbf{T}^{\mathrm{T}}\mathbf{A}\mathbf{T})\right)\right\|^2 + \left\|\mathbf{V} \circ \left(\mathbf{T}^{\mathrm{T}}\mathbf{B}\mathbf{T} - \mathcal{P}_2(\mathbf{T}^{\mathrm{T}}\mathbf{B}\mathbf{T})\right)\right\|^2\right) \equiv \\ &\equiv \frac{1}{2}\left(\left\|\mathbf{U} \circ \left(\mathbf{X} - \mathcal{P}_1(\mathbf{X})\right)\right\|^2 + \left\|\mathbf{V} \circ \left(\mathbf{Y} - \mathcal{P}_2(\mathbf{Y})\right)\right\|^2\right) \equiv \\ &\equiv F_1(\mathbf{T}) + F_2(\mathbf{T}) \end{aligned} \qquad (22)$$

Cette fonction objectif est identique à Chu exceptant un différence importante. Nous avons généralisé la norme standard de Frobenius $\|\mathbf{A}\| = \langle \mathbf{A},\mathbf{A} \rangle^{1/2}$ avec la norme "pondéré" de Frobenius $\|\mathbf{W} \circ \mathbf{A}\|$.

Après plusieurs manipulations et avec l'aide du théorème de représentation de Riesz-Fréchet (**17**) nous pouvons identifier le gradient de la fonction objectif

$$\nabla \mathrm{F}(\mathbf{T}) = 2\mathbf{A}\mathbf{T}\left[\alpha_1(\mathbf{X}) - \mathcal{P}_1(\alpha_1(\mathbf{X})) + \mathcal{P}_1(\mathbf{0})\right] + 2\mathbf{B}\mathbf{T}\left[\alpha_2(\mathbf{Y}) - \mathcal{P}_2(\alpha_2(\mathbf{Y})) + \mathcal{P}_2(\mathbf{0})\right] \qquad (23)$$

À l'aide du gradient trouvé, nous procédons encore une fois par flot "de descente maximale" identique à (**18**) dans la recherche de la solution optimale.

Chapitre V - Capteur de conductance à base de nanotubes de carbone pour la détection des acides amines physisorbés

Dans ce chapitre nous présentons des calculs théoriques sur un capteur de conductance à base de nanotubes de carbone. Une méthodologie, pour des calculs rapides de conductance quantique des dispositifs de captage visant les acides aminés aromatiques dans l'approximation des liaisons fortes, est développée. Les flots matriciels qui ont été décrits dans le chapitre précédent seront maintenant appliqués pour obtenir un hamiltonien d'ordre réduit optimisé pour des calculs de transport. Avec ce hamiltonien nous utilisons un algorithme de complexité linéaire pour calculer la conductance quantique dans le régime de transport cohérent.

Dans la **Section 1** nous expliquons brièvement comment un transistor à effet de champ de NTC peut être utilisé comme capteur chimique. Les défis du calcul *ab initio* de la conductance d'un tel dispositif, ainsi que la solution que nous proposons, sont développés dans la **Section 2**. Cette solution implique l'exécution des calculs *ab initio* sur un ad-système de référence considérablement plus petit, plus précisément chacun des quatre acides aminés sur une feuille de graphene. Ces calculs sont détaillés dans la **Section 3**, où entre autres résultats, nous constatons que l'adsorption induit des états près du niveau de Fermi et également un certain décalage du point de la neutralité de charge. La **Section 4** est consacrée à une méthode nouvelle que nous avons développée dans le but d'obtenir des modèles hamiltoniens optimisés pour des calculs de transport. À la base de cette méthode sont les puissants flots matriciels généralisés présentés dans le chapitre précédent, dont on démontre maintenant l'application dans une situation concrète. Une méthode efficace de calcul de conductance est présentée à la fin de ce chapitre dans la **Section 5**, où les premiers résultats sur la modification des spectres de transmission due à l'adsorption moléculaire sont également présentés.

Un capteur de conductance de NTC est fondamentalement un dispositif similaire au transistor à effet de champ. Le nanotube lie deux contacts métalliques, et son niveau de Fermi est contrôlé par une tension de grille de dessous. L'élément sensible est le nanotube lui-même qui signifie que sa surface est extérieurement exposée, n'étant pas couverte des oxydes où n'importe quels autres matériaux. Par rapport aux nanofils ou

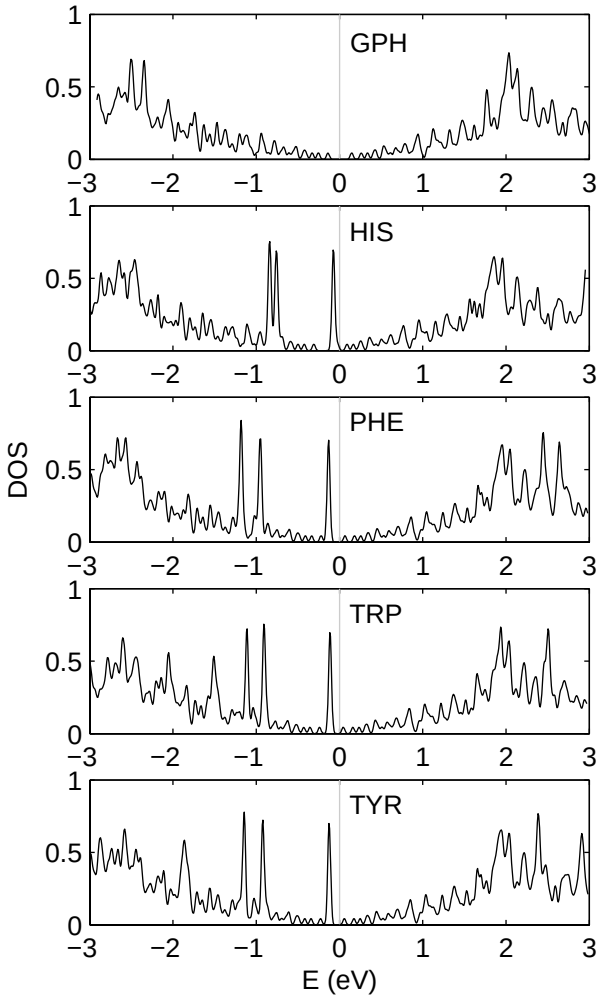

Figure 9. Densité totale des états pour le graphene pur et pour les quatre ad-systèmes, soulignant les pics spectraux dépendants d'acides aminés près du niveau de Fermi (ici mis à zéro)..

d'autres transistors chimiques, tous les atomes d'un nanotube de carbone sont des atomes de surface, ce qui est la clef pour expliquer l'excellente sensibilité de ce type de dispositifs.

Nous proposons un flot général pour étudier des capteurs de conductance à base de NTC (bien que non limité à des NTC ou à des sondes chimiques) qui comprend les étapes suivantes:

1. Structure électronique *ab initio* auto-cohérente de la molécule ciblé sur graphene.
2. Réduction d'ordre du modèle hamiltonien conservant le spectre autour du niveau de Fermi.
3. Transfert des paramètres du hamiltonien au capteur NTC et calculs de transport.

Les méthodes développées sont soumises à une étude de cas, où les molécules ciblées sont les quatre acides aminés aromatiques HIS, PHE, TRP et TYR. Chaque acide aminé a été individuellement placé sur une couche étendue de graphene et relaxé en NAMD. Les géométries obtenues peuvent être aperçues dans la **Figure 10**. Exceptant le tryptophane, qui a deux anneaux aromatiques, et qui s'est relaxé dans une configuration de "stack", tous les trois autres acides aminés se sont relaxés dans des configurations de "bridge".

Pour chaque ad-système, consistant en un acide aminé aromatique sur une feuille de graphene, des calculs *ab initio* auto-cohérents ont été exécutés avec SIESTA [**102**], un code DFT qui utilise des pseudopotentiels et pseudo orbitales atomiques localisés (PAOs).

On a observé que la physisorption change le niveau Fermi d'environ 150meV. Des bandes sans dispersion près de E_F sont évidentes dans chaque cas, alors que leurs positions spectrales dépendent du type d'acide aminé. Ces signatures individualisées pourraient s'avérer extrêmement utiles dans le contexte de l'identification d'acide aminé par les capteurs de conductance NTC.

La densité totale des états comme montrée dans la **Figure 9** souligne les états induits près du niveau de Fermi par la physisorption, et leur dépendance de l'acide aminé adsorbé. Ces états occupent les orbitales du groupe α-carboxyliques des acides aminés. Il est intéressant de noter que les orbitales des anneaux aromatiques de chaque acide aminé sont occupées seulement par des états trouvés à 3eV du niveau de Fermi, et ne peuvent donc pas influencer la conductance intrinsèque d'un nanotube de carbone. Par conséquent, on peut conclure que, bien que responsables du mécanisme de liaison, ce ne sont pas les anneaux aromatiques des acides aminés qui pourraient changer la conductance des nanotubes, mais plutôt les ions carboxyliques ou aminés.

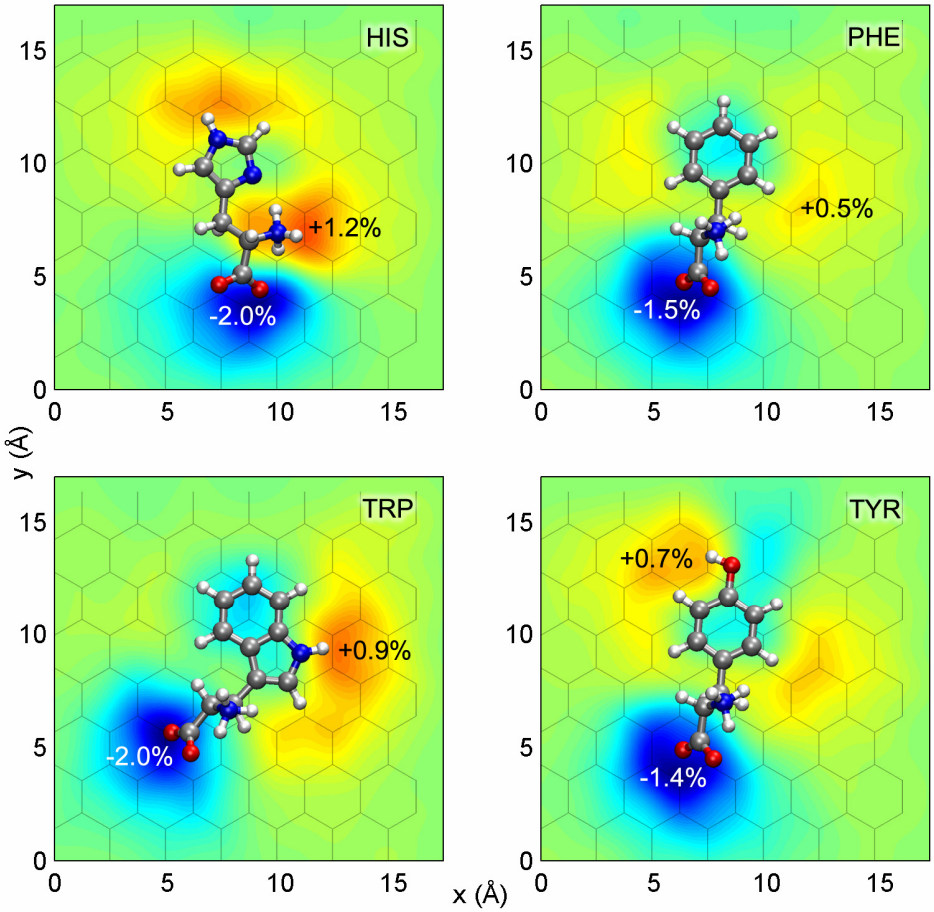

Figure 10. Transfert des charges Mulliken des orbitales $2p_z$ de graphene. La figure montre également la maille hexagonale de graphene pour servir d'indication de la configuration d'empilement des acides aminés.

Comme prévu, les bandes sans dispersion correspondent aux états localisés dans l'espace réel dans la proximité d'un groupe α-carboxylique. Les charges Mulliken calculés par SIESTA ont été utilisées pour étudier le possible transfert de charge. Les charges du graphene de l'ad-système ont été soustraites, pour chaque acide aminé, des charges du graphene pur, et ensuite convoluées par une fonction gaussienne pour obtenir la **Figure 10**. L'amplitude du transfert de charge situe notre cas dans le régime de physisorption. Comme il peut être observé, l'écrantage des charges ioniques à l'intérieur du graphene est fortement localisé. Ceci nous permet de transférer les éléments de matrice du hamiltonien et de la matrice de recouvrement, de ces petits systèmes de référence à un capteur de conductance NTC qui aurait un nombre considérable d'atomes, et évite des calculs cohérents insurmontables.

La **Section 4** présente une solution qui consiste en la projection du problème dans un sous-espace réduit, suivi des transformations de congruence infinitésimales (flots iso-spectrals) comme présenté en **Chapitre IV**, afin de corriger le spectre autour du niveau de Fermi. Cet algorithme est alors appliqué aux quatre ad-systèmes se composant des acides aminés aromatiques sur le graphene qui aura comme résultat un modèle hamiltonien optimal pour des calculs de transport.

Le transport élastique dans les nanostructures est déterminé par les propriétés spectrales proche du niveau de Fermi. Ceci signifie que seulement quelques vecteurs propres du hamiltonien avec les valeurs propres correspondantes à l'intérieur d'un certain intervalle d'énergie centré à E_F contribuent à la moyenne de l'opérateur de courant. Heureusement dans beaucoup de situations d'intérêt pratique, cet ensemble de vecteurs propres projette notamment sur un sous-ensemble de la base de PAO, comme il se produit par exemple avec les bandes π du nanotube de carbone. Dans ce cas, les matrices hamiltoniennes et de recouvrement peuvent simplement être projetées sur un sous-espace réduit de Hilbert, où les calculs sont accélérés jusqu'à quelques ordres de grandeur avec une perte mineure de précision numérique.

Nous commençons par des matrices hamiltonienne et de recouvrement *ab initio* auto-cohérentes. Ensuite nous obtenons, par des transformations appropriées, une paire de matrices effectives et réduites, qui possède un spectre correct autour du niveau de Fermi. Fondamentalement cette méthode consiste en l'élimination des PAOs basée sur la densité des états projetée, suivie d'un flot matriciel pour récupérer la sparsité et pour corriger le spectre. On peut démontrer que la valeur moyenne du courant peut être calculée directement dans un sous-espace de Hilbert représenté par le sous-ensemble des PAOs

$$\left\{ |\nu\rangle \,\middle|\, \langle\psi_n|\nu\rangle \neq 0,\ \hat{H}_0|\psi_n\rangle = \varepsilon_n|\psi_n\rangle,\ \varepsilon_n \in [\mu_L, \mu_R] \right\} \qquad (24)$$

Calculer des valeurs moyennes dans ce sous-espace de Hilbert est extrêmement efficace. C'est exactement le but de la méthode qu'on va détailler, qui offre un cadre formel pour trouver un sous-espace minimal de Hilbert dans lequel la valeur moyenne du courant peut être calculée avec n'importe quelle précision numérique.

La première étape dans l'algorithme de réduction du modèle décide quels PAOs seront projetés pour obtenir un sous-espace réduit de Hilbert. Il n'est pas difficile de voir que

l'ensemble défini en (**24**) est contenu dans la densité des états projetée sur les orbitales (PDOS) définie comme

$$\rho_v(E) = \frac{1}{N_k}\int_{BZ} \mathbf{dk} \sum_{n,\mu} \mathrm{Re}\left[\langle \chi_n(\mathbf{k})|\tilde{\mu}\rangle \mathbf{S}_{\mu\nu}(\mathbf{k}) \langle \tilde{\nu}|\chi_n(\mathbf{k})\rangle\right] \delta(E-\varepsilon_n(\mathbf{k})) \qquad (\mathbf{25})$$

Nous avons utilisé la PDOS donnée par SIESTA en décidant quels PAO éliminer de la base. L'ensemble de base de l'espace Hilbert réduit est alors pris pour être $\left\{|\nu\rangle \,\middle|\, |\rho_v| > \varepsilon_\rho \right\}$, ce qui veut dire que seulement ces PAOs pour lesquels la PDOS filtrée en énergie ρ_v était plus grande qu'un seuil donné ε_ρ ont été retenus. Cependant cette sorte de troncation de base a comme conséquence des erreurs dans structure de bande. Les bandes sans dispersion, que nous avons attribuées plus tôt aux états localisés, sont décalées par quelques dizaines de meV d'une façon non-prévisible. À l'origine de ces erreurs sont, très probablement, les nombres de condition grands de la paire des matrices $(\mathbf{H},\mathbf{S})$ que nous n'avons pas pris en compte pendant l'élimination des orbitales de base.

Corriger les erreurs de troncation de base peut être réalisé simplement en diagonalisant la paire projetée $(\mathbf{H}_\perp,\mathbf{S}_\perp)$, au point Γ par exemple, suivie par le remplacement de ses valeurs propres par les valeurs exactes prises de la paire initiale $(\mathbf{H},\mathbf{S})$. Le seul problème est que l'ainsi trouvé hamiltonien perd sa sparsité. Nous montrons cependant, que par un flot isospectral la sparsité peut être récupéré, rapportant de ce fait une paire sparse qui a un spectre correct autour du niveau de Fermi.

L'utilisation d'un flot iso-spectral généralisé implique l'identification des paramètres des deux principales surfaces, $\mathcal{M}$ et $\mathcal{V}$ comme marqués dans le chapitre précédent. Dans notre cas l'ensemble iso-spectral $\mathcal{M}$ est construit autour $(\tilde{\mathbf{H}}_\perp,\mathbf{S}_\perp)$. Par rapport aux notations du **Chapitre IV**, nous identifions $(\mathbf{A},\mathbf{B}) \equiv (\tilde{\mathbf{H}}_\perp,\mathbf{S}_\perp)$. Le sous-espace affine que nous considérons ici, a une structure triviale, impliquant seulement deux matrices constantes $\mathbf{P}^0_{1(2)}$ à l'intérieur de l'opérateur de projection défini par **Equation** (**20**). Pour notre but nous définissons ces deux matrices comme $(\mathbf{P}^0_1,\mathbf{P}^0_2) \equiv (\mathbf{H}_\perp,\mathbf{S}_\perp)$. Les derniers paramètres exigés sont les deux poids $(\mathbf{U},\mathbf{V})$ apparaissant dans la définition de la fonction objectif $F(\mathbf{T})$ en (**22**) qui sont discutés ci-dessous.

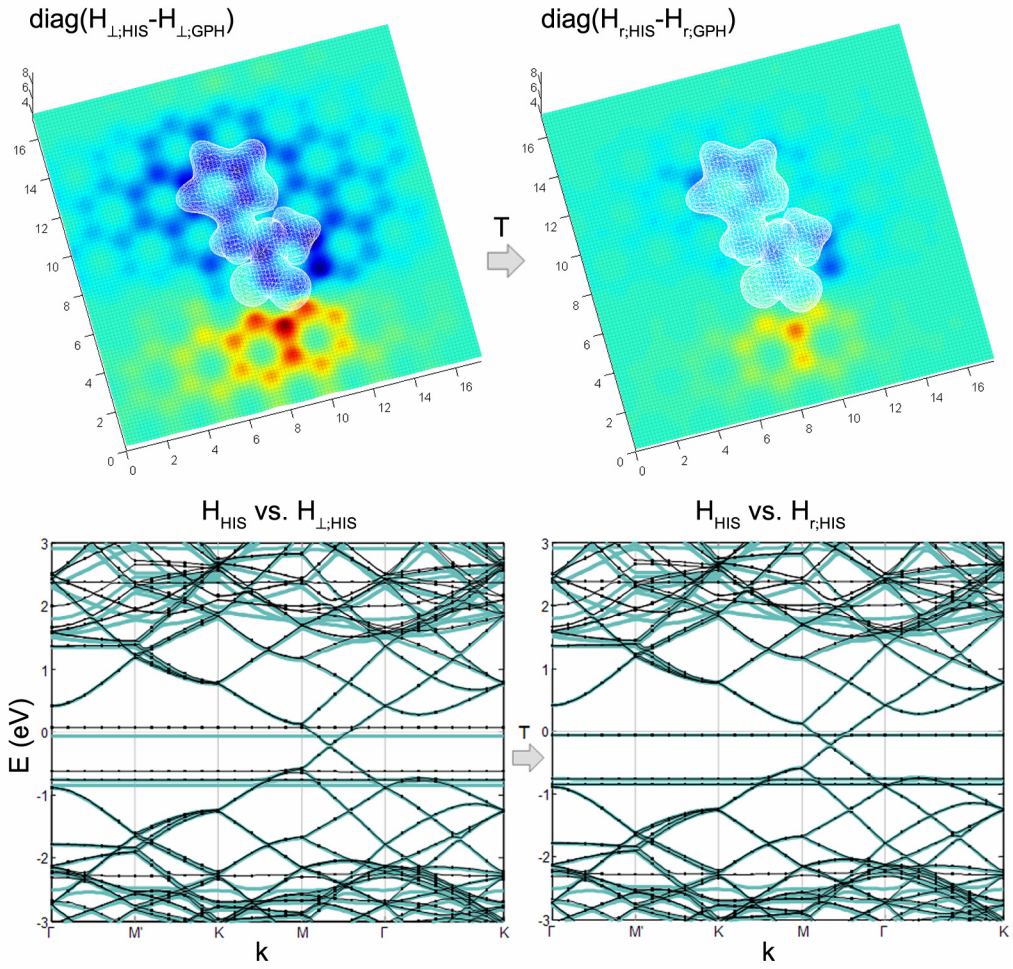

Figure 11. (haut) Perturbation du hamiltonien du graphene, avant (gauche) et après (droit) le flot iso-spectral de renormalisation. (bas) La structure des bandes avant (gauche) et après (droite) le flot iso-spectral de renormalisation. En cyan sont les bandes du hamiltonian initial, et en noir celles du hamiltonien projeté et renormalizé.

Le premier choix pour $(\mathbf{U},\mathbf{V})$ serait $(\mathbf{I}_\circ,\mathbf{I}_\circ)$, où $\mathbf{I}_\circ$ est l'élément neutre du produit Hadamard des matrices, étant simplement une matrice ayant toutes les entrées égales à un. Néanmoins nous exploitons la flexibilité de ce cadre et nous choisissons $(\mathbf{U},\mathbf{V})$ différemment, afin de réaliser des autres buts subtils. Pour $\mathbf{V}$ nous prenons simplement $\mathbf{I}_\circ$, comme nous souhaitons conserver la matrice de recouvrement. La **Figure 11** (haut-gauche) montre la différence diagonale du hamiltonien entre l'ad-système HIS+GPH et le GPH pur. Comme on peut observer, la perturbation d'énergie des sites se prolonge presque dans toute la cellule d'unité. Ceci pourrait poser un problème pour l'export des éléments de matrice hamiltoniens vers un capteur NTC. En

conséquence nous pouvons choisir $\mathbf{U}$ afin de confiner cette perturbation plus près de la molécule adsorbée. Ainsi pour $\mathbf{U}$ nous prenons $\mathbf{I}_\circ$ et nous annulons celles éléments de matrice sur lesquels nous souhaitons localiser la perturbation. Simultanément pour l'ad-système nous avons modifié la matrice $\mathbf{P}_1^0$ en remplaçant la sub-matrice hamiltonienne correspondant aux orbitales de graphene par le hamiltonien projeté du graphene pur $\mathbf{H}_{\perp;\mathrm{GPH}}$.

Après avoir identifié tous les ingrédients, nous mettons $\mathbf{T}=\mathbf{I}$ comme état initial et nous intégrons avec un solveur ODE le flot "de descente maximale" $\mathrm{d}_t\,\mathbf{T}=-\nabla F(\mathbf{T})$, avec l'aide du gradient (**23**). En raison de la forme triviale des opérateurs de projection $\mathcal{P}_{\mathrm{I}(2)}$ on obtient une formule simplifiée de gradient

$$\nabla \mathrm{F}(\mathbf{T})=2\tilde{\mathbf{H}}_\perp\mathbf{T}\left[\mathbf{U}\circ\mathbf{U}\circ\left(\mathbf{X}-\mathbf{P}_1^0\right)\right]+2\mathbf{S}_\perp\mathbf{T}\left[\mathbf{Y}-\mathbf{P}_2^0\right]$$

En prenant $\mathbf{T}_\infty$ comme limite de flot, la solution recherchée est simplement $(\mathbf{H}_r,\mathbf{S}_r)=(\mathbf{T}_\infty^{\mathrm{T}}\tilde{\mathbf{H}}_\perp\mathbf{T}_\infty,\mathbf{T}_\infty^{\mathrm{T}}\mathbf{S}_\perp\mathbf{T}_\infty)$. La structure de bande que nous avons calculée avec $(\mathbf{H}_r,\mathbf{S}_r)$ est montrée à la droite des bandes de la paire projetée $(\mathbf{H}_\perp,\mathbf{S}_\perp)$ dans la **Figure 11** (bas). Remarquons la reproduction parfaite de la structure des bandes de $(\mathbf{H},\mathbf{S})$ à l'intérieur du $[\mu_L,\mu_R]$, la **Figure 11** (haut) montre également le confinement réussi de la perturbation. La paire résultée $(\mathbf{H}_r,\mathbf{S}_r)$ est, comme prévue, très sparse, et les interactions sont pratiquement limités au troisième voisin le plus proche. Ceci permet l'implémentation de méthodes très efficaces de calcul de conductance quantique, que nous décrirons dans la prochaine section.

Puisque dans la **Section 5** nous ne traitons seulement que des dispositifs à deux bornes, nous avons développé une méthode efficace pour calculer les fonctions de Green nécessaires. Tout d'abord, il faut noter que n'importe quelle méthode efficace de calcul de conductance exploite le modèle de sparsité des matrices impliquées. Ceci a pour conséquence que la conductance d'un dispositif à deux bornes est complètement déterminée par la connaissance des fonctions de Green de surface des contactes $g^{0;r}_{L(R);\nu\nu'}(E)$ et des fonctions de Green de gauche à droite (de transfert) de la région centrale $G^r_{C;\mu\nu}(E)$

$$\mathcal{G}(E)=\frac{2e^2}{h}\sum_{\substack{\mu\mu'\in\Omega_{CL}\\ \nu\nu'\in\Omega_{CR}}}\Gamma_{L;\mu\mu'}(E)G^r_{C;\mu'\nu'}(E)\Gamma_{R;\nu'\nu}(E)G^a_{C;\mu\nu}(E) \qquad (26)$$

Algorithme 3. Méthode de décimation pour le calcul des fonctions de Green de surface

1. LET $\mathbf{K}_{ij;n-1} = E\mathbf{S}_{ij} - \mathbf{H}_{ij}$ FOR $i,j = \overline{0,1}$
2. REPEAT
   3. $\mathbf{K}_{00;n} = \mathbf{K}_{00;n-1} - \mathbf{K}_{01;n-1}\mathbf{K}_{11;n-1}^{-1}\mathbf{K}_{10;n-1}$
   4. $\mathbf{K}_{11;n} = \mathbf{K}_{11;n-1} - \mathbf{K}_{01;n-1}\mathbf{K}_{11;n-1}^{-1}\mathbf{K}_{10;n-1} - \mathbf{K}_{10;n-1}\mathbf{K}_{11;n-1}^{-1}\mathbf{K}_{01;n-1}$
   5. $\mathbf{K}_{01;n} = -\mathbf{K}_{01;n-1}\mathbf{K}_{11;n-1}^{-1}\mathbf{K}_{01;n-1}$
   6. $\mathbf{K}_{10;n} = -\mathbf{K}_{10;n-1}\mathbf{K}_{11;n-1}^{-1}\mathbf{K}_{10;n-1}$
   7. LET $\mathbf{K}_{ij;n-1} = \mathbf{K}_{ij;n}$ FOR $i,j = \overline{0,1}$
8. UNTIL $\|\mathbf{K}_{01;n}\| + \|\mathbf{K}_{10;n}\| \le 2\varepsilon$
9. $\mathbf{G}_{00} = \mathbf{K}_{00;n}^{-1}$
10. $\mathbf{G}_{11} = \mathbf{K}_{11;n}^{-1}$

Pour les fonctions de Green de transfert $G^r_{C;\Omega_{CL}\Omega_{CR}}(E)$, nous avons opté pour une méthode d'élimination qui est exacte et également ordre-N, au moins pour des systèmes 1D comme les nanotubes de carbone sont [**104**]. Cette méthode exploite la structure bloc tri-diagonale de $\mathbf{H}_C$ et $\mathbf{S}_C$ et suit les étapes décrites dans l'**Algorithme 2**.

Algorithme 2. Méthode d'élimination pour le calcul des fonctions de Green de transfert

1. LET $\mathbf{K} = E\mathbf{S}_C - \mathbf{H}_C - \mathbf{\Sigma}_L(E) - \mathbf{\Sigma}_R(E)$,
   $\mathbf{A}_1 = \mathbf{K}_{11}$, $\mathbf{B}_1 = \mathbf{I}$
2. FOR $i = \overline{2,n}$
   3. $\mathbf{A}_{i+1} = \mathbf{K}_{i+1;i+1} - \mathbf{K}_{i+1;i}\mathbf{A}_i^{-1}\mathbf{K}_{i;i+1}$
   4. $\mathbf{B}_{i+1} = -\mathbf{B}_i\mathbf{A}_i^{-1}\mathbf{K}_{i;i+1}$
5. ENDFOR
6. $\mathbf{G}_{1;n} = \mathbf{B}_n\mathbf{A}_n^{-1}$

Le calcul des fonctions de Green de surface a été réalisé par 'une méthode très efficace appelée la méthode de décimation qui est récapitulée dans l'**Algorithme 3**.

Nous avons appliqué cette méthode à un nanotube semi-conducteur (11,0) mesurant approximativement 15nm, empilé entre des contacts métalliques simulés par des tubes

(11,0) semi-infinis idéaux. Le résultat est présenté dans la **Figure 12** en noir, et est, comme prévu, égal à la fonction de transmission d'un nanotube infini (11,0). La forme globale et les discontinuités dans la transmission se conforment bien aux calculs des liaisons fortes non-orthogonaux validant la méthode que nous avons décrite dans ce chapitre.

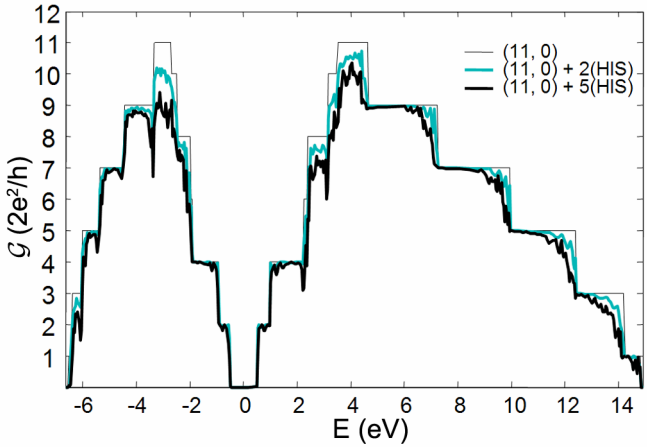

Figure 12. Spectre de transmission du capteur à base de NTC (11,0) pour le nanotube sans et avec HIS acides aminées.

Puis des molécules d'acide aminé ont été ajoutées aléatoirement le long du tube assurant un espacement minimum entre deux acides aminés voisins. Les matrices hamiltoniennes et de recouvrement du capteur ont été par la suite perturbées aux endroits d'adsorptions. Des spectres de transmission calculés pour ces cas sont tracés dans la **Figure 12** avec des lignes épaisses. L'abaissement de la transmission en fonction du nombre de molécules d'histidine adsorbé sur la surface du tube est évident à de grandes énergies loin du niveau de Fermi. Malheureusement près de E_F le transfert de charge semble trop faible pour modifier la transmission. Il est vrai cependant que nous n'avons pas inclus les orbitales moléculaires de l'acide aminé dans les calculs, ni nous n'avons pas considéré un éventuel décalage du point de neutralité de la charge dû à l'adsorption. Par contre les méthodes développées dans ce chapitre sont généralement valables et n'attendent que d'être appliquées à d'autres capteurs chimiques.

.

.

Table of contents

List of figures, tables and algorithms

Introduction

The last years have seen nanotech applications approaching rapidly a tangible existence, while in the near future it is reasonable to expect nanotechnologies pervade key application areas like energy, materials, devices and so on. The explosive development of nanotech has been fueled by the considerable progress made in controllably fabricating and manipulating nanostructures.

Discovered fifteen years ago by Sumio Iijima [**1**] carbon nanotubes have quickly become one of nanotech logos along with nanoparticles, nanowires, fullerenes and molecular layers [**2**]. Nanotubes come in several varieties and can be classified by their helicity (later named chirality), number of walls, the presence of pentagons-heptagons, etc. The simplest form is the single-wall carbon nanotube (SWNT), which can be visualized as a rolled honeycomb graphite sheet into a cylinder.

If carbon nanotubes occupy the role they do today, it is only due to their exceptional structural, mechanical, electronic and optical properties. From the electronic point of view, simply changing the graphite rolling direction, results in metallic or semiconducting tubes. The metallic tubes are ballistic conductors over micrometer length scales being thus able to carry currents very effectively without loosing power through Joule heating. This also means that nanotubes can support huge current densities. Semiconducting tubes have bandgaps depending on their diameter, and achieve carrier mobilities surpassing by far those of the archetypal material in electronics, silicon. When referring to mechanical properties of carbon nanotubes they are often called the ultimate fibers; nanotubes are as strong as diamond. Nevertheless nanotubes retain a high flexibility due to their high length to diameter aspect ratios. They also support several percent strains and remain elastic under large deformations. The list of nanotube advantages does not have to stop here, since carbon nanotubes

possess equally interesting optical, thermal, electromechanical and magnetic properties.

Although increasingly better controlled, the synthesis of carbon nanotubes involves mechanisms that are not perfectly understood at this moment. This missing chain is directly responsible for the inability to synthesize nanotubes with controlled features, and is probably the main reason for which CNTs are not used on a larger scale. However giant steps are made everyday in synthesis [**3**, **4**, **5**], functionalization [**6**, **7**, **8**], solubilization [**9**, **10**] and sorting [**11**, **12**] of nanotubes. Given this trend it is reasonable to extrapolate that in several years it will be possible to have nanotubes with well controlled properties at significantly lower costs, enabling a plethora of applications.

Aside from this, an essential aspect that allows envisioning the design of carbon-nanotube based devices is the increasingly better agreement between theoretical predictions and experimental data. As a side note, it is actually via simple theoretical calculations that the metallic/semiconducting nature of nanotubes, their Young's moduli and optical transitions were predicted in the first place. While an important part of the CNT research efforts focus on improving fabrication and manipulation techniques, another thread is continuously expanding the physical understanding of nanotubes, and others are trying to develop applications.

A brief analysis of the patenting activity on carbon nanotube based applications reveals that the major slots in the pie chart are taken by field emission, energy storage, composites, nanoelectronics, sensors and actuators, etc. In each of these possible applications nanotubes are far from achieving their potential. Moreover other applications are added on this list everyday. We can safely state then that the nanotube application research area is still in its infancy offering many development opportunities.

In this thesis we concentrate on the possible application of carbon nanotubes in biochemical detection relevant for biotechnologies, medicine and even for defense and security. Our primary goal is to move one step forward the theoretical models of nanotubes and use them as predictive tools, not in calculating fundamental properties, but rather in designing novel devices of potential practical interest. Thereby, the general pattern of this thesis consists in proposing sensing devices and modeling and

simulating them as proof of concept, sometimes doubled by feasibility assertions based on similar, experimentally-proven models.

Validating devices theoretically is obviously the less expensive choice in a context in which nanotube manipulation is still limited, time-consuming and thus expensive. This doesn't necessarily mean that one has to blindly accept the validity of any calculations, at least within the gross approximations sometimes one has to employ. In this situation an idea would be to build theoretical models sufficiently fast and accurate at least to a first order. If the proposed device would prove operational in theory it could be practically realized and characterized yielding data that could be used in improving the theoretical models. An additional advantage of simulation is the insight gained into the intimate operation mechanisms of a device.

Sometimes the models used in this thesis may appear rather simple to the reader, and indeed they are. However one has to remember that the large number of atoms a typical device may have is a major bottleneck. The recurrent problem in this thesis is a certain square or cubic scaling in the number of atoms which drives simulation in the intractable realm. Although the goal of nanotech is to miniaturize devices and thus decrease the number of atoms, it is often the case for simulations to involve 10^5 atoms or more. Storing a matrix with $10^5 \times 10^5 = 10^{10}$ elements is costly but this is nothing compared to the time it would take to invert or diagonalize such a matrix that would require $(10^5)^3$ operations. This somehow explains the different numerical approaches we were forced to take in solving the problems at hand.

Two different sensor structures are proposed in this thesis. The first involves an electromechanical principle and can be used either in measuring piconewton forces or zeptogram masses. The second sensor is based on conductance changes that a carbon nanotube would experience when exposed to aromatic amino acids. Both devices have interesting applications in biochemical sensing.

The content of this thesis is split in five chapters. **Chapter I** provides a succinct introduction to the structure and properties of carbon nanotubes. Basic crystallographic elements like lattice vectors, first Brillouin zone etc. are established starting from those of graphite. The standard tight-binding electronic structure of graphene will be used to derive the band structure of nanotubes within the zone-folding approximation. We have insisted here in presenting only those properties that

are relevant for this thesis, namely the transport and mechanical properties. Both this sections would contain apart theoretical predictions, experimental measurements that generally are found to support theory.

In **Chapter II** we detail the transport theory in nanostructures in the general multi-terminal device setting. Both the aforementioned nanotube sensors have an electric output, typically a current, and thus this chapter will serve as a theoretical background for transport calculations in **Chapter III** and **Chapter V**. We have chosen to arrive at the Landauer-Büttiker transport formalism starting from the rigorous ground of many-body non-equilibrium Green's functions. Thus the general scheme this chapter follows is a series of hypotheses applied to the general case in order to simplify the theory down to models that are both numerically tractable and that approximate well the transport properties of carbon nanotubes. As we will use non-orthogonal basis sets in our calculations we also discuss the changes required to adapt the transport theory to this situation.

The first contribution of this thesis is **Chapter III** which contains an ensemble of theoretical calculations we have performed in order to validate the operation principle of a carbon nanotube-based electromechanical sensor. The proposed device is a nanotube cross in which one tube plays the role of a cantilever, bending under external forces, and the other as a bearing and a potentiometer that transduces the deflection of the cantilever into an electric current imbalance. Measuring forces as low as a few piconewtons is demonstrated with this device via molecular mechanics calculations. We also prove in this chapter that at room temperature the deflection-current characteristic is monotonic and thus it can be used as a sensor. In yet another configuration, based on the frequency shift of the cantilever, the same device shows in theory that it can detect molecular bodies weighting a few kilodaltons, the mass of a small protein like streptavidin is. Thus this device is very useful in mass spectroscopy and biochemical detection.

In **Chapter IV** we develop the apparatus of continuous matrix flows which is a key element for the transport calculations of **Chapter V**. Although this theory in itself has been developed by Moody Chu, our modest contribution was to apply and extend it for quantum transport. This chapter is rather mathematical in scope and tries to accustom notions of functional analysis like the matrix Hilbert space and Fréchet

derivatives, and also to establish a parallel with the Schrödinger equation Hilbert space that is more familiar to physicists. Once these concepts are set in place the theory of matrix flows is illustrated over two examples. While the first is used only to familiarize the reader with the basic ingredients this theory uses, the second has important practical applications and will be used in **Chapter V**. This second example is a method allowing "shaping" a generalized matrix pair like Hamiltonian and overlapping matrices, while preserving their spectrum. With respect to Chu's theory we have extended this framework to increase the "shaping" flexibility by modifying the goal function.

Although **Chapters II** and **IV** should have probably been merged together into a theoretical background chapter, for the sake of clarity we felt the need to include before each type of sensor the theory necessary to understand its corresponding chapter alone. Thus all the theory at the base of **Chapter III** is found in **II** and for **Chapter V** is found in **II** and **IV**, decoupling thus the thesis in two independent parts grouped around the two sensors.

The validation of the second sensor is the object of **Chapter V** and it is the second main contribution of this thesis. In this chapter we have tried to answer the question of whether carbon nanotube conductance sensors could detect the four aromatic amino acids Histidine, Phenylalanine, Tryptophan and Tyrosine. As realistic carbon nanotube devices would have a large number of atoms, self-consistent calculations would be extremely difficult to achieve in practice, and we have thus chosen an alternative approach. The four amino acids are studied onto a simple graphene layer. Then, a procedure based on the matrix flows described in **Chapter IV** is used to obtain effective Hamiltonian and overlapping matrices that preserve a good spectral accuracy around the Fermi level, relevant for transport calculations. With this minimal model we will be able to calculate effectively the conductance of large carbon nanotube based sensors.

CHAPTER I.

Carbon nanotubes: Structure and properties

Introduction

An introductory overview of the structure and properties of carbon nanotubes is provided in this chapter. The basic terminology and physics are set in place to serve as a backbone for the rest of this thesis which is focused on carbon nanotube devices. Here we have selected only those features of the now-vast and perpetually expanding nanotube theory that are fundamental for the understanding of the following chapters. For a complete yet introductory overview of the theory of carbon nanotubes we refer the reader to **References 13**, **14**, **15**. Another goal of this section is to provide the reader with a certain body of experimental data that would come in support and be referenced by subsequent chapters.

Basic crystallography elements of nanotubes are the subject of **Section 1** beginning with graphite and graphene which facilitates both visualizing the structure of nanotubes and obtaining a first order approximation of their electronic and mechanical properties. The unrolled nanotube unit cell can be viewed as a super-cell of graphene which will prove to be extremely helpful in determining the band structure and densities of states of single-wall nanotubes (SWNTs). For SWNTs all their structural properties like diameter, unit cell length and number of atoms, are shown to depend on a single vector, the chiral vector, defined by two integer numbers.

In **Section 2**, the electronic properties of single-wall nanotubes are derived in a simple tight-binding approximation from those of graphene. Most of the derivations in detailed in **Sections 2** follow closely **Reference 13**. The zone-folding technique is applied revealing the quantization of the transversal wave vector in carbon nanotubes

and the celebrated metallic or semiconducting nature of nanotubes depending on their chiral vector alone.

The main regimes of the mesoscopic transport theory are quickly reminded in **Section 3** in order to identify the relevant length and time scales for carbon nanotubes. We then review experimental evidence of transport regimes in SWNT. A number of excellent reviews are available on this topic [**16**, **17**, **18**, **19**]. For metallic nanotubes it was found that the typical mean free-path is at least in the order of 100nm, while bandgaps in semiconducting tubes are consistent with theoretical predictions. Problems related to Schottky barriers and in general with contacting nanotubes by metallic leads are discussed at the end of this section together with doping and defect influence on nanotube transport properties.

In **Section 4** we turn our attention to the mechanical properties of nanotubes. At first a brief review of the computational methods available for nanotube simulation is provided. The reader is referred to a number of excellent reviews dealing with carbon nanotube mechanical properties [**16**, **20**, **21**]. Theory has predicted initially for SWNT huge Young's moduli, but on close investigation it has been established that at the base of these results was the inappropriate definition of the tube wall thickness. Finally theoretical and experimental evaluations of SWNT mechanical properties like Young's modulus, bending and torsion stiffness, etc. are enumerated at the end of this chapter.

1. Crystal structure

1.1. Graphite and graphene

From elementary chemistry we know that a carbon atom has six electrons, two of which fill completely the first shell ($1s^2$), are called core electrons, and are strongly bound to the nucleus. The remaining four populate the weakly spaced $2s^2$ and $2p^2$ levels, are called valence electrons, and are higher in energy than core electrons. There is a small energy separation between the 2s and 2p orbitals which facilitates re-hybridization. This gives rise to a high coordination flexibility of the carbon atom in forming new compounds and explains the large variety of carbon-based materials in nature.

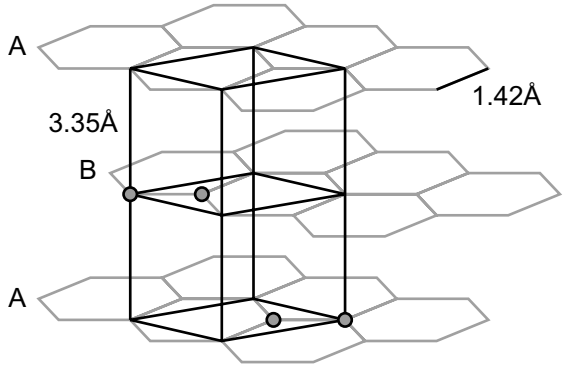

Figure I.1. Graphite atomic structure in ABAB stacking. The unit cell of graphite and its four inequivalent atoms are represented with black lines. The interlayer spacing and the carbon-carbon bond length are also displayed.

Among carbon mono-atomic crystals the best known are diamond and graphite. The coordination of a carbon atom in these materials is essentially different but the bonds are covalent in both and are the strongest in nature. Graphite is essentially a layered hexagonal lattice with carbon atoms forming covalent sheets stacked on top of each other in an ABAB sequence as in **Figure I.1**. The typical layer separation is 3.35Å and the carbon-carbon bond length is 1.42Å. In graphite the carbon atoms are sp^2 hybridized, i.e. one 2s electron mixes with two 2p electrons. This hybridization forms covalent σ bonds that make an angle of 120°. Thus each sp^2 hybridized atom has three coplanar neighbors leading to the hexagonal lattice of the layers seen in **Figure I.1**. The last electron occupies the remaining $2p_z$ orbital forming weak interlayer π bonds.

A single layer of graphite is called graphene. **Figure I.2** shows the unit cell of graphene as a shaded rhombus together with its corresponding reciprocal lattice and first Brillouin zone (BZ) as a shaded hexagon. The real-space lattice vectors are designated in this figure by $\mathbf{a}_{1(2)}$ and the reciprocal lattice vectors by $\mathbf{b}_{1(2)}$. In terms of the normal Euclidian coordinate system, the lattice vectors are given by

$$\mathbf{a}_{1(2)} \equiv \left(\frac{\sqrt{3}}{2} a, \pm \frac{1}{2} a \right) \qquad \textbf{(I.1)}$$

where a is the lattice constant ($a = \left\| \mathbf{a}_{1(2)} \right\|$) and for the typical carbon-carbon bond length in graphene of 1.42Å it has the value $a = \sqrt{3} \times 1.42\text{Å} = 2.46\text{Å}$.

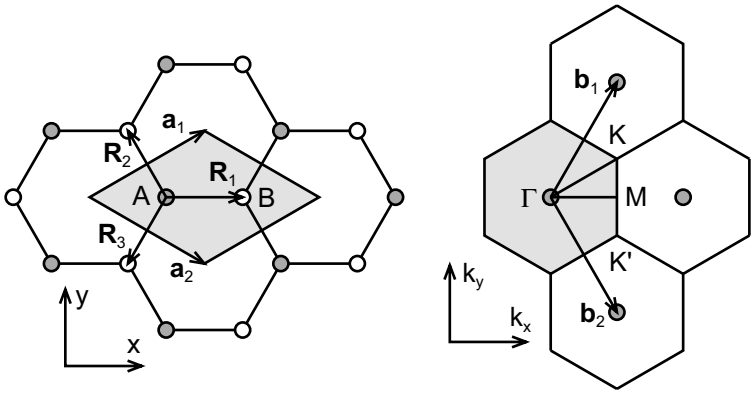

Figure I.2. Graphene (left) unit cell in gray with lattice vectors $\mathbf{a}_i$ and the two inequivalent atoms represented by gray and white circles, and (right) reciprocal lattice with lattice vectors $\mathbf{b}_i$ and first Brillouin zone in gray together with its high symmetry points Γ, M, K and K'.

The reciprocal lattice vectors of graphene are found as usually by solving the linear system of equations engendered by $\mathbf{a}_i \cdot \mathbf{b}_j = 2\pi\delta_{ij}$, which yields

$$\mathbf{b}_{1(2)} = \left(\frac{2\pi}{\sqrt{3}a}, \pm\frac{2\pi}{a} \right) \qquad \textbf{(I.2)}$$

corresponding to a reciprocal lattice constant of $4\pi/\sqrt{3}a$. As it can be observed from **Figure I.2** the first Brillouin zone is hexagonal but rotated by 90° with respect to a hexagon of the real-space lattice. The first Brillouin zone is characterized by four high symmetry points Γ, K, K' and M, representing its center, two opposing corners and the center of an edge respectively. Since the graphene unit cell contains two atoms the corner points K and K' are not equivalent and are treated separately. The crystallographic elements we have developed so far for graphene will be used in the following in explaining the structure and electronic properties of carbon nanotubes.

1.2. Single-wall carbon nanotubes

The structure of a carbon nanotube can be viewed mentally as resulting from rolling a properly cut graphene layer into a cylinder. Referring to **Figure I.3** this means bringing together the AD and OB segments. Upon inspection, the "rolling" of the graphene sheet can be achieved along different directions resulting in a large variety of tube structures. A few nanotube examples are given in **Figure I.4**. In the next

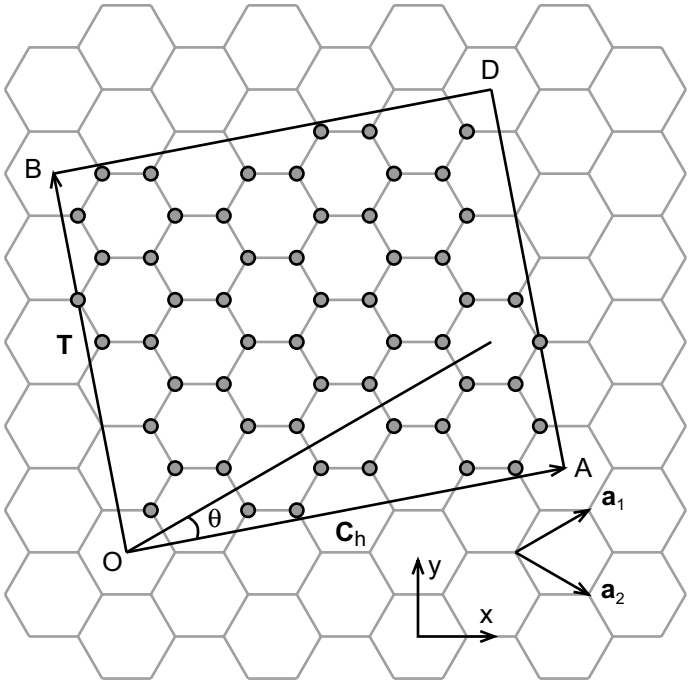

Figure I.3. The unrolled unit cell of a (4, 2) carbon nanotube delimited by the rectangle OADB. The tube is obtained by folding AD onto OB. Gray circles represent the tube's inequivalent atoms.

section we will prove that the rolling direction is in a very close relationship to the electronic properties of the resulting nanotube.

The structure of a carbon nanotube is uniquely determined by a single vector called chiral vector and labeled $\mathbf{C}_h$ in **Figure I.3**, which through the rolling process described above gets mapped onto the circumference. On the other hand the axis of the tube is parallel to a second vector called translation vector and labeled $\mathbf{T}$. Considering the one-dimensional nature of a nanotube $\mathbf{T}$ is actually its lattice vector. An infinite tube can thus obtained by repeating cells along the translation vector. Using the lattice vectors $\mathbf{a}_{1(2)}$ defined in (I.1) we can express the chiral vector as

$$\mathbf{C}_h = n\mathbf{a}_1 + m\mathbf{a}_2 \equiv (n,m) \qquad \text{(I.3)}$$

where (n,m) are two integer numbers. Due to the six fold symmetry of the hexagonal lattice m can be constrained to the values $0 \le m \le n$. Within this convention the examples of **Figure I.4** are indexed from left to right with chiral vectors (12, 0), (8, 4) and (6, 6) respectively. Tubes having $n = m$ are known as armchair, those having $m = 0$ as zigzag, and all other tubes are named chiral nanotubes.

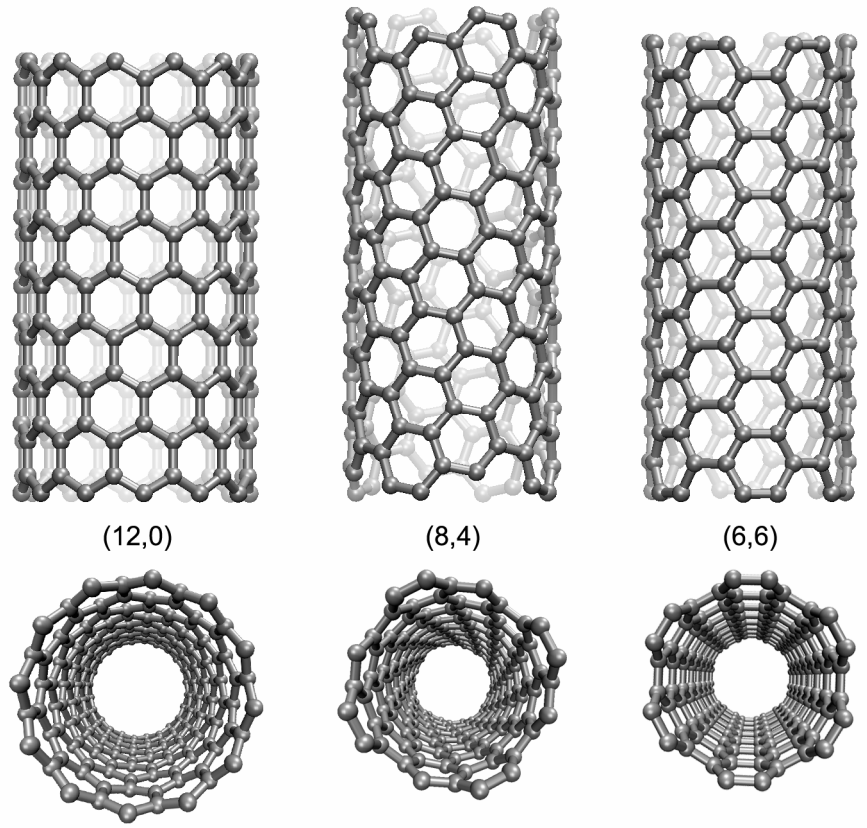

Figure I.4. A few carbon nanotube structures from side view (top) and axial view (bottom). From left to right (12, 0) is a zigzag (8, 4) a chiral and (6, 6) an armchair nanotube.

The tube's diameter is given by its circumference divided by π, i.e. $d_t = C_h/\pi$ which in terms of the lattice constant and the two integer indices has the value $d_t = (a/\pi)\sqrt{n^2 + m^2 + nm}$. The (6, 6) tube in **Figure I.4** has for instance a diameter of 8.13Å.

The tilt angle of the hexagons with respect to the direction of the tube's axis is called the chiral angle and can be computed by projecting the chiral vector $\mathbf{C}_h$ onto $\mathbf{a}_1$ which gives its cosine

$$\cos\theta = \frac{\mathbf{C}_h \cdot \mathbf{a}_1}{\|\mathbf{C}_h \cdot \mathbf{a}_1\|} = \frac{2n+m}{2\sqrt{n^2+m^2+nm}}$$

As stated earlier the translation vector $\mathbf{T}$ is the lattice vector of the one-dimensional nanotube. This vector can be derived from the chiral vector, by defining it to be the

vector normal to $\mathbf{C}_h$ that intercepts starting from the origin O the first graphene lattice point. Using the form

$$\mathbf{T} = t_1\mathbf{a}_1 + t_2\mathbf{a}_2 \qquad \textbf{(I.4)}$$

and $\mathbf{T}\cdot\mathbf{C}_h = 0$ the expressions of $t_{1(2)}$ are readily obtained

$$(t_1, t_2) = \left(\frac{2m+n}{d_R}, -\frac{2n+m}{d_R}\right) \qquad \textbf{(I.5)}$$

where d_R is the greatest common divisor of $2m+n$ and $2n+m$. Referring to **Figure I.3**, $\mathbf{C}_h = (4,2)$ that results in a translation vector $\mathbf{T} = (4,-5)$. Using the above relations (**I.5**), the length of the translation tube can also be calculated, and one obtains $T = \sqrt{3}C_h/d_R$. The two vectors $\mathbf{C}_h, \mathbf{T}$ define the unrolled unit cell of a carbon nanotube as $\mathbf{a}_{1(2)}$ is defining it for graphene. One can note that the unit cell of a nanotube is in fact a super-cell of graphene. Consequently the electronic structure of a tube can be derived from that of graphene, a property that we exploit in the following section.

To obtain the number of atoms in the nanotube's unit cell one divides its area to that of the graphene unit cell (the rhombus in **Figure I.2**) that gives the number of inequivalent atom pairs or equivalently the number of hexagons

$$N = \frac{\|\mathbf{T}\times\mathbf{C}_h\|}{\|\mathbf{a}_1\times\mathbf{a}_2\|} = \frac{2(n^2+m^2+nm)}{d_R} \qquad \textbf{(I.6)}$$

If a graphene unit cell contains two atoms, it results then that a carbon nanotube unit cell contains $2N$ atoms. The 56 atoms of the (4, 2) nanotube are emphasized in **Figure I.3**. The basic structural elements we have introduced in this section will help in the following section elucidate the electronic structure of carbon nanotubes.

2. Electronic structure

2.1. Graphene band structure

The large number of atoms in a carbon nanotube's unit cell hinders at a first view simple analytical results. Nevertheless due to the close relationship between the unit

cell of the nanotube and graphene, the electronic structure of the former can be derived from the electronic structure of the latter by imposing proper boundary conditions. We thus start with graphene electronic structure.

Periodic systems like graphene are treated in solid state physics using Bloch basis functions, a proper ansatz that respects the translational symmetry of these systems. These functions are defined with the help of an atomic, localized, orbital basis set $\{|\mu\rangle\}$ whose real-space projections we label $\varphi_\mu(\mathbf{r}) \equiv \langle \mathbf{r}|\mu\rangle$. Bloch functions assume the well known definition

$$\chi_\mu(\mathbf{k},\mathbf{r}) \equiv \frac{1}{\sqrt{N}} \sum_{\mathbf{R}_\mu} \varphi_\mu(\mathbf{r}-\mathbf{R}_\mu) e^{i\mathbf{k}\cdot\mathbf{R}_\mu} \qquad \textbf{(I.7)}$$

In the case of graphene $\varphi_\mu(\mathbf{r})$ is a $2p_z$ orbital localized either on site A or B seen in **Figure I.2**. The sum in **Equation (I.7)** runs over all equivalent atom position $\mathbf{R}_\mu$ in all unit cells. Born-von-Karman boundary conditions are imposed over $\sqrt{N}$ cells in each graphene lattice direction $\mathbf{a}_{1(2)}$ which quantizes the wave vector $\mathbf{k}$. However for large enough N the first Brillouin zone can be considered continuous.

With the above definition the basis overlap can be computed explicitly

$$S_{\mu\nu}(\mathbf{k}) \equiv \langle \chi_\mu(\mathbf{k})|\chi_\nu(\mathbf{k})\rangle = \sum_{\mathbf{R}_\mu,\mathbf{R}_\nu} e^{i\mathbf{k}\cdot(\mathbf{R}_\nu-\mathbf{R}_\mu)} \int d\mathbf{r}\varphi_\mu^*(\mathbf{r}-\mathbf{R}_\mu)\varphi_\nu(\mathbf{r}-\mathbf{R}_\nu) \qquad \textbf{(I.8)}$$

If the atomic orbitals are considered to be confined inside a disc of radius $R_C < a/2$, where a is the graphene lattice constant, one can observe that the right hand side of (**I.8**) cancels whenever $\|\mathbf{R}_\mu - \mathbf{R}_\nu\| \geq a$. With the help of the three vectors $\mathbf{R}_i$ defined in **Figure I.2**, and by changing the variable $(\mathbf{r}-\mathbf{R}_A) \rightarrow \mathbf{r}$ inside integrals, the basis overlap becomes

$$S_{AA}(\mathbf{k}) = \int d\mathbf{r}\varphi_A^*(\mathbf{r})\varphi_A(\mathbf{r}) = 1 = S_{BB}(\mathbf{k})$$
$$S_{AB}(\mathbf{k}) = \sum_i e^{i\mathbf{k}\cdot\mathbf{R}_i} \int d\mathbf{r}\varphi_A^*(\mathbf{r})\varphi_B(\mathbf{r}-\mathbf{R}_i) = \sum_i e^{i\mathbf{k}\cdot\mathbf{R}_i} s_0 \equiv s_0 f(\mathbf{k}) = S_{BA}^*(\mathbf{k})$$

where in $S_{AA}(\mathbf{k})$ we have used the fact that $\varphi_A(\mathbf{r})$ is normalized. In $S_{AB}(\mathbf{k})$ we labeled the integral with s_0 which is invariant under a $2\pi/3$ rotation in the x-y plane and therefore has the same value for all $\mathbf{R}_i$.

Obtaining the Hamiltonian matrix elements follows the same lines yielding

$$H_{AA}(\mathbf{k}) = \int \mathrm{d}\mathbf{r}\varphi_A^*(\mathbf{r})\hat{H}\varphi_A(\mathbf{r}) = \varepsilon_0 = H_{BB}(\mathbf{k})$$
$$H_{AB}(\mathbf{k}) = \sum_i \mathrm{e}^{i\mathbf{k}\cdot\mathbf{R}_i}\int \mathrm{d}\mathbf{r}\varphi_A^*(\mathbf{r})\hat{H}\varphi_B(\mathbf{r}-\mathbf{R}_i) = \sum_i \mathrm{e}^{i\mathbf{k}\cdot\mathbf{R}_i}\, t_0 \equiv t_0 f(\mathbf{k}) = H_{BA}^*(\mathbf{k})$$

except for the different labeling of the two involved integrals. The hopping integral t_0 is sometimes denoted $-\gamma_0$. The normalizing factor $1/\sqrt{N}$ appearing in (**I.7**) has been ignored since it cancels anyway in Schrödinger's equation (see below) where it appears both in the left and the right hand side.

Inserting the values of $\mathbf{R}_i$, defined in **Figure I.2**, into the definition of $f(\mathbf{k})$ and taking its absolute value, one obtains

$$|f(\mathbf{k})| = \sqrt{1+4\cos\frac{\sqrt{3}k_x a}{2}\cos\frac{k_y a}{2}+4\cos^2\frac{k_y a}{2}} \qquad \textbf{(I.9)}$$

We now write the eigenstates of the graphene layer as a linear combination over the Bloch basis

$$\psi_n(\mathbf{k},\mathbf{r}) = \alpha_n\chi_A(\mathbf{k},\mathbf{r}) + \beta_n\chi_B(\mathbf{k},\mathbf{r}) \qquad \textbf{(I.10)}$$

and setup Schrödinger's equation

$$\begin{pmatrix} \varepsilon_0 & t_0 f(\mathbf{k}) \\ t_0 f^*(\mathbf{k}) & \varepsilon_0 \end{pmatrix}\begin{pmatrix}\alpha_n \\ \beta_n\end{pmatrix} = \varepsilon_n(\mathbf{k})\begin{pmatrix} 1 & s_0 f(\mathbf{k}) \\ s_0 f^*(\mathbf{k}) & 1 \end{pmatrix}\begin{pmatrix}\alpha_n \\ \beta_n\end{pmatrix} \qquad \textbf{(I.11)}$$

This eigenvalue equation is solved by setting its determinant to zero and yields the energy dispersion relations (eigenvalues)

$$\varepsilon_{1(2)}(\mathbf{k}) = \frac{\varepsilon_0 \pm t_0|f(\mathbf{k})|}{1 \pm s_0|f(\mathbf{k})|} \qquad \textbf{(I.12)}$$

and also the eigenvectors

$$\psi_{1(2)}(\mathbf{k},\mathbf{r}) = \frac{1}{\sqrt{2}}\left(\pm\frac{f(\mathbf{k})}{|f(\mathbf{k})|}\chi_A(\mathbf{k},\mathbf{r}) + \chi_B(\mathbf{k},\mathbf{r})\right) \qquad \textbf{(I.13)}$$

The dispersion relations are plotted **Figure I.5** for the parameter values $\varepsilon_0 = 0$, $t_0 = -3.033\text{eV}$ and $s_0 = 0.129$. The upper surface represents the π^* anti-bonding band while the lower one represents the π bonding band. There are six special points labeled K in the first Brillouin zone where these bands intersect and become degenerate. As mentioned in the previous section only two of them are inequivalent and (K and K' in **Figure I.2**). The other four can be obtained by translations along the reciprocal lattice vectors.

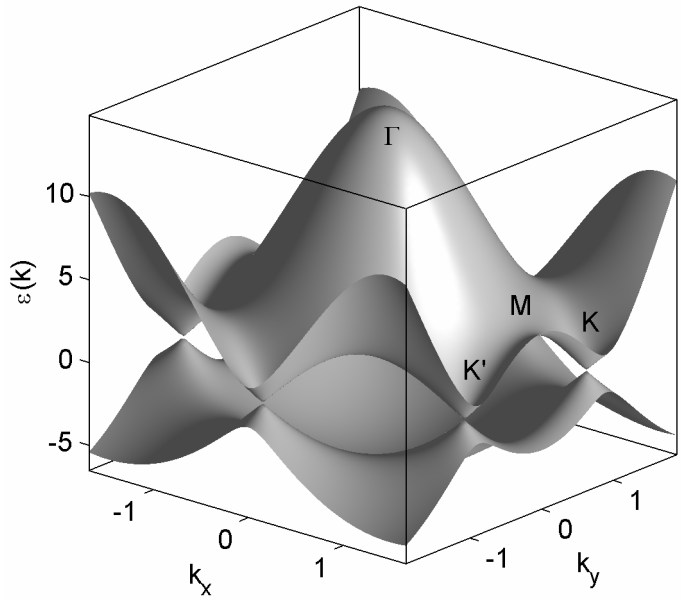

Figure I.5. Energy dispersion relations for graphene and its high symmetry points.

The Fermi level passes through the plane formed by the six K points, i.e. $E_F = \varepsilon_0$ because the unit cell contains two electrons which fully occupy the lower π band leaving the π^* band empty. As the density of states is zero at the Fermi level graphene is a zero-gap semiconductor or a semi-metal. This particularity of graphene band structure will reflect, as shown in the following, in nanotubes being either metallic or semiconducting depending on their chiral vector only.

2.2. Zone-folding band structure of SWNTs

The band structure of single-wall carbon nanotubes can be obtained in a first approximation from the dispersion relations of graphene by imposing periodic boundary conditions along the chiral vector $\mathbf{C}_h$. In reciprocal space the wave vector

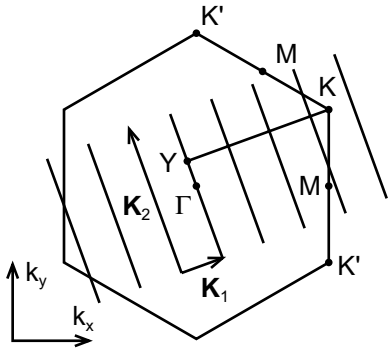

Figure I.6. Quantization of the transversal wave vector and the first Brillouin zone of a carbon nanotube (a line parallel to K_2) inside the BZ of graphene.

associated with $\mathbf{C}_h$ gets quantized, while the one associated with the translational vector $\mathbf{T}$ remains continuous for infinite length tubes.

The unit cell of a carbon nanotube is the rectangle OADB delimited by the orthogonal $\mathbf{C}_h$ and $\mathbf{T}$ vectors in **Figure I.3** and is simultaneously a super-cell of graphene. As shown earlier there are $2N$ carbon atoms in this unit cell and thus N pairs of π and π^* bands should be expected.

Before imposing the periodic boundary conditions it is convenient first to look at the reciprocal space of the graphene super-cell whose lattice vectors are obtained as usually by solving for $\mathbf{K}_{1(2)}$ in

$$\mathbf{C}_h \cdot \mathbf{K}_1 = 2\pi \qquad \mathbf{T} \cdot \mathbf{K}_1 = 0$$
$$\mathbf{C}_h \cdot \mathbf{K}_2 = 0 \qquad \mathbf{T} \cdot \mathbf{K}_2 = 2\pi$$

which in term of the reciprocal lattice vectors of graphite $\mathbf{b}_{1(2)}$, after some algebra, write

$$\mathbf{K}_1 = 1/N\left(-t_2\mathbf{b}_1 + t_1\mathbf{b}_2\right) \qquad \textbf{(I.14.a)}$$
$$\mathbf{K}_2 = 1/N\left(m\mathbf{b}_1 - n\mathbf{b}_2\right) \qquad \textbf{(I.14.b)}$$

The periodic boundary conditions force the wavefunction to satisfy

$$\psi(\mathbf{r} + \mathbf{C}_h) \equiv \mathrm{e}^{i\mathbf{k}\cdot\mathbf{C}_h}\,\psi(\mathbf{r}) = \psi(\mathbf{r})$$

which is equivalent to $\mathbf{k} \cdot \mathbf{C}_h = 2\pi p$ where p is an integer number. Projecting this

equation onto $\mathbf{K}_1$ we obtain the quantization of the transversal wave vector $\mathbf{k} = p\mathbf{K}_1$. As $N\mathbf{K}_1$ is a vector of the reciprocal super lattice and simultaneously of the reciprocal lattice and t_1, t_2 are relatively prime it results that $p = \overline{0, N-1}$ yields N distinct quantization directions. Thus the a carbon nanotube has N sub-bands labeled by p. On the contrary the projection of $\mathbf{k}$ onto $\mathbf{K}_2$ can have a continuous value and represents the first Brillouin zone of the carbon nanotube.

The first Brillouin zone of a carbon nanotube, which is a line segment, is depicted in **Figure I.6** inside the hexagonal BZ of graphene. As stated previously the band structure of a carbon nanotube is obtained from the dispersion relations of graphene (**I.12**) by sampling along $\mathbf{K}_2$ at p consecutive translations along $\mathbf{K}_1$ starting from Γ

$$\varepsilon_p(\mathbf{k}) = \varepsilon_{1(2)}\left(k\frac{\mathbf{K}_2}{\|\mathbf{K}_2\|} + p\mathbf{K}_1\right) \qquad \textbf{(I.15)}$$

with $p = \overline{0, N-1}$ and $k \in \left(-\pi/\|\mathbf{T}\|, \pi/\|\mathbf{T}\|\right)$

Figure I.6 reveals a crucial fact about the band structure of carbon nanotubes. If, referring to this figure, the length ratio of the YK segment to that of $\mathbf{K}_1$ is an integer, then the bands of the tube pass through the K point of graphene and thus they have a zero gap. In this situation a carbon nanotube is metallic, as its density of states at the Fermi level is finite (see **Figure I.7** (bottom)). If however this condition is not satisfied then there is a gap between the bands, and the tube is thus semiconducting. As the length of this YK segment is $\left((2n+m)/3\right)\|\mathbf{K}_1\|$ the above condition transforms to $(2n+m)$ or equivalently $(n-m)$ is divisible by 3. It follows then that in theory one third of nanotubes should be metallic and two thirds semiconducting, in particular armchair tubes being always metallic.

The band structures of a metallic (10, 10) and a semiconducting (14, 0) are plotted in **Figure I.7** (top). Their corresponding densities of states (DOS) are calculated by integrating along each band using

$$\rho(E) = \sum_p \int \mathrm{d}k \frac{1}{\partial_k \varepsilon_p(k)} \delta(\varepsilon_p(k) - E) \qquad \textbf{(I.16)}$$

In the density of states, the intrinsic one-dimensionality of the nanotubes gives rise to

a discrete set of singularities, called van Hove singularities. These singularities occur at wave vectors where the bands are dispersionless, or $\partial_k \varepsilon_p(k) = 0$ and determine the optical properties of carbon nanotubes which are beyond the scope of this thesis.

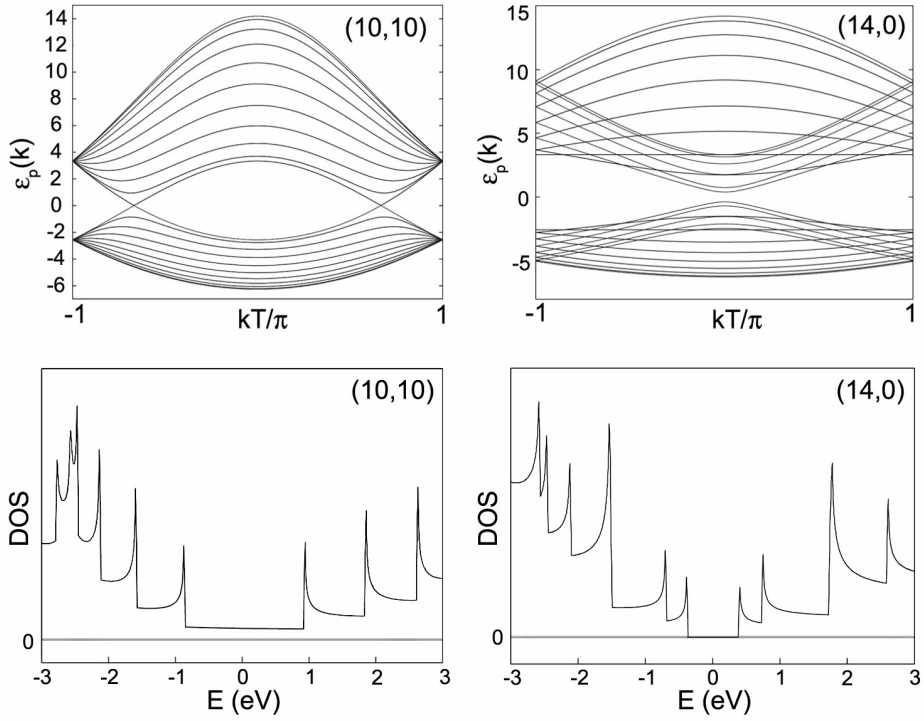

Figure I.7. (top) Band structures for a metallic (10, 10) nanotube and a semiconducting (14, 0) tube, and (bottom) their corresponding density of states.

For metallic SWNTs a development of the Fermi surface around any of the six special K points yields a Fermi velocity $v_F \simeq 10^6 \text{m/s}$, independent of chirality. Thus, in the absence of electron scattering the intrinsic conductance of a metallic tube should be $2G_0$, where $G_0 = 2e^2/h$ is the conductance quantum, as there are two open channels at the Fermi level, each one having a conductance G_0. On the other hand semiconducting SWNTs have a bandgap $E_g \simeq (0.9\,\text{eV})/d_t$, where d_t is the tube's diameter in nanometers. The next section will present a series of experimental and theoretical results that confirm or constrain the validity of the results obtained so far in the simple tight-binding approximation.

3. Transport properties

Perhaps the most striking feature of carbon nanotubes is that they can be either metallic or semiconducting based on their chirality only. As discussed in the previous

section the electronic properties of single-wall carbon nanotubes (SWNTs) are in a close relationship to those of graphene. Graphene has a varying, finite bandgap throughout the first Brillouin zone except for the six special K points (see **Figure I.5**). When a graphene sheet is rolled into a SWNT the transversal wave vector is quantized while the longitudinal vector remains continuous. The process of imposing periodic boundary conditions on a graphite sheet is thus equivalent to sampling the k space of graphene along a certain direction ($\mathbf{K}_2/\|\mathbf{K}_2\|$) at discrete intervals ($p\mathbf{K}_1$). Depending on whether the quantized sampling direction, shown in **Figure I.6**, crosses one of the six special K points the resulted tube is either metallic or semiconducting.

The above conclusions are probably valid for geometrically perfect SWNTs at zero temperature in the independent-electrons approximation. Unfortunately thus far real-life carbon nanotubes have almost always a certain degree of structural defects and often are doped by surface adsorbed impurities. Finite temperature effects should also be of concern as electron-phonon interactions can change radically the transport regime. In the next subsection we briefly define the concepts of mean free path and phase relaxation length from mesoscopic physics, which upon measurement will help identifying the transport regime in real-life carbon nanotubes.

3.1. Transport regimes

Mesoscopic physics, which studies transport in samples of low dimensions, has enabled in the past the identification of several transport regimes depending on the relation the sample's length L (in the direction of the particle flow) bears to the mean-free path (L_m) and the phase relaxation length (L_φ) [**22**, **23**]. Of course other length, and time scales are used in mesoscopic physics nomenclature, e.g. localization length, Fermi wavelength, transit time, thermal diffusion length, etc., but we consider here only the aforementioned two lengths as they offer enough insight into the transport mechanisms we focus on.

The mean-free path L_m is associated with those scatterers inside a two terminal sample that can change the momentum of an electron traversing the sample from one lead to the other. Such scatterers can be for instance boundaries between different materials, charged or magnetic impurities, phonons, etc. On the other hand, mesoscopic physics establishes that electron-electron interactions do not contribute to L_m, as in this type of scattering the total momentum is conserved and incident and

emergent electrons are indistinguishable quantum mechanical particles. The mean free-path is considered to be the length after which the standard deviation of an electron's momentum due to scattering exceeds a certain amount. This length is thus a measure of the degree of uniformity of the sample and also at finite temperature of the strength of the electron-phonon interactions.

In analogy, the phase relaxation length L_φ is associated with dynamical scatterers that tend to destroy the phase of a propagating electron wavefunction. This would be the case of phonons but also of electron-electron interactions and magnetic impurities. Another result from mesoscopic physics reveals that on static scatterers (with no freedom degrees) all collisions are elastic and do not contribute to phase relaxation. Thus the phase relaxation length can be defined as the length after which the mean spread of the phase of an electron wavefunction exceeds a certain value. This quantity gives thus a measure of the density and strength of dynamic scatterers inside the sample. At zero or low temperatures electron-electron interactions and magnetic impurities dominate as scattering mechanisms.

Now, in terms of the above defined lengths one defines three transport regimes, namely classical, diffusive and ballistic. In the classical regime the length of the sample is greater then both the mean-free path and phase relaxation length, i.e. $L \gg L_m, L_\varphi$. This regime satisfies Ohm's law where the resistance of the sample scales linearly with its length and the electron can be viewed as a classical, localized particle. The diffusive regime defined by $L > L_\varphi \gg L_m$ corresponds to the picture of a coherent electron (a wave) that gets scattered elastically many times inside the sample. These frequent, coherent scatterings lead to weak or strong Anderson localization of the wavefunction reducing drastically the sample's conductance. Finally, in the ballistic regime defined by $L_m, L_\varphi > L$ the electron is to be viewed as a wavefunction that extends over the entire sample.

Early experimental evidence revealed that metallic single-wall nanotubes, up to a few micrometers long, are ballistic wires even at room temperature. A first proof of ballistic conduction in individual carbon nanotubes came from Frank et *al.* [**24**] that measured the conductance of multi-wall nanotubes contacted by liquid mercury. They observed conductance quantization which is the signature of ballistic transport. Single-wall carbon nanotube conductance quantization has also been observed by

Tans et *al.* and Bockrath et *al.* [**25**, **26**]. Other groups have focused their work on determining the phase relaxation length and/or the mean free path. For example Liang et *al*. [**29**] detected Fabry-Perot interference for a 530nm SWNT at 4K. Additionally they found that the mean free path was superior to the tube's length, concluding that the transport regime must have been ballistic. At room temperature Bachtold and coworkers [**30**] used electrostatic force microscopy to get the voltage profile along metallic SWNTs longer than 1μm. They found that most of the voltage drop occurs at contacts, proving once more that the measured nanotube was ballistic.

While the mean free path seems to oscillate experimentally around 1μm at cryogenic temperatures, this is not the case for room temperature measurements. Recently, Gao et *al.* [**31**], using a non-invasive four-point configuration based on MWNT voltage probes, showed a clear linear scaling of the resistance with length which is the signature of Ohm's regime. The same reference presents mean free paths in the 100-300nm interval. However, Javey et *al.* [**32**] conclude that for nanotube devices below ~100nm the transport regime is surely not diffusive and thus ballistic.

Although theory predicts that semiconducting SWNTs should be intrinsic semiconductors, initial measurements performed by several groups [**33**, **35**, **36**] have found p-type conduction in nanotube-based field effect transistors (FETs). Hole or p-type doping of SWNTs has since then been attributed to unwanted oxygen adsorption caused by air exposure of the samples. Transconductances on the order of 200nA/V [**33**] and hole mobilities in the 100-10,000$cm^2/V{\cdot}s$ range have been measured. The surprisingly high mobility can be attributed to the lack of surface states present in typical silicon-based devices.

Nanotubes will certainly occupy a major role in the next-generation electronics since the list of intrinsic transport properties doesn't stop with ballistic conduction and huge mobilities. Recently, intrinsic superconductivity has been observed in nanotube ropes [**27**] and also important noise suppression [**28**] which enriches the physics available for novel nanotube-based devices.

3.2. Contacts and doping in nanotube-based devices

As argued at the end of **Section 2.2** a metallic nanotube should have at low bias a conductance of $4e^2/h$ corresponding to a resistance of approximately 6.5kΩ. This

value has indeed been achieved recently [29, 37] via Au or Pd evaporation over SWNT contacting ends followed by high temperature annealing. Earlier experiments on carbon nanotube devices displayed nevertheless contact resistances on the order of MΩ [25, 35]. For multi-wall nanotubes, Kasumov et *al.* [34] have demonstrated resistances as low as 2kΩ for Au contacts and as high as a few MΩ for other contacting metals. Alternatively the contact resistance can be reduced by local electron irradiation of the contact region which induces defects and thus presumably enhances the bonding between the tube and the underlying metal [39]. The poor tube-metal contact is however not very clear at this moment despite a few tentative theoretical explanations.

The problem of contacts is even more critical in the case of semiconducting devices. The Fermi level of most of the metals used so far for contacting nanotubes resides in their bandgap. Schottky barriers are found to arise for both n and p operating regions [40, 41]. Relatively good contacts on the order of hundreds of KΩ were obtained for semiconducting SWNT samples by Zhou et *al* [33]. Probably in the near future the contact resistances will continue to decrease until the intrinsic conductance of the tube will be directly probed.

There are situations in which the large Schottky barriers are beneficial [42]. Finite-size metallic nanotubes weakly coupled to leads can behave as quantum dots, exhibiting Coulomb blockade and other single-electron transport phenomena like the Kondo effect etc. [43, 44]. Owing to their relatively large Coulomb charging energy and level spacing carbon nanotubes have a certain potential for realizing single electron transistors at relatively high temperatures. We will however not deal with strongly correlated electron transport in this thesis.

Both p- and n-type nanotube doping have been studied in the past. The initial research wave focused on doping with electron donor alkali metals [45, 46, 47, 48, 49]. However alkali metals are not stable in air for which other doping strategies are to be developed. Using scanning tunneling spectroscopy the influence of boron and nitrogen doping on the electronic structure of carbon nanotubes has been investigated [50, 51]. Both B- and N-doped tubes are metallic regardless of the electronic nature of the undoped host nanotube. Nevertheless the LDOS reveals localized acceptor (donor) states close to the Fermi level responsible for p-type (n-type) doping.

We conclude the section dedicated to transport properties of carbon nanotubes with the observation that molecular adsorption can have an important effect on the conductance of carbon nanotubes. This effect has fostered the idea that extremely compact and sensitive carbon nanotube chemical sensors could be achieved, a concept that was tested already for NO_2 and NH_3 by Kong et *al*. [**52**]. In **Chapter V** we study theoretically the intrinsic conductance change of a similar carbon nanotube sensor aiming at detecting aromatic amino acids.

4. Mechanical properties

The sp^2 hybridization of carbon is known to produce the toughest covalent bond in nature. A graphene layer has a Young's modulus close to 1TPa which was expected and later proved to be conserved in nanotubes. This section will cover the basic mechanical properties of single-wall carbon nanotubes starting from theoretical predictions and ending with experimental measurements. We do not touch on vibrational properties as in this thesis we are interested mainly in the "macroscopic" elastic properties like bending and more generally the deformation of nanotubes which can be characterized with the help of classical elasticity theory quantities like Young's modulus, stiffness and strength and so on.

At the base of graphite's stiffness are the strong σ-bonds faintly helped by the π-bonds which also account for the weak interlayer interactions. Rolling a graphene sheet into a carbon nanotube would naturally increase the total strain energy. Small diameter tubes are accordingly less stable than the larger ones. As axial strain is mainly transferred into a deformation of the σ-bonds and their inter-bond angles a considerable tensile strength is to be expected. On the contrary loads normal to the tube's surface do not distort the hexagons considerably, resulting in a relatively high softness in this direction. In fact the walls of a SWNT can even collapse together if this load is large enough. Under tensile stress carbon nanotubes have been found to yield at 5-10% strain which cumulated with their strength and elastic recovery of their structural properties from large deformations led various authors to name them the ultimate fibers.

4.1. Molecular dynamics and continuum models

We begin our review of the mechanical properties of carbon nanotubes by a brief introduction into the theoretical models available for predicting carbon nanotube mechanical properties. We often make reference to classical continuum elastic theory which although questionable for nanometric objects, it is known to have produced the first predictions of nanotube mechanical properties that still constitute a good approximation.

The central quantity involved in classic elasticity theory is the material's Young's modulus Y defined as the ratio of the second derivative of the strain energy E to the sample's volume V, i.e. $Y \equiv (1/V)\partial_{\varepsilon}^{2}E$. Similarly Y can be obtained from the deflection d of a cantilever of length l subject to a force F at its free end

$$d = \frac{Fl^3}{3YI} \qquad \textbf{(I.17)}$$

where I is the moment of inertia of the cross-section. For tubular structures classical elasticity theory gives I as

$$I = \frac{\pi(R_o^4 - R_i^4)}{4} \qquad \textbf{(I.18)}$$

defined in terms of the tube's outer (inner) radius R_o (R_i) respectively. For SWNTs, defining the tube's thickness is not self-evident, and was even a source of confusion since early molecular simulations predicted Young's moduli of 5TPa (5 times stronger than diamond or graphene). In literature either 0.7Å or 3.5Å seem to have been established over the years as the wall thickness of nanotubes. With the latter thickness, which corresponds to the spatial extent of the π orbitals of a carbon atom, the Young's modulus is close to 1TPa which seems more realistic.

As measuring the mechanical properties of nanotubes involves the manipulation of objects of nanometric diameters, bending forces on the order of nN and the ability of measuring strains of a few nm, it is of no surprise that the first results on the mechanical properties came actually from calculations. Simplified analytical models with periodic boundary conditions were initially used for evaluating the Young's modulus of nanotubes and graphene from the Morse potential for instance. Latter

molecular dynamics (MD) imposed itself as the common choice allowing the simulation of finite systems composed of nanotubes in a variety of configurations.

There is currently a large force-field variety to drive MD simulations. For carbon based systems analytic many-body force-fields such as Tersoff-Brenner and Stillinger-Weber have long been available. The Tersoff-Brenner potential works particularly well for crystalline, amorphous and molecular phases of carbon, such as diamond, graphite, fullerenes, and nanotubes and has been thoroughly tested in a variety of settings. An important bonus for the Tersoff-Brenner potential is that it is reactive, i.e. chemical bonds can form and break during the simulation. Consequently the neighbor list of each atom is dynamic slowing down to a certain extent the simulation. Therefore, for larger systems it is often convenient to turn to simpler, fixed-topology force-fields like CHARMM, Amber, etc.

When accuracy becomes critical *ab initio* molecular dynamics schemes are involved in which the inter-atomic forces are computed at each time step by solving the appropriate Schrödinger's equation within the Born-Oppenheimer approximation. Both tight-binding MD and density functional theory MD simulations are in this category. Some of the results obtained with this and other kind of simulations together with a few experimental results are reviewed in the following subsection.

Interestingly all the above models confirmed a classical elasticity textbook behavior, at least under moderate strains. For instance as demonstrated recently, depending on their aspect ratio $\mu \equiv l/d_t$ alone (length over diameter), carbon nanotubes can behave as shells at low μ, as rods at intermediate μ and as soft bending wires at large μ [**53**]. In fact continuum models were never completely abandoned and still find application in the simulation of extremely large carbon nanotube systems. The validity of these models was thoroughly analyzed by Harik [**54**]. Much theoretical progress has been made recently with the work of Belytschko [**55**] on the shell theory of SWNTs that reproduces even tube buckling and Girifalco [**56**] on the van der Waals forces interactions between continuum nanotube models.

4.2. Elastic properties of SWNTs

At the moment there is still a matter of debate of what the value of Young's modulus is, of its scaling with the nanotube's diameter and of its chirality dependence. This is

due to intrinsic experimental uncertainties on the measured system and uncontrolled setup parameters. In the years to come experimental values will probably converge and approach the desired accuracy. In its turn theory has still to explain exotic mechanical effects in MWNTs and SWNT ropes like the rippling mechanism made responsible for the large drop in Young's modulus of MWNTs of diameters > 10 nm observed by Poncharal et *al* [**57**].

Using the Tersoff-Brenner potential Robertson et *al.* [**58**] found the strain energy of a SWNT to scale as the inverse square of the tube's diameter, i.e. d_t^{-2} and a Young's modulus of ~1TPa. Other calculations [**59**] using the same force-field reported a Young's modulus as high as 5.5TPa, which according to our earlier discussion is not surprising since a wall thickness of ~0.6Å was used in this study. More accurate semi-empirical tight-binding and DFT calculations [**60**, **61**] were later on performed concluding on a Young's modulus of approximately 1.2TPa and 1.06TPa respectively. Comparison with boron-nitride nanotubes [**61**, **62**] confirmed that carbon nanotubes are superior in strength and are the strongest fibers known yet.

Srivastava et *al.* [**62**] using the Tersoff-Brenner potential has computed both the bending and torsion stiffness for several armchair and zigzag carbon nanotubes. Their results indicate a bending stiffness K scaling as $d_t^{2.93}$ and a torsion stiffness scaling as $d_t^{3.01}$, both in very good agreement with the cubic scaling predicted by the continuum elastic theory. The corresponding bending Young's modulus for a small diameter SWNT was found to be about 0.9TPa being lower than the tensile modulus calculated from tight-binding or DFT. The found shear modulus of SWNTs was around 0.3TPa and it did not dependent strongly on tube diameters.

The first measurement of the Young's modulus was achieved by Treacy et *al.* [**63**] although for multi-wall nanotubes. Mean-square vibration amplitudes were determined with the help of a transmission electron microscope in the temperature range of 27 to 800°C. While the average value of the measured Young's modulus was ~1.8TPa, there was a considerable standard deviation attributed to experimental uncertainties. The same method of measuring thermal vibration was later on applied to SWNTs at room temperature [**64**] yielding a mean Young's modulus of ~1.3TPa. By measuring the restoring force Wong et *al.* [**65**] gave a modulus of about ~1.3TPa

and Salvetat et *al.* [**66**] obtained about 1TPa for SWNT ropes laid over porous alumina.

The mechanical properties presented so far will support the various affirmation and choices we made in modeling the carbon nanotube electromechanical sensor of **Chapter III**. Without disclosing too much, we have also obtained via *ab initio* density functional theory calculations with SIESTA a Young's modulus of 1.04TPa for a (5, 5) carbon nanotube. Moreover at 0°C the tube did not yield at neither tensile nor compressive strains of ±10%.

Conclusions

In this chapter we have briefly looked into the structural, mechanical and electronic properties of carbon nanotubes. Right from the beginning we established the strong connection between nanotubes and a single sheet of graphite, a graphene layer. The single-wall carbon nanotubes are indexed by the chiral vector, as a function of which all the other properties were shown to depend on and be uniquely determined by. Sampling the π dispersion relations for graphene we were able to find the unidimensional band structure of SWNTs. From both the band structure and density of states it was concluded that nanotubes can be either metallic or semiconducting in a 1:2 ratio respectively. Transport measurements have demonstrated that metallic tubes are ballistic in devices inferior to a few hundreds nanometers, and that Schottky barriers form at the interface between metallic leads and semiconducting nanotubes. As the phase relaxation length also exceeds the micrometer we could conclude that transport in short nanotubes should be coherent. Nanotubes were also proven to be extremely sensitive with respect to doping, a property exploited in **Chapter V** in the context of a nanotube-based chemical sensor. With respect to mechanical properties both calculations and measurements begun to agree on the cube scaling of the stiffness with respect to the tube's diameter, and a terapascal Young's modulus for small diameter SNWTs.

CHAPTER II.

Transport theory in nanostructures

Introduction

The aim of this chapter is to present the formalism at the base of modern transport calculations in nanostructures, the non-equilibrium Green's functions (NEGF) formalism. The resulting transport theory is build upon the solid grounds of non-equilibrium quantum statistics. NEGF gives access to particle densities and currents under strong driving field and strong interactions, encompassing thereby Kubo's linear response theory. Under several simplifying hypotheses NEGF reduces to the widely employed Landauer-Büttiker formalism which should be constrained only to coherent transport regime. Although it is this last formalism that we will use in this thesis, we felt that instead of giving a phenomenological derivation of the particle current expectation value, it would be preferable to start from non-equilibrium quantum statistics and simplify the theory down to the utilized model.

In **Section 1** the general NEGF transport theory in nanostructures will be detailed. We start by pin pointing the equilibrium quantum statistics formulae for computing operator expectation values in the grand canonical ensemble. For single-particle operators it is however more efficient to evaluate Green's functions instead, which contain sufficient information for computing the averages of one-body operators. The non-equilibrium picture is introduced next which will lead to the extension of Green's functions to their contour ordered versions. For practical purposes these Green's functions are projected onto the real axis via Langreth's continuation rules yielding the lesser (greater) and retarded (advanced) Green's functions. Henceforth to the end of the first section we follow closely the derivations due to Jauho in establishing the inelastic transport equations [**67**, **68**]. The current expectation value is obtained from the definition of the current operator in a many-body context, except for the leads

which are assumed to be non-interacting, i.e. they admit a mean field, effective particle description. At the end of this section applying the hypothesis according to which the leads remain in equilibrium even after switching on the driving fields and interactions will result in the Meir-Wingreen formula [**69**].

Section 2 will deal with the elastic transport situation, which as stated earlier is the theory of choice for this thesis' calculations. The Fischer-Lee formula [**70**], an extension of the Landauer one-channel formula, is derived from the previously obtained Meir-Wingreen current expectation value by adding the non-interacting central region electrons hypothesis. This assumption transforms the problem into an entirely one-body mean field transport picture for which efficient calculation schemes can be devised (see **Chapter III** and **Chapter V**.) The Fischer-Lee transmission formula is transformed into Todorov's formula [**71**] evidencing the elastic scattering view on which Landauer-Büttiker formalism relies. We end this section and the chapter by considering non-orthogonal basis sets, which is of major interest as most of the Hamiltonian models, either tight-binding or *ab initio*, use such basis sets for efficiency reasons. We show there that the transport theory remains unaffected as long as different matrices entering the formalism satisfy certain representation rules.

1. Non-equilibrium transport

1.1. Non-equilibrium Green's functions

We begin this chapter with a succinct introduction to the main results of non-equilibrium many-body quantum statistics. The reader is assumed to be familiar with the standard equilibrium quantum statistics theory detailed in many books. [**72**, **73**]

Standard quantum statistics describes the behavior of many-particle systems at finite temperature within the grand canonical ensemble. The system is thus assumed to be in thermodynamic equilibrium with a number of "reservoirs" with whom it can exchange both energy and particles. One of the main result of this theory is a compact formula for computing the quantum statistical average of a generic operator $\hat{A}$,

$$\left\langle \hat{A} \right\rangle = \frac{\mathrm{Tr}[\mathrm{e}^{-\beta(\hat{H}-\mu\hat{N})}\,\hat{A}]}{\mathrm{Tr}[\mathrm{e}^{-\beta(\hat{H}-\mu\hat{N})}]} \equiv \frac{\mathrm{Tr}[\hat{\rho}\hat{A}]}{\mathrm{Tr}[\hat{\rho}]} \qquad \textbf{(II.1)}$$

Equation (II.1) contains the definition of the density "matrix" operator

$\hat{\rho} \equiv \mathrm{e}^{-\beta(\hat{H}-\mu\hat{N})}$, a function of both the system's Hamiltonian $\hat{H}$ and the particle number $\hat{N}$. The thermodynamic state of the system is thus defined by two parameters, namely $\beta \equiv 1/k_B T$ also known as the inverse temperature, and μ the chemical potential. The trace in (**II.1**) runs over a basis of the particle Fock space with all allowed number of particles. This formula includes as particularizations the canonical ensemble in which the number of particles in the system is hold fixed which restricts the trace over a Hilbert space of given number of particles, and the many-body ground state at zero temperature or $\beta \to \infty$.

Obviously evaluating (**II.1**) is for all but the simplest situations a formidable task. However for one-body operators, like the particle charge and current density, one tries instead to compute the Matsubara Green's function defined by

$$G(\mathbf{1},\mathbf{1}') \equiv -i\left\langle T_\tau[\hat{\psi}(\mathbf{1})\hat{\psi}^\dagger(\mathbf{1}')]\right\rangle \qquad \textbf{(II.2)}$$

in which the shorthand notation $\mathbf{1} \equiv (\mathbf{r},\tau,\sigma)$ has been used, and $\hat{\psi}(\mathbf{1})$ represents the field operator in Heisenberg's picture that annihilates one particle of spin σ from the space-time point $(\mathbf{r},\tau)$. In the above Green's function definition T_τ corresponds to the Wick time-ordering operator with respect to the imaginary time $\tau \equiv it$, a mathematical trick introduced by Matsubara to cope with finite temperature effects. For two generic operators $\hat{A},\hat{B}$

$$T_\tau[\hat{A}(\tau)\hat{B}(\tau')] \equiv \theta(\tau-\tau')\hat{A}(\tau)\hat{B}(\tau') - \theta(\tau'-\tau)\hat{B}(\tau')\hat{A}(\tau)$$

where $\theta(\tau)$ is the usual Heaviside unit step function.

The Matsubara Green's function contains sufficient information for the calculation of any one-particle operator averages like mentioned earlier. Moreover the linear response theory gives access to transport properties like the particle current via the Kubo formula. However transport phenomena beyond the linear response theory cannot be modeled based on *equilibrium* Green's functions only. Fortunately there exists an extension of the equilibrium formalism to non-linear response regime which is based on the so called non-equilibrium Green's function

$$G(\mathbf{1},\mathbf{1}') \equiv -i\left\langle T_C[\hat{\psi}(\mathbf{1})\hat{\psi}^\dagger(\mathbf{1}')]\right\rangle \qquad \textbf{(II.3)}$$

which is identical to (**II.2**) except for the time-ordering operator T_C that now is defined along the contour displayed in **Figure II.1**. The contour-ordered Green's function formalism is also known as Keldysh-Kadanoff-Baym formalism [**74**, **75**].

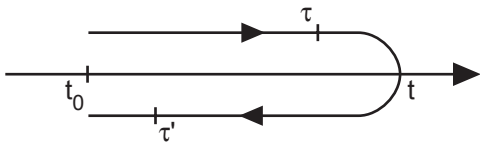

Figure II.1. Complex contour used to compute non-equilibrium Green's functions.

We will not go into details of how this contour is obtained, however we describe the physical considerations at the base of this formalism. Initially, for $t < t_0$ (see **Figure II.1**) the system is assumed in thermodynamic equilibrium being described by a Hamiltonian $\hat{H}_0$. Starting with t_0 couplings between previously non-interacting subsystems or parts of the above system, described by a time-dependent interaction Hamiltonian $\hat{V}(t)$, are turned on. This latter interaction term can contain, additionally to the subsystem couplings, an external time-dependent driving field. Thus at $t > t_0$ the system is no longer in equilibrium and cannot properly be described by the Matsubara Green's function in (**II.2**). However, as the state of the system was known before t_0, this state can be used as initial condition and formally integrated using the time evolution operator. Under general assumptions this integration is shown to be equivalent with a contour-ordered integration (see **Figure II.1**).

In **Equation** (**II.3**) the thermal average is taken with respect to $\hat{H}_0$ which is possible due to the fact that the contour begins and ends at t_0 when the couplings $\hat{V}(t)$ have not been yet applied.

Although a powerful formal tool, the contour-ordered Green's function is replaced in practice by the four real-time Green's functions

$$G^{<}(\mathbf{1},\mathbf{1}') \equiv i\left\langle \hat{\psi}^{\dagger}(\mathbf{1}')\hat{\psi}(\mathbf{1})\right\rangle \qquad \textbf{(II.4.a)}$$

$$G^{>}(\mathbf{1},\mathbf{1}') \equiv -i\left\langle \hat{\psi}(\mathbf{1})\hat{\psi}^{\dagger}(\mathbf{1}')\right\rangle \qquad \textbf{(II.4.b)}$$

$$G^{r}(\mathbf{1},\mathbf{1}') \equiv -i\theta(t-t')\left\langle \left\{\hat{\psi}(\mathbf{1}),\hat{\psi}^{\dagger}(\mathbf{1}')\right\}\right\rangle \qquad \textbf{(II.4.c)}$$

$$G^{a}(\mathbf{1},\mathbf{1}') \equiv i\theta(t'-t)\left\langle \left\{\hat{\psi}(\mathbf{1}),\hat{\psi}^{\dagger}(\mathbf{1}')\right\}\right\rangle \qquad \textbf{(II.4.d)}$$

called lesser, greater, retarded and advanced Green's functions respectively. Definitions (**II.4.c-d**) contain the fermion anti-commutator defined by $\left\{\hat{A},\hat{B}\right\}\equiv\hat{A}\hat{B}+\hat{B}\hat{A}$. The retarded (advanced) Green's function can be interpreted as the quantum probability amplitude to annihilate an electron (hole) of spin σ' at $(\mathbf{r}',t')$ knowing that an electron (hole) of spin σ has been created earlier at $(\mathbf{r},t)$. Conversely the lesser (greater) Green's function is the energy-resolved density of electrons (holes). It is not difficult to prove that $G^{<}(\mathbf{1},\mathbf{1}')$ contains all the necessary information required to compute any one-particle operator ensemble average

$$\left\langle\hat{A}(\mathbf{1})\right\rangle=-i\lim_{\mathbf{1}'\to\mathbf{1}}\hat{A}(\mathbf{1})G^{<}(\mathbf{1},\mathbf{1}') \qquad \textbf{(II.5)}$$

including the particle density and current operators which we approach in the next subsection.

The last result that we will however not prove here is Langreth theorem which provides the means to "project" contour-ordered integrals onto the real-time axis. Let A,B,C denote three contour-ordered correlation functions (Green's functions or self-energies) satisfying

$$C(\tau,\tau')=\int_C d\tau_1 A(\tau,\tau_1)B(\tau_1,\tau')$$

then the real-time projections of the above equations are

$$C^{<(>)}(t,t')=\int_{-\infty}^{+\infty}dt_1\left[A^r(t,t_1)B^{<(>)}(t_1,t')+A^{<(>)}(t,t_1)B^a(t_1,t')\right] \qquad \textbf{(II.6.a)}$$

$$C^{r(a)}(t,t')=\int_{-\infty}^{+\infty}dt_1 A^{r(a)}(t,t_1)B^{r(a)}(t_1,t') \qquad \textbf{(II.6.b)}$$

Langreth theorem together the continuation rules given by (**II.4.a-d**) allow one to transfer Dyson-like integral equations from the contour to real-time. This will prove extremely useful in the context of the transport theory developed in the following subsection.

1.2. Inelastic transport equations

This subsection focuses on the theory of non-equilibrium transport through nanostructures. The derivations start from the definition of the particle current thermal average. With the help of the non-equilibrium Green's functions (NEGF) apparatus

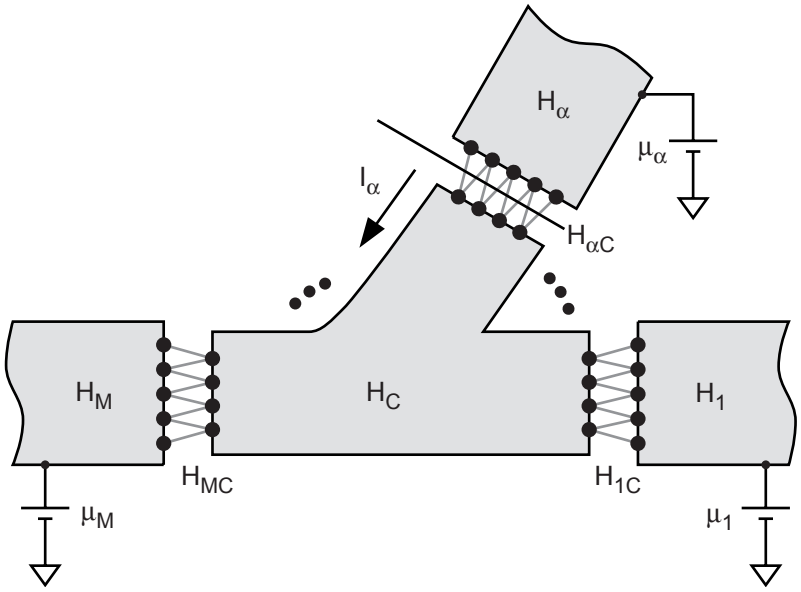

Figure II.2. A generic electronic multi-terminal device showing biasing and "real-space" Hamiltonian partitioning.

we obtain a compact formula for this quantity. Most of this subsection's derivations follow closely **Reference 67**.

The studied system, sketched in **Figure II.2**, is a multi-terminal device comprising an interacting scattering central region coupled to M leads. The leads are supposedly terminated with infinite particle reservoirs. To be consistent with the NEGF formalism, initially the leads are decoupled from the central region and all different subsystems are considered to be in thermal equilibrium and have a given chemical potential. As discussed earlier at a certain time t_0 the coupling Hamiltonian $\hat{V}$ between these subsystems is being turned on which causes particles to flow from one lead to another. Thus the overall Hamiltonian can be partitioned into

$$\hat{H} = \hat{H}_0 + \hat{V} = \left[\hat{H}_C + \sum_\alpha \hat{H}_\alpha\right] + \left[\sum_\alpha \hat{V}_\alpha\right] \qquad \textbf{(II.7.a)}$$

$$\hat{H}_\alpha = \sum_\nu \varepsilon_{\alpha;\nu} \hat{c}^\dagger_{\alpha;\nu} \hat{c}_{\alpha;\nu} \qquad \textbf{(II.7.b)}$$

$$\hat{V}_\alpha = \hat{V}_{\alpha C} + \hat{V}_{C\alpha} = \sum_{\nu,\mu} \left(V_{\alpha;\nu,\mu} \hat{c}^\dagger_{\alpha;\nu} \hat{d}_\mu + h.c. \right) \qquad \textbf{(II.7.c)}$$

defined with respect to $\hat{c}^\dagger_{\alpha;\nu}$ operators that create an electron in lead α into the single-particle state $|\nu\rangle_\alpha = \hat{c}^\dagger_{\alpha;\nu}|0\rangle$ and $\hat{d}_\mu$ which does the same but in a state of the central

region. It can already be noticed that (**II.7.b**) assumes non-interacting electrons in the leads. However in the central region any interactions are allowed including electron-phonon and electron-electron correlations. Thus $\hat{H}_C$ is not specified in (**II.7**) being problem dependent. Lastly (**II.7.c**) describes tunneling between states on the leads and the central region via matrix elements of the type $V_{\alpha;\nu,\mu} \equiv \langle \nu | \hat{V}_{\alpha C} | \mu \rangle$ which for the scope of this thesis we assume to be time-independent. The basis states $\{|\nu\rangle_\alpha\}, \{|\mu\rangle\}$ are mutually orthogonal and moreover they are localized in real-space to allow for the partition in (**II.7.a**). A tight-binding-like single particle basis can be used for this purpose.

In this thesis we consider only spin independent transport and the spin degeneracy is included numerically by a prefactor of 2. The particle current from lead α into the central-region is given by the time-derivative of the particle number in the same lead

$$I_\alpha(t) = -2e \cdot \partial_t \left\langle \hat{N}_\alpha \right\rangle \equiv -2e \cdot \partial_t \sum_\nu \hat{c}^\dagger_{\alpha;\nu} \hat{c}_{\alpha;\nu} = -\frac{2ie}{\hbar} \left\langle \left[\hat{H}, \hat{N}_\alpha \right] \right\rangle \qquad \textbf{(II.8)}$$

Because $\hat{N}_\alpha$ commutes both with $\hat{H}_C$ and $\hat{H}_\alpha$ it results upon insertion of (**II.7.c**) into (**II.8**) that

$$I_\alpha(t) = \frac{2ie}{\hbar} \sum_{\nu,\mu} \left(V_{\alpha;\nu,\mu} \left\langle \hat{c}^\dagger_{\alpha;\nu} \hat{d}_\mu \right\rangle - V^*_{\alpha;\nu,\mu} \left\langle \hat{d}^\dagger_\mu \hat{c}_{\alpha;\nu} \right\rangle \right) \qquad \textbf{(II.9)}$$

Using the following definitions for the two lesser Green's functions

$$G^<_{\mu,\alpha;\nu}(t,t') \equiv i \left\langle \hat{c}^\dagger_{\alpha;\nu}(t) \hat{d}_\mu(t') \right\rangle$$
$$G^<_{\alpha;\nu,\mu}(t,t') \equiv i \left\langle \hat{d}^\dagger_\mu(t) \hat{c}_{\alpha;\nu}(t') \right\rangle$$

the current in (**II.9**) becomes

$$\begin{aligned} I_\alpha(t) &= \frac{2e}{\hbar} \sum_{\nu,\mu} \left(V_{\alpha;\nu,\mu} G^<_{\mu,\alpha;\nu}(t,t) - V^*_{\alpha;\nu,\mu} G^<_{\alpha;\nu,\mu}(t,t) \right) = \\ &= \frac{2e}{\hbar} \int_{-\infty}^{+\infty} \frac{dE}{2\pi} \sum_{\nu,\mu} \left(V_{\alpha;\nu,\mu} G^<_{\mu,\alpha;\nu}(E) - V^*_{\alpha;\nu,\mu} G^<_{\alpha;\nu,\mu}(E) \right) \end{aligned} \qquad \textbf{(II.10)}$$

where in the last equation the inverse Fourier transform from the energy to real-time plane has been used. At this point the only unknown variable is the lesser Green's

function $G^{<}_{\alpha;\nu,\mu}(E)$ which we search for below starting from the general contour-ordered Green's function $G_{\alpha;\nu,\mu}(\tau,\tau')$ defined in (**II.3**). Dyson's equation is still valid at non-equilibrium except for the fact that all quantities should be ordered on the contour of **Figure II.1**, thus

$$G_{\alpha;\nu,\mu}(\tau,\tau') = \sum_{\mu'} \int_C d\tau_1 G_{\alpha;\nu,\alpha;\nu}(\tau,\tau_1) V_{\alpha;\nu,\mu'} G_{\mu',\mu}(\tau_1,\tau')$$

Using Langreth's analytic continuation rules (**II.6**) we transform the contour-ordered integral onto the real-axis

$$G^{<}_{\alpha;\nu,\mu}(t,t') = \sum_{\mu'} V_{\alpha;\nu,\mu'} \int_{-\infty}^{+\infty} dt_1 \left[G^{r}_{\alpha;\nu,\alpha;\nu}(t,t_1) G^{<}_{\mu',\mu}(t_1,t') + G^{<}_{\alpha;\nu,\alpha;\nu}(t,t_1) G^{a}_{\mu',\mu}(t_1,t') \right]$$

Since in steady-state the Green's functions depend only on time differences $t-t'$ we can Fourier transform the above equation in the energy plane, where time convolution becomes a simple multiplication. Following the same steps for $G_{\mu,\alpha;\nu}(\tau,\tau')$ we arrive at the following expressions for the lesser Green's functions

$$G^{<}_{\alpha;\nu,\mu}(E) = \sum_{\mu'} V_{\alpha;\nu,\mu'} \left[G^{r}_{\alpha;\nu,\alpha;\nu}(E) G^{<}_{\mu',\mu}(E) + G^{<}_{\alpha;\nu,\alpha;\nu}(E) G^{a}_{\mu',\mu}(E) \right]$$
$$G^{<}_{\mu,\alpha;\nu}(E) = \sum_{\mu'} V^{*}_{\alpha;\nu,\mu'} \left[G^{r}_{\mu',\mu}(E) G^{<}_{\alpha;\nu,\alpha;\nu}(E) + G^{<}_{\mu',\mu}(E) G^{a}_{\alpha;\nu,\alpha;\nu}(E) \right]$$

Before inserting the last two equations into Equation (**II.10**) we identify the lesser and greater lead self-energies

$$\Sigma^{<(>)}_{\mu,\mu'}(E) = \sum_{\nu} V^{*}_{\alpha;\nu,\mu'} G^{<(>)}_{\alpha;\nu,\alpha;\nu}(E) V_{\alpha;\nu,\mu} \qquad \textbf{(II.11)}$$

and with the help of the relation $G^r - G^a \equiv G^> - G^<$ (see (**II.4.a-d**)) we obtain the particle current average

$$\begin{aligned} I_\alpha &= \frac{2e}{h} \int_{-\infty}^{+\infty} dE \sum_{\mu,\mu'} \left(\Sigma^{<}_{\mu',\mu}(E) G^{>}_{\mu,\mu'}(E) - \Sigma^{>}_{\mu',\mu}(E) G^{<}_{\mu,\mu'}(E) \right) = \\ &= \frac{2e}{h} \int_{-\infty}^{+\infty} dE \, \mathrm{Tr} \left[\mathbf{\Sigma}^{<}_{\alpha}(E) \mathbf{G}^{>}(E) - \mathbf{\Sigma}^{>}_{\alpha}(E) \mathbf{G}^{<}(E) \right] \end{aligned} \qquad \textbf{(II.12)}$$

The trace in the last equation runs over all indices μ that belong to the central region, while boldface quantities represent matrices written in basis $\{|\mu\rangle\}$. This simple

formula says that in order to get the current through an interacting region one has to simply take the trace over energy resolved scattering-in rate minus the scattering-out rate.

If we assume that lead α remains in thermal equilibrium with chemical potential μ_α even after the coupling Hamiltonian has been turned on, then the lesser and greater Green's functions in (**II.12**) can be replaced by their equilibrium versions

$$\mathbf{G}^{>}(E) = i[f(E-\mu_\alpha)-1]\mathbf{A}(E)$$
$$\mathbf{G}^{<}(E) = if(E-\mu_\alpha)\mathbf{A}(E) \equiv i\left(e^{\beta(E-\mu_\alpha)}+1\right)^{-1}\mathbf{A}(E)$$

where we have used the spectral function, defined by $\mathbf{A}(E) \equiv i\left[\mathbf{G}^{r}(E)-\mathbf{G}^{a}(E)\right]$. In analogy with the spectral function we also define the level broadening function $\mathbf{\Gamma}(E) \equiv i\left[\mathbf{\Sigma}^{>}(E)-\mathbf{\Sigma}^{<}(E)\right]$ which we insert into (**II.12**) to obtain the well known to Meir-Wingreen formula [**69**].

$$I_\alpha = \frac{2e}{h}\int_{-\infty}^{+\infty} dE\,\mathrm{Tr}\left[\mathbf{\Gamma}_\alpha(E)i\mathbf{G}^{<}(E) + f(E-\mu_\alpha)\mathbf{\Gamma}_\alpha(E)\mathbf{A}(E)\right] \qquad \textbf{(II.13)}$$

In the following section by adding the non-interacting central region hypothesis we transform the Meir-Wingreen formula into the Fischer-Lee formula. We thus arrive at an elastic transport theory equivalent of the famous Landauer-Büttiker formalism that will be used intensively in the following chapters of this thesis.

2. Equilibrium elastic transport

2.1. Fisher-Lee current formula

The theoretical foundations of the general non-equilibrium interacting transport within the NEGF formalism were laid down in the previous section culminating with a compact formula for the particle current expectation value given by **Equation** (**II.12**). Here we apply two more hypotheses that will simplify even further this formula rendering it computationally tractable for carbon nanotube transport studies.

The first hypothesis assumes that even after coupling the leads to the central region at t_0 via $\hat{V}$ the leads remain in thermal equilibrium and have a certain chemical potential μ_α. This hypothesis has already been used in deriving the Meir-Wingreen

formula (**II.13**). The second hypothesis assumes that the central region is non-interacting that is to say electrons in this region behave like free particles in the one-body potential created by nuclei. "Free" means here that electrons don't interact with phonons and interact with other electrons via an effective mean field. In practical calculations the mean field theory chosen to describe the electrons in the central region and also in the leads is typically Hartree-Fock, Density Functional Theory or some semi-empirical tight-binding scheme.

The latter hypothesis brings the problem down to an entirely one-body problem since the leads were already assumed to be non-interacting (see (**II.7.b**)). Solving this problem is considerably simpler than a many-body problem and allows thereby studying transport through considerably larger nanostructures. Non-interacting electrons in the central region implies that the only self-energies to be included are the lead self-energies. In matrix notation

$$\mathbf{\Sigma}^{<(>)}(E) = \mathbf{\Sigma}_{\alpha}^{<(>)}(E) + \sum_{\alpha' \neq \alpha} \mathbf{\Sigma}_{\alpha'}^{<(>)}(E) \qquad \textbf{(II.14)}$$

In steady-state the Keldysh equation relates the lesser and greater Green's functions to the total self-energies given above, and the retarded/advanced Green's functions, i.e.

$$\mathbf{G}^{<(>)}(E) = \mathbf{G}^{r}(E)\mathbf{\Sigma}^{<(>)}(E)\mathbf{G}^{a}(E) \qquad \textbf{(II.15)}$$

Inserting the **Equations** (**II.14**) and (**II.15**) together with

$$\mathbf{\Sigma}_{\alpha}^{>}(E) = i\left[f(E-\mu_{\alpha})-1\right]\mathbf{\Gamma}_{\alpha}(E) \qquad \textbf{(II.16.a)}$$
$$\mathbf{\Sigma}_{\alpha}^{<}(E) = if(E-\mu_{\alpha})\mathbf{\Gamma}_{\alpha}(E) \qquad \textbf{(II.16.b)}$$

into (**II.12**) results after a few manipulations in

$$I_{\alpha} = \sum_{\alpha' \neq \alpha} \frac{2e}{h} \int_{-\infty}^{+\infty} dE \mathcal{T}_{\alpha,\alpha'}(E)\left[f(E-\mu_{\alpha}) - f(E-\mu_{\alpha'})\right] = \sum_{\alpha' \neq \alpha} I_{\alpha,\alpha'} \qquad \textbf{(II.17.a)}$$
$$\mathcal{T}_{\alpha,\alpha'}(E) = \mathrm{Tr}\left[\mathbf{\Gamma}_{\alpha}(E)\mathbf{G}^{r}(E)\mathbf{\Gamma}_{\alpha'}(E)\mathbf{G}^{a}(E)\right] \qquad \textbf{(II.17.b)}$$

known as the Fisher-Lee formula, in which $\mathcal{T}_{\alpha,\alpha'}(E)$ is the energy-resolved transmission from lead α to α'. This formula will be used throughout this thesis especially in **Chapter III** and **Chapter V** for computing particle currents or transmission spectra of carbon nanotube based devices. As seen from the previous

chapter experimental evidence shows a weak electron-phonon coupling in carbon nanotubes at room temperature over <1μm lengths. Thus for carbon nanotubes a non-interacting "central" region is suitable.

2.2. Todorov's scattering current formula

Another particle current formula based on scattering theory was developed in **Reference 71** to which we refer the reader for the general assumptions made there and derivation of that formula. Here we prove the exact equivalence of Todorov's formula to Fisher-Lee's formula (**II.17**) obtained in the previous subsection. This equivalence is interesting for two reasons. First it proves again that Fisher-Lee formula is valid for elastic tunneling only, and second, Todorov's formula simplifies algebraic manipulations we will use latter to prove an important fact. Within a mean-field approximation the particle current expectation value is uniquely determined by the spectral properties (i.e. eigenvalues and eigenvectors) of the Hamiltonian around the Fermi level.

In a first step we express the level broadening functions $\mathbf{\Gamma}_\alpha(E)$ in terms of the lead spectral functions $\mathbf{A}_\alpha(E)$ and couplings $\mathbf{V}_{C\alpha(\alpha C)}$

$$\mathbf{\Gamma}_\alpha(E) = i\left[\mathbf{\Sigma}_\alpha^r(E) - \mathbf{\Sigma}_\alpha^a(E)\right] = \mathbf{V}_{C\alpha} i\left[\mathbf{G}_\alpha^r(E) - \mathbf{G}_\alpha^a(E)\right]\mathbf{V}_{\alpha C} \equiv \mathbf{V}_{C\alpha}\mathbf{A}_\alpha(E)\mathbf{V}_{\alpha C}$$

which we then insert into the transmission function $\mathcal{T}_{\alpha,\alpha'}(E)$ given by **Equation** (**II.17.b**) to obtain

$$\begin{aligned}\mathcal{T}_{\alpha,\alpha'}(E) &= \mathrm{Tr}_C\left[\mathbf{\Gamma}_\alpha(E)\mathbf{G}_C^r(E)\mathbf{\Gamma}_{\alpha'}(E)\mathbf{G}_C^a(E)\right] = \\ &= \mathrm{Tr}_C\left[\mathbf{V}_{C\alpha}\mathbf{A}_\alpha(E)\mathbf{V}_{\alpha C}\mathbf{G}_C^r(E)\mathbf{V}_{C\alpha'}\mathbf{A}_{\alpha'}(E)\mathbf{V}_{\alpha' C}\mathbf{G}_C^a(E)\right] = \\ &= \mathrm{Tr}_\alpha\left[\mathbf{A}_\alpha(E)\mathbf{V}_{\alpha C}\mathbf{G}_C^r(E)\mathbf{V}_{C\alpha'}\mathbf{A}_{\alpha'}(E)\mathbf{V}_{\alpha' C}\mathbf{G}_C^a(E)\mathbf{V}_{C\alpha}\right]\end{aligned} \qquad \textbf{(II.18)}$$

Matrices were labeled with indices showing to which subsystem of **Figure II.2** they refer to. In the last equality the cyclic invariance of the trace was used. We have labeled the traces in order to emphasize that the final trace will run over the infinite lead space instead of the finite central-region space as was initially.

Next we define the operator $\hat{t}(E) \equiv \hat{V} + \hat{V}\hat{G}^r(E)\hat{V}$. Since we have assumed no direct coupling between any two leads (see **Equation** (**II.7.c**)) we note that formally the

block matrix $\mathbf{V}_{\alpha\alpha'} \equiv \langle \mu | \hat{V} | \mu' \rangle$ with $\mu(\mu') \in \alpha(\alpha')$ vanishes. The same happens to $\mathbf{V}_{\alpha\alpha}, \mathbf{V}_{CC}$ leading to

$$\mathbf{t}_{\alpha\alpha'}(E) = \mathbf{V}_{\alpha C}\mathbf{G}_C^r(E)\mathbf{V}_{C\alpha'}$$

This matrix block $\mathbf{t}_{\alpha\alpha'}(E)$ is then identified and replaced into **Equation** (**II.18**) yielding

$$\begin{aligned} \mathcal{T}_{\alpha,\alpha'}(E) &= \mathrm{Tr}_C\left[\mathbf{\Gamma}_\alpha(E)\mathbf{G}_C^r(E)\mathbf{\Gamma}_{\alpha'}(E)\mathbf{G}_C^a(E)\right] = \\ &= \mathrm{Tr}_\alpha\left[\mathbf{A}_\alpha(E)\mathbf{t}_{\alpha\alpha'}(E)\mathbf{A}_{\alpha'}(E)\mathbf{t}_{\alpha\alpha'}(E)^\dagger\right] = \\ &= 4\pi^2\,\mathrm{Tr}_\alpha\left[\boldsymbol{\rho}_\alpha(E)\mathbf{t}_{\alpha\alpha'}(E)\boldsymbol{\rho}_{\alpha'}(E)\mathbf{t}_{\alpha\alpha'}(E)^\dagger\right] \end{aligned} \qquad \textbf{(II.19)}$$

where in the last equality we used the fact that for non-interacting electrons in the leads, the spectral function is $\mathbf{A}_\alpha(E) = 2\pi\boldsymbol{\rho}_\alpha(E)$ where $\boldsymbol{\rho}_\alpha(E)$ is the lead-projected density of states. This transmission function reinserted into (**II.17.a**) gives Todorov's particle current formula as described in [**71**].

Although equivalent, the Fisher-Lee and Todorov transmission formulae differ in philosophy. The former involves a trace over central-region states and describes finite life-time particles escaping into the leads due to complex imaginary self-energies. The latter however is a trace over lead states, in which the central-region is treated as a black-box scatterer. Both these formulas will be used in this thesis since they offer advantages in particular situations.

2.3. Non-orthogonal basis sets

For practical calculations the elastic transport formalism either in the Fisher-Lee or Todorov's derivation need to be extended to non-orthogonal basis sets. Most of the modern transport calculations are done with extensions of quantum chemistry codes [**76**, **77**, **78**, **79**, **80**] where linear combinations of atomic orbitals or plane waves are the typical basis set choice. However plane waves don't satisfy the real-space localization assumption we have used in deriving the transport formulae of this chapter so we focus on atomic orbitals. Besides their advantages in quantum chemical calculations atomic orbitals suffer from one drawback, namely their lack of orthogonality. In this subsection we show how non-orthogonality can be

straightforwardly taken into account in transport calculations with practically no overhead by a proper notation convention.

Let $\{|\nu\rangle\}$ denote the atomic orbital basis set. The essence of non-orthogonality is the fact that the identity operator expressed in this basis is not the identity matrix $\mathbf{I}$ but rather a general symmetric and positive definite matrix $\mathbf{S}$ known as the overlap matrix or Gram matrix or metric tensor. Thus by definition this matrix' elements are $S_{\nu\mu} = \langle\nu|\hat{I}|\mu\rangle \equiv \langle\nu|\mu\rangle$.

The algebraic manipulations in a non-orthogonal basis is greatly simplified by defining the dual basis

$$|\tilde{\nu}\rangle = \sum_{\mu} S^{-1}_{\mu\nu}|\mu\rangle \qquad \textbf{(II.20)}$$

It is straightforward to verify that $\langle\mu|\tilde{\nu}\rangle = \langle\tilde{\nu}|\mu\rangle = \delta_{\mu\nu}$ and $\langle\tilde{\nu}|\tilde{\mu}\rangle = S^{-1}_{\nu\mu}$. With the help of this dual basis the four closure relations of the spanned Hilbert space can be obtained.

$$\sum_{\nu}|\tilde{\nu}\rangle\langle\nu| = \sum_{\nu}|\nu\rangle\langle\tilde{\nu}| = \sum_{\nu\mu}|\nu\rangle S^{-1}_{\nu\mu}\langle\mu| = \sum_{\nu\mu}|\tilde{\nu}\rangle S_{\nu\mu}\langle\tilde{\mu}| = \hat{I} \qquad \textbf{(II.21)}$$

Observing that the two basis sets yield four matrix representations for an operator $\hat{O}$ depending on the position at the left or right of a direct or dual orbital it is at this point convenient to introduce the following notations (which are similar to [81])

$$O_{\uparrow\downarrow;\mu\nu} \equiv O^{\mu}_{\nu} \equiv \langle\tilde{\mu}|\hat{O}|\nu\rangle \qquad \textbf{(II.22.a)} \qquad O_{\uparrow\uparrow;\mu\nu} \equiv O^{\mu\bar{\nu}} \equiv \langle\tilde{\mu}|\hat{O}|\tilde{\nu}\rangle \qquad \textbf{(II.22.b)}$$

$$O_{\downarrow\downarrow;\mu\nu} \equiv O_{\bar{\mu}\nu} \equiv \langle\mu|\hat{O}|\nu\rangle \qquad \textbf{(II.22.c)} \qquad O_{\downarrow\uparrow;\mu\nu} \equiv O^{\bar{\nu}}_{\bar{\mu}} \equiv \langle\mu|\hat{O}|\tilde{\nu}\rangle \qquad \textbf{(II.22.d)}$$

According to **Reference 81** an index is proper (improper) when referring to a ket (bra) of the direct basis or to a bra (ket) of the dual basis. Direct (dual) basis is represented in our notation by a down-pointing $\downarrow$ (up-pointing $\uparrow$) sign called the external index in contrast with the internal matrix indices ν,μ. Thus e.g. $\mathbf{O}_{\uparrow\downarrow}$ is the proper-proper representation of operator $\hat{O}$ while $\mathbf{O}_{\downarrow\downarrow}$ is its improper-proper representation. A general vector $|\psi\rangle$ also admits four representations following the same conventions as operators

$$\psi_{\downarrow;\nu} \equiv \psi^{\nu} \equiv \langle \tilde{\nu} | \psi \rangle \quad \textbf{(II.23.a)} \qquad \psi_{\uparrow;\nu} \equiv \psi_{\bar{\nu}} \equiv \langle \nu | \psi \rangle \quad \textbf{(II.23.b)}$$

$$\psi_{\downarrow;\nu} \equiv \psi_{\nu} \equiv \langle \psi | \nu \rangle \quad \textbf{(II.23.c)} \qquad \psi_{\uparrow;\nu} \equiv \psi^{\bar{\nu}} \equiv \langle \psi | \tilde{\nu} \rangle \quad \textbf{(II.23.d)}$$

With these notations the representations of the identity operator are $\mathbf{I}_{\downarrow\downarrow} = \mathbf{S}$, $\mathbf{I}_{\uparrow\uparrow} = \mathbf{S}^{-1}$ and $\mathbf{I}_{\uparrow\downarrow} = \mathbf{I}_{\downarrow\uparrow} = \mathbf{I}$. We define a proper matrix multiplication a multiplication of two operator representations having opposite inner external indices, i.e. $\mathbf{A}_{\mathsf{x}\uparrow}\mathbf{B}_{\downarrow\mathsf{y}}$ or $\mathbf{A}_{\mathsf{x}\downarrow}\mathbf{B}_{\uparrow\mathsf{y}}$ where $\mathsf{x},\mathsf{y} \in \{\downarrow,\uparrow\}$. Using the closure relations (**II.21**) one can express then any operator sequence $\hat{A}\hat{B}$ in terms of proper matrix multiplications

$$\mathbf{A}_{\mathsf{x}\uparrow}\mathbf{B}_{\downarrow\mathsf{y}} = \mathbf{A}_{\mathsf{x}\uparrow}\mathbf{I}_{\downarrow\downarrow}\mathbf{B}_{\uparrow\mathsf{y}} = \mathbf{A}_{\mathsf{x}\downarrow}\mathbf{I}_{\uparrow\uparrow}\mathbf{B}_{\downarrow\mathsf{y}} = \mathbf{A}_{\mathsf{x}\downarrow}\mathbf{B}_{\uparrow\mathsf{y}} \qquad \textbf{(II.24)}$$

The same holds true for the action of an operator on a vector, $\hat{A}|\psi\rangle$ yielding

$$\mathbf{A}_{\mathsf{x}\uparrow}\boldsymbol{\psi}_{\downarrow} = \mathbf{A}_{\mathsf{x}\downarrow}\boldsymbol{\psi}_{\uparrow} = \mathbf{A}_{\mathsf{x}\downarrow}\mathbf{I}_{\uparrow\uparrow}\boldsymbol{\psi}_{\downarrow} = \mathbf{A}_{\mathsf{x}\uparrow}\mathbf{I}_{\downarrow\downarrow}\boldsymbol{\psi}_{\uparrow}$$

Schrödinger's equation $\hat{H}|\psi_n\rangle = \varepsilon_n|\psi_n\rangle$ can assume various matrix forms among which the generalized eigenvalue form known from quantum chemistry $\mathbf{H}_{\downarrow\downarrow}\boldsymbol{\psi}_{\uparrow;n} = \varepsilon_n\mathbf{I}_{\downarrow\downarrow}\boldsymbol{\psi}_{\uparrow;n} \Leftrightarrow \mathbf{H}\boldsymbol{\psi}_n = \varepsilon_n\mathbf{S}\boldsymbol{\psi}_n$. Another equation of interest to us is the equation defining the Green's function associated with a one-body Hamiltonian $\hat{G}(E)\left[E\hat{I} - \hat{H}\right] \equiv \hat{I}$. Again this equation can assume different forms but we will however use mainly one particular form

$$\mathbf{G}(E)_{\uparrow\uparrow}\left[E\mathbf{I}_{\downarrow\downarrow} - \mathbf{H}_{\downarrow\downarrow}\right] = \mathbf{I}_{\uparrow\downarrow} = \mathbf{I} \Rightarrow \mathbf{G}(E)_{\uparrow\uparrow} = \left[E\mathbf{I}_{\downarrow\downarrow} - \mathbf{H}_{\downarrow\downarrow}\right]^{-1} \qquad \textbf{(II.25)}$$

We turn now our attention to the representation of the trace in non-orthogonal bases. Let $|a_n\rangle$ denote an eigenvector of an operator $\hat{A}$ corresponding to the eigenvalue a_n. Writing the trace of $\hat{A}$ in the basis of its eigenvectors and then using the closure relation (**II.21**) we find

$$\begin{aligned}
\mathrm{Tr}_n[\hat{A}] &= \sum_n a_n = \sum_n \langle a_n|\hat{A}|a_n\rangle = \sum_{n,\nu,\mu} \langle a_n|\nu\rangle A^{\nu}_{\mu} \langle \tilde{\mu}|a_n\rangle = \\
&= \sum_{n,\nu,\mu} \langle \tilde{\mu}|a_n\rangle\langle a_n|\nu\rangle A^{\nu}_{\mu} = \sum_{\nu,\mu} \langle \tilde{\mu}|\nu\rangle A^{\nu}_{\mu} = \sum_{\nu,\mu} \delta^{\mu}_{\nu} A^{\nu}_{\mu} = \sum_{\nu} A^{\nu}_{\nu} = \qquad \textbf{(II.26)} \\
&= \mathrm{Tr}_{\nu}[\mathbf{A}_{\uparrow\downarrow}] = \mathrm{Tr}[\mathbf{I}_{\uparrow\uparrow}\mathbf{A}_{\downarrow\downarrow}] = \mathrm{Tr}[\mathbf{A}_{\downarrow\uparrow}] = \mathrm{Tr}[\mathbf{I}_{\downarrow\downarrow}\mathbf{A}_{\uparrow\uparrow}]
\end{aligned}$$

where the last three equalities were obtained using representation transformations based on proper matrix multiplications. Traces in non-orthogonal bases are thus taken

over either proper-proper ($\uparrow\downarrow$) or improper-improper ($\downarrow\uparrow$) operator representations.

Applying the above we can select a useful representation for the trace of **Equation** (**II.17.b**)

$$\mathcal{T}_{\alpha,\alpha'}(E) = \mathrm{Tr}\left[\mathbf{\Gamma}_{\alpha;\downarrow\downarrow}(E)\mathbf{G}^{r}_{C;\uparrow\uparrow}(E)\mathbf{\Gamma}_{\alpha';\downarrow\downarrow}(E)\mathbf{G}^{a}_{C;\uparrow\uparrow}(E)\right] \qquad \textbf{(II.27)}$$

which yields inside the trace a $\downarrow\uparrow$ representation consistent with (**II.26**) and also consistent with the representation of the Green's function in (**II.25**). This gives insight into the fact that a coherent formalism (in the sense of operator representations) can be obtained if one considers Hamiltonians, self-energies and level broadening functions ($\hat{H},\hat{\Sigma},\hat{\Gamma}$) to be of type $\downarrow\downarrow$, and Green's functions, densities of states and spectral functions ($\hat{G},\hat{\rho},\hat{A}$) of type $\uparrow\uparrow$, thus

$$\left(\hat{H},\hat{\Sigma},\hat{\Gamma}\right) \rightarrow \left(\mathbf{H}_{\downarrow\downarrow},\mathbf{\Sigma}_{\downarrow\downarrow},\mathbf{\Gamma}_{\downarrow\downarrow}\right) \qquad \textbf{(II.28.a)}$$

$$\left(\hat{G},\hat{\rho},\hat{A}\right) \rightarrow \left(\mathbf{G}_{\uparrow\uparrow},\boldsymbol{\rho}_{\uparrow\uparrow},\mathbf{A}_{\uparrow\uparrow}\right) \qquad \textbf{(II.28.b)}$$

These are the conventions we use throughout this thesis when performing transport calculations. Even though for the sake of brevity we sometimes drop external indices it should always be remembered that in non-orthogonal bases operators assume the representations defined by (**II.28**)

Conclusions

A series of derivations aimed at establishing the transport theory in nanostructures were detailed in this chapter. After arguing why the equilibrium quantum statistical picture is not appropriate for describing transport phenomena under strong perturbations, we have introduced the apparatus of non-equilibrium Green's functions. Contour ordering replaces the normal real-time ordering but with the help of Langreth's continuation rules many of the equilibrium Green's functions can be extended to the non-equilibrium case. A compact formula for the particle current expectation value in multi-terminal devices was obtained in terms of Green's functions, which reduces to Meir-Wingreen formula assuming leads in equilibrium. Adding the non-interacting electrons hypothesis in the central region brought the current expectation value to the familiar Fisher-Lee formula employed throughout this thesis. Using the cyclic invariance of the trace we were then able to prove the

equivalence of Fisher-Lee formula with Todorov's derivation which relies on an elastic scattering picture. As transport calculation often reuse quantum chemistry codes we had to show that nothing changes in the transport theory when working in a non-orthogonal basis set. We were thus able to prove that if representations (**II.28**) are respected the transmission formulae remain unchanged.

CHAPTER III.

A CNT-based electromechanical sensor for mass and force measurements

Introduction

A *potential* carbon-nanotube-based electromechanical sensor is theoretically investigated in this chapter. Such a device has not yet been experimentally demonstrated, however, among the purported goals of this chapter is to prove that such a device would operate in normal conditions and moreover it could be manufactured with state-of-the-art micro- and nano-fabrication techniques. By means of modeling and simulation we will prove later that the aforementioned carbon-nanotube device can measure low-magnitude forces on the order of tens of piconewtons (pN), or with minor modifications it can detect small bodies weighting kilodaltons (kDa) or equivalently zeptograms (zg). The same device can thereby be used in two distinct configurations, one for measuring forces and another for weighting small bodies. In both configurations the output is an electric signal, which is a current imbalance, i.e. the difference between two currents.

Cell motility is one of the central research fields in biology that is trying to explain the myriad of mechanical functions cells accomplish on a regular basis, ranging from migration and division to neural plasticity. Quantifying the forces developed by cells during these processes would shed light into many of the underlying mechanisms (For a review on cell motility and force measurements please consult **Reference 82**.) Measuring these forces [**83**, **84**, **85**] is however a challenging task primarily because of their small magnitude but also because it involves accessing active regions of less than a few micrometers. We will argue in this chapter that carbon nanotubes are appropriate for this task because of their unique structural and mechanical properties. In particular, the force-meter sensor configuration detailed later satisfies all the

abovementioned requirements, namely it can measure pN forces and it has nanometric features.

The second application we target with our proposed device is biochemical sensing. A current priority for homeland security agencies is fast, sensitive and specific detection of biowarfare agents but many other applications like health diagnosis or proteomics would benefit from an integrated biosensing technology. An excellent review on the available sensing techniques is contained in **Reference 86**. Several papers have reported the conversion of bio-molecular recognition into micro-cantilever deflections [**87**, **88**, **89**]. Furthermore, mass measurements on the order of femtograms (fg) were achieved using carbon nanotube-based cantilevers [**57**]. Compared to microcantilevers, carbon nanotubes offer the advantage of a far better scale compatibility with elementary biological processes. This scale compatibility comes as the first of four requirements for future generation biosensors as identified in **Reference 89**, followed by label-free detection, scalability in view of massive parallelization and wide dynamic range.

We start this chapter with a section describing the operation principle of the core device referred to as strain transducer which is common to both the force meter and the nanobalance. The differences of the two configurations are underlined next. A few practical considerations are listed at the end of **Section 1** in order to show that such a device can be realized experimentally. **Section 2** consists in an assessment of the mechanical behavior and the sensitivity of the device under forces on the order of pN. For this purpose a classical molecular mechanics force-field is parameterized via highly accurate *ab initio* calculations and then used to study the unit step response of the transducer yielding information about friction and mechanical stability.

Section 3 focuses on the transduction of the cantilever's deflection into an electrical signal in the coherent transport regime. An efficient real-space partitioning scheme is developed in order to compute the multi-terminal Landauer-Büttiker conductance. Several issues related to the importance of thermal effects in the proper operation of the sensor are discussed. With a simple procedure we include non-zero temperature effects through molecular dynamics in quantum conductance calculations that results in a thermally smeared displacement-current characteristic. This characteristic displays monotonic behavior and constitutes the proof-of-concept for our device.

The nanobalance operation mode is characterized in **Section 4** where we establish that a single streptavidin molecule can be detected; an unprecedented sensitivity for an electromechanical device. Parametric simulations found at the end of this section display a large robustness of the transducer with respect to hard to control operation and device parameters like the binding position of the molecule along the cantilever and the cantilever's radius.

1. Sensor structure and operating principle

1.1. A carbon nanotube-based strain transducer

Although the force measuring sensor and the nanobalance differ in the way they are actuated, they are both based on a core device which transduces the mechanical deformation of a cantilever into an electrical signal. This device will be named hereafter strain transducer. In this section we describe the operation principle of the transducer and the basic setups for measuring with it either forces or masses.

The proposed transducer is sketched in **Figure III.1** and involves two perpendicular carbon nanotubes, i.e. a nanotube cross. Three of the four nanotube ends are clamped to metallic leads and the remaining one is free to move. It is at this end that a bending force will be applied. From the mechanical point of view one tube is a cantilever and the other is a linear bearing. The bearing is placed underneath the cantilever in order to restrain its vertical movement, which is necessary because long nanotubes tend to bend and stick to the substrate attracted by van der Waals forces. Naturally one might raise questions about cantilever-bearing friction. As it will be shown in **Section 2**, the inter-tube friction does not impede the cantilever from bending laterally under an external force, although it modifies the amplitude of thermal fluctuations especially in the region of the junction.

Apart mechanical stability, the three metallic leads serve as electrical contacts to the device. In this thesis we adopt a simple DC biasing scheme with the two terminals of the bearing set to +V (where V is some potential) and the single terminal of the cantilever set to -V. In steady-state, when no external force is applied on the cantilever, the currents flowing through the two branches of the bearing should be approximately equal. In practice there will always be an offset owing to unequal branch-length or differences in the doping or structural imperfections of the branches.

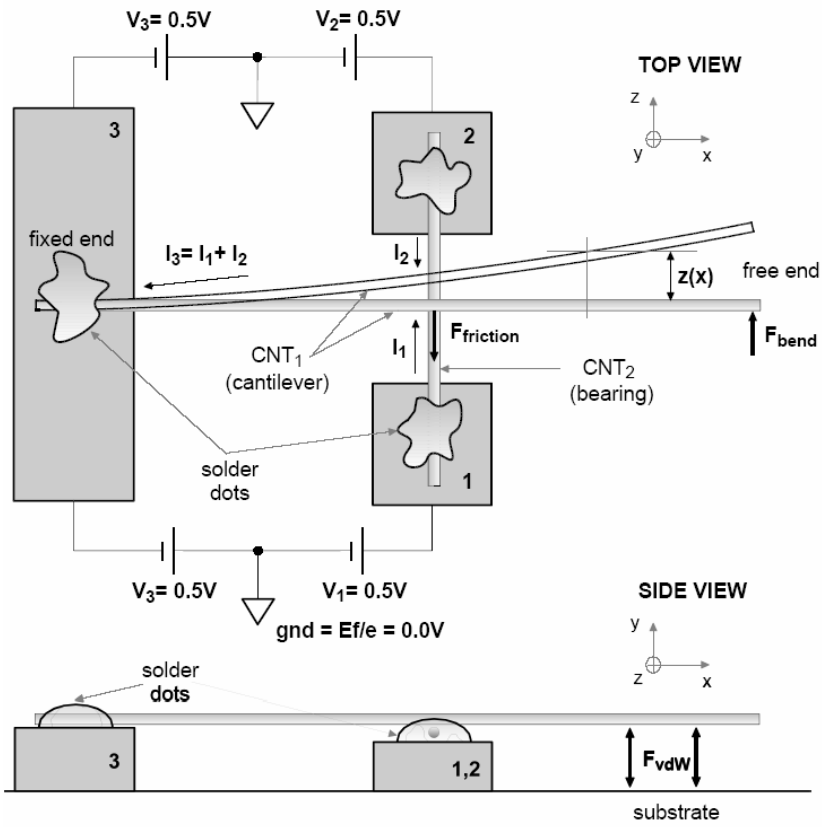

Figure III.1. Schematic representation of the operation principle of a carbon nanotube-based strain transducer, including electronic biasing.

However if an external force is applied, the cantilever will bend elastically, modifying the length and consequently the current ratio of the two branches. It is this branch current imbalance that we "measure" in order to obtain the deformation of the cantilever.

As seen in **Chapter I** for a ballistic tube the conductance doesn't scale with length so regardless of the cantilever's deflection no substantial branch current difference should be recorded. Therefore some scattering should be induced in the bearing to force length-scaling which can be achieved in practice by doping or structural defects.

The integrity of the junction is maintained mainly by van der Waals forces, the vertical bending stiffness of the cantilever and additionally by hydrophobic-hydrophilic forces if the system is in water. However a positive off-plane force (along y) could compromise the weak junction formed between the tubes. This undesirable effect can be tackled either by mechanically confining the applied force in the x-z

plane or by adding a third tube, a bearing on top of the cantilever in a bearing-lever-bearing sequence. However we will not look into this solution in this thesis and leave it for future work.

Summarizing, the sensor is basically a molecular potentiometer whose actuation could be performed for instance by cell motility or by any other external excitation. Even though it performs the same task as a lateral force microscope this sensor has the huge advantage of being embeddable, allowing the fabrication of sensor arrays containing a large number of devices.

1.2. Force meter sensor configuration

Measuring forces with the previously described transducer is straightforward and doesn't require any additions. The cantilever's deflection is transformed into a current difference which is captured by front-end electronics. Both the magnitude and the sign of the external force can be obtained by multiplying the spring constant of the system with the previously determined deflection using an equation similar to (**I.17**). Inspecting this equation one immediately realizes that except for the case of perfectly controlled nanotube dimensions and assembly, which is hard to achieve with today's technology, the Young's modulus and moment of inertia of the cantilever is undetermined. However this incertitude can be eliminated altogether by a calibration phase in which the strain transducer is pushed by forces within a known set of values and the branch current displacement is measured yielding the force-current curve.

Later on we will prove that with carbon nanotube dimensions and inter-lead spacing feasible in the near future such a device could measure forces as low as a few pN. This is quite remarkable for such a trivial device that doesn't rely on laser interferometry or other complex front-ends. Also, the force sensor might become one day suitable for large scale integration and could be used for instance in mapping the force field that cell motility produce. Other applications could certainly be imagined in which a single AFM tip would not be sufficient.

1.3. Nanobalance sensor configuration

The second type of application we found for our transducer is small mass weighting or molecular detection. Transduction of a molecular binding event into an electrical

signal is based on the oscillating frequency difference between the fundamental mode of a free cantilever versus the cantilever with a body attached on it; kind of a nanometric resonance mass spectrometer. By measuring this frequency shift one could obtain precise information about the mass of the attached body which could be a macromolecule, virus or any other small particle. The frequency shift detection alone is however enough in getting a signature of a binding event.

Accordingly, there are two operating modes of this device configuration which we call nanobalance. The first involves measuring the frequency shift from which the mass of the attaching body can be inferred, and the second involves just detecting a frequency drop which is the signature of molecular binding.

As the resonance frequency is in the GHz range front-end electronics would be relatively expensive for this device. However if the system is brought to electromechanical resonance and forced to asymmetrically stay in just one x-z semi-plane, then, at low frequencies it would appear like the cantilever has a "static" deflection about half the oscillation amplitude. In the single-molecule detector mode of this device the actuator's frequency is initially locked on the resonance frequency of the free cantilever. When a body attaches to the cantilever, the normal modes of the latter will get shifted by an amount that depends on the weight of the body and the elastic properties of the transducer; to name a few, tube radius, length, number of walls, attachment position and so on. If the frequency shift is large enough the cantilever will be pushed off resonance and a major drop in the amplitude of oscillation will be recorded. On the contrary in the balance mode the drop in the cantilever's fundamental mode frequency should be determined. This would yield the mass of the particle attached to the cantilever.

1.4. Practical considerations

To be of any practical interest, the proposed transducer should satisfy a few manufacturability constraints, and should prove robust enough to face real-life environment constraints. Due to limitations in computational resources theory one is often forced to appeal to common sense arguments. Below we point just a few of these practical considerations.

The force in the force meter configuration should be confined in the x-y plane otherwise it could undo the weak inter-tube junction. Pre-tensioning is possible but tube-tube sandwich junctions would probably behave better. From a theoretical point of view it would be interesting to see how the currents flowing through two parallel bearings would compose in the coherent transport regime.

In the nanobalance mode we have not mentioned how the actuation can be achieved. We see at least two ways. A forth electrode at the tip of the cantilever could electrostatically bend the cantilever as demonstrated by Poncharal et *al.* [57]. Second, Lorentz forces might be used to bend the cantilever since a current is supposed to flow through it. The second solution seems more appropriate for the case where the sensor is immersed in some ionic solution that would effectively screen any electrostatic field created by a nearby electrode.

A still unanswered question regards the point of immersion of these devices. It is well-known that in MEMS manufacturing capillarity forces can fracture suspended parts. Nevertheless processing techniques have been developed during the years that might help alleviate this problem, which we don't know if it would affect nanotubes anyway.

2. Mechanical transducer behavior

2.1. Mechanical models, suitability and limitations

This section is dedicated to modeling and simulation of the strain transducer whose operation principle has been outlined in the previous section. We feel again the need to warn the reader of the simplicity of the models we are about to employ. Nevertheless present computational resources do not allow for significantly more and moreover many interesting conclusions can already be derived even from these idealized models.

The mechanical properties of single-wall carbon nanotubes have been listed in **Chapter I**, together with the common choices available for their modeling. Here we re-discuss some concepts in the light of the particularities our system has. The starting choice would be the continuum Euler-Bernoulli beam theory [90], that has been validated in moderate strain regimes for nanotube-based AFM tips [91, 92],

nanotweezers [93], electro-mechanical resonators [57] and nano-switches [94]. However, above a certain threshold, bending or compressive stress can induce buckling in nanotubes, a process accompanied by sp^2-sp^3 re-hybridization. Another argument against using this continuum theory is the inter-tube interaction. Atomic-scale fluctuations of the van der Waals potential coupled with the position-dependent shape of the cross junction, yield pseudorandom friction forces. These phenomena can hardly be taken into account by a continuum theory, although attempts have been made with shell theories extended by homogeneous van der Waals potentials [56, 95].

Since studying friction is important in assessing the strain transducer's sensitivity we have to adopt an atomistic description of the system. A natural choice for modeling nanotubes in such situations is molecular dynamics. Carbon nanotubes were studied extensively using various force-fields ranging from *ab initio* [61], tight-binding [96], Tersoff-Brenner [97] and even classical force-fields like CHARMM [98]. We adopted the last type of force-field as implemented in the freely available program NAMD [99]. This force-field is incomparably faster than *ab initio* and semi-empirical methods allowing simulations with more than 10^6 atoms for a few nanoseconds. Compared with the Brenner potential, that was successful in describing carbon-carbon interactions, the CHARMM force field was also parameterized for a large spectrum of organic molecules, notably for amino-acids and phospholipids [100]. This advantage becomes obvious when simulating the sensor, or just part of it, in contact with a cellular membrane or with a protein like it will be done in **Section 4**.

2.2. Ab initio energy-strain curve

Force-fields in CHARMM's class were previously used for modeling carbon nanotubes [98, 101] being nevertheless focused on hydrophobic-hydrophilic effects and not on the nanotube mechanics at large deformations. Thus we have decided to obtain a new set of carbon atom parameters for nanotubes that would accurately reproduce the mechanical properties within a reasonable range of strains. As discussed in **Chapter I.4** accurate experimental information about Young's modulus and Poisson's ratio of carbon nanotubes is still missing from literature [65], forcing the parameterization procedures to rely on *ab initio* calculations. All quantum mechanical computations presented throughout this chapter were performed with SIESTA [102], within the density functional theory (DFT).

Table III.1. Mean bond length, angles and Urey-Bradley terms

chirality (n, m)		(5,5)	(8,0)	(6,3)
		mean	*mean*	*mean*
bond (Å)	A	1.430	1.438	1.434
	B	1.434	1.438	1.426
	C	1.434	1.431	1.442
angle (°)	AB	118.640	116.789	119.614
	AC	118.645	119.719	119.239
	BC	119.460	119.719	117.305
UB (Å)	AB	2.463	2.449	2.472
	AC	2.463	2.481	2.482
	BC	2.476	2.481	2.450
improper (°)		84.004	87.191	84.954

A first set of simulations were performed in order to obtain statistics on bond length, angle, Urey-Bradley (UB) and improper dihedral values as required by the CHARMM force-field, formally defined by **Equation** (**III.1**). In this equation the first bracket delimits the energy contribution of the bonded atoms while the second bracket corresponds to non-bonded atoms.

$$\begin{aligned} E_{total} &= \left[E_{bond} + E_{angle} + E_{UB} + E_{dihed./impr.}\right] + \left[E_{vdW} + E_{elec.}\right] = \\ &= \left[\sum_{i\neq j} k_{ij}\left(r_{ij} - r_{0ij}\right)^2 + \sum_{i\neq j\neq k} k_{\theta ijk}\left(\theta_{ijk} - \theta_{0ijk}\right)^2 + \sum_{i\neq j\neq k} k_{UBij}\left(r_{ik} - r_{0UBik}\right)^2 + \right. \\ &\left. + \sum_{i\neq j\neq k} k_{\phi ijkl}\left(1 + \cos(n\phi + \delta)\right)\right] + \left[\sum_{i\neq j}\left(\frac{A}{r_{ij}^{12}} - \frac{B}{r_{ij}^{6}}\right) + \sum_{i\neq j} \varepsilon_{14}\frac{Cq_iq_j}{\varepsilon_0 r_{ij}}\right] \end{aligned} \quad \textbf{(III.1)}$$

Three different nanotubes were selected for this purpose, one armchair (5,5), one zigzag (8,0) and one chiral (6,3) having approximately the same diameters. The nanotubes, considered infinitely long, were relaxed in a variable-cell until residual

Table III.2. CHARMM force-field parameters as used in molecular dynamics simulations

k	189.581 (kcal/mole/Å^2)	r_0	1.433 (Å)
k_θ	115.724 (kcal/mole/deg^2)	θ_0	118.892 (deg)
k_{UB}	22.699 (kcal/mole/Å^2)	r_{0UB}	2.467 (Å)
intra-tube			
ε_{vdW}	-0.105 (kcal/mole)	R_{vdW}	4.000 (Å)
inter-tube			
ε_{vdW}	-0.070 (kcal/mole)	$R_{vdW}/2$	1.992 (Å)

forces fell below 0.01eV/Å. We used a LDA Hamiltonian, an integration grid cutoff of 60Ry, a double-ζ (DZ) atomic orbital basis set with an energy shift of 160meV or equivalently a confinement/cutoff radius of 2.85Å. The results are summarized in **Table III.1**.

In general we found that there are three inequivalent bonds for chiral nanotubes, while armchair and zigzag tubes have only two. This yields as well three inequivalent angles and UBs, and nine inequivalent improper dihedrals. The improper dihedrals histogram revealed that there is no unique equilibrium value, leading to the exclusion of this term from the total energy. The final values for r_0, θ_0, r_{0UB} and R_{vdW} are presented in **Table III.2**.

2.3. Molecular mechanics force-field parameter fitting

The second phase of the parameterization procedure consisted in fitting the spring constants k, k_θ, k_{UB} and the Lennard-Jones well-depth ε_{vdW} against energy versus strain curves as obtained with SIESTA. Since our calculations are similar with those performed in **Reference 61** and rely on the same code, we took into account their calculated Poisson's ratio ν of 0.14 when preparing pre-strained tubes for relaxation. As opposed to the same reference we extended the study to strains in the range [-10,10]% with a step of 1%, in order to obtain well-behaved parameters even at large deformations. The system under study was a (5, 5), 5 cells-long carbon nanotube. To accelerate the forthcoming relaxation, for each strain we took the already relaxed tube

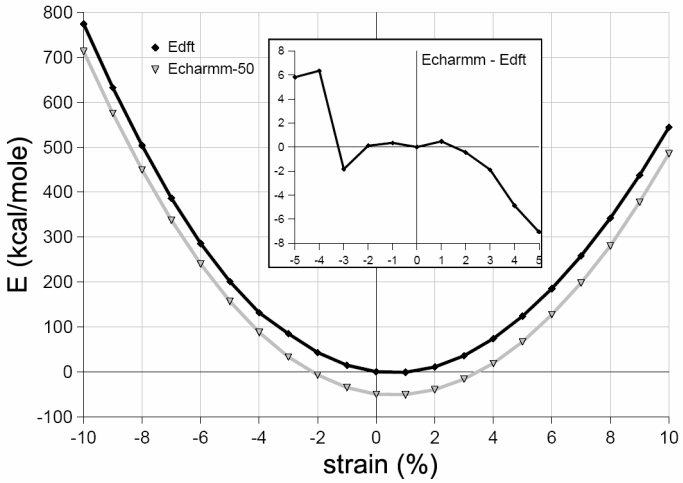

Figure III.2. Energy-strain characteristics as obtained with SIESTA (DFT) and NAMD (CHARMM) respectively. The inset details the error around origin (the curves were shifted for better visualization).

and modify its length to $l_0(1+\varepsilon)$ and radius to $r_0(1-\nu\cdot\varepsilon)$, where here $\varepsilon \equiv \Delta l/l_0$ represents the tensile strain. A full energy minimization was again performed, but not before constraining the boundary atoms in planes perpendicular to the tube's axis.

In order to maintain physical relevant quantities like positive spring constants and a negative Lennard-Jones well-depth we used Lagrange multipliers within the goal function involved in the fitting process. **Figure III.2** shows the comparative energy-strain curves, where the one corresponding to CHARMM was obtained using the optimized force-field parameters summarized in **Table III.2**; these parameters were used in every molecular dynamics simulation throughout the remainder of this chapter. The Young's modulus extracted from the DFT curve corresponds to 1.04TPa which is a realistic value for this type of nanotube. A closer look at the same figure reveals that the DFT curve is asymmetric with respect to zero strain and is especially noticeable at large strains. In order to include this anharmonic behavior we had to add an intra-tube Lennard-Jones potential term that has different parameters from the inter-tube one.

2.4. Coordinate relaxation and simulation

Once the CHARMM force-field was properly parameterized as described in the previous section we have performed several MD simulations aimed at gaining insight into the dynamical behavior of the strain transducer. In the first MD simulation, the

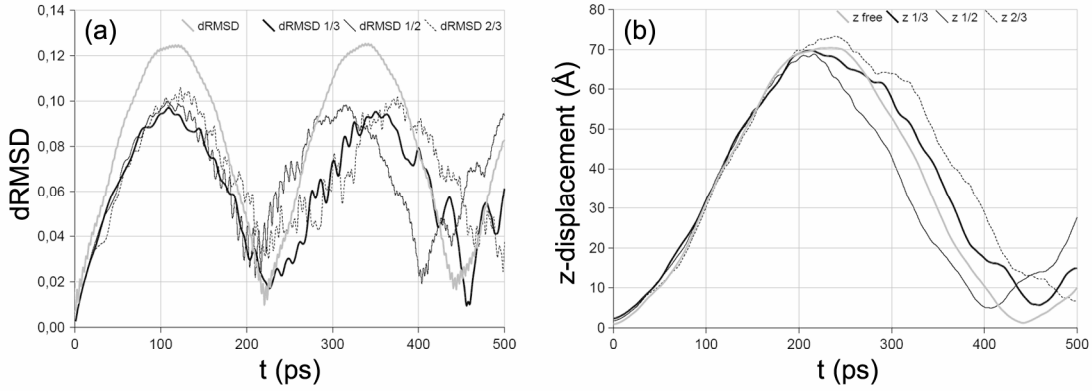

Figure III.3. Different curves relevant to the mechanical behavior of the strain transducer (a) Differential RMSD of all atoms of the cantilever. (b) Cantilever's deflection along z-axis (from one atom found on the tip).

cantilever measuring 36nm was pushed upon with a constant force of 10pN equally distributed between its ten terminal atoms while fixing the other end of the tube.

Turning on the force at the initial simulation step was equivalent with applying a unit step function stimulus, that excited simultaneously all the frequency modes of the system. Lacking dissipation the cantilever would oscillate indefinitely. Nevertheless this impulse response type of simulation contains a lot of information about the mechanical properties of the system. For instance the continuous component of the spectrum gives the final displacement as would be obtained in the presence of dissipation.

Three different positions of the (5,5) bearing tube, measuring 20nm, were chosen to study the influence of the friction; at $1/3$, $1/2$ and $2/3$ from either edge of the cantilever. Relaxation under van der Waals forces was performed before any dynamical simulation, resulting in the formation of the non-covalent junction between the tubes. As before the simulation step of the molecular dynamics was of 1fs and the total simulation time was of 0.5ns (corresponding to 2GHz). The fundamental's mode frequency agrees well with the classical Euler cantilevered beam value of ~2.17GHz.

This time interval proved to be sufficient in capturing at least one period of the cantilever's fundamental mode (**Figure III.3**). Although this interval suffices to obtain an estimate of the fundamental mode's frequency, it is not long enough to allow the extraction of the superior modes via Fourier analysis. The same is true for the quality

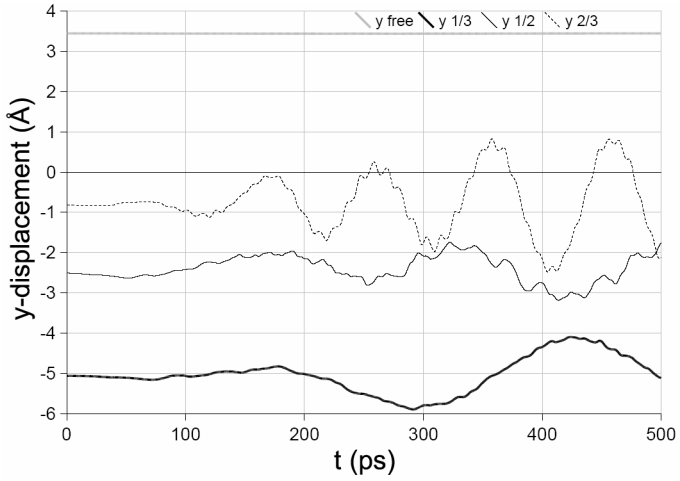

Figure III.4. Cantilever's deflection along the ordinate for the free cantilever case and for the three other positions of the bearing. The oscillations appear as a consequence of friction-induced heating as explained in the text.

factor, which would have been and interesting quantity to compare in the with/without bearing situations.

2.5. Friction and junction stability

Except for the inter-tube van der Waals interactions, there should be in principle no deflection along y since the applied force is constrained in the x-z plane. However **Figure III.4** reveals a different situation. Even if initially at constant height, the cantilever's tip starts to oscillate with increasing vertical amplitude. A closer examination confirmed that the motion of the cantilever is stick-and-slip like due to rapid fluctuations of the van der Waals potential of the underlying tube. As we will see in the next section this spurious movement will greatly influence the charge transport through the junction as the latter is extremely sensitive to the inter-tube distance.

As opposed to the free cantilever case, the bearing adds friction. The mechanical work that is done to move the cantilever against friction, transforms to heat as can it be observed in the differential RMSD (**Figure III.3** (a).)

A magnitude of the friction forces at the level of the cantilever-bearing junction can be obtained by measuring the free oscillation frequency shift or by energy balance.

Measuring the dumping of the oscillation amplitude would also be useful but a large simulation time would be required in this case. We can conclude already though, that friction is well bellow 10pN which is the value of the imposed bending force.

3. Electrical behavior. Strain-current characteristic

3.1. Hamiltonian models, suitability and limitations

The molecular mechanics simulations we have described in the previous section managed to prove that from the mechanical point of view the strain transducer operates indeed as expected. The cantilever remains at all times in contact with the bearing and its lateral motion doesn't seem to be perturbed too much by friction. We concentrate in this section on the electrical behavior of the transducer in trying to prove that the deflection of the cantilever transforms into a branch current difference as explained in **Figure III.1**.

Modeling transport through carbon nanotube cross-junctions is truly a very delicate task. First, there is the problem of identifying the transport regime through the junction which should not be treated with ease. The tunneling current through the junction strongly depends on the inter-tube distance that in turn fluctuates considerably at room temperature. Although not mentioned yet, we have performed other MD simulations at room temperature to sample thermal motion around the equilibrium cantilever deflection, and these simulations show indeed large fluctuations, in agreement to the equipartition theorem. This adds thermal activated transport on the list of possibilities. Also, because the tunneling current is very weak it means that electrons accumulate on the cantilever where they dwell for a while before tunneling into the bearing. Thus charging effects may be of concern. Phonon assisted tunneling is another possibility as charges accumulated in the cantilever would tend to bring it closer to the depleted bearing shrinking the gap until a charge tunnels relaxing the electrostatic attraction and distancing again the junction. These are in fact just a few many-body effects that could influence transport in our system.

The second difficulty associated with modeling transport through carbon nanotube cross-junctions is the large number of atoms involved that hinder diagonalization based approaches. A DFT-level computation of a carbon nanotube cross-junction was previously realized [**103**] but it involved only around 250 atoms in a fixed

configuration. Our system has a few thousand atoms forcing us to consider a simplified tight-binding description. Moreover a current imbalance at the two terminals of the bearing is expected only when its conductance scales in the two branches with length, that requires a clear delimitation of the bearing from the leads, along with the need to include the leads in the overall system.

We assume that at zero temperature, junction tunneling is phase-coherent, which in the light of our previous discussion is not self-evident. However, due to the short lengths of the nanotube segments involved in our simulations, it is safely to affirm that the transport within the tubes is coherent, ballistic. We also assume that thermal fluctuation of the junction happens slowly enough that the electron remains coherent throughout its path from the cantilever's lead to one of the bearing leads. Phonon-assisted tunneling is also ignored in this treatment. We do however take into account finite temperature by averaging over the ensemble of nuclear positions when computing branch currents from the transmission spectra. Including finite temperature in calculations was necessary both because in practice our sensor should work at room temperature and because at zero temperature in the ballistic regime the sensing mechanism can be non-monotonic being thus of no practical use.

The scheme we used in our transport calculations is similar with the one described in **Reference 104**. However we modified this technique to include multiple leads in the presence of tunneling through a non-covalent junction. We used the tight-binding Hamiltonian [**105**] detailed in **Equation (III.2)** including only π orbitals but as opposed to typical calculations we included the cosine factor of Slater-Koster's TB scheme that accounts for the anisotropic inter-tube coupling.

$$\hat{H} = \left[\sum_{\nu}\left(\varepsilon_{0\nu} + \delta\varepsilon_{0\nu} - eV(r_\nu)\right)\hat{c}_\nu^\dagger\hat{c}_\nu + \sum_{(\nu\neq\mu)} t_{0\nu\mu}\exp\left(\frac{a_{C-C} - r_{\nu\mu}}{d}\right)\hat{c}_\nu^\dagger\hat{c}_\mu\right] + \left[\sum_{(\nu\neq\mu)} \tau_{0\nu\mu}\cos(\theta_{\nu\mu})\exp\left(\frac{a_{g-g} - r_{\nu\mu}}{\delta}\right)\hat{c}_\nu^\dagger\hat{c}_\mu\right] \quad \textbf{(III.2)}$$

An exponential decay was also considered to limit the interaction range between non-covalently bonded atoms of the two distinct tubes. The first square bracket in the Hamiltonian delimits intra-tube sites and hopping while the second describes inter-tube interaction.

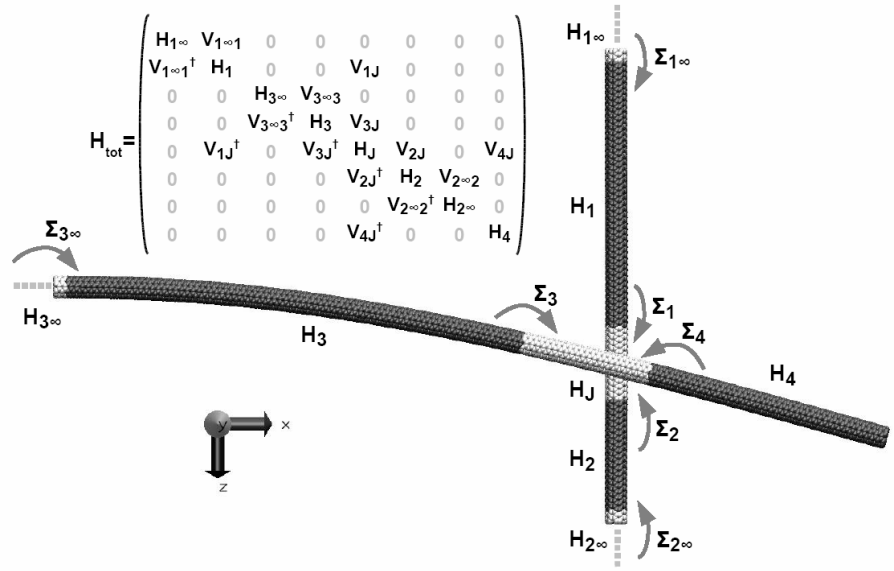

Figure III.5. Real-space partitioning and the Hamiltonian of the system.

The voltage biasing of the system corresponds to **Figure III.1**, and was chosen this way to amplify the length difference of the two branches. Any other scheme involving a voltage drop on the bearing would wash-out this effect since the intra-tube conductance is unquestionably higher than the inter-tube one.

A controversial issue might be the electrostatic potential profile we adopted in this study. The cantilever can be considered in equilibrium with its lead and thus we considered that the potential on this tube is uniform and equal to –V. For the bearing a constant potential was considered as well even though it contained doping atoms that could hinder an effective screening of the local field produced by the cantilever, especially in the region of the junction. We believe that a charge self-consistent tight-binding method could clarify this issue and leave it for future work.

3.2. Real-space partitioning for conductance calculations

The central quantity in the Landauer-Büttiker formalism is the transmission matrix which can be computed, using the Fisher-Lee relation derived in Chapter **II.2.1**, from the Green's functions of the system (see **Equation** (**II.17**)). To accelerate the computation of the Green's functions we partitioned the system as in **Figure III.5**. Pristine, infinite (5,5) CNTs were placed at the end of each the first three domains of the transducer's tubes (denoted with $\mathbf{H}_{1,2,3}$) to simulate the effect of electron

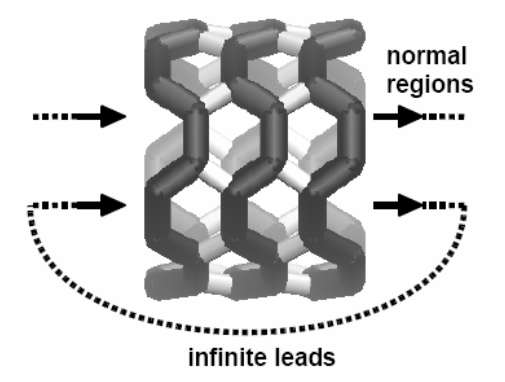

Figure III.6. Real-space sub-partition of the Hamiltonian in rings of 20 atoms (black). In the nearest-neighbor TB bonds correspond to hopping integrals. The white bonds represent interactions between rings.

reservoirs, i.e. leads. The bearing tube was artificially "doped" by modifying the on-site energy from ε_0 to a random value equally distributed in $[\varepsilon_0 - 1\text{eV}, \varepsilon_0 + 1\text{eV}]$ which appears as $\delta\varepsilon_0$ in the Hamiltonian of **Equation** (**III.2**). The leads along with the tubes they contact were set to an electrochemical potential μ of ±0.5eV by shifting the on-site energy by $-eV \equiv \mu$.

After completing the Hamiltonian's matrix elements, a fast, self-energy-based elimination method that is described in the following was used to invert an otherwise large system matrix. Briefly, according to this method self-energies were propagated backwards from leads to junction as illustrated in **Figure III.5**. Practically just the junction Green's functions were obtained by inversion because its Hamiltonian is not sparse as opposed to the other domains where the inter-tube interaction could be neglected. After computing the Green's functions and self-energies for the junction, the Fisher-Lee relation in conjunction with the Landauer-Büttiker formula allowed us to obtain the energy-dependent conductance functions: $\mathcal{G}_{12}$, $\mathcal{G}_{13}$ and $\mathcal{G}_{23}$, which were further integrated to obtain the three currents $I_{1,2,3}$.

An important simplification is obtained by partitioning the Hamiltonian in several domains, as depicted in **Figure III.5**. Except for the junction every other domain is free of inter-tube interaction terms in the Hamiltonian. Thus the Hamiltonian of these domains is sparse making it possible to apply very fast matrix-inversion algorithms. On the contrary the junction's Hamiltonian has many non-zero terms corresponding to

Table III.3. Tight-binding Hamiltonian parameters

ε_0 ($\equiv E_F$)	0 (eV)	d	2 (Å)
$\delta\varepsilon_0$	1 (eV)	τ_0	-0.346 (eV)
$\mu_1=\mu_2=-\mu_3$	-0.5 (eV)	$a_{g\text{-}g}$	3.35 (Å)
t_0	-2.77 (eV)	δ	0.45 (Å)
$a_{C\text{-}C}$	1.43 (Å)	s_0	0.129

non-bonded inter-tube hopping, even though their number was reduced to only those pairs that fall within the cutoff distance of 7Å. This is why the Green's functions of the junction could be obtained only by direct inversion. However it should be noted that the matrix to invert was compact with respect to the overall system's matrix and in consequence it did not dominate the computation time.

For non-junction domains, a further refinement can accelerate the computation. The Hamiltonian of these domains can be sub-partitioned by splitting it in units of 20 atoms (see **Figure III.6**) and then identify the interactions between successive units. The Hamiltonian becomes thus block-tridiagonal and easily invertible through elimination methods. However, there is a difference between leads (domains 1∞ to 3∞) and the cantilever-bearing complex (domains 1 to 4), in that the Hamiltonian of the leads is a semi-infinite periodic matrix and a different procedure is required to calculate its Green's functions. This procedure will be detailed in the next subsection.

$$\mathbf{H}=\begin{bmatrix}
\mathbf{H}_{1\infty} & \mathbf{V}_{1\infty 1} & & & & & & \\
\mathbf{V}_{1\infty 1}^{\dagger} & \mathbf{H}_1 & & & \mathbf{V}_{1J} & & & \\
 & & \mathbf{H}_{3\infty} & \mathbf{V}_{3\infty 3} & & & & \\
 & & \mathbf{V}_{3\infty 3}^{\dagger} & \mathbf{H}_3 & \mathbf{V}_{3J} & & & \\
 & \mathbf{V}_{1J}^{\dagger} & & \mathbf{V}_{3J}^{\dagger} & \mathbf{H}_J & \mathbf{V}_{2J} & & \mathbf{V}_{4J} \\
 & & & & \mathbf{V}_{2J}^{\dagger} & \mathbf{H}_2 & \mathbf{V}_{2\infty 2} & \\
 & & & & & \mathbf{V}_{2\infty 2}^{\dagger} & \mathbf{H}_{2\infty} & \\
 & & & & \mathbf{V}_{4J}^{\dagger} & & & \mathbf{H}_4
\end{bmatrix} \qquad \textbf{(III.3)}$$

The parameters used in the construction of the Hamiltonian and overlap matrix are listed in **Table III.3**. Orbital overlapping was considered in order to improve the calculation accuracy and also because it added no significant complexity, as the

overlap matrix is very similar and practically constructed in parallel with the Hamiltonian, by plugging the value of 0.129 in those positions occupied by nearest-neighbors (or covalently bonded) atoms. A cosine factor was considered for non-bonded atoms. The coarse-partitioned Hamiltonian looks like in **Equation** (**III.3**), where **V** matrices represent interactions between domains. By convention all the omitted elements are zero. The overlap matrix has the same pattern as **H**. Let **K** denote the inverse of the retarded Green's function, a notation we will very often employ in this thesis. It follows that **K** has the same pattern as **H** and is defined by

$$\mathbf{K}(E) \equiv \left(E\mathbf{S} - \mathbf{H}\right) \equiv \mathbf{G}(E)^{-1} = \begin{bmatrix} \mathbf{G}_{11} & \mathbf{G}_{12} & \cdots & \mathbf{G}_{18} \\ \mathbf{G}_{21} & \mathbf{G}_{22} & \cdots & \mathbf{G}_{28} \\ \vdots & \vdots & \ddots & \vdots \\ \mathbf{G}_{81} & \mathbf{G}_{82} & \cdots & \mathbf{G}_{88} \end{bmatrix}^{-1} \qquad \textbf{(III.4)}$$

The elimination procedure we mentioned earlier works as follows. Within the identity $\mathbf{I} = \mathbf{K} \cdot \mathbf{G}$ we can recognize the (8,5) block $\boldsymbol{\delta}_{85} = \mathbf{K}_{4J}^{\dagger}\mathbf{G}_{55} + \mathbf{K}_{4}\mathbf{G}_{85} = \mathbf{0}$ from where one can express $\mathbf{G}_{85}$ as a function of $\mathbf{G}_{55}$. For brevity we have omitted the energy dependence. Similarly, looking at other lines and columns we can express generally $\mathbf{G}_{i5}, i \neq 5$ as a function of $\mathbf{G}_{55}$. Summarizing

$$\boldsymbol{\delta}_{85} \Rightarrow \mathbf{G}_{85} = -\mathbf{K}_{4}^{-1}\mathbf{K}_{4J}^{\dagger}\mathbf{G}_{55} \equiv -\mathbf{G}_{4}\mathbf{K}_{4J}^{\dagger}\mathbf{G}_{55} \qquad \textbf{(III.5.a)}$$

$$\begin{aligned} \boldsymbol{\delta}_{15}, \boldsymbol{\delta}_{25} \Rightarrow \mathbf{G}_{25} &= -\left(\mathbf{K}_{1} - \mathbf{K}_{1\infty 1}^{\dagger}\mathbf{K}_{1\infty}^{-1}\mathbf{K}_{1\infty 1}\right)^{-1}\mathbf{K}_{1J}\mathbf{G}_{55} \equiv \\ &\equiv -\left(\mathbf{K}_{1} - \boldsymbol{\Sigma}_{1\infty}\right)^{-1}\mathbf{K}_{1J}\mathbf{G}_{55} \equiv -\mathbf{G}_{1}\mathbf{K}_{1J}\mathbf{G}_{55} \end{aligned} \qquad \textbf{(III.5.b)}$$

$$\begin{aligned} \boldsymbol{\delta}_{35}, \boldsymbol{\delta}_{45} \Rightarrow \mathbf{G}_{45} &= -\left(\mathbf{K}_{3} - \mathbf{K}_{3\infty 3}^{\dagger}\mathbf{K}_{3\infty}^{-1}\mathbf{K}_{3\infty 3}\right)^{-1}\mathbf{K}_{3J}\mathbf{G}_{55} \equiv \\ &\equiv -\left(\mathbf{K}_{3} - \boldsymbol{\Sigma}_{3\infty}\right)^{-1}\mathbf{K}_{3J}\mathbf{G}_{55} \equiv -\mathbf{G}_{3}\mathbf{K}_{3J}\mathbf{G}_{55} \end{aligned} \qquad \textbf{(III.5.c)}$$

$$\begin{aligned} \boldsymbol{\delta}_{65}, \boldsymbol{\delta}_{75} \Rightarrow \mathbf{G}_{65} &= -\left(\mathbf{K}_{2} - \mathbf{K}_{2\infty 2}\mathbf{K}_{2\infty}^{-1}\mathbf{K}_{2\infty 2}^{\dagger}\right)^{-1}\mathbf{K}_{2J}^{\dagger}\mathbf{G}_{55} \\ &\equiv -\left(\mathbf{K}_{2} - \boldsymbol{\Sigma}_{2\infty}\right)^{-1}\mathbf{K}_{2J}^{\dagger}\mathbf{G}_{55} \equiv -\mathbf{G}_{2}\mathbf{K}_{2J}^{\dagger}\mathbf{G}_{55} \end{aligned} \qquad \textbf{(III.5.d)}$$

$$\boldsymbol{\delta}_{55} \Rightarrow \mathbf{G}_{55} = \left(\mathbf{K}_{J} - \boldsymbol{\Sigma}_{4} - \boldsymbol{\Sigma}_{2} - \boldsymbol{\Sigma}_{1} - \boldsymbol{\Sigma}_{3}\right)^{-1} \equiv \mathbf{G}_{J} \qquad \textbf{(III.5.e)}$$

where the last equation was derived by replacing $\mathbf{G}_{i5}, i \neq 5$ with their found values (**III.5.a-d**) into $\boldsymbol{\delta}_{55}$. Thus at the end we obtain the junction Green's function $\mathbf{G}_{J} \equiv \mathbf{G}_{55}$ which describes the propagation of electrons in the region of the junction (see **Figure III.5**). Assuming that once an electron escapes the junction it is reflected

Algorithm III.1. Fast elimination method for computing the junction's Green's functions

1. LET $\mathbf{K}_4 = E\mathbf{S}_4 - \mathbf{H}_4$
2. $\mathbf{G}_4 = \mathbf{K}_4^{-1}$; $\mathbf{\Sigma}_4 = \mathbf{K}_{4J}\mathbf{G}_4\mathbf{K}_{4J}^{\dagger}$
3. LET $\mathbf{K}_{p\infty} = E\mathbf{S}_{p\infty} - \mathbf{H}_{p\infty}$ FOR $p = \overline{1,3}$
4. $\mathbf{g}_{p\infty} = \left[\mathbf{K}_{p\infty;00} - \mathbf{K}_{p\infty;01}\mathbf{g}_{p\infty}\mathbf{K}_{p\infty;01}^{\dagger}\right]^{-1}$; $\mathbf{\Sigma}_{p\infty} = \mathbf{K}_{p\infty p}^{\dagger}\mathbf{g}_{p\infty}\mathbf{K}_{p\infty p}$
5. LET $\mathbf{K}_p = E\mathbf{S}_p - \mathbf{H}_p$ FOR $p = \overline{1,3}$
6. $\mathbf{G}_p = \left(\mathbf{K}_p - \mathbf{\Sigma}_{p\infty}\right)^{-1}$; $\mathbf{\Sigma}_p = \mathbf{K}_{pJ}^{\dagger}\mathbf{G}_p\mathbf{K}_{pJ}$
7. LET $\mathbf{K}_J = E\mathbf{S}_J - \mathbf{H}_J$
8. $\mathbf{G}_J = \left(\mathbf{K}_J - \mathbf{\Sigma}_1 - \mathbf{\Sigma}_2 - \mathbf{\Sigma}_3 - \mathbf{\Sigma}_4\right)^{-1}$

from neither one of the two bearing branches we can then compute the currents via Fischer-Lee relation in **Equation** (**II.17**) from $\mathbf{G}_J$.

Only assuming reflectionless bearing branches the currents computed from $\mathbf{G}_J$ will be equal to the currents deep inside the leads (see **Reference 22** and discussions therein). This assumption is somehow contradictory. We have stated earlier that the bearing is disordered to allow conductance length-scaling, or this disorder would naturally induce back-scattering. The validity of these calculations is thus questionable. However our goal is to prove that the strain transducer is monotonic and for this purpose qualitative calculations should suffice.

3.3. Free lead surface Green's functions

Matrices that have an ∞ sub-index, like for instance $\mathbf{K}_{1\infty}^{-1}$ in **Equation** (**III.5.b**), are semi-infinite. Fortunately for these matrices it suffices to compute just the Green's function sub-matrix that corresponds to atoms interacting with atoms in adjacent regions. This sub-matrix, called the *surface* Green's function, was calculated using the relation captured in

$$\mathbf{g}_{p\infty} = \left[\mathbf{K}_{p\infty;00} - \mathbf{K}_{p\infty;01}\mathbf{g}_{p\infty}\mathbf{K}_{p\infty;01}^{\dagger}\right]^{-1} \qquad \textbf{(III.6)}$$

where $\mathbf{K}_{p\infty;00}$ is with respect to **Figure III.6** the $\mathbf{K}$ matrix of the rightmost black ring and $\mathbf{K}_{p\infty;01}$ stands for the interaction between any two successive black rings. The

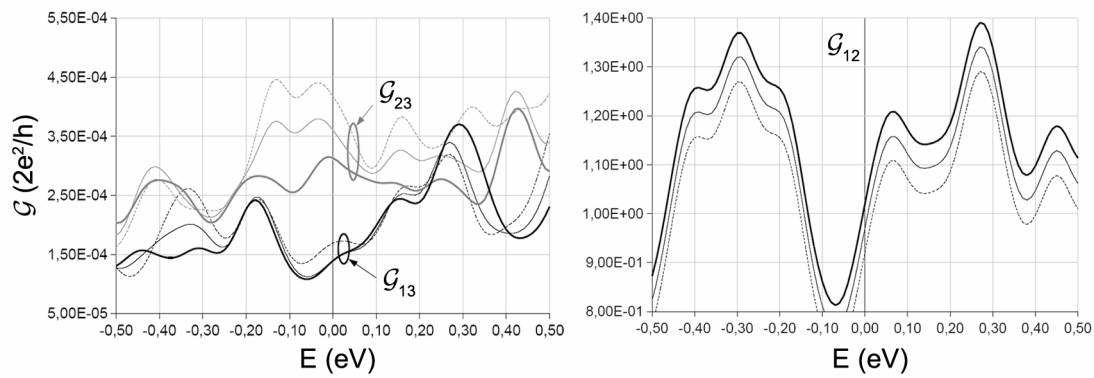

Figure III.7. Smeared conductance functions. (left) Inter-tube conductances vary strongly with small displacements of the cantilever. (right) Intra-tube conductance is insensitive to cantilever's position (the curves were shifted for better visualization).

above equation is then solved starting from $\mathbf{g}_{p\infty} = \mathbf{I}$ which is then iterated to convergence, using two previous iterates in a linear mixing scheme (Pulay mixing).

In **Algorithm III.1** we have condensed all the steps described in the last two subsections that allow the computation of the junction Green's functions. Once these functions are calculated at a given energy, the transmissions between the four different extremities of the junction are obtained using (**II.17.b**), i.e.

$$\mathcal{T}_{\alpha,\alpha'}(E) = \mathrm{Tr}\left[\mathbf{\Gamma}_{\alpha}(E)\mathbf{G}_J^r(E)\mathbf{\Gamma}_{\alpha'}(E)\mathbf{G}_J^r(E)^{\dagger}\right]$$

with $\alpha,\alpha' = \overline{1,4}$, $\alpha \neq \alpha'$ and $\mathbf{\Gamma}_{\alpha}(E)$ are the usual level broadening functions defined by $\mathbf{\Gamma}_{\alpha}(E) = i\left[\mathbf{\Sigma}_{\alpha}^r(E) - \mathbf{\Sigma}_{\alpha}^r(E)^{\dagger}\right]$. The required self-energies appearing in this formula are readily available at steps 2 and 6 of **Algorithm III.1**. Finally using (**II.17.a**) one obtains either the lead currents I_{α} or as in electrical engineering the loop currents $I_{\alpha,\alpha'}$ which summed over α' yield I_{α}. At this point we remind the reader that, since the calculations are performed a non-orthogonal basis, the matrices involved in **Algorithm III.** assume the representations defined by (**II.28**)

3.4. The strain-current characteristic

Initial zero temperature simulations with the cantilever deflected at different positions proved the transducer to be non-monotonic. As "classically" counter-intuitive this may appear it is acceptable within coherent transport theory. Since the bearing branches contain less than a few thousand atoms each, conductance fluctuation is

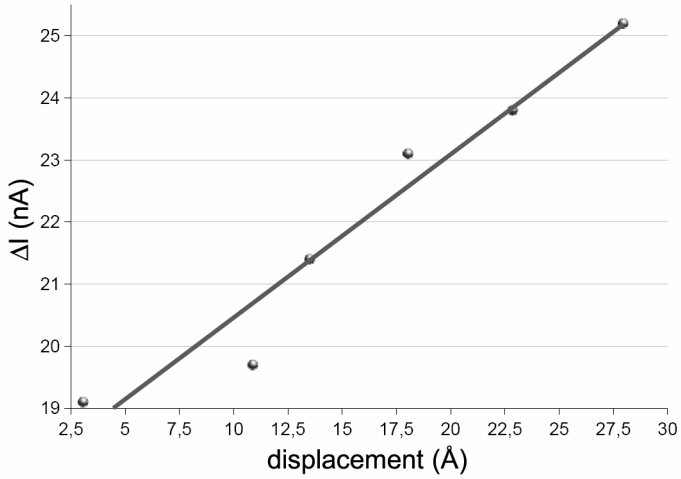

Figure III.8. Overall current-deflection characteristic of the sensor plus a linear fitting line.

possible, and this could further be enhanced by the sharp doping distribution we used. Probably even more important is the atomic detail of the junction. Deflections as low as 0.5Å give rise to important fluctuations in $\mathcal{G}_{13}$ and $\mathcal{G}_{23}$ as can be observed in **Figure III.7**, while $\mathcal{G}_{12}$, seems to be insensitive in the same conditions. The energy-dependent conductances $\mathcal{G}_{\alpha,\alpha'}$ follow throughout this thesis the definition $\mathcal{G}_{\alpha,\alpha'}(E) \equiv \left(2e^2/h\right)\mathcal{T}_{\alpha,\alpha'}(E)$.

The zero-temperature, non-monotonic sensing curve constrains the operation of the transducer at finite temperatures, where thermal fluctuations would smear the sharp conductance fluctuations. This is however not a constraint since the sensor either in the force meter or nanobalance configuration is supposed to work in biocompatible conditions that include a 300K ambient temperature.

In view of taking into account thermal effects we took samples from the dynamical trajectory of the system as obtained in the previous section. We did that instead of properly sampling the trajectory of a thermally fluctuating cantilever around each equilibrium deflection of interest, because the molecular mechanics relaxation of the transducer is very slow. This inconvenience is caused by the low fundamental frequency mode of the cantilever which somewhere at 2GHz, having correspondingly a period of 0.5ns. We plan however in the future to use internal coordinates in a conjugate gradient minimization to accelerate relaxation.

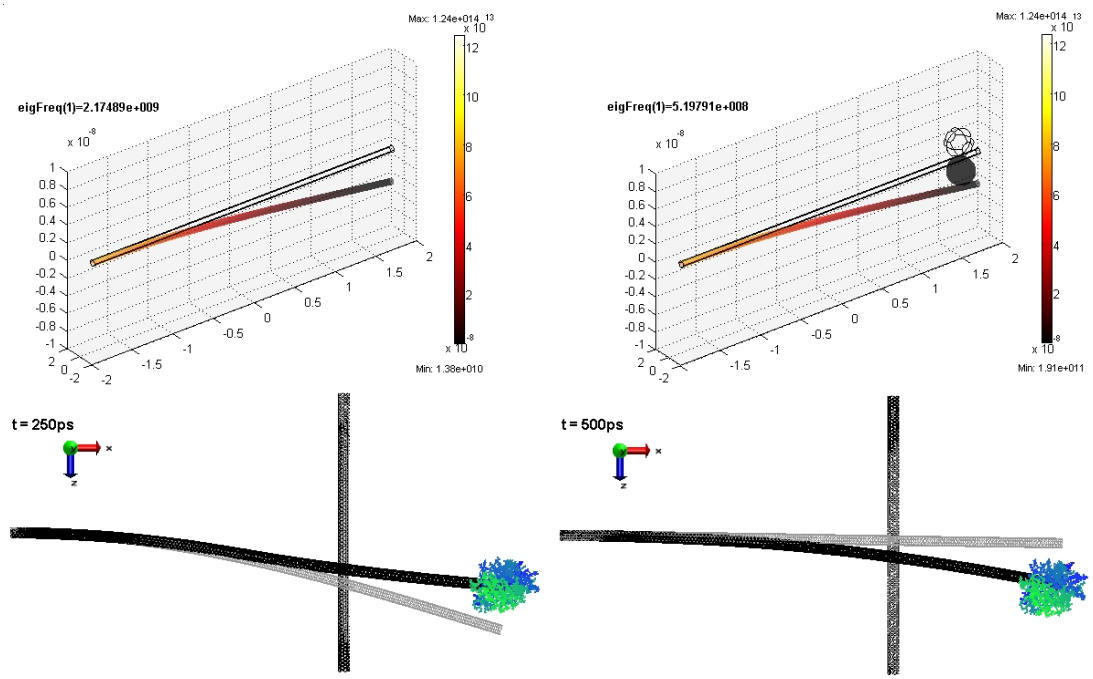

Figure III.9. (top) Shell theory model of free (left) and body-attached (right) sensor showing the fundamental mode four fold frequency drop. (bottom) Atomistic free-cantilever tip (gray) and streptavidin-(green-blue) bound tip (black).

We took thus around a given junction position twenty five closely located samples from a molecular mechanics simulation. The length of the distribution interval was of ~2Å, consistent with thermal displacement fluctuations as known from the classical cantilever theory. After computing the currents as described in the previous subsection we convoluted the found values for the different sampling positions with a thermal-smearing function yielding the curve in **Figure III.8**. This is actually a second smearing and it was considered here in order to obtain the ensemble average of branch currents. This should not be confused with the smearing applied to obtain the smooth conductance functions of **Figure III.7**, as this first smearing corresponds to the thermal broadening of the Fermi-Dirac distribution.

Figure III.8 manages to display an overall monotonic increase of the current difference between the two branches of the bearing validating the operation principle of the strain transducer. We are however aware of the limitations of the model involved here which should not be interpreted quantitatively but rather qualitatively.

4. Modal analysis

4.1. Molecular and continuum shell simulations

In this section our goal is to validate the nanobalance operation principle by showing that resonant frequency shifting occurs when an external body (typically a molecule) binds to the cantilever tube. The system under study in this section is the biotin-streptavidin complex. Biotin can be modified to accommodate non-covalent binding on the surface of the nanotube as demonstrated in **Reference 7**. In **Figure III.9** (bottom) this complex can be recognized at the tip of the carbon nanotube cantilever.

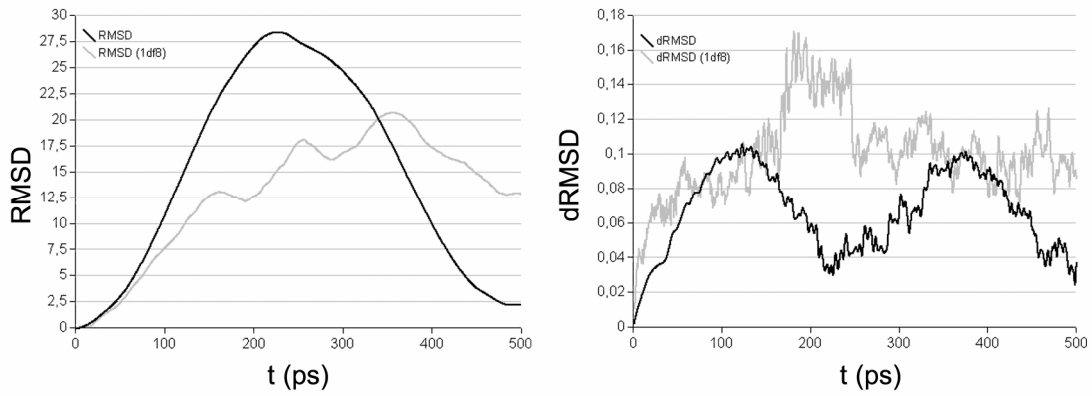

Figure III.10. Root Mean Square Displacement (left) and its derivative (right) for the free (black) and molecule attached (gray) cantilevers.

We employed again molecular mechanics as in **Section 2** of this chapter in order to assess the frequency response of the system, with and without the streptavidin attached. The bearing was placed at $2/3$ of cantilever's length closer to the latter's tip. **Figure III.10** shows that the cantilever's deflection in the molecule-attached case is retarded with respect to the free cantilever. This proves that the mechanical transducer is sensitive enough to detect a single molecule of streptavidin which weights only a few kDa. The frequency drop is four fold from ~2.2GHz in the free cantilever case to 0.5GHz in the molecule attached case which is rather important. Already seen in the RMSD (left) but highlighted the dRMSD figure (right), is the abundance of additional modes introduced by the protein (noise like looking) reducing the quality factor of the nanotube cantilever, which is however not severe.

Our molecular mechanics simulations were performed in vacuum where proteins generally unfold. Thus we had to stabilize the structure of streptavidin by adding

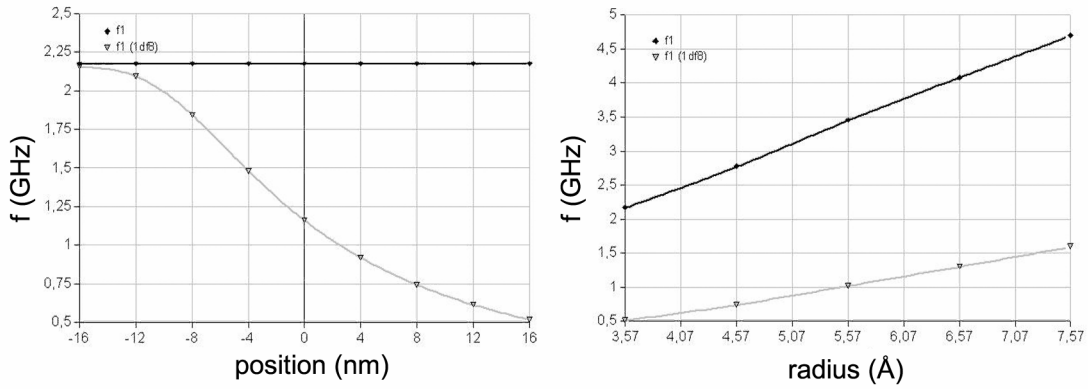

Figure III.11. Fundamental's mode dependence on molecule position along the cantilever (left) and on cantilever's radius (right).

virtual bonds between the center of mass of several domains of this molecule, defined by peptides of ten or so residues. We also had to use a relative dielectric constant of 20 which proved sufficient at stabilizing the structure of the protein.

4.2. Sensitivity analysis of the resonance frequency shift

Following the successful validation of the mechanical transducer via molecular mechanics was a characterization phase of transducer's behavior with respect to uncontrolled device parameters. As mentioned somewhere at the beginning of this chapter in practice many parameters depending on either the fabrication process or the thermodynamics of tube-target binding are hard if not impossible to control having to be treated statistically. Here we focus on the variations associated with the binding position of the streptavidin along the cantilever and cantilever's radius since its length is more or less controllable and its chirality doesn't influence to a first order its bending modulus as discussed in **Chapter I**. Briefly we perform a sensitivity analysis.

As molecular dynamics is computationally too demanding, to achieve any kind of parametric characterization, a continuous, shell theory was employed for this task following closely the details of **Reference 106**. From the energy-strain curve in **Figure III.2** we have obtained a Young's modulus of 1.04TPa at a shell thickness of 3.44Å which is in relative good agreement with experimentally determined values and other calculations as listed in **Chapter I.4.2**. The streptavidin molecule was replaced by a simple sphere with a corresponding diameter and mean density.

The results of sweeping the two parameters, namely the binding position and tube's radius are plotted in **Figure III.11** (left) and (right) respectively. The left figure shows that if streptavidin binds instead of the cantilever's tip somewhere at its middle the frequency shift still remains two fold. Naturally the transducer ceases to detect the molecule when the latter binds close to the clamped end of the cantilever. The second graph reveals that assuming a large deviation in tube's radius (from 3.5 to 7.5Å) the frequency shift continues to be important although the relative frequency shift defined as $\Delta f / f_0$ decreases mildly from 77% to 66%.

We have thus found an unexpectedly large range of working conditions and an impressively frequency shift even for such a small protein like streptavidin is. Thus the proposed transducer is relatively insensitive to manufacturing fluctuations making it extremely suitable for large scale integration. The specificity of such molecular detectors is determined by the specificity of the protein-ligand complex which begins to be more and more within the reach of bio-chemistry.

Perspectives and further developments

The benefits of such sensors lie in their reduced features, and integrated electronic read-in circuitry that would eliminate the need of massive and expensive laboratory sensing instruments. The primary goal of this chapter was to prove rather qualitatively and not necessarily quantitatively that such a molecular transducer is operational. We do consider however that further studies are required before any fabrication plans are made for one of these devices. We lay out a few studies that we consider for the future.

Concerning the mechanical behavior of the strain transducer, one of the most difficult parts to achieve was the relaxation of the cantilever under an external force. In **Section 2** we focused mainly on the unit step response of the transducer because obtaining the final displacement of the cantilever was beyond our reach. As stated earlier with a relatively short, and thus high-frequency, cantilever we were barely able to simulate 0.5ns which is close to a period of the cantilever's fundamental mode. Due to low dumping, waiting for the cantilever to stabilize would be impossible via molecular mechanics. There are at least two solutions for this problem. The first involves using cantilever internal coordinates within a conjugate gradient minimization which is known to accelerate the convergence by up to one order of

magnitude [**107**]. The second solution would rely on a continuum shell theory plus van der Waals forces to obtain the deflection of the cantilever at the equilibrium position. Then the axis of the cantilever could be extracted and imposed on the molecular mechanics model. This yields a pre-conditioned solution that can be refined for instance through a heat-bath coupled molecular mechanics relaxation.

Running room temperature, close to equilibrium deflection, simulations is the next important thing to do. This would produce better thermalized trajectories for smearing the junction tunneling currents. A thermostat would probably also bring the simulations closer to a realistic environment. Apart temperature the presence of the transducer in water might influence importantly the mechanical behavior of the system. As adding a water box around our system would increase intractably the number of atoms in molecular mechanics simulations, simplified systems involving short tubes dragged in water at different speeds should give an idea of what values per unit length the viscosity forces should have.

Studying a bearing-cantilever-bearing sandwich would be interesting from both mechanical and transport point of view. Mechanically it would give some insight into the nanotribology of this system. Naturally one may expect that the friction would increase even further but as the friction is caused by atomic scale fluctuations in the van de Waals potential and since the two bearing lattices would most probably be parallel-incommensurate how would then increase the mechanical resistance. Electrically the problem would shed light onto how coherent conductances compose, and maybe the current-strain characteristic would benefit from a linearization from this composition.

Although we have assumed during the transport calculation that the bearing was doped we have not yet used a defected or doped nanotube in molecular mechanics. Again for nanotribology reasons an imperfect nanotube bearing would expectedly influence the mechanics of the transducer. A step closer to reality would however be made for the transport model if instead of the sharp random distribution of virtual dopants used in **Section 3** one would use tight-binding parameters for boron (B) or nitride (N) in realistic densities as obtained by Latil et *al.* [**108**]

Concerning the transport calculations, future work will have to take into account more thoroughly and systematically the influence of temperature on the operation of the

transducer. Thermal activated transport and phonon-assisted tunneling are just a few effects that would surely change quantitatively our resulted current-strain characteristic. Schottky barriers could also influence especially in the case of a short bearings contacted by metallic leads.

For the nanobalance configuration we plan to study several other small protein-ligand complexes and see if antibodies or DNA strands can be used as well. A true sensitivity characterization would be achieved if the mass-frequency-shift curve would be obtained and composed with the strain-current curve.

Conclusions

A carbon nanotube electromechanical sensor was the subject of several studies aiming at validating the operation principle outlined in **Section 1**. There are two distinct configurations which allow either to measure forces as low as a few piconewtons or to weight small molecular bodies as light as a few kilodaltons. The first series of simulations were focused on the mechanical behavior of the transducer independent of configuration. Molecular mechanics force-filed parameters were obtained from a calculated *ab initio* energy-strain curve. The extracted Young's modulus was found in good agreement with respect to previous calculations and experimental data. Unit step response of the transducer was assessed with the fitted force-field parameters. The fundamental mode frequency of the free cantilever agrees with Euler-Bernoulli beam theory. When the bearing is added, friction shifts the modes and introduces noise in the spectrum, but is found however to be weak enough not to impede the lateral bending of the cantilever. Another series of simulations at room temperature showed that the junction is stable although is hold together only by weak van der Waals interactions. In the third section we have introduced a fast method for computing the junction Green's functions with which we were able to compute the multi-terminal conductances resulting in the current-strain characteristic. This final curve showed monotonic behavior at room temperature which is our proof of concept. We have concluded this chapter with another series of molecular and continuum mechanics simulations in order to demonstrate that the nanobalance configuration is sensitive enough to detect a single streptavidin molecule. Moreover we proved that our transducer is relatively insensitive to the cantilever's diameter and the binding position of the streptavidin molecule along the tube.

CHAPTER IV.

Matrix flows and renormalization

Introduction

The powerful mathematical apparatus of continuous matrix flows is introduced in this chapter. This framework was proposed as solution to a class of inverse eigenvalue problems and relies on infinitesimal congruence transformations acting on a pair of matrices whose spectrum one wishes to conserve [**111**]. Through a properly designed goal function, the congruently transformed pair of matrices can be attracted towards a specific affine structure. Thus the matrix flow theory allows one to find a pair of matrices having a given set of eigenvalues and being as close as possible to a given affine structure. This theory will be used in **Chapter V** in the context of a Hamiltonian model order reduction we have proposed for the purpose of simplifying transport calculations in nanostructures.

We start this chapter with a succinct functional analysis overview that insists in presenting matrices as ordinary "vectors" in a Hilbert space build upon a subgroup of the set of invertible matrices plus the matrix Frobenius inner product. Matrix functions and linear functionals are introduced next, followed by the definition of the Fréchet derivative. The Riesz-Fréchet representation theorem, which occupies a central role in this chapter's formalism, is stated. This theorem provides the means to compute the gradient of a functional from its Fréchet derivative.

Section 2 is dedicated to the matrix flow framework. A simple flow is at first detailed in order to introduce the reader to the various entities that this framework employs, like the isospectral and affine surface, the goal function as the distance between the two surfaces, affine projectors, functional gradients and the flow itself as an ordinary differential equation (ODE). This flow is generalized then to matrix pairs, which is

more close to our generalized eigenvalue context. For maximum flexibility we also extend the goal functional from the simple Frobenius inner product to a weighted version of this product. A very compact formula results for the gradient of the functional which will be instantiated in **Chapter V**. We end the current chapter by mentioning a few perspectives and further developments for the matrix flow framework.

1. Matrix spaces and functions

1.1. The matrix Hilbert space

Matrix sets can form vector spaces and Hilbert spaces when extended with some inner product. These spaces were intensively studied in the fields of statistics and econometrics [**112**, **113**] and penetrated physics as well in the form of Group Theory [**114**] and Renormalization Group [**115**]. In this section we develop to a minimal extent the theory of these spaces and list a few useful properties along with a few hints on how these methods can be applied to problems in quantum physics.

Throughout this chapter we will not employ the Dirac bra-ket notation that is familiar among physicists. This is mainly due to the fact that quantum physics focuses on vectors in some Hilbert space $\mathcal{H}$ and their modification under the action of linear operators that map $\mathcal{H}$ onto itself. Here we are concerned with general nonlinear functions that can be defined on a Hilbert space and take values into another space. However we have included **Table IV.1** that sketches a few equivalences between Dirac notations and notations used in this chapter.

Referring to the same **Table IV.1** it is interesting to note that although we treat matrices in this chapter as abstract vectors in some Hilbert space, the same matrices correspond to linear operators that act on an "underlying" Hilbert space. The "underlying" space can correspond for instance to the space spanned by the states of a particle in a potential, or equivalently the eigenstates found by solving the Schrödinger equation $\hat{H}\left|\psi_n\right\rangle = \varepsilon_n \left|\psi_n\right\rangle$. This equation can simply be re-written in matrix form in which case the Hamiltonian operator becomes a matrix $\mathbf{H}$ and eigenstates become vectors. The matrix Hilbert space is build onto the set of these matrices, operators in the "underlying" space. In the following chapter this correspondence will become evident.

Table IV.1. Some equivalencies between Dirac's notation and notations used in this chapter

Description	***Dirac***	***This chapter***
vector	$\lvert\psi\rangle, \lvert\varphi\rangle$	$\mathbf{A}, \mathbf{B}$
inner product	$\langle\varphi\rvert\psi\rangle$	$\langle\mathbf{B},\mathbf{A}\rangle$
basis set	$\{\lvert\nu\rangle\}_\nu$	$\{\mathbf{E}^k\}_k$
vector coordinate	$\psi_\nu \equiv \langle\nu\rvert\psi\rangle$	$A_k \equiv \langle\mathbf{E}^k,\mathbf{A}\rangle$
Gram matrix	$S_{\mu\nu} \equiv \langle\mu\rvert\nu\rangle$	$g_{jk} \equiv \langle\mathbf{E}^j,\mathbf{E}^k\rangle$
linear operator	$\hat{O}\lvert\psi\rangle$	not used
function(al)	not used	$f(\mathbf{A}), F(\mathbf{A})$
operator average	$\langle\psi\rvert\hat{O}\rvert\psi\rangle$	not used

In our work we focused only on invertible real matrices $n\times n$ belonging to some subgroup of the general linear group, a Lie group of order n^2. It is however straightforward to extend the results obtained here to $GL_n(\mathbb{K})$ defined over a generic field $\mathbb{K}$ like the complex number field $\mathbb{C}$ is. We are aware of the fact that the methods developed here have to be extended to complex matrices in order to become generally applicable to quantum physics.

Apart a vector (or linear) space which as mentioned previously is a subspace $\mathcal{U}_n(\mathbb{R}) \subset GL_n(\mathbb{R})$, a Hilbert space has to be also equipped with an inner product $\langle\cdot,\cdot\rangle : \mathcal{U}_n(\mathbb{R})\times\mathcal{U}_n(\mathbb{R}) \to \mathbb{R}$. For matrices a natural choice is the Frobenius inner product defined as

$$\langle\mathbf{A},\mathbf{B}\rangle = \sum_{i,j} \mathbf{A}_{ij}\mathbf{B}_{ij} = \mathrm{Tr}\left[\mathbf{A}^{\mathrm{T}}\mathbf{B}\right] \qquad \textbf{(IV.1)}$$

leading to the definition of the Frobenius norm

$$\|\mathbf{A}\| = \langle\mathbf{A},\mathbf{A}\rangle^{1/2} \qquad \textbf{(IV.2)}$$

The Frobenius inner product has many useful properties among which the adjoint property both with respect to the normal matrix product and with respect to the

Hadamard (or element-wise) matrix product labeled $\circ$ and defined via

$$\mathbf{C}_{ij} = [\mathbf{A} \circ \mathbf{B}]_{ij} \equiv \mathbf{A}_{ij}\mathbf{B}_{ij} \qquad \textbf{(IV.3)}$$

In the former case the so called adjoint property refers to the following relations

$$\langle \mathbf{A}, \mathbf{BC} \rangle = \langle \mathbf{B}^{\mathrm{T}}\mathbf{A}, \mathbf{C} \rangle \qquad \textbf{(IV.4.a)}$$
$$\langle \mathbf{A}, \mathbf{BC} \rangle = \langle \mathbf{AC}^{\mathrm{T}}, \mathbf{B} \rangle \qquad \textbf{(IV.4.b)}$$

which follow from definition (**IV.1**) using the cyclic invariance of the trace. For example for (**IV.4.a**)

$$\langle \mathbf{A}, \mathbf{BC} \rangle = \mathrm{Tr}\left[\mathbf{A}(\mathbf{BC})^{\mathrm{T}}\right] = \mathrm{Tr}\left[\mathbf{AC}^{\mathrm{T}}\mathbf{B}^{\mathrm{T}}\right] = \mathrm{Tr}\left[(\mathbf{B}^{\mathrm{T}}\mathbf{A})\mathbf{C}^{\mathrm{T}}\right] = \langle \mathbf{B}^{\mathrm{T}}\mathbf{A}, \mathbf{C} \rangle$$

The second adjoint property, with respect to the Hadamard matrix product is very similar

$$\langle \mathbf{A}, \mathbf{B} \circ \mathbf{C} \rangle = \langle \mathbf{B} \circ \mathbf{A}, \mathbf{C} \rangle \qquad \textbf{(IV.5.a)}$$
$$\langle \mathbf{A}, \mathbf{B} \circ \mathbf{C} \rangle = \langle \mathbf{A} \circ \mathbf{C}, \mathbf{B} \rangle \qquad \textbf{(IV.5.b)}$$

and its proof is straightforward once we note that according to (**IV.1**) and (**IV.3**)

$$\langle \mathbf{A}, \mathbf{B} \rangle = \sum_{i,j} A_{ij}B_{ij} = \sum_{i,j} [\mathbf{A} \circ \mathbf{B}]_{ij}$$

Now we turn our attention to the basis definition of the matrix Hilbert space. A simple basis set $\left\{\mathbf{E}^k\right\}_{k \le n^2}$, which of course is not unique, is for instance the set consisting in matrices that are zero except for a single entry which is equal to one, which writes explicitly

$$\left\{ \begin{bmatrix} 1 & 0 & \cdots & 0 \\ 0 & 0 & \ldots & 0 \\ \vdots & \vdots & \ddots & \vdots \\ 0 & 0 & \cdots & 0 \end{bmatrix}, \begin{bmatrix} 0 & 1 & \cdots & 0 \\ 0 & 0 & \ldots & 0 \\ \vdots & \vdots & \ddots & \vdots \\ 0 & 0 & \cdots & 0 \end{bmatrix}, \cdots, \begin{bmatrix} 0 & 0 & \cdots & 1 \\ 0 & 0 & \ldots & 0 \\ \vdots & \vdots & \ddots & \vdots \\ 0 & 0 & \cdots & 0 \end{bmatrix}, \begin{bmatrix} 0 & 0 & \cdots & 0 \\ 1 & 0 & \ldots & 0 \\ \vdots & \vdots & \ddots & \vdots \\ 0 & 0 & \cdots & 0 \end{bmatrix}, \cdots, \begin{bmatrix} 0 & 0 & \cdots & 0 \\ 0 & 0 & \ldots & 0 \\ \vdots & \vdots & \ddots & \vdots \\ 0 & 0 & \cdots & 1 \end{bmatrix} \right\} \qquad \textbf{(IV.6)}$$

The set (**IV.6**) admits a more compact definition using the integer part and modulo n division $\left\{\mathbf{E}^k \middle| E^k_{i,j} = \delta_{i,\lfloor k/n \rfloor}\delta_{j,k \bmod n}, 0 \le k < n^2, 0 \le i,j < n\right\}$ which is nothing more than

a decomposition of the vector index k into matrix indices i, j. It is very easy to verify that this basis is orthonormal, i.e. $\left\langle \mathbf{E}^k, \mathbf{E}^{k'} \right\rangle = \delta_{k,k'}$.

With the help of the Frobenius inner product any matrix can be expressed as a linear combination with real coefficients over the previously defined basis

$$\mathbf{A} = \sum_k \left\langle \mathbf{E}^k, \mathbf{A} \right\rangle \mathbf{E}^k \equiv \sum_k A_k \mathbf{E}^k \qquad \textbf{(IV.7)}$$

where italics were used for A_k to emphasize that it is a scalar. Using the basis definition (**IV.6**) it can be seen that A_k is the matrix element $A_{[k/n],k \bmod n}$ corresponding to the single non-zero entry in $\mathbf{E}^k$.

In many other situation it is more convenient to define the matrix Hilbert space over a subspace like for instance the set of all real symmetric matrices labeled $s_n(\mathbb{R})$ or another Lie-group like $O_n(\mathbb{R})$, the group of real orthogonal matrices as it will be exemplified latter.

1.2. Matrix functions and the Fréchet derivative

Before getting into the development of matrix flow theory, the concepts and notations for the derivatives of matrix functions need to be established. The reader is referred to **References** **112**, **113**, **116** for a thorough introduction to these concepts within a mathematically rigorous framework. Many theorems and their associated proofs will be omitted here for the sake of brevity and notations will be adapted so as to use the scheme introduced in the previous subsection (see also **Table** **IV.1**).

A matrix function in general $f : \mathcal{U}_n(\mathbb{R}) \to \mathcal{V}_m(\mathbb{R})$ bridges two matrix Hilbert spaces $\mathcal{U}_n(\mathbb{R}), \mathcal{V}_m(\mathbb{R}) \subset GL_n(\mathbb{R})$, each equipped with the Frobenius inner product defined in **Equation** (**IV.1**). Within this setup, functional analysis establishes that a generalized derivative known as the Fréchet derivative $\left[\mathcal{D}f(\mathbf{A})\right](\boldsymbol{\delta})$ can be defined via the following relationship:

$$f(\mathbf{A}+\boldsymbol{\delta}) = f(\mathbf{A}) + \left[\mathcal{D}f(\mathbf{A})\right](\boldsymbol{\delta}) + \mathcal{O}(\boldsymbol{\delta}) \qquad \textbf{(IV.8)}$$

where $\boldsymbol{\delta}$ is a matrix of infinitesimal norm and $\mathcal{O}(\boldsymbol{\delta})$ a higher order term in $\boldsymbol{\delta}$ satisfying

$$\lim_{\|\boldsymbol{\delta}\|\to 0}\frac{\|\mathcal{O}(\boldsymbol{\delta})\|}{\|\boldsymbol{\delta}\|}=0$$

Alternatively the Fréchet derivative can be defined through

$$\lim_{\|\boldsymbol{\delta}\|\to 0}\frac{\|(f(\mathbf{A}+\boldsymbol{\delta})-f(\mathbf{A}))-[\mathcal{D}f(\mathbf{A})](\boldsymbol{\delta})\|}{\|\boldsymbol{\delta}\|}=0$$

as being the unique linear operator $[\mathcal{D}f(\mathbf{A})]$ that for all vanishing norm matrices belonging to some subgroup $\boldsymbol{\delta}\in\mathcal{U}_n(\mathbb{R})$ converges in norm to $f(\mathbf{A}+\boldsymbol{\delta})-f(\mathbf{A})$. The action of this operator produces another function $[\mathcal{D}f(\mathbf{A})]:\mathcal{U}_n(\mathbb{R})\to\mathcal{V}_m(\mathbb{R})$. Intuitively the Fréchet derivative $[\mathcal{D}f(\mathbf{A})](\boldsymbol{\delta})$, which reads the "derivative of f at $\mathbf{A}$ acting on $\boldsymbol{\delta}$", is the first order change in the function's value at some point $\mathbf{A}$ in the Hilbert space when applying an infinitesimal matrix perturbation $\boldsymbol{\delta}$ on $\mathbf{A}$. It is thus a "vector" derivative along the "direction" $\boldsymbol{\delta}$ in the matrix Hilbert space. Higher Fréchet derivatives can be defined in a similar manner. Although they could prove useful for computing the Hessian they are somehow beyond the scope of this thesis and are left aside for the moment.

It will often be the case in practice for the matrix function to have several arguments, in which case partial Fréchet derivatives can also be defined. For instance for a two argument function $f(\mathbf{A},\mathbf{B}):\mathcal{U}_n(\mathbb{R})\times\mathcal{W}_p(\mathbb{R})\to\mathcal{V}_m(\mathbb{R})$ the two partial derivatives can be identified from

$$f(\mathbf{A}+\boldsymbol{\delta}_{\mathbf{A}},\mathbf{B})=f(\mathbf{A},\mathbf{B})+[\mathcal{D}_{\mathbf{A}}f(\mathbf{A},\mathbf{B})](\boldsymbol{\delta}_{\mathbf{A}})+\mathcal{O}(\boldsymbol{\delta}_{\mathbf{A}})$$
$$f(\mathbf{A},\mathbf{B}+\boldsymbol{\delta}_{\mathbf{B}})=f(\mathbf{A},\mathbf{B})+[\mathcal{D}_{\mathbf{B}}f(\mathbf{A},\mathbf{B})](\boldsymbol{\delta}_{\mathbf{B}})+\mathcal{O}(\boldsymbol{\delta}_{\mathbf{B}})$$

Another special case of particular interest to us is when the codomain of the f function, namely $\mathcal{V}_m(\mathbb{R})$ is $\mathbb{R}$ itself, i.e. f is a functional. To emphasize functionals we will use majuscules to label them. Functional analysis has an important result concerning linear functionals acting on Hilbert spaces known under the name of Riesz-Fréchet representation theorem that states

THEOREM. (Riesz-Fréchet) Let $F:\mathcal{U}_n(\mathbb{R})\to\mathbb{R}$ be a linear functional acting on a Hilbert space. Then for $\forall\mathbf{A}\in\mathcal{U}_n(\mathbb{R})$ there exist a unique $\mathbf{B}\in\mathcal{U}_n(\mathbb{R})$ such that

$$F(\mathbf{A}) = \langle \mathbf{B}, \mathbf{A} \rangle \qquad \textbf{(IV.9)}$$

The proof of this theorem can be found in any functional analysis book [**116**]. If (**IV.9**), in which the inner product is as usually the Frobenius inner product, is applied to the result of the Fréchet derivative of F, $[\mathcal{D}F(\mathbf{A})](\boldsymbol{\delta})$ which is also a functional, it follows that

$$[\mathcal{D}F(\mathbf{A})](\boldsymbol{\delta}) = \langle \mathbf{B}, \boldsymbol{\delta} \rangle \equiv \langle \nabla F(\mathbf{A}), \boldsymbol{\delta} \rangle \qquad \textbf{(IV.10)}$$

In order to prove that the $\mathbf{B}$ matrix of the last equation is exactly the gradient of the functional F we use the matrix basis set $\{\mathbf{E}^k\}_{k \leq n^2}$ defined in (**IV.6**). Computing the derivative along one of the basis "vectors" $\mathbf{E}^k$ can be achieved by replacing $\boldsymbol{\delta}$ with $t\mathbf{E}^k$ into (**IV.8**), i.e.

$$F(\mathbf{A} + t\mathbf{E}^k) - F(\mathbf{A}) = [\mathcal{D}F(\mathbf{A})](t\mathbf{E}^k) + \mathcal{O}(t\mathbf{E}^k) = t[\mathcal{D}F(\mathbf{A})](\mathbf{E}^k) + \mathcal{O}(t\mathbf{E}^k)$$

where t is a small real parameter necessary to render infinitesimal the norm of $\mathbf{E}^k$, which is equal to one according to (**IV.6**). In the last equality the linearity of derivative operator with respect to scalar-matrix multiplication has been used. Upon dividing the left and the rightmost terms of the latter equation by t and taking the limit, one obtains

$$\lim_{t \to 0} \frac{F(\mathbf{A} + t\mathbf{E}^k) - F(\mathbf{A})}{t} \equiv \frac{\partial F(\mathbf{A})}{\partial A_k} = [\mathcal{D}F(\mathbf{A})](\mathbf{E}^k)$$

By definition the projection of the functional gradient onto a basis vector $\mathbf{E}^k$ is equal to the partial derivative of the functional with respect to each "coordinate" of its argument $\mathbf{A}$, i.e.

$$\langle \nabla F(\mathbf{A}), \mathbf{E}^k \rangle \equiv \frac{\partial F(\mathbf{A})}{\partial A_k} = [\mathcal{D}F(\mathbf{A})](\mathbf{E}^k)$$

The latter identity along with the fact that any other matrix $\boldsymbol{\delta}$ can be written as a linear combination over $\{\mathbf{E}^k\}$ (see (**IV.7**)) proves **Equation** (**IV.10**). This equation is extremely useful in the context of matrix flows as it provides the means to compute the gradient of a matrix functional from the Fréchet derivative. A few examples will be given in the following sections.

Many of the simple derivatives from basic calculus are still valid in this setup, e.g. derivatives of constant and linear functions. One very useful property namely the chain rule has also its equivalent in the matrix space. Let $f(\mathbf{A}) = g(h(\mathbf{A}))$ and $\boldsymbol{\delta}_h = h(\mathbf{A}+\boldsymbol{\delta}_\mathbf{A}) - h(\mathbf{A})$ then

$$\begin{aligned} f(\mathbf{A}+\boldsymbol{\delta}_\mathbf{A}) - f(\mathbf{A}) &= g(h(\mathbf{A}+\boldsymbol{\delta}_\mathbf{A})) - g(h(\mathbf{A})) = g(h(\mathbf{A})+\boldsymbol{\delta}_h) - g(h(\mathbf{A})) = \\ &= \left[\mathcal{D}g(h(\mathbf{A}))\right](\boldsymbol{\delta}_h) + \mathcal{O}(\boldsymbol{\delta}_h) = \\ &= \left[\mathcal{D}g(h(\mathbf{A}))\right]\left(\left[\mathcal{D}h(\mathbf{A})\right](\boldsymbol{\delta}_\mathbf{A}) + \mathcal{O}(\boldsymbol{\delta}_\mathbf{A})\right) + \mathcal{O}(\boldsymbol{\delta}_h) \leq \\ &\leq \left[\mathcal{D}g(h(\mathbf{A}))\right]\left(\left[\mathcal{D}h(\mathbf{A})\right](\boldsymbol{\delta}_\mathbf{A})\right) + \mathcal{O}(\boldsymbol{\delta}_\mathbf{A}) \end{aligned}$$

The last inequality sign should be interpreted as an upper bound. This is rendered possible by the fact that in order for h to be differentiable it should first be continuous. However continuity in Hilbert spaces is equivalent with boundedness which implies that both $\left[\mathcal{D}g(h(\mathbf{A}))\right]\left(\mathcal{O}(\boldsymbol{\delta}_\mathbf{A})\right)$ and $\mathcal{O}(\boldsymbol{\delta}_h)$ are bounded from above by some matrix in $\mathcal{O}(\boldsymbol{\delta}_\mathbf{A})$ times a constant. With these observations it is possible to identify the derivative of f as

$$\left[\mathcal{D}f(\mathbf{A})\right](\boldsymbol{\delta}_\mathbf{A}) = \left[\mathcal{D}g(h(\mathbf{A}))\right]\left(\left[\mathcal{D}h(\mathbf{A})\right](\boldsymbol{\delta}_\mathbf{A})\right) \qquad \textbf{(IV.11)}$$

The properties of the Frobenius norm, Hadamard product, Fréchet derivatives the representation theorem together with the derivative chain rule are all the basic ingredients needed in the matrix flow theory which will be detailed in the next section.

2. Continuous matrix flows

2.1. Projected gradient flows

The term matrix flow stands for a continuous ordinary differential equation (ODE) defined in the abstract matrix Hilbert space with respect to a virtual "time" parameter. The different constituents of the ODE are devised so as to bring the "evolving" system to a desired state which typically is the optimizer of some goal function.

Numerous matrix flows have been developed by Moody Chu as solutions to various problems including least squares matrix approximations, structured inverse eigenvalue problems, simultaneous matrix reduction and many other variants [**109**,

110, **111**]. Generally matrix flow techniques can be used whenever one wants to find a matrix with a certain linear or affine structure that has simultaneously a certain spectrum, i.e. eigenvalues. The method is extremely flexible and should rather be perceived as a framework since it allows one to derive new flows following a certain recipe.

At first two manifolds are being defined one for instance consisting of all matrices of a certain affine structure and the other consisting of all matrices that have a given spectrum. Then a distance function is defined between these two manifolds which becomes the goal function to be minimized. In trying to optimize this function the Riesz-Fréchet theorem (**IV.10**) provides the means to compute the gradient of this function which is then used to define a "steepest" descent flow with respect to the aforementioned virtual time parameter. Finally an ODE solver will integrate this flow and the minimizer of the objective function will be obtained after sufficient virtual time has passed.

An example would better illustrate how this framework can be applied in a practical situation. Let $s_n(\mathbb{R})$ denote the set of all real symmetric $n \times n$ matrices

$$s_n(\mathbb{R}) = \left\{ \mathbf{A} \in GL_n(\mathbb{R}) \middle| \mathbf{A} - \mathbf{A}^{\mathrm{T}} = 0 \right\}$$

From basic algebra it is known that the so called similarity transformations which consist in pre- and post-multiplying a matrix $\mathbf{A}$ with another matrix $\mathbf{B}$ and its inverse $\mathbf{B}^{-1}$ doesn't change the former's spectrum, i.e. $\sigma(\mathbf{A}) = \sigma(\mathbf{B}\mathbf{A}\mathbf{B}^{-1})$ where

$$\sigma(\mathbf{A}) = \left\{ \lambda \in \mathbb{C} \middle| \det(\lambda \mathbf{I} - \mathbf{A}) = 0 \right\}$$

The proof of this affirmation follows easily by pre- and post-multiplying the equation $\det(\lambda \mathbf{I} - \mathbf{A}) = 0$ by $\det(\mathbf{B})$ and $\det(\mathbf{B}^{-1})$ respectively and merging the determinant products into a singular one, thus $\det(\lambda \mathbf{I} - \mathbf{B}\mathbf{A}\mathbf{B}^{-1}) = 0$. If $\mathbf{B}$ is moreover orthogonal, i.e. $\mathbf{B} \in O_n(\mathbb{R}) = \left\{ \mathbf{Q} \in GL_n(\mathbb{R}) \middle| \mathbf{Q}\mathbf{Q}^{\mathrm{T}} = \mathbf{I} \right\}$ the matrix $\mathbf{B}\mathbf{A}\mathbf{B}^{\mathrm{T}}$ is additionally symmetric to being isospectral to $\mathbf{A}$. This leads to a natural definition of the isospectral manifold

$$\mathcal{M}(\mathbf{A}) = \left\{ \mathbf{Q}^{\mathrm{T}}\mathbf{A}\mathbf{Q} \in \middle| \mathbf{Q} \in O_n(\mathbb{R}) \right\}$$

The second manifold required by the matrix flow framework can be defined with

respect to a basis of a subspace $\mathcal{V} \subset GL_n(\mathbb{R})$ of dimension typically smaller than n^2. Let that basis be denoted by $\left\{\mathbf{P}^k\right\}_k$. $\mathcal{V}$ can be more generally an affine subspace defined as the coset of some matrix $\mathbf{P}^0$ plus the linear subspace spanned by $\left\{\mathbf{P}^k\right\}_k$. As a linear space is recovered when $\mathbf{P}^0$ is set to zero we will use the affine space in the following derivations. The affine space is thus defined as

$$\mathcal{V} = \left\{ \mathbf{P}^0 + \sum_k c^k \mathbf{P}^k \middle| c^k \in \mathbb{R} \right\}$$

The third step in the matrix flow framework consists in specifying a distance function separating the two previously defined manifolds, namely the isospectral $\mathcal{M}(\mathbf{A})$ and affine $\mathcal{V}$ manifolds respectively. Such a distance function can for instance be the functional $F : O_n(\mathbb{R}) \to \mathbb{R}$

$$F(\mathbf{Q}) = \frac{1}{2} \left\| \mathbf{Q}^{\mathrm{T}} \mathbf{A} \mathbf{Q} - \mathcal{P}(\mathbf{Q}^{\mathrm{T}} \mathbf{A} \mathbf{Q}) \right\|^2 \qquad \textbf{(IV.12)}$$

where $\mathcal{P}$ plays the role of a projection operator that projects matrices found on the isospectral manifold onto the affine subspace, i.e. $\mathcal{P} : \mathcal{M}(\mathbf{A}) \to \mathcal{V}$, although its domain can be extended to $GL_n(\mathbb{R})$ as well. We now try to identify the action of the projection operator onto a matrix $\mathbf{X}$. As $\mathcal{P}(\mathbf{X}) \in \mathcal{V}$ it has the form

$$\mathcal{P}(\mathbf{X}) = \mathbf{P}^0 + \sum_k c^k \mathbf{P}^k$$

for which linear combination coefficients $\left\{c^k\right\}_k$ need to be determined. Naturally these coefficients have to satisfy the "minimum distance" rule which states that in order for $\mathcal{P}(\mathbf{X})$ to be the projection of $\mathbf{X}$ onto some space it is necessary for $\left\|\mathbf{X} - \mathcal{P}(\mathbf{X})\right\|$ to be minimal. In other words for each j

$$\frac{\partial \left\|\mathbf{X} - \mathcal{P}(\mathbf{X})\right\|}{\partial c^j} = 0 \Leftrightarrow \nabla_{\mathbf{c}} \left\|\mathbf{X} - \mathcal{P}(\mathbf{X})\right\| = 0$$

which yields after a few basic manipulations

$$\sum_k c^k \left\langle \mathbf{P}^k, \mathbf{P}^j \right\rangle = \left\langle \mathbf{X} - \mathbf{P}^0, \mathbf{P}^j \right\rangle$$

Labeling $\left\langle \mathbf{P}^k, \mathbf{P}^j \right\rangle$ with g_{kj} one can identify $\mathbf{g}$ as being the metric tensor or Gram

matrix of the linear subspace. The previous equation can now be transformed in matrix form $\mathbf{cg} = \ldots$ which upon right multiplication with $\mathbf{g}^{-1}$ yields

$$c^k = \sum_j \left\langle \mathbf{X} - \mathbf{P}^0, \mathbf{P}^j \right\rangle g_{jk}^{-1}$$

from where it results immediately

$$\mathcal{P}(\mathbf{X}) = \mathbf{P}^0 + \sum_{j,k} \left\langle \mathbf{X} - \mathbf{P}^0, \mathbf{P}^j \right\rangle g_{jk}^{-1} \mathbf{P}^k \qquad \textbf{(IV.13)}$$

With this definition it can be verified that $\mathcal{P}$ is indeed a projection operator as $\mathcal{P}(\mathcal{P}(\mathbf{X})) = \mathcal{P}(\mathbf{X})$

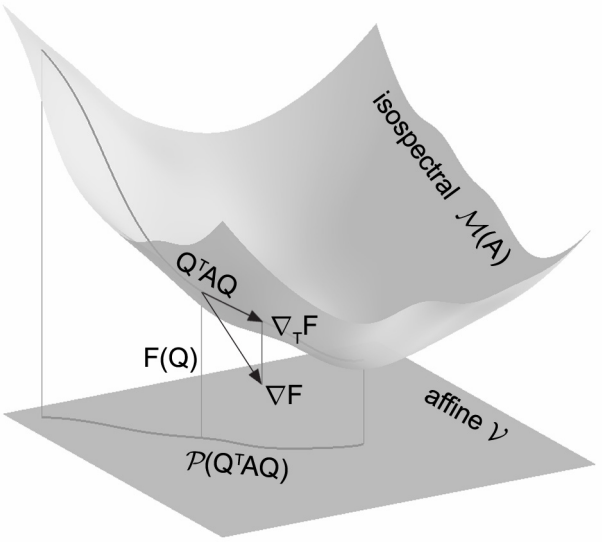

Figure IV.1. The geometry of the isospectral flow algorithm showing the isospectral and affine manifolds. The gradient and its projection onto the tangent space are also shown.

Returning to the definition of F one can observe that this goal function, which we try to minimize, measures how far from the affine manifold is a matrix on the isospectral manifold, in an element-wise manner. Ideally this function would have a single minimum and this minimum should be zero, in which case there would exist a unique matrix that has both a given spectrum and a given linear structure. The geometry of this problem is summarized in **Figure IV.1**.

The next step required for the matrix flow is the computation of the functional

gradient, which as mentioned earlier starts with the Fréchet derivative of F. Let $\alpha(\mathbf{Q}) = \mathbf{Q}^{\mathrm{T}}\mathbf{A}\mathbf{Q} - \mathcal{P}(\mathbf{Q}^{\mathrm{T}}\mathbf{A}\mathbf{Q})$ then

$$\begin{aligned}\left[\mathcal{D}F(\mathbf{Q})\right](\boldsymbol{\delta}_{\mathbf{Q}}) &\equiv \frac{1}{2}\left[\mathcal{D}\left\langle\alpha(\mathbf{Q}),\alpha(\mathbf{Q})\right\rangle\right](\boldsymbol{\delta}_{\mathbf{Q}}) = \\ &= \left\langle\alpha(\mathbf{Q}),\left[\mathcal{D}\alpha(\mathbf{Q})\right](\boldsymbol{\delta}_{\mathbf{Q}})\right\rangle = \\ &= \left\langle\alpha(\mathbf{Q}),\left[\mathcal{D}\mathbf{Q}^{\mathrm{T}}\mathbf{A}\mathbf{Q}\right](\boldsymbol{\delta}_{\mathbf{Q}}) - \left[\mathcal{D}\mathcal{P}(\mathbf{Q}^{\mathrm{T}}\mathbf{A}\mathbf{Q})\right](\boldsymbol{\delta}_{\mathbf{Q}})\right\rangle = \\ &= \left\langle\alpha(\mathbf{Q}) + \alpha(\mathbf{Q})^{T},\mathbf{Q}^{\mathrm{T}}\mathbf{A}\boldsymbol{\delta}_{\mathbf{Q}}\right\rangle - \left\langle\alpha(\mathbf{Q}),\left[\mathcal{D}\mathcal{P}(\mathbf{Q}^{\mathrm{T}}\mathbf{A}\mathbf{Q})\right](\boldsymbol{\delta}_{\mathbf{Q}})\right\rangle\end{aligned} \qquad \textbf{(IV.14)}$$

It can be demonstrated by using the projector's definition (**IV.13**) that the second term of the last equality is zero. Intuitively this can be explained if we notice that $\left[\mathcal{D}\mathcal{P}(\mathbf{Q}^{\mathrm{T}}\mathbf{A}\mathbf{Q})\right](\boldsymbol{\delta}_{\mathbf{Q}})$ lays in the tangent space to $\mathcal{V}$ while $\alpha(\mathbf{Q})$ in the normal space to $\mathcal{V}$, being as such orthogonal to each other. Finally we obtain the result

$$\left[\mathcal{D}F(\mathbf{Q})\right](\boldsymbol{\delta}_{\mathbf{Q}}) = \left\langle\mathbf{A}\mathbf{Q}\left(\alpha(\mathbf{Q}) + \alpha(\mathbf{Q})^{T}\right),\boldsymbol{\delta}_{\mathbf{Q}}\right\rangle \equiv \left\langle\nabla F(\mathbf{Q}),\boldsymbol{\delta}_{\mathbf{Q}}\right\rangle$$

The last step of the framework is setting a matrix flow which typically is chosen to be the "steepest" descent flow

$$\mathrm{d}_t\,\mathbf{Q} = -\nabla F(\mathbf{Q}) \qquad \textbf{(IV.15)}$$

although many other flows not necessarily steepest but possessing other properties can be defined. Various choices of other interesting flows are discussed by Moody Chu extensively in [**109**].

One more thing remains to be discussed before generalizing these flows to definite pencils which is achieved in the following subsection. By carefully inspecting (**IV.15**) one can see that by integrating the flow at a certain point it might happen for this to quit the isospectral surface as $\mathbf{Q}$ quits the orthogonal manifold $O_n(\mathbb{R})$. To prevent this, the gradient is first projected onto the tangent space $T_{\mathbf{Q}}O_n(\mathbb{R})$ before being integrated. Fortunately this tangent space can be found explicitly as $T_{\mathbf{Q}}O_n(\mathbb{R}) = \mathbf{Q}s_n(\mathbb{R})^{\perp}$ where $s_n(\mathbb{R})^{\perp}$ is the subspace of all real skew-symmetric matrices. It then follows (see [**109**]) that the projected gradient is

$$\nabla_{\mathrm{T}}F(\mathbf{Q}) = \mathbf{Q}\left[\mathbf{Q}^{\mathrm{T}}\mathbf{A}\mathbf{Q},\mathcal{P}(\mathbf{Q}^{\mathrm{T}}\mathbf{A}\mathbf{Q})\right]$$

which is defined using the Lie bracket $[\mathbf{A},\mathbf{B}] \equiv \mathbf{AB}-\mathbf{BA}$. The gradient and its projection are also depicted in **Figure IV.1**. Replacing in **Equation (IV.15)** the gradient $\nabla F(\mathbf{Q})$ with $\nabla_{\mathrm{T}} F(\mathbf{Q})$ will guarantee the flow to stay onto $\mathcal{M}(\mathbf{A})$. After a sufficient time the flow would converge to a minimizer of $F(\mathbf{Q})$ which is the sought solution.

2.2. Generalized isospectral flows

Typically in quantum chemical calculations a non-orthogonal basis is used, in which case one is forced to take into account also the metric tensor or Gram matrix or as known by physicists the overlap matrix (see **Table IV.1**). In the "underlying" Hilbert space (see **Section 1.1** of this chapter) Schrödinger's equation no longer writes $\mathbf{H}\boldsymbol{\psi}_n = \varepsilon_n \boldsymbol{\psi}_n$ but rather $\mathbf{H}\boldsymbol{\psi}_n = \varepsilon_n \mathbf{S}\boldsymbol{\psi}_n$. It will be thus necessary to extend the framework defined in the previous subsection to matrix pairs. This extension has already been developed by Moody Chu's least squares approximation of symmetric-definite pairs subject to generalized spectral constraints [**111**].

In this subsection we will however extend it even further to use a weighted Frobenius inner product. As it will be shown in the next chapter this change will further augment the flexibility of the matrix flow framework. The framework is in essence, as mentioned earlier, a constrained inverse eigenvalue problem in which the goal is to find a matrix or more generally a matrix pair that has a given spectrum and satisfies a given affine structure.

For the sake of clarity we will use a generic symmetric-definite pair denoted $(\mathbf{A},\mathbf{B})$. It can be revealed already that **A** and **B** correspond to a Hamiltonian and an overlap matrix respectively defined in an "underlying" Hilbert space, and consequently **A** is symmetric and **B** symmetric and positive definite, from where the term symmetric-definite pair. The spectrum of this pair refers to its generalized eigenvalues contained in the set $\sigma(\mathbf{A},\mathbf{B}) = \left\{\lambda \in \mathbb{R} \middle| \det[\mathbf{A}-\lambda\mathbf{B}] = 0\right\}$.

Again as for the projected gradient flow, there are two constraints relevant to our discussion, one related to the spectrum and the other to the structure, each defining a particular manifold this time in $s_n(\mathbb{R}) \times s_n(\mathbb{R})$. The former manifold is defined as

$$\mathcal{M}(\mathbf{A},\mathbf{B}) = \left\{(\mathbf{T}^{\mathrm{T}}\mathbf{A}\mathbf{T}, \mathbf{T}^{\mathrm{T}}\mathbf{B}\mathbf{T}) \in s_n(\mathbb{R}) \times s_n(\mathbb{R}) \middle| \mathbf{T} \in GL_n(\mathbb{R})\right\} \qquad \textbf{(IV.16)}$$

The **T** matrix is a congruence transformation that applied to the pair $(\mathbf{A},\mathbf{B})$ does not change its eigenvalues. In the previous subsection we have avoided congruence transformations and used orthogonal transformations because the former class of transformations destroys the orthogonality of the "underlying" basis. Here we can afford using them as our basis is already non-orthogonal. The advantage is the increase in flexibility as $GL_n(\mathbb{R})$ includes $O_n(\mathbb{R})$.

It can be proved that the isospectral surface $\mathcal{M}(\mathbf{A},\mathbf{B})$ consists of all symmetric-definite pairs of spectrum equal to $\sigma(\mathbf{A},\mathbf{B})$ and moreover it is a disjoint union of smooth manifolds in $s_n(\mathbb{R})\times s_n(\mathbb{R})$ with respect to **T** (see Theorems 2.1 and 2.2 in [**111**]).

The second manifold of importance to our problem which is related to the structural constraints is the product of two affine subspaces $\mathcal{V}=\mathcal{V}_{\mathbf{A}}\times\mathcal{V}_{\mathbf{B}}$ that can be obtained from $s_n(\mathbb{R})\times s_n(\mathbb{R})$ via a projection operator $\mathcal{P}: s_n(\mathbb{R})\times s_n(\mathbb{R})\to\mathcal{V}_{\mathbf{A}}\times\mathcal{V}_{\mathbf{B}}$ defined as $\mathcal{P}(\mathbf{X},\mathbf{Y})=(\mathcal{P}_1(\mathbf{X}),\mathcal{P}_2(\mathbf{Y}))$. In analogy to (**IV.13**) $\mathcal{P}_{1(2)}$ are given by

$$\mathcal{P}_{1(2)}(\mathbf{X})=\mathbf{P}^0_{1(2)}+\sum_{j,k}\left\langle\mathbf{P}^j_{1(2)},\mathbf{X}-\mathbf{P}^0_{1(2)}\right\rangle g^{-1}_{1(2);jk}\mathbf{P}^k_{1(2)} \qquad \textbf{(IV.17)}$$

Minimizing the distance between these two manifolds would produce a matrix pair

$$(\mathbf{X},\mathbf{Y})=(\mathbf{T}^{\mathrm{T}}\mathbf{A}\mathbf{T},\mathbf{T}^{\mathrm{T}}\mathbf{B}\mathbf{T}) \qquad \textbf{(IV.18)}$$

that is isospectral with $(\mathbf{A},\mathbf{B})$ and that approaches as much as possible, in a least squares sense, the structure imposed by the projection operator $\mathcal{P}$. Nevertheless the problem can be looked at from a complementary perspective as it also produces a pair with a strict structure that has the generalized eigenvalues $\sigma(\mathcal{P}_1(\mathbf{X}),\mathcal{P}_2(\mathbf{Y}))$ close to $\sigma(\mathbf{A},\mathbf{B})$. Although easy to observe using perturbation theory that the two sets of eigenvalues are indeed close to each other it is however not clear if they are minimally distanced. This is a different and considerably more delicate problem solved by Moody Chu [**110**] via a lift and project method which is beyond the scope of this thesis.

Returning to our problem, ideally the two manifolds would intersect in a single point giving thus a unique solution. In practice however they might be separated by a certain distance in which case we still get a least squares approximation of the

solution and have the freedom to choose among the affine pair or the isospectral pair. However it is also possible that the two surfaces intersect at a continuous path yielding an infinite number of solutions in which case further linear constraints can be applied to refine or reduce the cardinality of the solution set.

The goal function we use here is the distance between the isospectral and affine manifolds

$$\begin{aligned} F(\mathbf{T}) &= \frac{1}{2}\left(\left\|\mathbf{U}\circ\left(\mathbf{T}^{\mathrm{T}}\mathbf{A}\mathbf{T}-\mathcal{P}_1(\mathbf{T}^{\mathrm{T}}\mathbf{A}\mathbf{T})\right)\right\|^2+\left\|\mathbf{V}\circ\left(\mathbf{T}^{\mathrm{T}}\mathbf{B}\mathbf{T}-\mathcal{P}_2(\mathbf{T}^{\mathrm{T}}\mathbf{B}\mathbf{T})\right)\right\|^2\right)\equiv \\ &\equiv \frac{1}{2}\left(\left\|\mathbf{U}\circ\left(\mathbf{X}-\mathcal{P}_1(\mathbf{X})\right)\right\|^2+\left\|\mathbf{V}\circ\left(\mathbf{Y}-\mathcal{P}_2(\mathbf{Y})\right)\right\|^2\right)\equiv \\ &\equiv F_1(\mathbf{T})+F_2(\mathbf{T}) \end{aligned} \qquad \textbf{(IV.19)}$$

This goal function is identical with Chu's except for one important feature. We have generalized the standard Frobenius norm $\|\mathbf{A}\|=\langle\mathbf{A},\mathbf{A}\rangle^{1/2}$ with the "weighted" Frobenius norm $\|\mathbf{W}\circ\mathbf{A}\|$. Obviously Chu's theory is a special case having $(\mathbf{U},\mathbf{V})$ equal to $(\mathbf{I}_\circ,\mathbf{I}_\circ)$ where $\mathbf{I}_\circ$ is the neutral element with respect to the Hadamard product and is simply a matrix having all the entries equal to one. Later we will try to proof the versatility of this framework via examples of choosing the weights $(\mathbf{U},\mathbf{V})$ together with the affine structure.

The Fréchet derivative of the $F_1(\mathbf{T})$ function at $\mathbf{T}$ acting on a matrix $\boldsymbol{\delta}$ of infinitesimal Frobenius norm is

$$\begin{aligned} \left[\mathcal{D}F_1(\mathbf{T})\right](\boldsymbol{\delta}) &= \frac{1}{2}\left[\mathcal{D}_{\mathbf{T}}\left\langle\mathbf{U}\circ\left(\mathbf{X}-\mathcal{P}_1(\mathbf{X})\right),\mathbf{U}\circ\left(\mathbf{X}-\mathcal{P}_1(\mathbf{X})\right)\right\rangle\right](\boldsymbol{\delta})= \\ &= \left\langle\mathbf{U}\circ\mathbf{U}\circ\left(\mathbf{X}-\mathcal{P}_1(\mathbf{X})\right),\left[\mathcal{D}_{\mathbf{T}}\mathbf{X}\right](\boldsymbol{\delta})-\left[\mathcal{D}_{\mathbf{T}}\mathcal{P}_1(\mathbf{X})\right]\left(\left[\mathcal{D}_{\mathbf{T}}\mathbf{X}\right](\boldsymbol{\delta})\right)\right\rangle\equiv \\ &\equiv \left\langle\alpha_1(\mathbf{X}),\left[\mathcal{D}_{\mathbf{T}}\mathbf{X}\right](\boldsymbol{\delta})-\left[\mathcal{D}_{\mathbf{T}}\mathcal{P}_1(\mathbf{X})\right]\left(\left[\mathcal{D}_{\mathbf{T}}\mathbf{X}\right](\boldsymbol{\delta})\right)\right\rangle= \\ &= \left\langle\alpha_1(\mathbf{X}),\left[\mathcal{D}_{\mathbf{T}}\mathbf{X}\right](\boldsymbol{\delta})\right\rangle-\left\langle\alpha_1(\mathbf{X}),\left[\mathcal{D}_{\mathbf{T}}\mathcal{P}_1(\mathbf{X})\right]\left(\left[\mathcal{D}_{\mathbf{T}}\mathbf{X}\right](\boldsymbol{\delta})\right)\right\rangle \end{aligned} \qquad \textbf{(IV.20)}$$

Both the chain rule of the Fréchet derivative and the adjoint Hadamard product property (**IV.5**) were used in passing from the first to the second equality. The last equality's first term is then easily derived

$$\begin{aligned}\left\langle \alpha_1(\mathbf{X}),[\mathcal{D}_{\mathbf{T}}\mathbf{X}](\boldsymbol{\delta})\right\rangle &= \left\langle \alpha_1(\mathbf{X}),\mathbf{T}^{\mathrm{T}}\mathbf{A}\boldsymbol{\delta}+\boldsymbol{\delta}^{\mathrm{T}}\mathbf{A}\mathbf{T}\right\rangle = \\ &= \left\langle \mathbf{A}\mathbf{T}\left(\alpha_1(\mathbf{X})+\alpha_1^{\mathrm{T}}(\mathbf{X})\right),\boldsymbol{\delta}\right\rangle = \left\langle 2\mathbf{A}\mathbf{T}\alpha_1(\mathbf{X}),\boldsymbol{\delta}\right\rangle\end{aligned} \qquad \textbf{(IV.21)}$$

where we have used the commutative and the adjoint property of the Frobenius inner product (**IV.4**) this time with respect to the normal matrix product. Also the last equality involves $\alpha_1(\mathbf{X})=\alpha_1^{\mathrm{T}}(\mathbf{X})$ that is simple to observe from the symmetry of the matrices involved.

Because of the "weights" $(\mathbf{U},\mathbf{V})$, the second term of the last equality in **Eq.** (**IV.20**) doesn't cancel anymore as in (**IV.14**), and is obtained using the definition of the projection operators given by **Eq**. (**IV.17**)

$$\begin{aligned}\left\langle \alpha_1(\mathbf{X}),[\mathcal{D}_{\mathbf{T}}\mathcal{P}_1(\mathbf{X})]\left([\mathcal{D}_{\mathbf{T}}\mathbf{X}](\boldsymbol{\delta})\right)\right\rangle &= \left\langle \alpha_1(\mathbf{X}),\sum_{j,k}\left\langle \mathbf{P}_1^j,[\mathcal{D}_{\mathbf{T}}\mathbf{X}](\boldsymbol{\delta})\right\rangle \mathbf{g}^{-1}_{1;jk}\mathbf{P}_1^k\right\rangle = \\ &= \sum_{j,k}\left\langle \alpha_1(\mathbf{X}),\mathbf{P}_1^k\right\rangle \mathbf{g}^{-1}_{1;jk}\left\langle \mathbf{P}_1^j,[\mathcal{D}_{\mathbf{T}}\mathbf{X}](\boldsymbol{\delta})\right\rangle = \\ &= \left\langle \sum_{j,k}\left\langle \alpha_1(\mathbf{X}),\mathbf{P}_1^k\right\rangle \mathbf{g}^{-1}_{1;jk}\mathbf{P}_1^j,[\mathcal{D}_{\mathbf{T}}\mathbf{X}](\boldsymbol{\delta})\right\rangle = \\ &= \left\langle \mathcal{P}_1(\alpha_1(\mathbf{X}))-\mathcal{P}_1(\mathbf{0}),[\mathcal{D}_{\mathbf{T}}\mathbf{X}](\boldsymbol{\delta})\right\rangle = \left\langle 2\mathbf{A}\mathbf{T}\left[\mathcal{P}_1(\alpha_1(\mathbf{X}))-\mathcal{P}_1(\mathbf{0})\right]\middle|\boldsymbol{\delta}\right\rangle\end{aligned} \qquad \textbf{(IV.22)}$$

Merging the last two equations into **Eq.** (**IV.20**) we obtain

$$[\mathcal{D}_{\mathbf{T}}F_1(\mathbf{T})](\boldsymbol{\delta}) = \left\langle 2\mathbf{A}\mathbf{T}\left[\alpha_1(\mathbf{X})-\mathcal{P}_1(\alpha_1(\mathbf{X}))+\mathcal{P}_1(\mathbf{0})\right],\boldsymbol{\delta}\right\rangle \qquad \textbf{(IV.23)}$$

For $F_2(\mathbf{T})$ the calculations are identical. With the help of the Riesz-Fréchet representation theorem (**IV.10**) we can identify the gradient of the goal function

$$\nabla \mathrm{F}(\mathbf{T}) = 2\mathbf{A}\mathbf{T}\left[\alpha_1(\mathbf{X})-\mathcal{P}_1(\alpha_1(\mathbf{X}))+\mathcal{P}_1(\mathbf{0})\right]+2\mathbf{B}\mathbf{T}\left[\alpha_2(\mathbf{Y})-\mathcal{P}_2(\alpha_2(\mathbf{Y}))+\mathcal{P}_2(\mathbf{0})\right] \qquad \textbf{(IV.24)}$$

In the special case $(\mathbf{U},\mathbf{V})=(\mathbf{I}_\circ,\mathbf{I}_\circ)$ because of the projection operator's idempotence $\mathcal{P}_1(\mathbf{X})=\mathcal{P}_1(\mathcal{P}_1(\mathbf{X}))$ it can be shown that $\mathcal{P}_1(\alpha_1(\mathbf{X}))-\mathcal{P}_1(\mathbf{0})=0$ simplifying even further the gradient formula in **Eq.** (**IV.24**).

With the found gradient, we proceed again in setting a steepest descent flow identical with (**IV.15**). Since $\mathbf{T}$ is only a congruence transformation that is a matrix belonging to $GL_n(\mathbb{R})$ we do not project the gradient onto the tangent space to $\mathcal{M}(\mathbf{A},\mathbf{B})$ and

hope that the flow will stay away from the boundary of singular matrices. In practical situations we have observed that indeed this seems to be the case. Nevertheless it is possible to introduce a penalty function like $\log(\det(\mathbf{T}))$ that will repel iterates from this unfeasible boundary.

The application of the matrix flow is to our belief only limited by imagination. Many things can be achieved via this framework, to name just a few orthogonalization, renormalization, tight-binding model parameterization, matrix element elimination (without worrying about condition factors), matrix tridiagonalization, diagonalization and zero patterning in general. It might even be used in many-body physics as the method is closely related to Wegner matrix-flow renormalization.

Perspectives and further developments

At this moment we believe that the matrix flow framework is largely unexplored in the field of quantum transport and quantum physics in general, despite the important potential it has. From a theoretical point of view probably trying to compare this formalism with Wegner's Numerical Renormalization Group (NRG) [**117**, **118**, **119**, **120**] would lead to new ideas of how to apply it to many-body problems.

An interesting feature of matrix flows is that since they involve congruence transformations (at least so far) the hermiticity of the isospectral pair can be conserved. In fact hermiticity can be recovered by properly specifying the affine surface. For instance one could define the affine projection operator as $\mathcal{P}(\mathbf{X}) = \left(\mathbf{X} + \mathbf{X}^{\mathrm{T}}\right)/2$ which clearly is a symmetric matrix and will attract the flow towards a symmetric solution. The freedom in choosing the projection operator can be exploited for imposing other symmetries or scaling behavior as well. One may impose for instance equal matrix elements for equivalent atoms in a super-cell, or a certain scaling of the interaction distance. This opens an unexplored path between the matrix flow framework and Group Theory in physics.

There is also a major gain in having extended the goal functional to a weighted Frobenius norm. This provides the handles to manipulate even further the solution by noticing that zero entries in the weight matrices cancel the contribution of the corresponding matrix elements in the $\mathbf{X} - \mathcal{P}(\mathbf{X})$ matrices to the overall value of the goal function. On the other hand larger weights would make the solution sensitive to

these matrix elements. Thus the weights specify how important it is to have individual entries in $\mathbf{X}$ as close as possible to $\mathcal{P}(\mathbf{X})$. It remains to be seen how the weight matrices could be correlated with the imposed affine structure.

All of the above objectives are rather long-term in scope. In the near term there are a few refinements which we plan to apply. Chu discusses in **Reference 111** many other descent flows that are not necessarily steepest but have other interesting properties and suggests what flow to choose for the problem at hand so as to avoid numerical instability as the dynamical trajectory approaches the boundary of singular matrices. Although we did not detect any numerical instability yet, we would like to investigate these alternatives, because part of the symmetries of the problem can be embedded in the flow equations directly.

Accelerating the flow convergence is also of certain interest. Computing the Hessian, which we mentioned in this chapter's first section that can be obtained as a second Fréchet derivative, might prove useful for this purpose. Also, the flow uses at this point a steepest descent strategy but we wonder if the convergence would not be accelerated in a conjugate gradient framework.

As will be seen in the next chapter we will mainly focus on shaping matrices and conserve only *part* of their spectrum. Intuitively this would increase the number of freedom degrees, but we do not know yet how to exploit this particularity directly into the isospectral flow. Chu [**110**] has proposed another algorithm for solving a similar problem based on a lift and project strategy which might be more suitable for our particular problems.

Conclusions

The fundamentals of the matrix flow theory were laid down in this chapter. Apart giving a modest introduction into the subject, our goal was show that the matrix flow theory is actually a framework allowing for straightforward extensions. Although we have detailed only two examples here, there is no impediment in defining other surfaces and goal functionals within the matrix Hilbert space. Fréchet derivatives are easy to compute for simple matrix functions and many of the classical derivative rules from basic calculus are still valid in this Hilbert space. Gradients, building blocks of optimization algorithms, are accessible via the Riesz-Fréchet representation theorem

from Fréchet derivatives. We have used these concepts earlier in deriving a simple framework for setting a matrix flow on a pair of matrices on which simultaneously a specific affine structure and isospectrality were imposed. An extension to Chu's generalized isospectral flow has also been provided by adding weight matrices within the goal function, which increases the flexibility of the theory as demonstrated in the next chapter.

CHAPTER V.

A CNT-based conductance sensor for physisorbed amino acid detection

Introduction

In this chapter we present theoretical calculations on a carbon nanotube-based conductance sensor. A framework for fast quantum conductance calculations of carbon nanotube-based sensing devices targeting aromatic amino acids within a tight-binding-like approximation is developed. The isospectral matrix flows which were described in the previous chapter will now be applied to obtain a reduced order Hamiltonian optimized for transport calculations. With this Hamiltonian we employ a linearly scaling algorithm to compute the quantum conductance in the coherent transport regime.

The development of biotechnologies seems to increasingly depend on the availability of selective biochemical sensors capable to determine for instance the amino acid composition of a protein. That alone is often enough to identify a protein [**121**] or even predict its secondary structure [**122**, **123**]. However, the required sensitivity and dynamic range rule out most of the potential sensing mechanisms. As carbon nanotubes emerge as a very promising alternative to now standard conductance thin-film sensors we have assumed the task of studying whether sensing amino acids is possible via this paradigm.

Carbon nanotube-based chemical sensors have been experimentally demonstrated for NO_2, NH_3 [**52**], H_2 [**124**], O_2 [**125**], aromatic molecules [**126**] and even large molecules like proteins [**127**] and represents the main R&D effort of start-ups like Nanomix. In this chapter we will focus on similar devices that might respond to amino acid adsorption with a change in their conductance. The study will be limited

to zwitterion aromatic Histidine (HIS), Phenylalanine (PHE), Tryptophan (TRP) and Tyrosine (TYR) amino acids, binding through π stacking onto single-wall carbon nanotubes. Although an aromatic amino acid sensor in itself would have a questionable use, our long goal is to study peptide wrapped carbon nanotubes for which the present study is a prerequisite.

In **Section 1** we briefly explain how a carbon nanotube field effect transistor can be used as a chemical sensor. The challenges in computing the conductance of such a device from first principles together with the solution we propose are laid down in **Section 2**. The solution involves performing *ab initio* calculations on a considerably smaller reference adsystem, namely each of the four amino acids on top of a flat graphene sheet. These calculations are detailed in **Section 3** where among other results we find that adsorption induces states close to the Fermi level and also some charge neutrality point shifting. **Section 4** is dedicated to a novel method we have developed for the purpose of obtaining optimized Hamiltonian models for transport calculations. At the base of this method stand the powerful generalized matrix flows introduced in the previous chapter which we now show how to apply in a concrete situation. An efficient conductance calculation scheme is presented at the end of this chapter in **Section 5** where the first results on the transmission spectra modification due to molecular adsorption are also presented.

1. Sensor structure and operating principle

When listing the experimental findings regarding the transport properties of carbon nanotube-based devices in **Chapter I.3.2**, we saw that semiconducting SWNT display p-type conduction in normal conditions. This phenomenon was attributed to oxygen adsorption on nanotube surface accompanied by charge transfer. As the influence of oxygen on the transport properties was so important, the idea of using nanotubes as chemical sensors followed almost naturally.

A carbon nanotube conductance sensor is basically a field effect transistor-like device. The nanotube bridges two terminals and its Fermi level is controlled by a gate voltage from beneath. The sensitive element is the nanotube itself which means that its surface is externally exposed and not be covered by oxides or any other material. As opposed to nanowires or other chemical FETs, all atoms of a carbon nanotube are

surface atoms, which is the key in explaining the excellent sensitivity of this type of devices.

Generally speaking a conductance sensor is a device which transforms the binding of a certain chemical stimulus to one of its sensitive regions, into a conductance change. In the context of carbon nanotubes a few mechanisms can explain the important conductance changes observed experimentally upon exposure to certain chemical stimuli. In metallic nanotubes, adsorbing molecules can act as scattering centers that may induce localization and open a conductance gap at the Fermi level. With semiconducting tubes things are slightly more complex. Apart increased scattering, the adsorbed molecules can exchange charge with the nanotubes shifting the Fermi level of the system and accordingly leading to conductance modifications. Adsorbed molecules may also modify transport in CNT FETs by lowering the Schottky barriers and thus facilitating electron tunneling from the leads to the conduction channel.

In the following sections we develop a model that would enable us to study the adsorption-caused conductance modification of carbon nanotubes in the ballistic regime. As a case study we have chosen four aromatic amino acids that can bind through π stacking on a carbon nanotube's wall. For these particular molecules no experimental measurement has been performed to our knowledge and thus our calculations would have a predictive value.

2. Avoiding intractable calculations

As the goal of this chapter is to calculate the conductance shift in SWNT sensors upon adsorption of aromatic amino acids, we review some of the challenges such a task would involve. Although we assume ballistic transport in a non-interacting electrons picture and ignore phonons altogether, computing the conductance of such a device is very demanding because of the large number of atoms involved.

In **Chapter III** we showed that within the Landauer-Büttiker formalism highly efficient methods can be devised for obtaining the transmission functions in carbon nanotube crosses. Nevertheless, there, we employed a simple π band description which is a minimal basis set, adequate to describe those systems. Here the same basis is far from sufficient, as delicate charge transfer and orbital re-hybridization can occur during molecular adsorption on carbon nanotubes.

Even the most efficient conductance calculation algorithm would scale as the third power in the mean number of atomic orbitals per atom *M*. Although linear-scaling in the number of atoms *N* may be achieved, the size of the underlying basis set always imposes a pre-factor that in our experience cannot scale better than M^3. As realistic CNT sensors would have at least 10^4 atoms it becomes clear that reducing the basis size is actually a necessity. We will prove later that this basis reduction can be achieved as long as one desires to preserve only a part of the spectral properties of the Hamiltonian.

A second time-saving solution is in close relationship with the portability of the Hamiltonian model. In theory one always studies the influence of parameters like nanotube radius and chirality either for gaining insight or for proving the versatility of the concept. This is an extremely time-consuming process especially for self-consistent, accurate calculations. It is also a redundant process, if the tube's radius is large enough, as in this case the Hamiltonian matrix elements can be approximated with those of graphene.

In the light of the above discussions we propose a general workflow for studying CNT-based conductance sensors (although not restricted to CNTs or chemical sensors) which consists of the following steps:

1. Self-consistent *ab initio* electronic structure of the target molecule on graphene.
2. Hamiltonian model order reduction conserving the spectrum around the Fermi level.
3. Hamiltonian parameter transfer to the CNT sensor and transport calculations.

These steps will be detailed in exactly this order in the following three sections. The methods developed are applied to a case-study in which the targeted molecules are the four aromatic amino-acids HIS, PHE, TRP and TYR.

3. Ab initio electronic structure of reference adsystems

3.1. Molecular mechanics relaxation of molecules on graphene

The first step and one of the most difficult parts in simulating from first-principles the kind of systems considered here is relaxing the atomic coordinates under weak π-π interactions. In fact this represents an active research area and even a benchmark for

ab initio electronic structure methods. [**128**, **129**, **130**, **131**] For instance, mean field theories like Hartree-Fock (HF) and Density Functional Theory (DFT) were found to have difficulties in predicting binding energies for systems where the binding mechanism involves weak dispersion forces. In this situation improvements can be obtained either through wave function correlation methods like Moller-Plesset or Coupled Cluster [**129**, **131**] or through DFT plus van der Waals corrections. [**132**] Nevertheless they all involve a significant computational effort, to which adds complications associated with the basis set superposition error (BSSE) [**133**] inherent to finite basis set calculations.

In **Reference 128** binding energies as obtained by simple Molecular Mechanics (MM) calculations were compared to *ab initio* results for different π-stacking systems. Among other conclusions was that properly fitted MM force-field parameters reasonably reproduce molecular geometries and binding energies. In this light we have opted for the classical force-field CHARMM as implemented in NAMD [**99**] along with MacKerell's [**100**] set of amino acid parameters for the task of relaxing the molecular structures. The van der Waals parameters for graphitic carbon were taken from benzene. Another reason for choosing this oversimplified model was that we plan to compute the transport properties of nanotubes wrapped by small peptides containing aromatic amino acids for which an *ab initio* relaxation is at present intractable. In fact *ab initio* relaxation is already difficult for small, asymmetric molecules like amino acids because of the large number of degrees of freedom which during relaxation increases considerably the configuration space.

Titration curves reveal that at normal pH the selected amino acids are zwitterions having an α-carboxyl (COO^-) and α-amino (NH_3^+) charged groups. Although neutrally charged, zwitterions present an important dipole that could play an important role in the molecular configuration when the adsystem will be subjected to an external electric field like the one created by the leads of a nanotube conductance sensor. In this thesis we have ignored these effects together with issues related to self-assembly of amino acids at high surface densities.

Each amino acid was then individually placed on top of a large graphene layer and relaxed in NAMD. The graphene atoms were hold fixed to their ideal honeycomb positions during the conjugate gradient minimization with a carbon-carbon distance of

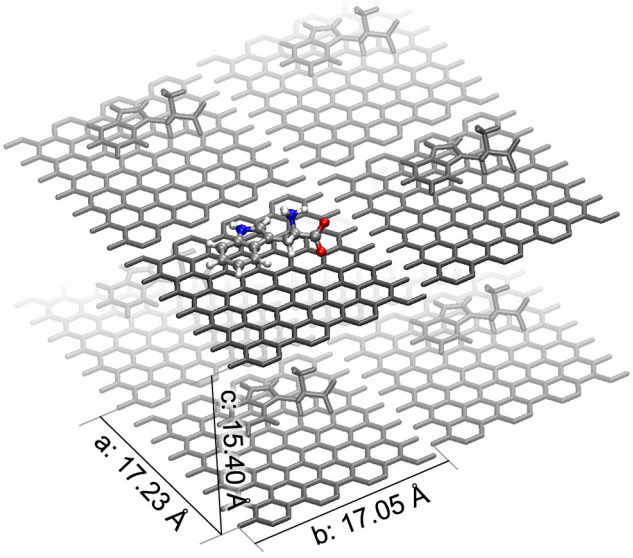

Figure V.1. Tryptophan on graphene orthorhombic unit cell (the same for all the other three adsystems) together with a few periodic images in dim gray and the common lattice vectors **a**, **b** and **c**.

1.43Å. The obtained geometries can be seen in **Figure V.5**. Except for Tryptophan which has two aromatic rings and who relaxed into a "stack" configuration all the other three amino acids relaxed into "bridge" configurations. This together with a mean ring-graphene distance of approximately 3.3Å confirms the validity of the MM relaxation method for obtaining molecular geometries, at least for weakly interacting systems.

Following relaxation, a common orthorhombic unit cell for all four adsystems was found, that simultaneously accommodates the largest of them all, namely Tryptophan on graphene, and avoids undesirable self-interactions. This unit cell and the common lattice vectors are illustrated in **Figure V.1**. The next subsection will focus on the electronic properties of these four adsystems.

3.2. Ab initio electronic structure

For each adsystem consisting in one aromatic amino acid onto a graphene layer, *ab initio* self-consistent calculations were performed with SIESTA [**102**] a highly efficient DFT code involving pseudopotentials and localized pseudo atomic orbitals (PAOs) for valence-only calculations. The maximal cutoff radius of the double-ζ PAO

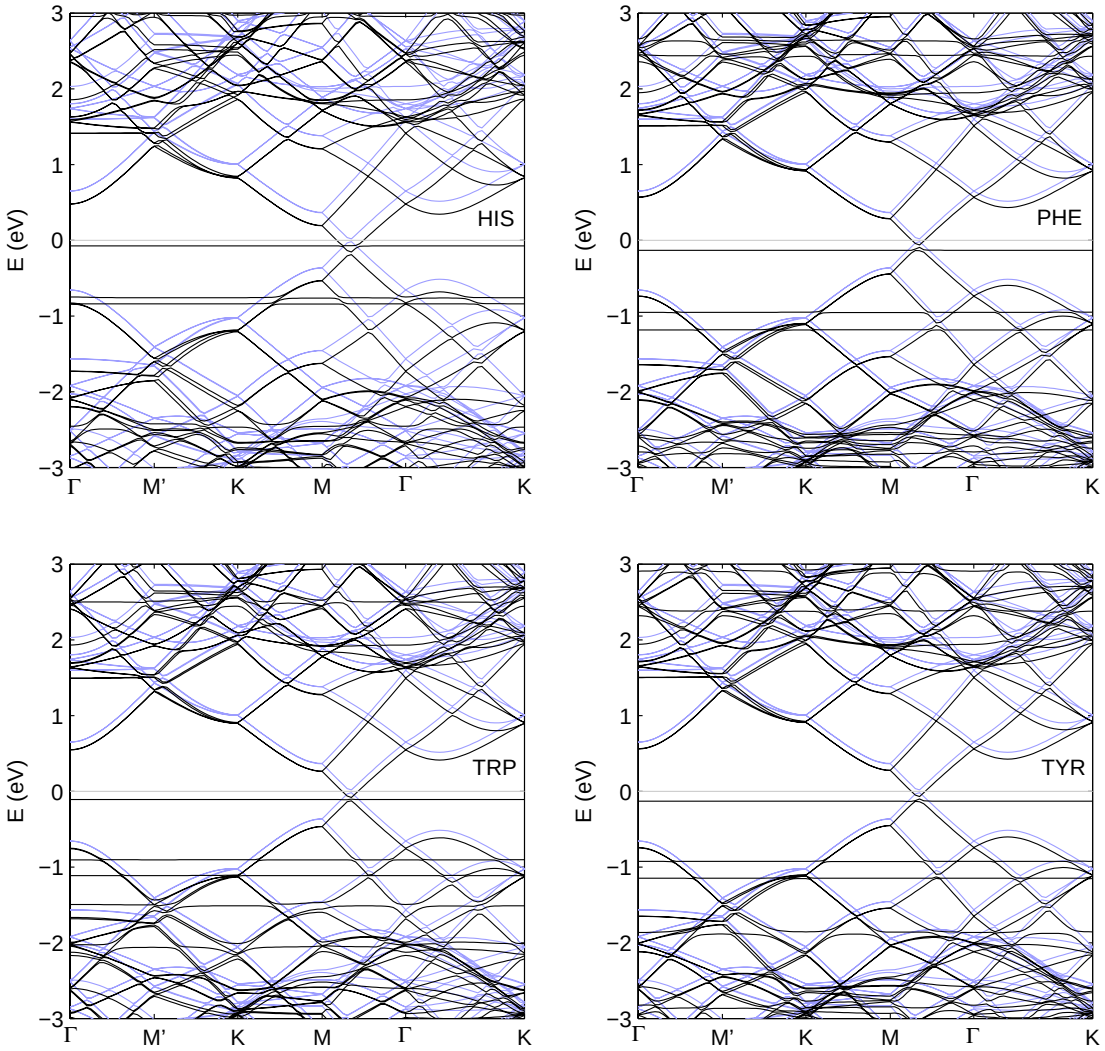

Figure V.2. Band structures of the four adsystems plotted on top of the bands of pristine graphene (light blue). The Fermi level was shifted to zero.

basis was set to 2.84Å in order to capture third nearest-neighbor interactions within the graphene layer.

As our systems are slabs we choose an 8x8x1 Monkhorst-Pack k-grid for sampling the rectangular first Brillouin zone with 32 k-points. The real-space grid corresponded to an equivalent 70Ry plane-wave cutoff. Pristine graphene and isolated amino acids were simulated as well, within the same unit cell, in order to obtain reference data for latter comparisons.

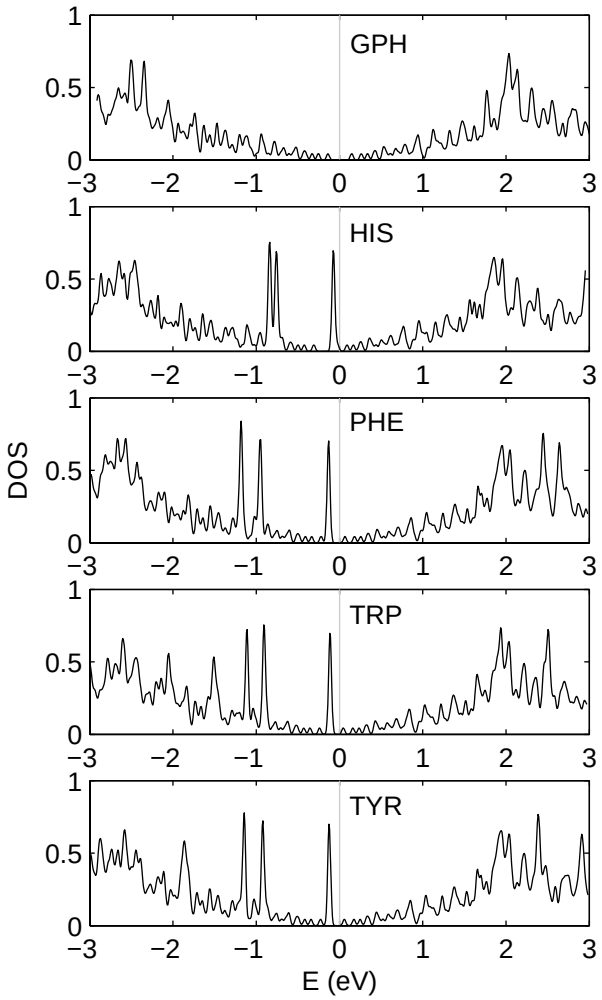

Figure V.3. Total density of states for pristine graphene and the four adsystems emphasizing the amino acid-dependent spectral peaks close to the Fermi level (here set to zero).

The band structures as obtained with SIESTA are presented in **Figure V.2**, in which pristine graphene bands are plotted in light blue together with each one of the four adsystem bands. In all spectra of this chapter, the Fermi level was shifted to zero. The physisorption causes an approximately 150meV Fermi level up-shift. Dispersionless bands close to E_F are clearly visible in each case, while their spectral positions depend on the type of amino acid. These individualized signatures could prove extremely useful in the context of amino acid identification by nanotube conductance sensors, which are known for their high sensitivity but relatively poor specificity.

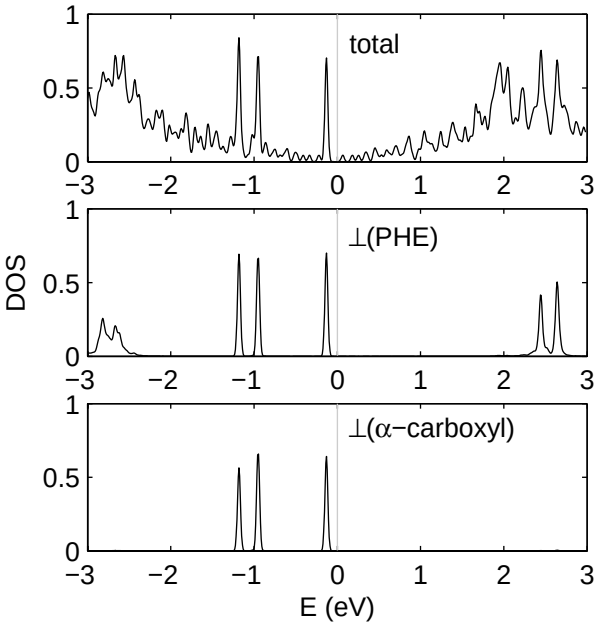

Figure V.4. Total density of states for the Phenylalanine on graphene system (top) and projected density of states (PDOS) onto amino acid orbitals (middle) and α-carboxyl group orbitals (bottom). The peaks far from the Fermi level (middle PDOS) populate mainly the aromatic ring's orbitals.

Total density of states as displayed in **Figure V.3** emphasizes the amino acid-dependent states induced close to the Fermi level by physisorption. These states are found to populate the α-carboxyl group orbitals of the amino acids as can be observed from the projected density of states series in **Figure V.4**. Interestingly the aromatic ring orbitals of each amino acid are populated significantly only by states found 3eV away from the Fermi level and cannot, at least in theory, influence the intrinsic conductance of a carbon nanotube. Unpublished benzene on graphene calculations within the same setting confirmed this observation and was found to be in perfect agreement with studies performed by other groups. [**135**, **136**] Hence, it can be concluded that although responsible for the binding mechanism, it is not the aromatic rings of the amino acids that could change a nanotube's conductance but rather the carboxyl or amino ions.

As expected the dispersionless bands correspond to states localized in real-space in the proximity of the α-carboxyl group. Mulliken charges as computed by SIESTA

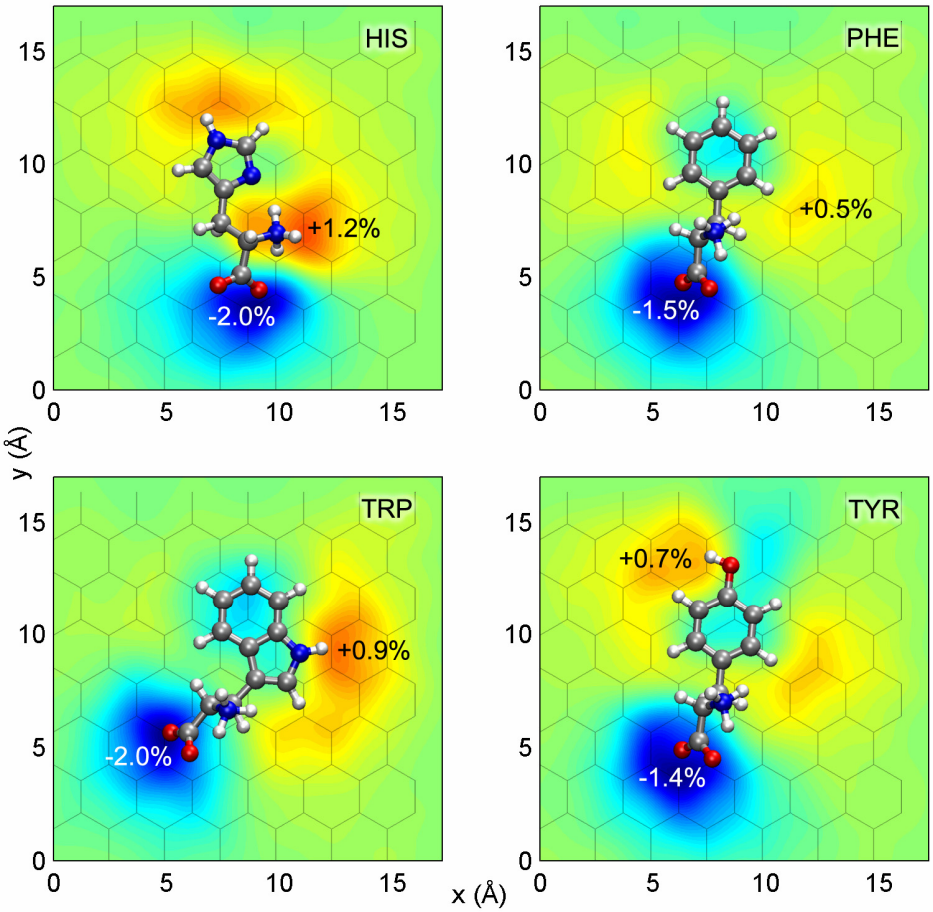

Figure V.5. Mulliken charge transfer from/to $2p_z$ orbitals of graphene. The figure also shows the underlying graphene lattice as an indication of the stacking configuration of the amino acids.

were used to study the possible charge transfer. Graphene charges from the adsystem were subtracted for each amino acid from pristine graphene charges and then convoluted by a real-space Gaussian kernel of 2.85Å effective cutoff to obtain **Figure V.5**. As known Mulliken charges are strongly dependent on the basis set. Moreover in our calculations, since we avoided the relaxation at the *ab initio* level and dropped the counterpoise correction the charge analysis might further suffer from BSSE. Nevertheless the maps presented in **Figure V.5** can be accepted qualitatively as they correlate well with the expected amino acid charges. The magnitude of the transferred charges situates our case in the physisorption regime.

As can be observed screening of the ionic charges inside graphene is strongly localized. This enables us to transfer the Hamiltonian and overlap matrix elements

from these small reference systems to a carbon nanotube conductance sensor that would have a considerable number of atoms, and avoid intractable self-consistent calculations.

The charge is mostly transferred from/to the $2p_z$ orbitals with values of up to 2%. With the other orbitals the charge transfer is typically 5 times lower. The Fermi level shift together with the charge transfer from the $2p_z$ orbitals and the localized states close to E_F are mechanisms that can result in important conductance changes. This supports our suggestion that carbon nanotubes might be suitable for aromatic amino acid detection.

4. Hamiltonian model order reduction

4.1. Why reduce the order of the Hamiltonian?

To be practical for electronic transport calculations, the Hamiltonian and overlap matrices computed self-consistently with SIESTA [**102**] as detailed in **Section 3**, should somehow be adapted to exploit as much as possible the particularities of the transport theory. This section focuses on these issues and introduces a solution that consists in projecting the problem in a reduced subspace followed by infinitesimal congruence transformations or isospectral flows, as introduced in **Chapter IV**, in order to correct the spectrum around the Fermi level. This algorithm is then applied to the four adsystems consisting of aromatic amino acids onto graphene which will result in a highly optimal Hamiltonian model for transport calculations.

Accurate results of *ab initio* self-consistent calculations require a large basis set. In our case a relatively modest double-ζ PAO basis in SIESTA for valence-only calculations involved a mean of about 10 orbitals per atom. For example the Tryptophan on graphene system had 139 atoms and 1040 PAO basis elements. Computing the conductance of a realistic nanotube sensor containing at least 10^4-10^5 atoms by simply transferring the matrix elements from the reference adsystem would therefore be extremely difficult.

Elastic transport in nanostructures is determined by the spectral properties close to the Fermi level as it will be shown in the next subsection. This means that only a few Hamiltonian eigenvectors with corresponding eigenvalues falling inside a certain

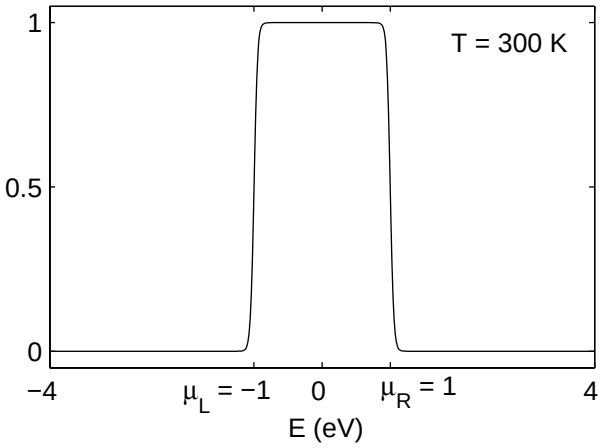

Figure V.6. A typical Fermi-Dirac energy window at 2eV biasing and room temperature.

energy interval centered at E_F contribute to the ensemble average of the current operator. Fortunately in many situations of practical interest, this set of eigenvectors project notably only onto a subset of the PAO basis, like it happens for instance with carbon nanotube π bands. In this case the Hamiltonian and overlap matrices can simply be projected onto a reduced Hilbert subspace where the computations are sped-up by up to a few orders of magnitude with just a minor loss in accuracy.

The same considerations are at the basis of the π-band tight-binding (TB) model widely employed in predicting the electronic structure, transport and optical properties of carbon nanotubes [**104**, **137**, **138**, **139**], which we have also employed in **Chapter I** and **Chapter III**. This model has, after shifting E_F to zero and assuming an orthogonal basis, a single parameter $t_0 \equiv -\gamma_0$ that represents the hopping integral between nearest neighbor atoms. Later, Latil et *al.* have extended this model to adsorption on or atom substitution in carbon nanotubes by modifying the on site energies and hopping integrals so as to reproduce correctly the band structure or density of states around the Fermi level [**108**].

It should be noted however that tight-binding parameterization is a delicate problem as it typically involves iterative matrix diagonalizations within some minimization algorithm. It is our belief that this method would work poorly for low symmetry systems that have a large number of parameters and might even freeze at a local minimum yielding unphysical solutions. Moreover as eigenvalue derivatives with respect to a matrix element cannot be analytically determined for the general case, the

optimization must rely on function evaluations-only or genetic algorithms and is as thus extremely slow or even uncontrollable.

Our approach has another philosophy. We start from the *ab initio* self-consistent Hamiltonian and overlap matrix and produce via proper transformations a reduced-order effective pair that has a correct spectrum around the Fermi level. Basically it consists in an elimination of PAOs based on the projected density of states followed by an appropriate isospectral matrix flow to recover the sparsity pattern and correct the spectrum.

4.2. Spectral bandwidth of the current operator

The theory of Hamiltonian model order reduction starts from the particle current expectation value in the Landauer-Büttiker formalism. We choose Todorov's transmission formula (**II.19**) instead of Fischer-Lee formula (**II.17.b**) as it simplifies some of the manipulations. As we are interested in the drain-source transmission and the gate is accounted for only via the rigid shift it introduces in the Fermi level, $\alpha,\alpha' = L,R$, and the trace in (**II.19**) writes

$$\mathrm{Tr}\left[\hat{\mathbf{\rho}}_L(E)\hat{\mathbf{t}}_{LR}(E)\hat{\mathbf{\rho}}_R(E)\hat{\mathbf{t}}_{LR}(E)^{\dagger}\right]$$

where $\hat{\mathbf{\rho}}_{L(R)}$ represents the density of states projected onto the free lead states. The trance runs over the lead's orbitals $\{|\nu\rangle\}$ as pointed out in **Chapter II**.

Now, we transform the trace from the $\{|\nu\rangle\}$ basis to the $\{|\psi_n\rangle\}$ basis formed by the eigenvalues of the free Hamiltonian $\hat{H}_0$ (see **Equation** (**II.7**)) obtained by solving Schrödinger's equation $\hat{H}_0|\psi_n\rangle = \varepsilon_n|\psi_n\rangle$. In this basis the projected density of states is diagonal having the matrix elements

$$\rho_{L(R),nm}(E) = \langle\psi_n|\hat{\rho}(E)\hat{P}_{L(R)}|\psi_m\rangle = \langle\psi_n|\delta(E\hat{I}-\hat{H}_0)\delta_{mL(R)}|\psi_m\rangle = \delta(E-\varepsilon_n)\delta_{nm}\delta_{mL(R)}$$

Inserting the above in the current expectation value given by **Equation** (**II.17.a**) results in (ignoring the pre-factor)

$$I \propto \int_{-\infty}^{+\infty} dE\left[f(E-\mu_R)-f(E-\mu_L)\right]\sum_{n\in L,m\in R}\rho_{L,nn}(E)t_{nm}(E)\rho_{R,mm}(E)t_{nm}(E)^{\dagger} \qquad \textbf{(V.1)}$$

Examining this formula it is not too difficult to observe that contributions to the current average coming from those eigenstates that correspond to eigenenergies ε_n falling outside $[\mu_L, \mu_R]$ are canceled by the term $f(E-\mu_R)-f(E-\mu_L)$ represented in **Figure V.6** for a biasing of ±1eV at room temperature. This allows one to drop the corresponding summation indices *n* and *m* in **Eq. (IV.1)**.

The subset of eigenstates $\{|\psi_n\rangle\}$ respecting the above condition is now projected back onto the PAO basis, with the help of the expansion coefficients $c_n^\nu = \langle \nu | \psi_n \rangle$. Fortunately in many practical situations most of these coefficients are zero. This means that the current expectation value can be computed directly into a Hilbert subspace spanned by the PAO subset.

$$\left\{ |\nu\rangle \,\middle|\, \langle \psi_n | \nu \rangle \neq 0,\ \hat{H}_0 |\psi_n\rangle = \varepsilon_n |\psi_n\rangle,\ \varepsilon_n \in [\mu_L, \mu_R] \right\} \qquad \textbf{(V.2)}$$

Computing expectation values in this Hilbert subspace is extremely efficient. In particular this is exactly the goal of the method to be detailed in the remainder of this section that offers a formal framework for finding a minimal Hilbert subspace in which the current expectation value can be computed with controlled numerical accuracy.

4.3. Subspace projection methods

The first step in the model reduction algorithm is deciding which PAOs will be projected out in view of obtaining a reduced Hilbert subspace. We remind the reader at this point that we apply the subspace projection for the reference adsystems and not for a carbon nanotube two-terminal device. This is based on the assumption that the set of orbitals in an adsystem not being populated by eigenvectors inside the energy interval $[\mu_L, \mu_R]$ will also not be populated in a carbon nanotube, in the same energy interval. If the tube curvature is not too high this assumption is indeed valid.

It is not difficult to see that the set defined in **(V.2)** is informationally contained in the orbital projected density of states (PDOS) defined as

$$\rho_\nu(E) = \frac{1}{N_k} \int_{BZ} \mathbf{dk} \sum_{n,\mu} \mathrm{Re}\left[\langle \chi_n(\mathbf{k}) | \tilde{\mu} \rangle \mathbf{S}_{\mu\nu}(\mathbf{k}) \langle \tilde{\nu} | \chi_n(\mathbf{k}) \rangle \right] \delta(E - \varepsilon_n(\mathbf{k})) \qquad \textbf{(V.3)}$$

where the basis non-orthogonality and periodicity of the adsystems has been taken into account. The integration in the k-space is done in the first Brillouin zone, and $\mathbf{S}_{\mu\nu}$ represents the overlap matrix, $|\tilde{\mu}\rangle$ are the dual PAOs satisfying $\langle\nu|\tilde{\mu}\rangle = \delta_{\nu\mu}$, and $|\chi_n(\mathbf{k})\rangle$ are Bloch states of corresponding dispersion relations $\varepsilon_n(\mathbf{k})$.

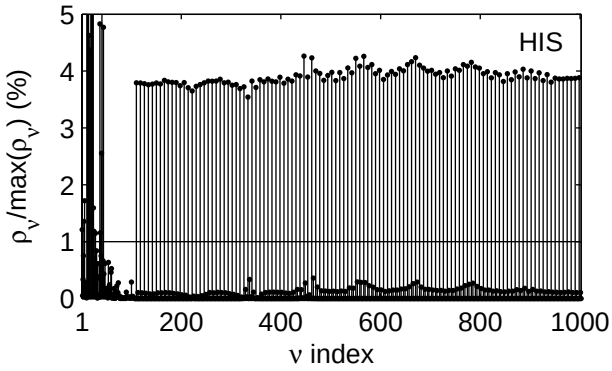

Figure V.7. Energy filtered projected density of states for the Histidine on graphene system. The black horizontal line at 1% represents the cutoff threshold.

We used the PDOS given by SIESTA in deciding which PAOs to eliminate from the basis. Each $\rho_\nu(E)$ is first multiplied by the Fermi-Dirac energy window function $f(E-\mu_R)-f(E-\mu_L)$ and then integrated over all energies to obtain the numbers

$$\rho_\nu = \int dE \rho_\nu(E)\left[f(E-\mu_R)-f(E-\mu_L)\right] \qquad \textbf{(V.4)}$$

The basis set of the reduced Hilbert space is then taken to be $\left\{|\nu\rangle \,\middle|\, |\rho_\nu| > \varepsilon_\rho\right\}$. In simple words only those PAOs for which the energy filtered PDOS ρ_ν was greater then a given threshold ε_ρ were retained. For instance, setting $\mu_{L(R)}$ to ±1eV and ε_ρ to 1% of the maximum $\max\left(|\rho_\nu|\right)$, reduced the number of orbitals for the Histidine on graphene adsystem from 1002 to 141, which is very close to 134 that represents the total number of atoms. **Figure V.7** shows ρ_ν for the aforementioned adsystem.

The PDOS-based subspace projection method would be numerically exact, in the sense of error-free estimation of the current's expectation value, if a zero $\varepsilon_\rho \equiv 0$ threshold would be used. A larger threshold value would result in a lower order projected Hilbert space but it would also result in a higher numerical error. As such the threshold is to be perceived as a tradeoff between accuracy and efficiency.

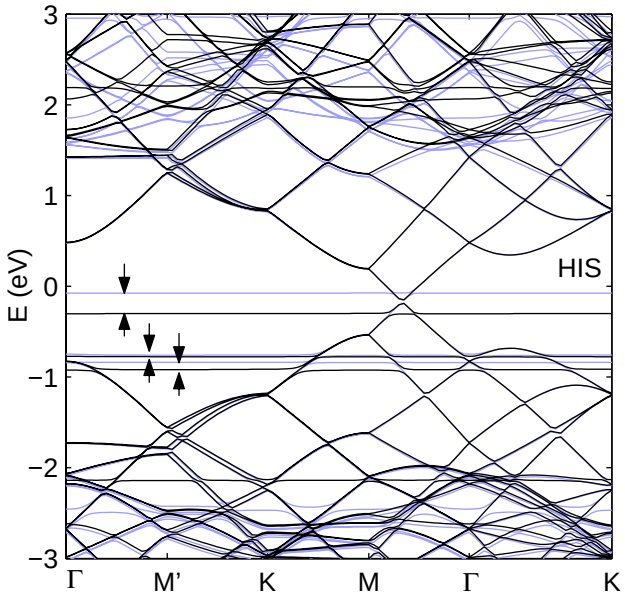

Figure V.8. Band structure as obtained after PAO elimination (subspace projection). Pairs of arrows indicate the errors produced by basis truncation.

In some situations computing the PDOS can be avoided if the chemistry of the system under study is known. For pristine graphene we found that the $2p_z$ orbitals should be retained, a result that could have been predicted from the large body of *ab initio* studies on graphitic systems. Nevertheless for exotic or strongly perturbed adsystems the projected density of states has to be calculated as hybridization can become important promoting new bands close to the Fermi level. This is however not a bottleneck as highly-efficient methods for computing the PDOS based on Haydock's recursion method are readily available [**140**].

4.4. Spectrum correction

After eliminating PAOs with the PDOS elimination procedure described in the previous subsection we have recalculated the band structure with the projected Hamiltonian and overlap matrices. Graphitic bands, i.e. bands associated with eigenvectors that populate mainly orbitals in graphene, are indeed properly conserved around the Fermi level after the elimination. Nevertheless the flat dispersionless bands, which we have attributed earlier to localized states, get shifted by a few tens of meV in a non-predictable fashion. The bands of the initial Hamiltonian together with those of the projected one are plotted in **Figure V.8**. The abovementioned band shifts

are emphasized in this figure by arrows. Most probably at the origin of these errors are large condition numbers of the generalized matrix pencil $(\mathbf{H},\mathbf{S})$ that we have not taken into account when eliminating basis orbitals.

Correcting the basis truncation errors can be achieved simply by diagonalizing the projected pencil $(\mathbf{H}_\perp,\mathbf{S}_\perp)$, at the Γ point for instance, and replacing its eigenvalues with the exact ones taken from the initial $(\mathbf{H},\mathbf{S})$ pencil. Using the matrix notation one can write the Schrödinger equation for the $(\mathbf{H}_\perp,\mathbf{S}_\perp)$ pair

$$\mathbf{H}_\perp\boldsymbol{\psi}_\perp = \mathbf{S}_\perp\boldsymbol{\psi}_\perp\boldsymbol{\varepsilon}_\perp \qquad \textbf{(V.5)}$$

and similarly for $(\mathbf{H},\mathbf{S})$, where $\boldsymbol{\psi}_\perp$ and $\boldsymbol{\varepsilon}_\perp$ are two matrices, the first containing the eigenvectors as its columns and the second is a diagonal matrix containing the eigenvalues. Mathematically $\boldsymbol{\psi}_\perp$ is a congruence transformation that simultaneously diagonalizes $\mathbf{H}$ and $\mathbf{S}$, i.e. $\boldsymbol{\psi}_\perp^{\mathrm{T}}\mathbf{H}_\perp\boldsymbol{\psi}_\perp = \boldsymbol{\varepsilon}_\perp$ and $\boldsymbol{\psi}_\perp^{\mathrm{T}}\mathbf{S}_\perp\boldsymbol{\psi}_\perp = \mathbf{I}$. Now, we replace the shifted eigenvalues inside $[\mu_L,\mu_R]$ with the correct ones

$$\tilde{\varepsilon}_\perp = \begin{cases}\varepsilon, \varepsilon_\perp \in [\mu_L,\mu_R] \\ \varepsilon_\perp, \text{otherwise}\end{cases}$$

and with the help of $\boldsymbol{\psi}_\perp^{-1}$ we can derive a new, renormalized Hamiltonian $\tilde{\mathbf{H}}_\perp = \boldsymbol{\psi}_\perp^{-\mathrm{T}}\tilde{\boldsymbol{\varepsilon}}_\perp\boldsymbol{\psi}_\perp^{-1}$. The overlap matrix is unaffected by this process. The only problem is that the newly found Hamiltonian $\tilde{\mathbf{H}}_\perp$ loses its sparsity. In the following we show that via an isospectral flow the sparsity can be recovered yielding thus a sparse pencil that has a correct spectrum around the Fermi level.

4.5. Sparsity recovering via isospectral flows

As stated earlier, the goal of the model reduction method is to project out as many PAOs as possible while minimizing the errors coming from basis truncation. In this subsection we use the mathematical apparatus introduced in **Chapter IV** to recover the sparsity pattern that was lost through the spectral correction applied in the previous subsection.

Setting up a generalized isospectral flow involves in a first place identifying the parameters of the two principal manifolds, namely $\mathcal{M}$ and $\mathcal{V}$ as labeled in the previous chapter. In our case the isospectral set $\mathcal{M}$ is build around $(\tilde{\mathbf{H}}_\perp,\mathbf{S}_\perp)$. With

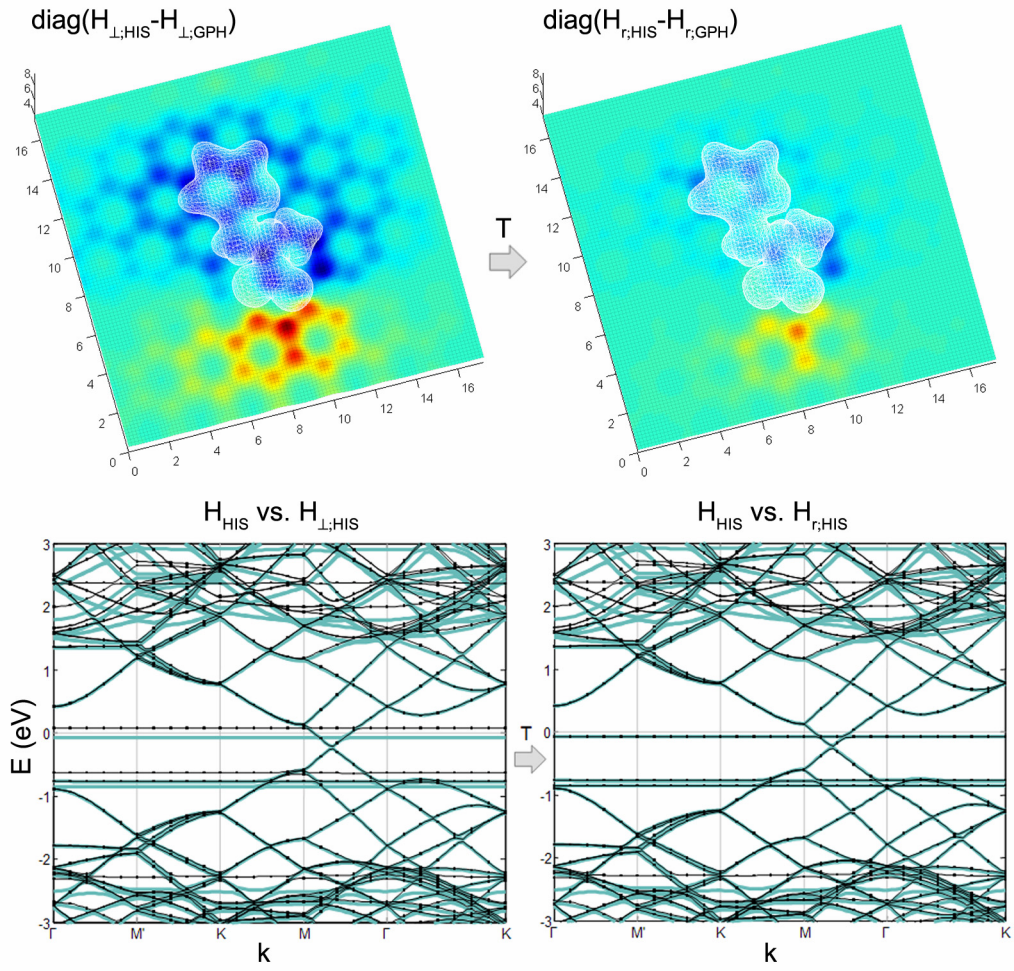

Figure V.9. (top) Graphene Hamiltonian perturbation before (left) and after (right) the isospectral renormalizing flow. (bottom) Band structures before (left) and after (right) the isospectral renormalizing flow. In cyan are the bands of the initial full-size Hamiltonian, and in black those of the projected and renormalized one.

respect to notations used in **Chapter IV**, we identify $(\mathbf{A},\mathbf{B}) \equiv (\tilde{\mathbf{H}}_{\perp},\mathbf{S}_{\perp})$. The affine subspace we consider here has a trivial structure involving only the two constant matrices $\mathbf{P}^{0}_{1(2)}$ inside the projection operator defined by **Equation (IV.17)**. For our purpose we define these two matrices as $(\mathbf{P}^{0}_{1},\mathbf{P}^{0}_{2}) \equiv (\mathbf{H}_{\perp},\mathbf{S}_{\perp})$. The last parameters required are the two weights $(\mathbf{U},\mathbf{V})$ appearing in the definition of the goal function $F(\mathbf{T})$ in **(IV.19)** which is discussed below.

The first choice for $(\mathbf{U},\mathbf{V})$ would be $(\mathbf{I}_{\circ},\mathbf{I}_{\circ})$ where $\mathbf{I}_{\circ}$ is the neutral element with respect to the Hadamard product and is simply a matrix having all the entries equal to

one. Nevertheless we exploit the flexibility of this framework and choose $(\mathbf{U},\mathbf{V})$ differently to achieve another subtle feature. For $\mathbf{V}$ we simply take $\mathbf{I}_\circ$, as we wish to conserve the overlap matrix. **Figure V.9** (top-left) shows the Hamiltonian's diagonal difference between the HIS+GPH adsystem and the pristine GPH. As can be observed the on-site energy perturbation extends almost throughout the unit cell and this might pose a problem when exporting the Hamiltonian matrix elements to a carbon nanotube sensor. Accordingly we can choose $\mathbf{U}$ so as to confine this perturbation closer to the adsorbed molecule. Thus for $\mathbf{U}$ we take $\mathbf{I}_\circ$ and cancel those matrix elements onto which we wish to localize the perturbation. Simultaneously for the adsystem we have modified the $\mathbf{P}_1^0$ matrix by replacing the Hamiltonian sub-matrix corresponding to graphene orbitals with the projected Hamiltonian of pristine graphene $\mathbf{H}_{\perp;\mathrm{GPH}}$.

We now argue the choices made above. First, choosing $\mathcal{M}(\tilde{\mathbf{H}}_\perp,\mathbf{S}_\perp)$ as the isospectral set guarantees that the spectrum, we have corrected in the previous subsection, is conserved. Second, specifying the affine set via $\mathbf{P}_{1(2)}^0$ in the way described above, forces the isospectral flow towards matrices that are as close as possible to $(\mathbf{H}_\perp,\mathbf{S}_\perp)$ which we know to be sparse. Those entries set to 0 in $\mathbf{U}$, which correspond to sites very close to the adsorbed amino acid, do not contribute to the overall goal function's value and thus are free to vary as much as necessary. Because we overwrote a part of $\mathbf{P}_1^0$ with the pristine graphene's Hamiltonian $\mathbf{H}_{\perp;\mathrm{GPH}}$, the flow will be attracted towards a final Hamiltonian that is close to $\mathbf{H}_{\perp;\mathrm{GPH}}$ except for the zero sites in $\mathbf{U}$ where it may differ radically. Re-scaling of the perturbation can in this way be achieved.

Having identified all the ingredients, we set the initial condition $\mathbf{T}=\mathbf{I}$ and integrate with an ODE solver the steepest descent flow $\mathrm{d}_t\,\mathbf{T}=-\nabla F(\mathbf{T})$, where the gradient is computed with the help of (**IV.24**). Because of the trivial form of the projection operators $\mathcal{P}_{1(2)}$ one obtains a simplified gradient formula

$$\nabla \mathrm{F}(\mathbf{T})=2\tilde{\mathbf{H}}_\perp\mathbf{T}\left[\mathbf{U}\circ\mathbf{U}\circ\left(\mathbf{X}-\mathbf{P}_1^0\right)\right]+2\mathbf{S}_\perp\mathbf{T}\left[\mathbf{Y}-\mathbf{P}_2^0\right]$$

where we have used the shorthand notation $(\mathbf{X},\mathbf{Y})=(\mathbf{T}^{\mathrm{T}}\tilde{\mathbf{H}}_\perp\mathbf{T},\mathbf{T}^{\mathrm{T}}\mathbf{S}_\perp\mathbf{T})$ and the fact that $\mathbf{V}\equiv\mathbf{I}_\circ$. The solution to our problem is considered to be obtained when the norm of the gradient falls bellow a certain threshold. Denoting $\mathbf{T}_\infty$ as the limit of the flow, the searched solution is simply $(\mathbf{H}_r,\mathbf{S}_r)=(\mathbf{T}_\infty^{\mathrm{T}}\tilde{\mathbf{H}}_\perp\mathbf{T}_\infty,\mathbf{T}_\infty^{\mathrm{T}}\mathbf{S}_\perp\mathbf{T}_\infty)$. The band structure

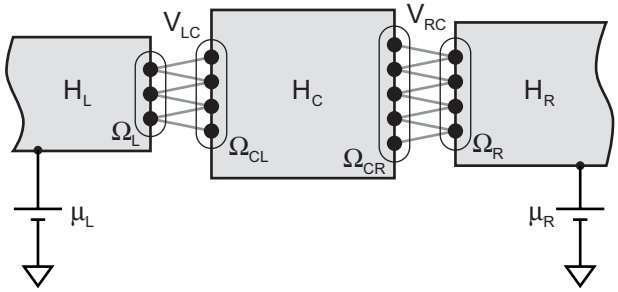

Figure V.10. Generic two terminal device emphasizing boundary atoms between the leads and the central region.

we have calculated with $(\mathbf{H}_r,\mathbf{S}_r)$ is displayed at the right of the bands of the projected pencil $(\mathbf{H}_\perp,\mathbf{S}_\perp)$ in **Figure V.9** (bottom). Remarkably apart the perfect reproduction of the band structure of $(\mathbf{H},\mathbf{S})$ within $[\mu_L,\mu_R]$ one can also see the successful perturbation scaling in **Figure V.9** (top). The resulted pencil $(\mathbf{H}_r,\mathbf{S}_r)$ is as expected also very sparse and the interactions are practically limited to the third nearest neighbor, which allows the implementation of a very efficient quantum conductance calculation scheme which we describe in the next section.

5. Elastic transport calculations

5.1. Efficient real-space partitioning scheme

Even with the reduced Hamiltonian and overlap matrices obtained in the previous section the calculation of the quantum conductance in the ballistic regime is still very demanding due to the large number of atoms involved. A realistic conductance sensor would have thousands to tens of thousands of atoms. Inverting a matrix having this number of rows and columns (e.g. computing Green's functions) requires $\mathcal{O}(N^3)$ operations that could approach the billion flops limit. As this operation would have to be repeated hundreds of times for each energy inside a certain interval, it is clear that other methods have to be set in place to compute the conductance.

In **Chapter III** we have detailed a procedure for computing the multi-terminal conductance of a carbon nanotube cross junction. The efficient method for computing the conductance involved there partitioning the tubes up to the junction, propagating self-energies and inverting only a small matrix to obtain the required Green's functions. In this section we deal only with two terminal devices for which we have

developed a very similar and efficient method for computing the necessary Green's functions.

Referring to **Figure V.10**, where a generic two terminal device is illustrated, using a PAO basis set $\{|\nu\rangle\}$, like the one provided by SIESTA, one can partitioned the Hamiltonian and overlap matrices in the form

$$\mathbf{H}=\begin{pmatrix}\mathbf{H}_L & & \mathbf{H}_{LC}\\ & \mathbf{H}_R & \mathbf{H}_{RC}\\ \mathbf{H}_{LC}^{\dagger} & \mathbf{H}_{RC}^{\dagger} & \mathbf{H}_C\end{pmatrix};\ \mathbf{S}=\begin{pmatrix}\mathbf{S}_L & & \mathbf{S}_{LC}\\ & \mathbf{S}_R & \mathbf{S}_{RC}\\ \mathbf{S}_{LC}^{\dagger} & \mathbf{S}_{RC}^{\dagger} & \mathbf{S}_C\end{pmatrix} \qquad \textbf{(V.6)}$$

from which the Green's function of the central region can easily be obtained as discussed in **Chapter II**,

$$\mathbf{G}_C(z)=\left[z\mathbf{S}_C-\mathbf{H}_C-\boldsymbol{\Sigma}_L(z)-\boldsymbol{\Sigma}_R(z)\right]^{-1} \qquad \textbf{(V.7.a)}$$

$$\boldsymbol{\Sigma}_{L(R)}(z)=\mathbf{K}_{L(R)C}(z)^{\dagger}\mathbf{G}^0_{L(R)}(z)\mathbf{K}_{L(R)C}(z)$$

$$\mathbf{G}^0_{L(R)}(z)\equiv\mathbf{K}_{L(R)}(z)^{-1} \qquad \textbf{(V.7.b)}$$

As usual $\mathbf{K}$ matrices correspond to $\mathbf{K}(z)\equiv z\mathbf{S}-\mathbf{H}=\mathbf{G}(z)^{-1}$. In the Fischer-Lee formula (**II.17**) derived in **Chapter II** the energy dependent conductance is given by

$$\mathcal{G}(E)=\frac{2e^2}{h}\mathcal{T}(E)\equiv\frac{2e^2}{h}\mathrm{Tr}\left[\boldsymbol{\Gamma}_L(E)\mathbf{G}^r_C(E)\boldsymbol{\Gamma}_R(E)\mathbf{G}^a_C(E)\right] \qquad \textbf{(V.8)}$$

The employed retarded and advanced quantities follow the general convention $\mathbf{G}^{r(a)}(E)=\mathbf{G}(z=E\pm i0^+)$. The leads are included as boundary conditions into the central region as usually via the level broadening functions $\boldsymbol{\Gamma}_{L(R)}=i\left[\boldsymbol{\Sigma}^r_{L(R)}-\boldsymbol{\Sigma}^{r\dagger}_{L(R)}\right]$.

Any efficient conductance calculation scheme exploits the sparsity pattern of the matrices involved in (**V.8**) and we show next what we mean by this. As we said at the end of the previous subsection the Hamiltonian matrix obtained via the isospectral flow doesn't contain interactions going beyond the third nearest neighbor. Then from **Figure V.10** it is easy to observe that $\mathbf{V}_{L(R)C}$ has non-zero matrix elements only when linking orbitals found inside the boundary regions $\Omega_{L(R)}$ in the leads and $\Omega_{CL(R)}$ in the central region respectively, i.e.

$$K_{L(R)C;\mu\nu}=\delta_{\mu\Omega_{L(R)}}\delta_{\nu\Omega_{CL(R)}}K_{L(R)C;\mu\nu} \qquad \textbf{(V.9)}$$

In our notation, $K_{L(R)C;\mu\nu} = \langle \mu | \hat{K}_{L(R)C} | \nu \rangle$. Replacing **Equation** (**V.9**) into (**V.7.b**) yields then

$$\Sigma^{r(a)}_{L(R);\mu\mu'}(E) = \sum_{\nu\nu'} K_{L(R)C;\mu\nu}(E)^{\dagger} G^{0;r(a)}_{L(R);\nu\nu'}(E) K_{L(R)C;\nu'\mu'}(E) = \\ = \delta_{\mu\Omega_{CL(R)}} \delta_{\mu'\Omega_{CL(R)}} \sum_{\nu\nu'\in\Omega_{L(R)}} K^{\dagger}_{L(R)C;\mu\nu} g^{0;r(a)}_{L(R);\nu\nu'} K_{L(R)C;\nu'\mu'} \qquad \textbf{(V.10)}$$

which signifies that $\Sigma_{L(R);\mu\mu'}$ will be non-zero only when orbitals $\mu,\mu' \in \Omega_{CL(R)}$. Moreover only $G^0_{L(R);\nu\nu'}$ with $\nu,\nu' \in \Omega_{L(R)}$ need to be calculated which represent exactly the surface Green's functions $g^0_{L(R);\nu\nu'}$ for which an efficient method will be described in the next subsection. Consequently

$$\Gamma_{L(R);\mu\mu'}(E) = \delta_{\mu\Omega_{CL(R)}} \delta_{\mu'\Omega_{CL(R)}} \Gamma_{L(R);\mu\mu'}(E)$$

and **Equation** (**V.8**) reduces to

$$\mathcal{G}(E) = \frac{2e^2}{h} \sum_{\substack{\mu\mu'\in\Omega_{CL} \\ \nu\nu'\in\Omega_{CR}}} \Gamma_{L;\mu\mu'}(E) G^{r}_{C;\mu'\nu'}(E) \Gamma_{R;\nu'\nu}(E) G^{a}_{C;\mu\nu}(E) \qquad \textbf{(V.11)}$$

Summarizing, the conductance of a two terminal device is completely determined by the knowledge of the lead surface Green's functions $g^{0;r}_{L(R);\nu\nu'}(E)$ with $\nu,\nu' \in \Omega_{L(R)}$ and the left-right Green's functions of the central region $G^{r}_{C;\mu\nu}(E)$ with $\mu \in \Omega_{CL}, \nu \in \Omega_{CR}$.

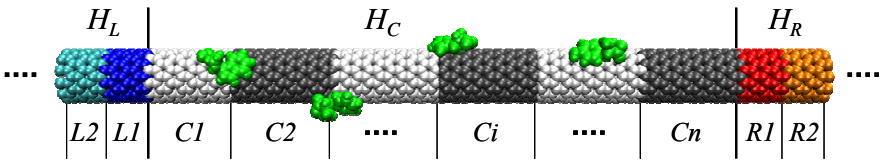

Figure V.11. Hamiltonian of the carbon nanotube toy-sensor and its real-space partitioning.

In this chapter we opted for a simplified toy sensor depicted in **Figure V.11** that has a central region, coupled to two semi-infinite leads made of nanotubes with the same-chirality. This kind of configuration is suitable for computing the intrinsic conductance change due to adsorption and is computationally less demanding than a system including realistic metallic leads. We now concentrate on the calculation of matrix elements involved in (**V.11**).

The surface Green's functions, $g^0_{L(R)}$ will be dealt with in the next subsection. For the transfer Green's functions $G^r_{C;\Omega_{CL}\Omega_{CR}}(E)$ a promising recursion method was recently developed [**134**]. The method involves a two-sided Lanczos process for non-hermitian matrices and consequently its numerical stability must be considered carefully. Moreover a terminator is not as easy to find as it is for the hermitian case.

In this light we opted for an elimination-based method that is exact and also order-N at least for 1D systems like carbon nanotubes are [**104**]. This method exploits the block tridiagonal structure of $\mathbf{H}_C$ and $\mathbf{S}_C$ when partitioned as in **Figure V.11**. This structure reflects also in $\mathbf{K}_C(E) = E\mathbf{S}_C - \mathbf{H}_C - \mathbf{\Sigma}_L(E) - \mathbf{\Sigma}_R(E)$ which thereby assumes also a block tridiagonal form. This is possible only because $\mathbf{\Sigma}_{L(R)}(E)$ only affects the boundary atoms. Henceforth we drop the C index to abbreviate notations and remember that for the remainder of this subsection all matrices refer to the central region and its partitioning, thus

$$\mathbf{K}_C \equiv \mathbf{K} = \begin{bmatrix} \mathbf{K}_{11} & \mathbf{K}_{12} & & \\ \mathbf{K}_{21} & \mathbf{K}_{22} & \ddots & \\ & \ddots & \ddots & \mathbf{K}_{n-1,n} \\ & & \mathbf{K}_{n,n-1} & \mathbf{K}_{n,n} \end{bmatrix}$$

The goal is to compute $\mathbf{G}_{1,n}$ which is the sought left-right transfer Green's function. Using the identity $\mathbf{GK} \equiv \mathbf{I}$ we can identify the sub-block

$$\boldsymbol{\delta}_{1,i} = \sum_j \mathbf{G}_{1,j}\mathbf{K}_{j,i}$$

which because of the tri-diagonal form of $\mathbf{K}$ simplifies to

$$\begin{aligned} \mathbf{I} &= \mathbf{G}_{11}\mathbf{K}_{11} + \mathbf{G}_{12}\mathbf{K}_{21} \\ &\vdots \\ \mathbf{0} &= \mathbf{G}_{1,i-1}\mathbf{K}_{i-1,i} + \mathbf{G}_{1,i}\mathbf{K}_{i,i} + \mathbf{G}_{1,i+1}\mathbf{K}_{i+1,i} \\ &\vdots \\ \mathbf{0} &= \mathbf{G}_{1,n-1}\mathbf{K}_{n-1,n} + \mathbf{G}_{1,n}\mathbf{K}_{n,n} \end{aligned}$$

Finding $\mathbf{G}_{1,n}$ can be achieved at this point by elimination. From the first equation we express $\mathbf{G}_{11}$ function of $\mathbf{G}_{12}$, insert into the second equation and regroup terms. Then we express $\mathbf{G}_{12}$ function of $\mathbf{G}_{13}$, insert into the third equation, regroup terms and so

on, down to the last equation. Labeling at step i the left hand side term with $\mathbf{B}_i$ and the post-factor of $\mathbf{G}_{1,i}$ by $\mathbf{A}_i$ one gets for step i+1

$$\mathbf{A}_{i+1} = \mathbf{K}_{i+1,i+1} - \mathbf{K}_{i+1,i}\mathbf{A}_i^{-1}\mathbf{K}_{i,i+1}$$
$$\mathbf{B}_{i+1} = -\mathbf{B}_i\mathbf{A}_i^{-1}\mathbf{K}_{i,i+1}$$

which can be seen to start from $\mathbf{A}_1 = \mathbf{K}_{11}$ and $\mathbf{B}_1 = \mathbf{I}$. At the last step, the transfer Green's function simply results as being $\mathbf{G}_{1,n} = \mathbf{B}_n\mathbf{A}_n^{-1}$. The steps described so far are assembled in **Algorithm V.1**.

Algorithm V.1. Elimination method for calculation of transfer Green's functions

1. LET $\mathbf{K} = E\mathbf{S}_C - \mathbf{H}_C - \mathbf{\Sigma}_L(E) - \mathbf{\Sigma}_R(E)$, $\mathbf{A}_1 = \mathbf{K}_{11}$, $\mathbf{B}_1 = \mathbf{I}$
2. FOR $i = \overline{2,n}$
   3. $\mathbf{A}_{i+1} = \mathbf{K}_{i+1;i+1} - \mathbf{K}_{i+1;i}\mathbf{A}_i^{-1}\mathbf{K}_{i;i+1}$
   4. $\mathbf{B}_{i+1} = -\mathbf{B}_i\mathbf{A}_i^{-1}\mathbf{K}_{i;i+1}$
5. ENDFOR
6. $\mathbf{G}_{1;n} = \mathbf{B}_n\mathbf{A}_n^{-1}$

We feel again the need to remind the reader that, since the calculations are performed a non-orthogonal basis, the matrices involved in **Algorithm V.1** respect the representations (**II.28**). Briefly the external indices are in this situation $\mathbf{G}_{\uparrow\uparrow}$, $\mathbf{K}_{\downarrow\downarrow}$, $\mathbf{A}_{i;\downarrow\downarrow}$, $\mathbf{A}^{-1}_{i;\uparrow\uparrow}$ and $\mathbf{B}_{i;\uparrow\downarrow}$. The same holds true for the next subsection.

5.2. Decimation method for computing surface Green's functions

We detail now a very efficient method for computing the "free" lead surface Green's functions. "Free" means here that the lead(s) is decoupled from the two-terminal device. Thus we deal with a semi-infinite periodic Hamiltonian like those encountered in surface physics. An abstract representation of such a structure is represented in **Figure V.12**. The system is indeed periodic but only along the positive abscissa. The decimation method [**141**] described in this subsection, gives access to both the surface and asymptotic "bulk" Green's functions.

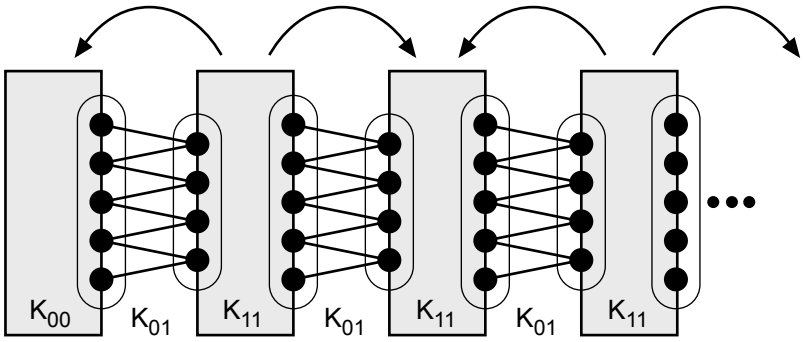

Figure V.12. A generic semi-infinite regular structure decomposed in principal layers. Arrows indicate the way layers are being eliminated by the decimation method.

The Hamiltonian of this system has again a tridiagonal form as suggested in **Figure V.12**. Thus its $\mathbf{K}$ matrix, $\mathbf{K}_{L(R)}(E)=\mathbf{G}^{-1}_{L(R)}(E)=E\mathbf{S}_{L(R)}-\mathbf{H}_{L(R)}$, has the form

$$\mathbf{K}_{L(R)}\equiv\mathbf{K}=\begin{bmatrix}\mathbf{K}_{00} & \mathbf{K}_{01} & & \\ \mathbf{K}_{10} & \mathbf{K}_{11} & \mathbf{K}_{01} & \\ & \mathbf{K}_{10} & \mathbf{K}_{11} & \ddots \\ & & & \end{bmatrix} \qquad \textbf{(V.12)}$$

For the sake of brevity we drop hereafter indices $L(R)$. Although $\mathbf{K}_{00}\equiv\mathbf{K}_{11}$ and $\mathbf{K}_{10}=\mathbf{K}_{01}^{\dagger}$ we have chosen this notation for reasons that will become obvious later. The decimation method is iterative and at some step these quantities will depart. Expanding the identity $\mathbf{GK}=\mathbf{I}$ the following system of equations follows

$$\begin{aligned}
\boldsymbol{\delta}_{2i,0} &= \mathbf{G}_{2i,0}\mathbf{K}_{00}+\mathbf{G}_{2i,1}\mathbf{K}_{10}\\
\boldsymbol{\delta}_{2i,1} &= \mathbf{G}_{2i,0}\mathbf{K}_{01}+\mathbf{G}_{2i,1}\mathbf{K}_{11}+\mathbf{G}_{2i,2}\mathbf{K}_{10}\\
&\vdots\\
\boldsymbol{\delta}_{2i,2j-1} &= \mathbf{G}_{2i,2j-2}\mathbf{K}_{01}+\mathbf{G}_{2i,2j-1}\mathbf{K}_{11}+\mathbf{G}_{2i,2j}\mathbf{K}_{10}\\
\boldsymbol{\delta}_{2i,2j} &= \mathbf{G}_{2i,2j-1}\mathbf{K}_{01}+\mathbf{G}_{2i,2j}\mathbf{K}_{11}+\mathbf{G}_{2i,2j+1}\mathbf{K}_{10}\\
\boldsymbol{\delta}_{2i,2j+1} &= \mathbf{G}_{2i,2j}\mathbf{K}_{01}+\mathbf{G}_{2i,2j+1}\mathbf{K}_{11}+\mathbf{G}_{2i,2j+2}\mathbf{K}_{10}\\
&\vdots
\end{aligned} \qquad \textbf{(V.13)}$$

with $j\geq 1$. Next all equations in odd second index, i.e. of type $2j+1$, are substituted into those of even index, the substitution variables being the Green's functions $\mathbf{G}_{i,2j+1}$. Because $\boldsymbol{\delta}_{2i,2j+1}=0$ regardless of i,j it follows that

$$\begin{aligned}
\mathbf{G}_{2i,1} &= -\mathbf{G}_{2i,0}\mathbf{K}_{01}\mathbf{K}_{11}^{-1} - \mathbf{G}_{2i,2}\mathbf{K}_{10}\mathbf{K}_{11}^{-1} \\
&\vdots \\
\mathbf{G}_{2i,2j-1} &= -\mathbf{G}_{2i,2j-2}\mathbf{K}_{01}\mathbf{K}_{11}^{-1} - \mathbf{G}_{2i,2j}\mathbf{K}_{10}\mathbf{K}_{11}^{-1} \\
\mathbf{G}_{2i,2j+1} &= -\mathbf{G}_{2i,2j}\mathbf{K}_{01}\mathbf{K}_{11}^{-1} - \mathbf{G}_{2i,2j+2}\mathbf{K}_{10}\mathbf{K}_{11}^{-1} \\
&\vdots
\end{aligned}$$

which upon insertion in (**V.13**) yields

$$\begin{aligned}
\boldsymbol{\delta}_{2i,0} &= \mathbf{G}_{2i,0}\tilde{\mathbf{K}}_{00} + \mathbf{G}_{2i,2}\tilde{\mathbf{K}}_{10} \\
\boldsymbol{\delta}_{2i,2} &= \mathbf{G}_{2i,0}\tilde{\mathbf{K}}_{01} + \mathbf{G}_{2i,2}\tilde{\mathbf{K}}_{11} + \mathbf{G}_{2i,4}\tilde{\mathbf{K}}_{10} \\
&\vdots \\
\boldsymbol{\delta}_{2i,2j-2} &= \mathbf{G}_{2i,2j-4}\tilde{\mathbf{K}}_{01} + \mathbf{G}_{2i,2j-2}\tilde{\mathbf{K}}_{11} + \mathbf{G}_{2i,2j}\tilde{\mathbf{K}}_{10} \\
\boldsymbol{\delta}_{2i,2j} &= \mathbf{G}_{2i,2j-2}\tilde{\mathbf{K}}_{01} + \mathbf{G}_{2i,2j}\tilde{\mathbf{K}}_{11} + \mathbf{G}_{2i,2j+2}\tilde{\mathbf{K}}_{10} \\
\boldsymbol{\delta}_{2i,2j+2} &= \mathbf{G}_{2i,2j}\tilde{\mathbf{K}}_{01} + \mathbf{G}_{2i,2j+2}\tilde{\mathbf{K}}_{11} + \mathbf{G}_{2i,2j+4}\tilde{\mathbf{K}}_{10} \\
&\vdots
\end{aligned} \qquad \textbf{(V.14)}$$

where we have used the notations

$$\begin{aligned}
\tilde{\mathbf{K}}_{00} &= \mathbf{K}_{00} - \mathbf{K}_{01}\mathbf{K}_{11}^{-1}\mathbf{K}_{10} & \tilde{\mathbf{K}}_{01} &= -\mathbf{K}_{01}\mathbf{K}_{11}^{-1}\mathbf{K}_{01} \\
\tilde{\mathbf{K}}_{10} &= -\mathbf{K}_{10}\mathbf{K}_{11}^{-1}\mathbf{K}_{10} & \tilde{\mathbf{K}}_{11} &= \mathbf{K}_{11} - \mathbf{K}_{01}\mathbf{K}_{11}^{-1}\mathbf{K}_{10} - \mathbf{K}_{10}\mathbf{K}_{11}^{-1}\mathbf{K}_{01}
\end{aligned} \qquad \textbf{(V.15)}$$

The system of equations (**V.14**) contains now only Green's functions with an even second index. Naturally these equations can be re-indexed via $2j \to j$ which brings (**V.14**) into the same form as (**V.13**) with the sole difference that $\mathbf{K}$ matrices are replaced by tilded matrices as defined in (**V.15**).

The substitution process corresponds physically to the elimination of odd layers like suggested by arrows in **Figure V.12**. The eliminated layers are included in the remaining ones via self-energies that in (**V.15**) are those terms having the form $\mathbf{K}_{10}\mathbf{K}_{11}^{-1}\mathbf{K}_{10}$. In other words the layer Hamiltonians embedded in $\mathbf{K}_{00}, \mathbf{K}_{11}$ and the interlayer interactions embedded in $\mathbf{K}_{01}, \mathbf{K}_{10}$ are being renormalized into tilded quantities. These correspond to effective Hamiltonians and interactions inside and between layers that "feel" the eliminated layers.

The substitution process is now iterated until a properly chosen norm of $\tilde{\mathbf{K}}_{01}, \tilde{\mathbf{K}}_{10}$, e.g. the Frobenius norm, falls below some threshold. These steps are equivalent to

Algorithm V.2. Decimation method for calculation of surface and bulk Green's functions

1. LET $\mathbf{K}_{ij;n-1} = E\mathbf{S}_{ij} - \mathbf{H}_{ij}$ FOR $i,j = \overline{0,1}$
2. REPEAT
   3. $\mathbf{K}_{00;n} = \mathbf{K}_{00;n-1} - \mathbf{K}_{01;n-1}\mathbf{K}_{11;n-1}^{-1}\mathbf{K}_{10;n-1}$
   4. $\mathbf{K}_{11;n} = \mathbf{K}_{11;n-1} - \mathbf{K}_{01;n-1}\mathbf{K}_{11;n-1}^{-1}\mathbf{K}_{10;n-1} - \mathbf{K}_{10;n-1}\mathbf{K}_{11;n-1}^{-1}\mathbf{K}_{01;n-1}$
   5. $\mathbf{K}_{01;n} = -\mathbf{K}_{01;n-1}\mathbf{K}_{11;n-1}^{-1}\mathbf{K}_{01;n-1}$
   6. $\mathbf{K}_{10;n} = -\mathbf{K}_{10;n-1}\mathbf{K}_{11;n-1}^{-1}\mathbf{K}_{10;n-1}$
   7. LET $\mathbf{K}_{ij;n-1} = \mathbf{K}_{ij;n}$ FOR $i,j = \overline{0,1}$
8. UNTIL $\|\mathbf{K}_{01;n}\| + \|\mathbf{K}_{10;n}\| \leq 2\varepsilon$
9. $\mathbf{G}_{00} = \mathbf{K}_{00;n}^{-1}$
10. $\mathbf{G}_{11} = \mathbf{K}_{11;n}^{-1}$

iterating over (V.15) where $\tilde{\mathbf{K}}$ should be replaced by $\mathbf{K}_n$ and $\mathbf{K}$ by $\mathbf{K}_{n-1}$ where n is the iteration index. The **Algorithm V.2** summarizes the decimation method.

After convergence is achieved over steps 3-7 the surface $\mathbf{G}_{00}$ and bulk $\mathbf{G}_{11}$ Green's functions are easily obtained in steps 9-10. This can be observed if we set first $i = 0$ and $\mathbf{K}_{10} = \mathbf{0}$ in the first equation of (V.13) from which results $\mathbf{G}_{00}$ and then set $j = i$ and $\mathbf{K}_{10} = \mathbf{K}_{01} = \mathbf{0}$ in the fourth equation of (V.13) to get $\mathbf{G}_{11}$.

The decimation method is exponentially convergent. In the first iteration step odd layers are embedded into even layers via their self-energies. In the next iteration step the remaining odd layers are embedded into the even ones. At this point each renormalized layer contains the influence of two layers from the initial structure. If the procedure is now repeated, at some step n, each renormalized layer would "feel" the effective environment created by 2^n initial layers. In practice we found this method far more stable numerically and rapidly converging than the one described in **Chapter III.3.3**.

5.3. Transmission spectra

This final subsection has the role of gathering all the pieces developed throughout the chapter together and use them for computing the transmission spectra of a carbon nanotube sensor. At the end of **Section 4** we have obtained an optimal pencil $(\mathbf{H}_r, \mathbf{S}_r)$

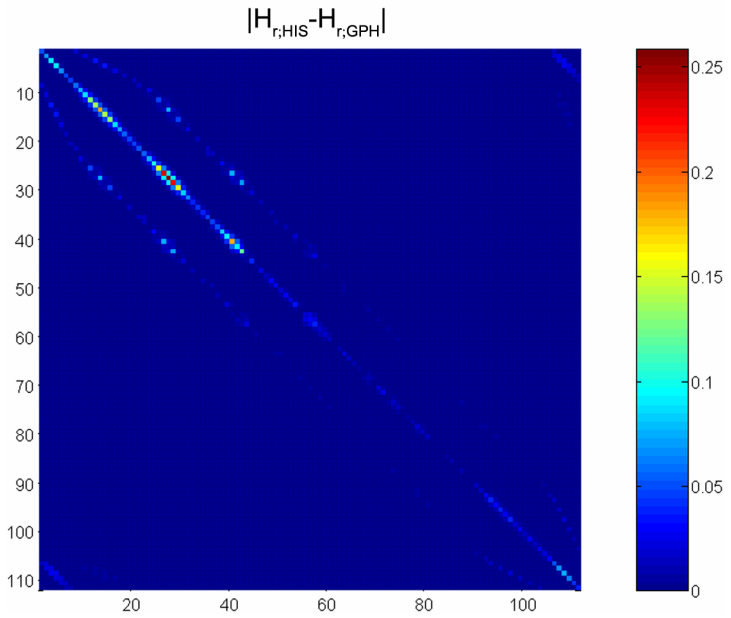

Figure V.13. Absolute Hamiltonian matrix element difference between the graphitic parts of GPH+HIS and pristine GPH that were used in perturbing the Hamiltonian for conductance calculations (see text for details).

for the reference adsystems represented by an aromatic amino acid onto a graphene layer. This pencil is sparse, yields accurate bands around the Fermi level and has a few other interesting properties as discussed in the abovementioned section.

The $(\mathbf{H}_r, \mathbf{S}_r)$ matrix elements are then exported to the toy sensor represented in **Figure V.11** as follows. First for pristine graphene we have found that symmetry is respected within the $(\mathbf{H}_r, \mathbf{S}_r)$ matrix elements (i.e. all carbon atoms have the same parameters) and thus we have extracted parameters for a single carbon atom. This carbon atom model is very similar to a third nearest neighbor tight-binding scheme. The Hamiltonian and overlap matrices for the pristine sensor were then instantiated with values corresponding to the aforementioned model. The toy sensor, which has no adsorbed amino acid yet on its surface, is then partitioned as in **Figure V.11**. Leads are decoupled from the central region, and their surface Green's functions are computed at all energies using **Algorithm V.2**. With the help of **Equation (V.10)** we obtain the required lead-self energy matrix elements $\Sigma^r_{L(R);\mu\mu'}$ from where level broadening functions $\Gamma_{L(R);\mu\mu'}$ follow immediately. The same self-energies renormalize additively the Hamiltonian of the central region from which via

Algorithm V.1 the transfer Green's function matrix elements $G^r_{C;\mu\nu}$ are calculated. Finally summing **Equation (V.11)** one gets the energy dependent conductance $\mathcal{G}(E)$.

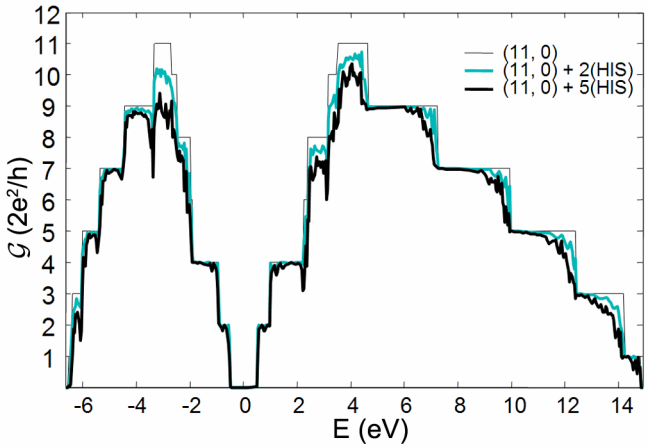

Figure V.14. Transmission spectra for (11,0) CNT-based sensor for pristine nanotube and the CNT+HIS amino acids.

We have applied this method to a semiconducting (11,0) nanotube measuring approximately 15nm stacked in between leads simulated by ideal semi-infinite (11,0) tubes. The result is presented in **Figure V.14** with a thin black line, and is, as expected, equal to the transmission function through an infinite (11,0) nanotube. The sharp stairs in the transmission and their positions agree well with non-orthogonal tight-binding calculations validating the workflow we have described in this chapter.

Amino acid molecules were added afterwards randomly along the tube assuring a minimum spacing between two neighboring amino acids. The Hamiltonian and overlap matrices of the toy sensor were then perturbed at the adsorption sites by mapping the matrix perturbation in **Figure V.13** which represents the absolute Hamiltonian matrix element difference between the graphitic parts of the GPH+HIS adsystem and pristine GPH. Transmission spectra computed for this case are plotted in **Figure V.14** with thick black and cyan lines. The lowering of the transmission as increasingly many Histidine molecules adsorb at the surface of the tube is evident at large energies away from the Fermi level. Unfortunately close to E_F the charge transfer seems too weak to modify the transmission. It is true though that we have not included yet the molecular orbitals of the amino-acid in calculations, nor have we considered any eventual charge neutrality point shifting due to adsorption.

At this point we would tend to conclude that conductance of carbon nanotubes is not sufficiently affected by aromatic amino acids, at least for practical applications. Nevertheless we have yet to test this conclusion and explain why the sharp peaks close to the Fermi level induced by the adsorption in the density of states do not seem to influence the conductance. Also we have not computed yet the conductance of metallic tubes in which the amino acid adsorption could increase back scattering leading to conductance suppression at the Fermi level. Even if we do find after other simulations that carbon nanotubes cannot be used in amino-acid detection the methodology we have developed in this chapter would still survive as it allows in a unified, reproducible manner to study other chemical stimuli.

Perspectives and further developments

Before the concluding remarks we wish to list a few thoughts concerning untouched subjects or refinements possible within the methods developed in this chapter. Considering the relaxation of the amino acids on graphene, which we have achieved at a molecular mechanics level, there is at least one questionable neglection, namely the electrostatic interaction between the α-amino(carboxyl) group(s) and their charge images inside the semi-metallic graphene layer. Properly this would be avoided by relaxing at DFT level; practically it is intractable as discussed earlier due to the huge number of possible configurations. It remains to be seen if adding a Lennard-Jones 10-4 potential [**142**] in NAMD would change anything.

Self-assembly of molecules may lead to regular patterns at the surface of the tubes and this is a straightforward study in which one disperses randomly amino acids at the surface of a long nanotube and waits to see if order emerges. In this case symmetry may amplify mixing between the delocalized nanotube orbitals and the patterned molecular disposition leading to large conductance modifications. The field created by leads may also twist amino acids due to the net dipole they have as zwitterions.

In what concerns the Hamiltonian model reduction method, there is still a long way to go before becoming the powerful tool we believe it to be. First the PDOS based elimination procedure should be extended with condition number analysis that would produce more controllable results. For Histidine we managed to obtain truly excellent results yet for Phenylalanine the same method works poorly. Instead of including all

amino acid orbitals in calculations we chose to get further insight into what causes these large band shifts.

Obviously more theoretical results are expected for the isospectral flow in the model reduction context. For instance it is not clear yet why our procedure yields perfect dispersion relations throughout the k space although the flow was set at the Γ point only. The matrix flow theory should also be extended to complex valued matrices and goal functions over the k space.

Careful thought about what our method achieves is really intriguing. The old Bloch-Feshbach formalism gives one the possibility to project out part of a Hilbert space and obtain an effective Hamiltonian that describes the dynamics of the system inside the projected Hilbert space. But the resulting Hamiltonian is energy dependent and often even divergent. Our method obtains a projected and *energy-independent* Hamiltonian that we feel describes the dynamics in the projected space in a minimal root mean square fashion.

Being essentially a Hamiltonian renormalization flow we could have applied the isospectral flow directly on the initial full-sized pair (**H**,**S**) to directly decouple the eigenvectors of energies close to the Fermi level from the rest of eigenvectors. The matrix flow which at the moment is a $\mathcal{O}(N^3)$ process is defined in the projected space to reduce the computational burden.

Regarding the conductance calculation method we do consider it efficient enough for our present requirements. There are however many calculations left to do with this method, to name a few: amino acids on metallic tubes, peptide or DNA wrapped nanotubes and many other chemical sensors.

Conclusions

We have presented a framework for studying carbon nanotube-based conductance sensors. At first we have described how intractable calculations can be avoided by running *ab initio* self-consistent calculations on reference subsystems of considerably smaller size than a carbon nanotube sensor. These simulations have shown that the four studied aromatic amino acids HIS, PHE, TRP and TYR induce states close to the Fermi level when adsorbing onto a graphene layer. A Mulliken charge analysis

identified the adsorption to be weak (physisorption) and moreover the charge perturbation of the graphene unit cell to be localized around the α-carboxyl group. Furthermore, after concluding that CNTs might detect these amino acids, we have applied a novel method for reducing the order of the Hamiltonian so as to preserve simultaneously its spectrum around the Fermi level, and its sparsity pattern. This simplification was argued starting from Todorov's transmission formula to demonstrate that the conductance is indeed determined by the spectral properties of the Hamiltonian around the Fermi level-only. This method can be viewed as a top-down tight-binding parameterization procedure for low-symmetry systems. A very efficient conductance formula was derived at the end of this chapter and was applied to a sensor toy model in view of computing transmission spectra of CNT sensors. However it is not clear yet if the aromatic amino acids considered here do or do not modify a carbon nanotube's conductance but as presented in the perspectives section work is underway in this purpose.

Conclusions

This thesis was focused on two sensing devices with applications in biochemical detection. The first presented device was an electromechanical carbon nanotube-based strain transducer that was proved to be suitable to both measuring piconewton forces and detecting kilodaltons masses. The second device is a simple two terminal conductance nanotube sensor aimed at detecting aromatic amino acids. Generally the scheme followed in this thesis was as stated in the introduction, the proposal of sensing mechanisms followed by modeling and simulation of several characteristics (like the mechanical behavior, electronic structure, etc.) in order to validate the operation of the devices.

In **Chapter III** we have proposed a novel carbon nanotube-based electromechanical sensor. As explained thoroughly in this chapter this sensor consists of only two nanotubes in a cross configuration where a tube has one free end and is a cantilever and the second has both ends clamped, being simultaneously a bearing supporting the cantilever and a potentiometer for measuring the former's deflection. Although CNT cantilevers have been already proposed as force microscopy probes [**92**] or resonating nanobalances [**57**], we have added here the possibility to electrically measure its deflection, avoiding laser interferometry optics or TEM imaging respectively.

In **Chapter V** we have proposed carbon nanotubes as possible detectors of aromatic amino acids. The sensing mechanism proposed there is not new [**52**, **126**, **132**], yet to our knowledge it has not been proved for these molecules so far. The four amino acids were chosen because they include aromatic rings which bind on nanotube surfaces via weak pi-stacking interactions. Detecting amino acids, although a target in itself, is an intermediary step in sensing small peptides which would truly be important for biotech research and not only.

The main effort of this thesis was spent in choosing appropriate models or developing new methods for the difficult task of simulating nanotube-based devices. On the modeling and simulation side we have dealt with heterogeneous simulations aimed at assessing the mechanical behavior, electronic properties or transport properties spanning different time-scales and levels of theory.

The mechanical behavior of our systems was captured typically at a molecular mechanics (MM) level. We have often preferred MM to more expensive *ab initio* or semi-empirical tight binding molecular dynamics for assessing the dynamics of the systems or sometimes for minimizing the total energy in view of obtaining relaxed coordinates. Using these classical force fields has a huge speed advantage but also adds a certain complexity overhead associated with parameterization. For this purpose we have used *ab initio* simulation for reference systems with rather good results.

One of the main contribution of this thesis are a class of methods developed for computing transport properties with a simulation time scaling linearly with the system's number of atoms. By extrapolation we can assert that the proposed methods allow conductance calculations of million atom systems, although in our cases we typically dealt with only a few thousand atom systems. Here we have used intensively real-space localized PAO basis sets which enabled us to split the studied systems in several smaller parts. Generally we have employed decimation or elimination based procedures that are typically exponentially convergent or linearly scaling respectively, in which the central idea is to project out system component and include their influence in the remaining components via self-energies.

Another major contribution of this thesis consists in the matrix flow-based Hamiltonian model reduction framework we have proposed in **Chapter IV** and applied in **Chapter V**. This method employs infinitesimal congruence transformations and results in a reduced effective Hamiltonian that has an imposed linear structure and a correct spectrum around the Fermi level being optimally appropriate for conductance calculations. The case studies for this method were the four aromatic amino acids on graphene, but the theory behind it is largely unexplored and applicable to other systems of interest from field effect transistors to chemical sensors.

References

[1] Iijima S., "Helical microtubules of graphitic carbon", *Nature* **354**, 56 (1991)

[2] Ionescu A. M., Banerjee K., "Emerging Nanoelectronics: Life with and after CMOS", *Springer* (2004)

[3] Bronikowski M. J., Willis P. A., Colbert D. T., Smith K. A. and Smalley R. E., "Gas-phase production of carbon single-walled nanotubes from carbon monoxide via the HiPco process: A parametric study", *J. Vacuum Sci. Tech. A* **19**, 1800 (2001)

[4] Zhu H. W., Xu C. L., Wu D. H., Wei B. Q., Vajtai R., and Ajayan P. M., "Direct synthesis of long single-walled carbon nanotube strands", *Science* **296**, 884 (2002)

[5] Liu J., Fan S., Dai H., "Recent advances in methods of forming carbon nanotubes", *MRS Bulletin* **29**, 244 (2004)

[6] Chen Y., Haddon R. C., Fang S., Rao A. M., Eklund P. C., Lee W. H., Dickey E. C., Grulke E. A., Pendergrass J. C., Chavan A., Haley B. E., Smalley R. E., "Chemical attachment of organic functional groups to single-walled carbon nanotube material", *J. Mat. Research* **13**, 2423 (1998)

[7] Shim M., Kam N. W. S., Chen R. J., Li Y.M., Dai H. J., "Functionalization of carbon nanotubes for biocompatibility and biomolecular recognition", *Nano Lett.* **2**, 285 (2002)

[8] de la Torre G., Blau W. and Torres T., "A survey on the functionalization of single-walled nanotubes. The chemical attachment of phthalocyanine moieties", *Nanotechnology* **14**, 765 (2003)

[9] O'Connell M. J., Boul P., Ericson L. M., Huffman C., Wang Y., Haroz E., Kuper C., Tour J., Ausman K. D. and Smalley R. E., "Reversible water-solubilization of single-walled carbon nanotubes by polymer wrapping", *Chem. Phys. Lett.* **342**, 265 (2001)

[**10**] Steuerman D. W., Star A., Narizzano R., Choi H., Ries R. S., Nicolini C., Stoddart J. F., Heath J. R., "Interactions between conjugated polymers and single-walled carbon nanotubes", *J. Phys. Chem B.* **106**, 3124 (2002)
[**11**] Zheng M. et *al.*, "Structure-based carbon nanotube sorting by sequence-dependent DNA assembly", *Science* **302**, 1545 (2003)
[**12**] Krupke R., Hennrich F., v. Löhneysen H., Kappes M. M., "Separation of metallic from semiconducting single-walled carbon nanotubes", *Science* **301**, 344 (2003)
[**13**] Saito R., Dresselhaus G., Dresselhaus M. S., "Physical properties of carbon nanotubes", *Imperial College Press* (1998)
[**14**] Harris P. J. F., "Carbon nanotubes and related structures", *Cambridge University Press* (2002)
[**15**] Meyyappan M., "Carbon nanotubes: Science and applications", *CRC Press* (2004)
[**16**] Bernholc J., Brenner D., Nardelli M. B., Meunier V., and Roland C., "Mechanical and electrical properties of nanotubes", *Annu. Rev. Mater. Res.* **32**, 347 (2002)
[**17**] Dai H., "Carbon nanotubes: Opportunities and challenges", *Surf. Sci.* **500**, 218 (2002)
[**18**] Charlier J.-C., "Defects in carbon nanotubes", *Acc. Chem. Res.* **35**, 1063 (2002)
[**19**] McEuen P. L. and Park J. Y., "Electron transport in single-walled carbon nanotubes", *MRS Bulletin* **29**, 272 (2004)
[**20**] Salvetat J. P., Bonard J. M., Thomson N. H., Kulik A. J., Forro L., Benoit W., Zuppiroli L., "Mechanical properties of carbon nanotubes", *Appl. Phys. A* **69**, 255 (1999)
[**21**] Srivastava D., Wei C., Cho K., "Nanomechanics of carbon nanotubes and composites", *Appl. Mech. Rev.* **56**, 215 (2003)
[**22**] Datta S., "Electronic transport in mesoscopic systems", *Cambridge University Press* (1995)
[**23**] Ferry D. K., Goodnick S. M., "Transport in nanostructures", *Cambridge University Press* (1997)
[**24**] Frank S., Poncharal P., Wang Z. L., de Heer W. A., "Carbon nanotube quantum resistors", *Science* **280**, 1744 (1998)
[**25**] Tans S., Devoret M., Dai H., Thess A., Smalley R., Geerligs L., Dekker C., "Individual single-wall carbon nanotubes as quantum wires", *Nature* **386**, 474 (1997)

[26] Bockrath M., Cobden D., McEuen P., Chopra N., Zettl A., Thess A., Smalley R., "Single-electron transport in ropes of carbon nanotubes", *Science* **275**, 1922 (1997)
[27] Kasumov A., Kociak M., Ferrier M., Deblock R., Gueron S., Reulet B., Khodos I., Stephan O., Bouchiat H., "Quantum transport through carbon nanotubes: Proximity-induced and intrinsic superconductivity", *Phys. Rev. B.* **68**, 214521 (2003)
[28] Roche P. E., Kociak M., Gueron S., Kasumov A., Reulet B., Bouchiat H., "Very low shot noise in carbon nanotubes", *Euro. Phys. J. B.* **28**, 217 (2002)
[29] Liang W. J., Bockrath M., Bozovic D., Hafner J. H., Tinkham M., Park H., "Fabry-Perot interference in a nanotube electron waveguide", *Nature* **411**, 665 (2001)
[30] Bachtold A., Fuhrer M., Plyasunov S., Forero M., Anderson E., Zettl A., McEuen P., "Scanned probe microscopy of electronic transport in carbon nanotubes", *Phys. Rev. Lett.* **84**, 6082 (2000)
[31] Gao B., Chen Y. F., Fuhrer M. S., Glattli D. C. and Bachtold A., "Four-point resistance of individual single-wall carbon nanotubes", *Phys. Rev. Lett.* **95**, 196802 (2005)
[32] Javey A., Guo J., Wang Q., Lundstrom M. and Dai H., "Ballistic carbon nanotube field-effect transistors", *Nature* **424**, 654 (2003)
[33] Zhou C., Kong J., Dai H., "Electrical measurements of individual semiconducting single-walled nanotubes of various diameters", *Appl. Phys. Lett.* **76**, 1597 (1999)
[34] Kasumov A. Yu., Bouchiat H., Reulet B., Stephan O., Khodos I. I., Gorbatov, Yu. B., Colliex C., "Conductivity and atomic structure of isolated multiwalled carbon nanotubes", *Europhys. Lett.* **43**, 89 (1998)
[35] Tans S., Verschueren A., Dekker C., "Room-temperature transistor based on a single carbon nanotube", *Nature* **393**, 49 (1998)
[36] Martel R., Schmidt T., Shea H. R., Hertel T., Avouris P., "Single- and multi-wall carbon nanotube field-effect transistors", *Appl. Phys. Lett.* **73**, 2447 (1998)
[37] Kong J., Yenilmez E., Tombler T. W., Kim W., Dai H. J, et *al.*, "Quantum interference and ballistic transmission in nanotube electron waveguides", *Phys. Rev. Lett.* **87**, 106801 (2001)
[38] Chen R., Franklin N., Kong J., Cao J., Tombler T., et *al.*, "Molecular photo-desorption from carbon nanotubes", *Appl. Phys. Lett.* **79**, 2258 (2001)

[**39**] Bachtold A., Henny M., Tarrier C., Strunk C., Schonenberger C., et *al*., "Contacting carbon nanotubes selectively with low-ohmic contacts for four-probe electric measurements", *Appl. Phys. Lett.* **73**, 274 (1998)
[**40**] Heinze S., Tersoff J., Martel R., Derycke V., Appenzeller J., Avouris P., "Carbon nanotubes as Schottky barrier transistors ", *Phys. Rev. Lett.* **89**, 106801 (2002)
[**41**] Appenzeller J., Knoch J., Derycke V., Martel R., Wind S., Avouris P., "Field-modulated carrier transport in carbon nanotube transistors", *Phys. Rev. Lett.* **89**, 126801 (2002)
[**42**] Mahapatra S., Ionescu A. M., et *al.*,"A quasi-analytical SET model for few electron circuit simulation", *IEEE Electron Device Letters* **23**, 366 (2002)
[**43**] Jarillo-Herrero P., Kong J., van der Zant H. S. J., Dekker C., Kouwenhoven L. P., De Franceschi S., "Orbital Kondo effect in carbon nanotubes", *Nature* **434**, 484 (2005)
[**44**] Marty L., Bouchiat V., Naud C., Chaumont M., Fournier T., Bonnot A. M., "Schottky barriers and Coulomb blockade in self-assembled carbon nanotube FETs", *Nano Lett.* **3**, 1115 (2003)
[**45**] Bockrath M., Hone J., Zettl A., McEuen P. L., Rinzler A. G. and Smalley R. E., "Chemical doping of individual semiconducting carbon-nanotube ropes", *Phys. Rev. B* **61**, R10606 (2000)
[**46**] Kong J., Zhou C., Yenilmez. E. and Dai H., "Alkaline metal-doped n-type semiconducting nanotubes as quantum dots", *Appl. Phys. Lett.* **77**, 3977 (2000)
[**47**] Derycke V., Martel R., Appenzeller J., and Avouris P., "Carbon nanotube inter- and intramolecular logic gates", *Nano Lett.* **1**, 453 (2001)
[**48**] Zhou C., Kong J., Yenilmez E., and Dai H., "Modulated chemical doping of individual carbon nanotubes", *Science* **290**, 1552 (2000)
[**49**] Kong J., Cao J., Anderson E., Dai H., "Chemical profiling of single nanotubes: Intramolecular pnp junctions and on-tube single electron transistors", *Appl. Phys. Lett.* **80**, 73 (2002)
[**50**] Carroll D. L., Redlich Ph., Blase, X., Charlier, J.-C., Curran, S., Ajayan, P. M., Roth, S., Rühle, M., "Effects of nanodomain formation on the electronic structure of doped carbon nanotubes", *Phys. Rev. Lett.* **81**, 2332 (1998)
[**51**] Czerw R., Terrones M., Charlier J.-C., Blase, X., et *al.*, "Identification of electron donor states in N-doped carbon nanotubes", *Nano Lett.* **1**, 457 (2001)

[52] Kong J., Franklin N. R., Zhou C. W., Chapline M. G., Peng S., et *al.* , "Nanotube molecular wires as chemical sensors", *Science* **287**, 622 (2000)
[53] Buehler M. J., Kong Y., Gao H., "Deformation mechanisms of very long single-wall carbon nanotubes subject to compressive loading", *J. Eng. Mat. Tech.* **126**, 245 (2004)
[54] Harik V. M., Gates T. S. and Nemeth M. P., "Applicability of the continuum-shell theories to the mechanics of carbon nanotubes", *NASA/CR-2002-211460*, ICASE Report No. 2002-7 (2002)
[55] Arroyo M. and Belytschko T., "Finite crystal elasticity of carbon nanotubes based on the exponential Cauchy-Born rule", *Phys. Rev. B* **69**, 115415 (2004)
[56] Girifalco L. A., Hodak M. and Lee R. S., "Carbon nanotubes, buckyballs, and a universal graphitic potential", *Phys. Rev. B* **62**, 13104 (2000)
[57] Poncharal P., Wang Z. L., Ugarte D., de Heer W. A., "Electrostatic deflections and electromechanical resonances of carbon nanotubes", *Science* **283**, 1513 (1999)
[58] Robertson D. H., Brenner D. W., and Mintmire J. W., "Energetics of nanoscale graphitic tubules", *Phys. Rev. B* **45**, 12592 (1992)
[59] Yakobson B. I., Brabec C. J., and Bernholc J., "Nanomechanics of carbon tubes: Instabilities beyond linear response", *Phys. Rev. Lett.* **76**, 2511 (1996)
[60] Hernandez E., Goze C., Bernier P., and Rubio A., "Elastic properties of C and BxCyNz composite nanotubes", *Phys. Rev. Lett.* **80**, 4502 (1998)
[61] Sanchez-Portal D., Artacho E., Soler J. M., Rubio A., Ordejon P., "Ab initio structural, elastic, and vibrational properties of carbon nanotubes", *Phys. Rev. B* **59**, 12678 (1999)
[62] Srivastava D., Menon M., and Cho K., "Anisotropic nanomechanics of boron nitride nanotubes: Nanostructured "skin" effect", *Phys. Rev. B* **63**, 195413 (2001)
[63] Treacy M. M. J., Ebbesen T. W., and Gibson J. M., "Exceptionally high Young's modulus observed for individual carbon nanotubes", *Nature* **381**, 678 (1996)
[64] Krishnan A., Dujardin E., Ebbesen T. W., Yianilos P. N., and Treacy M. M. J., "Young's modulus of single-walled nanotubes", *Phys. Rev. B* **58**, 14013 (1998)
[65] Wong E. W., Sheehan P. E., Lieber C. M., "Nanobeam mechanics: Elasticity, strength, and toughness of nanorods and nanotubes", *Science* **277**, 1971 (1997)
[66] Salvetat J.-P., Briggs G. A. D., Bonard J. M., Bacsa R. R. , Kulik A. J., Stockli T., Burnham N. A., and Forro L., "Elastic and shear moduli of singlewalled carbon nanotube ropes", *Phys. Rev. Lett.* **82**, 944 (1999)

[**67**] Jauho A. P., Wingreen N. S., Meir Y., "Time-dependent transport in interacting and noninteracting resonant-tunneling systems", *Phys. Rev. B* **50**, 5528 (1994)
[**68**] Haug H., Jauho A. P., "Quantum kinetics and optics of semiconductors", *Springer Verlag* (1996)
[**69**] Meir Y., Wingreen N. S., "Landauer formula for the current through an interacting electron region", *Phys. Rev. Lett.* **68**, 2512 (1992)
[**70**] Fisher D. S. and Lee P. A., "Relation between conductivity and transmission matrix", *Phys. Rev. B* **23**, 6851 (1981)
[**71**] Todorov T. N., Briggs G. A. D. and Sutton A. P., "Elastic quantum transport through small structures", *J. Phys.: Condens. Matter* **5**, 2389(1993)
[**72**] Bogoliubov N. N., "An introduction to quantum statistical mechanics", *World Scientific Publishing* (1982)
[**73**] Bransden B. H., Joachain C. J., "Introduction to quantum mechanics", *Longman Publishing Group* (1989)
[**74**] Keldysh L. V., "Diagram technique for nonequilibriun processes", *Sov. Phys. JETP* **20**, 1018 (1965)
[**75**] Kadanoff L. P., and Baym G., "Quantum statistical mechanics; Green's function methods in equilibrium and nonequilibrium", *W. A. Benjamin* (1962)
[**76**] Brandbyge M., Mozos J.-L., Ordejon P., Taylor J. and Stokbro K., "Density functional method for nonequilibrium electron transport", *Phys. Rev. B* **65**, 165401 (2002)
[**77**] Taylor J., Brandbyge M., Stokbro K., "Conductance switching in a molecular device: the role of side groups and intermolecular interactions", *Phys. Rev. B* **68**, 121101 (2003)
[**78**] Taylor J., Brandbyge M., Stokbro K., " Theory of rectification in tour wires: The role of electrode coupling", *Phys. Rev. Lett.* **89**, 138301 (2002)
[**79**] Weinberger P., "Ab initio theories of electric transport in solid systems with reduced dimensions", *Phys. Rep.* **377**, 281 (2003)
[**80**] Pecchia A., Di Carlo A., "Atomistic theory of transport in organic and inorganic nanostructures", *Rep. Prog. Phys.* **67**, 1497 (2004)
[**81**] Artacho E., Milans del Bosch L., "Nonorthogonal basis sets in quantum mechanics: Representations and second quantization", *Phys. Rev. A* **43**, 5770 (1991)
[**82**] Fletcher D. A. and Theriot J. A., "An introduction to cell motility for the physical scientist", *Phys. Biol.* **1**, T1 (2004)

[**83**] Rotsch C., Jacobson K., Radmacher M., "Dimensional and mechanical dynamics of active and stable edges in motile fibroblasts investigated by using atomic force microscopy ", *Proc. Natl. Acad. Sci.* **96**, 921 (1999)
[**84**] Radmacher M., "Measuring the elastic properties of living cells by the atomic force microscope", *Methods Cell. Biol.* **68**, 67 (2002)
[**85**] Finer J. T., Simmons R. M. and Spudich J. A., "Single myosin molecule mechanics: piconewton forces and nanometer steps", *Nature* **368**, 113 (1994)
[**86**] Iqbal S. S., Mayo M. W., Bruno J. G., Bronk B. V., Batt C. A., Chambers J. P., "A review of molecular recognition technologies for detection of biological threat agents", *Biosens. Bioelectron*. **15**, 549 (2000)
[**87**] Fritz J., Baller M. K., Lang H. P., Rothuizen H., Vettiger P., Meyer E., Güntherodt H. J., Gerber Ch., Gimzewski J. K., "Translating biomolecular recognition into nanomechanics", *Science* **288**, 316 (2000)
[**88**] Grogan C., Raiteri R., O'Connor G. M., Glynn T. J., Cunningham V., Kane M., Charlton M. and Leech D., "Characterisation of an antibody coated microcantilever as a potential immuno-based biosensor", *Biosens. Bioelectron.* **17**, 201 (2002)
[**89**] Arntz Y., Seelig J. D., Lang H. P., Zhang J., Hunziker P., Ramseyer J. P., Meyer E., Hegner M. and Gerber Ch., "Label-free protein assay based on a nanomechanical cantilever array", *Nanotechnology* **14**, 86 (2003)
[**90**] Timoshenko S., and Goodier J. N., "Theory of elasticity", *McGraw Hill* (1983)
[**91**] Dai H., Hafner J. H., Rinzler A. G., Colbert D. T., Smalley R. E., "Nanotubes as nanoprobes in scanning probe microscopy", *Nature* **384**, 147 (1996)
[**92**] Cheung C. L., Hafner J. H. and Lieber C. M., "Carbon nanotube atomic force microscopy tips: Direct growth by chemical vapor deposition and application to high-resolution imaging", *Proc. Natl. Acad. Sci.* **97**, 3809 (2000)
[**93**] Kim P. and Lieber C. M., "Nanotube nanotweezers", *Science* **286**, 2148 (1999)
[**94**] Dequesnes M., Rotkin S. V. and Aluru N. R., "Calculation of pull-in voltages for carbon-nanotube-based nanoelectromechanical switches", *Nanotechnology* **13**, 120 (2003)
[**95**] Henrard L., Hernandez E., Bernier P., Rubio A., "van der Waals interaction in nanotube bundles: Consequences on vibrational modes", *Phys. Rev. B* **60**, R8521 (1999)
[**96**] Hernandez E., Goze C., Bernier P. and Rubio A., "Elastic properties of single-wall nanotubes", *App. Phys. A* **68**, 287 (1999)

[**97**] Belytschko T., Xiao S. P., Schatz G. C., and Ruoff R. S., "Atomistic simulations of nanotube fracture", *Phys. Rev. B* **65**, 235430 (2002)
[**98**] Noon W. H., Ausman K. D., Smalley R. E., Ma J. P., "Helical ice-sheets inside carbon nanotubes in the physiological condition", *Chem. Phys. Lett.* **355**, 445 (2002)
[**99**] Kale L., Skeel R., Bhandarkar M., Brunner R., Gursoy A., Krawetz N., Phillips J., Shinozaki A., Varadarajan K., and Schulten K., "NAMD2: Greater scalability for parallel molecular dynamics", *J. Comp. Phys.* **151**, 283 (1999)
[**100**] MacKerell Jr. A. D., Bashford D., Bellott M., Dunbrack R. L., Jr. et *al.*, "All-atom empirical potential for molecular modeling and dynamics studies of proteins", *J. Phys. Chem. B* **102**, 3586 (1998)
[**101**] Werder T., Walther J. H., Jaffe R., Halicioglu T. and Koumoutsakos P., "Molecular dynamics simulation of contact angles of water droplets in carbon canotubes", *Nano Lett.* **1**, 697 (2001)
[**102**] Soler J. M., Artacho E., Gale J. D., Garcia A., Junquera J., Ordejon P. and Sanchez-Portal D., "The Siesta method for ab initio order-N materials simulation", *J. Phys.: Cond. Matter.* **14**, 2745 (2002)
[**103**] Yoon Y. G., Mazzoni M. S. C., Choi H. J., Ihm J., and Louie S. G., "Structural deformation and intertube conductance of crossed carbon nanotube junctions", *Phys. Rev. Lett.* **86**, 688 (2001)
[**104**] Anantram M. P., Govindan T. R., "Conductance of carbon nanotubes with disorder: A numerical study", *Phys. Rev. B* **58**, 4882 (1998)
[**105**] Roche S., Triozon F., Rubio A. and Mayou D., "Electronic conduction in multi-walled carbon nanotubes: Role of intershell coupling and inconmensurability", *Phys. Lett. A* **285**, 94 (2001)
[**106**] Tu Z. C., Ou-Yang Z., “Single- and multi-walled carbon nanotubes viewed as elastic tubes with Young's moduli dependent on layer number”, *Phys. Rev. B* **65**, 233407 (2002)
[**107**] Fernandez-Serra M. V., Artacho E., Soler J. M., "Model Hessian for accelerating first-principles structure optimizations", *Phys. Rev. B* **67**, 100101 (2003)
[**108**] Latil S., Roche S., Mayou D., Charlier J. C., "Mesoscopic transport in chemically doped carbon nanotubes", *Phys. Rev. Lett.* **92**, 256805 (2004)
[**109**] Chu M. T., Driessel K. R., "The projected gradient method for least squares matrix approximations with spectral constraints", *SIAM J. Numer. Anal.* **27**, 1050 (1990)

[**110**] Chen X., Chu M. T., "On the least squares solution of inverse eigenvalue problems", *SIAM J. Numer. Anal.* **33**, 2417 (1996)
[**111**] Chu M. T., Guo Q., "On the least squares approximation of symmetric-definite pencils subject to generalized spectral constraints", *SIAM J. Matrix Anal. Appl.* **19**, 1 (1998)
[**112**] Graham A., "Kronecker products and matrix calculus: With applications", *Ellis Horwood Ltd.* (1981)
[**113**] Magnus J. R. and Neudecker H., "Matrix differential calculus with applications in statistics and econometrics", *John Wiley & Sons Ltd.* (1999)
[**114**] Tinkham M., "Group theory and quantum mechanics", *Dover Publications* (2003)
[**115**] Binney J. J., Dowrick N. J., Fisher A. J., Newman M. E. J., "The theory of critical phenomena: An introduction to the renormalization group", *Oxford University Press* (1992)
[**116**] Wouk A., "A course of applied functional analysis", *Wiley-Interscience* (1979)
[**117**] Mielke A. "Similarity renormalization of the electron-phonon coupling", *Ann. Physik (Leipzig)* **6**, 215 (1997)
[**118**] Kehrein S. K., Mielke A., "Diagonalization of system plus environment Hamiltonians", *J. Stat. Phys.* **90**, 889 (1998)
[**119**] Wegner F., "Flow equations for Hamiltonians", *Phys. Rep.* **348**, 77 (2001)
[**120**] Stauber T., Mielke A., "Flow equations for Hamiltonians: Contrasting different flow equations for a numerically solvable model", *J. Phys. A* **36**, 2707 (2003)
[**121**] Wilkins M. R., Ou K., Appel R. D., Sanchez J.-C., et *al.*, "Rapid protein identification using N-terminal "sequence tag" and amino acid analysis", *Biochem. Biophys. Res. Commun.* **221**, 609 (1996)
[**122**] Eisenhaber F., Imperiale F., Argos P., Froemmel C., "Prediction of secondary structural content of proteins from their amino acid composition alone. I. New analytic vector decomposition methods", *Proteins: Struct. Funct. Design* **25**, 157 (1996) N2
[**123**] Eisenhaber F., Froemmel C., Argos P., "Prediction of secondary structural content of proteins from their amino acid composition alone. II. The paradox with secondary structural class", *Proteins: Struct. Funct. Design* **25**, 169 (1996) N2
[**124**] Kong J., Chapline M. G., Dai H., "Functionalized carbon nanotubes for molecular hydrogen sensors", *Adv. Mater.* **13**, 1384 (2001)

[**125**] Collins P. G., Bradley K., Ishigami M., Zettl A.., "Extreme oxygen sensitivity of electronic properties of carbon nanotubes", *Science* **286**, 1801 (2000)
[**126**] Star A., Han T.-R., Gabriel J.-C. P., Bradley K., and Grüner, G. "Interaction of aromatic compounds with carbon nanotubes: Correlation to the Hammett parameter of the substituent and measured carbon nanotube FET response", *Nano Lett.* **3**, 1421 (2003)
[**127**] Star A., Gabriel J.-C. P., Bradley K., and Grüner, G., "Electronic detection of specific protein binding using nanotube FET devices", *Nano Lett.* **3**, 459 (2003)
[**128**] Morozov A. V., Misura K. M. S., Tsemekhman K., and Baker D., "Comparison of quantum mechanics and molecular mechanics based energy landscapes for interactions between pairs of ring containing amino acids in proteins", *J. Phys. Chem. B* **108**, 8489 (2004)
[**129**] Gervasio F. L., Procacci P., Cardini G., Guarna A., Giolitti A., "Interaction between aromatic residues. Molecular dynamics and ab initio exploration of the potential energy surface of the Tryptophan-Histidine pair", *J. Phys. Chem. B* **104**, 1108 (2000)
[**130**] Misura K. M. S., Morozov A. V., Baker D., "Analysis of anisotropic side-chain packing in proteins and application to high-resolution structure prediction", *J. Mol. Biol.* **342**, 651 (2004)
[**131**] Sinnokrot M. O., Valeev E. F., and Sherrill C. D., "Estimates of the ab initio limit for pi-pi interactions: The benzene dimer", *J. Am. Chem. Soc.* **124**, 10887 (2002)
[**132**] Ortmann F., Schmidt W. G., and Bechstedt F., "Attracted by long-range electron correlation: Adenine on graphite", *Phys. Rev. Lett* **95**, 186101 (2005)
[**133**] Boys S. F. and Bernardi F., "The calculation of small molecular interactions by the differences of separate total energies. Some procedures with reduced errors", *Mol. Phys.* **19**, 553 (1970)
[**134**] Triozon F. and Roche S., "Efficient linear scaling method for computing the Landauer-Büttiker conductance ", *Eur. Phys. J. B* **46**, 427 (2005)
[**135**] Tournus F. and Charlier J.-C., "Ab initio study of benzene adsorption on carbon nanotubes", *Phys. Rev. B* **71**, 165421 (2005)
[**136**] Tournus F., Latil S., Heggie M. I., and Charlier J.-C., "π-stacking interaction between carbon nanotubes and organic molecules", *Phys. Rev. B* **72**, 075431 (2005)
[**137**] Gutierrez R., Fagas G., Cuniberti G., Grossmann F., Schmidt R., and Richter K., "Theory of an all-carbon molecular switch", *Phys. Rev. B* **65**, 113410 (2002)

[**138**] Triozon F., Lambin Ph., Roche S., "Electronic transport properties of carbon nanotube based metal/semiconductor/ metal intramolecular junctions", *Nanotechnology* **16**, 230 (2005)
[**139**] Reich S., Maultzsch J., Thomsen C., Ordejon P., "Tight-binding description of graphene", *Phys. Rev. B* **66**, 035412 (2002)
[**140**] Haydock R., "The recursive solution of the Schrödinger equation", *Comput. Phys. Commun.* **20**, 11 (1980)
[**141**] Lopez Sancho M. P., Lopez Sancho J. M. and Rubio J., "Quick iterative scheme for the calculation of transfer matrices: Application to Mo (100)", *J. Phys. F: Met. Phys.* **14**, 1205 (1984)
[**142**] Braun R., Sarikaya M., and Schulten K., "Genetically engineered gold-binding polypeptides: Structure prediction and molecular dynamics", *J. Biomat. Sci.* **13**, 747, (2002)

MODÉLISATION DE DISPOSITIFS À BASE DE NANOTUBES DE CARBONE POUR LA DÉTECTION DE BIOMOLECULES

RÉSUMÉ: À seulement quinze ans après leur découverte par Sumio Iijima, les nanotubes de carbone sont devenus un des piliers de la nanotechnologie. La géométrie parfaite et la nature unidimensionnelle confère aux nanotubes des propriétés structurelles, mécaniques, électroniques et optiques exceptionnelles. En conséquence, on s'attend à ce que les nanotubes envahissent des applications clef telles que les écrans à émission de champ, le stockage d'énergie, les composites structuraux, la nanoélectronique, les capteurs et les actuateurs, etc.

Cette thèse porte sur l'application de nanotubes de carbone dans le captage biochimique. Son but principal est d'utiliser et d'étendre les outils théoriques des nanotubes pour la conception des dispositifs de captage. Dans cette thèse nous proposons deux architectures différentes de captage. Le premier implique un principe électromécanique et peut être employé dans la mesure des forces faibles (~piconewtons) ou la détection des supramolécules (~zeptogrammes). Le deuxième capteur est basé sur le changement de conductance d'un nanotube de carbone exposé aux acides aminés aromatiques. La validation de ces deux architectures différentes est réalisée à l'aide de la modélisation et de la simulation.

L'effort principal de cette thèse a été concentré sur le développement de méthodes de simulation très efficaces par rapport au grand nombre d'atomes employés. Un problème récurrent que nous avons rencontré est le scaling cubique dans le nombre d'atomes, du calcul de la conductance quantique. Nous sommes parvenus à rendre le calcul de la conductance linéaire par des techniques d'espace réel.

MOTS CLÉS: nanotubes de carbone, biocapteurs, dynamique moléculaire, transport quantique, NEMS

MODELING OF CARBON NANOTUBE-BASED DEVICES FOR THE DETECTION OF BIOMOLECULES

ABSTRACT: At only fifteen years after their discovery by Sumio Iijima, carbon nanotubes can be considered as one of the support pylons of nanotechnology. The seamless geometry and one-dimensional nature confers to carbon nanotubes exceptional structural, mechanical, electronic and optical properties. Accordingly, nanotubes are expected to pervade key applications such as field emission displays, energy storage, structural composites, nanoelectronics, sensors and actuators, etc.

This thesis focuses on the possible application of carbon nanotubes in biochemical sensing. Its main goal is to employ and extend the theoretical tools of nanotubes in designing sensing devices. Two different sensor architectures are proposed in this thesis. The first involves an electromechanical principle and can be used in measuring either piconewton forces or zeptogram masses. The second sensor is based on conductance changes of a carbon nanotube when exposed to aromatic amino acids. The validation of these two different architectures is achieved via modeling and simulation at various levels of theory.

The main effort of this thesis went into developing highly efficient simulation approaches to cope with the large number of atoms that a typical sensing device has. One of the recurrent problems we have encountered is a certain square or cubic scaling in the number of atoms when computing the quantum conductance. We have managed to render the conductance calculation linearly scaling by real-space partitioning techniques.

KEYWORDS: carbon nanotubes, biosensors, molecular dynamics, quantum transport, NEMS

Techniques de l'Informatique et de la Microélectronique pour l'Architecture d'Ordinateurs, TIMA - 46 Av. Félix Viallet, 38031 Grenoble Cedex

ISBN : 2-84813-086-5